Proceedings of EUROMECH Colloquium 603

Dynamics of micro and nano electromechanical systems: multi-field modelling and analysis

Editors

Pedro Ribeiro

Stefano Lenci

Sondipon Adhikari

2018

Proceedings of EUROMECH Colloquium 603, Dynamics of micro and nano electromechanical systems: multi-field modelling and analysis, held in Porto, Portugal, 5 – 7 September 2018

Edited by

Pedro Ribeiro • Stefano Lenci • Sondipon Adhikari

Publisher: Universidade do Porto. Reitoria

3 September 2018

Porto, Portugal

ISBN 978-989-746-185-9

Colloquium supported by

SciTech

NORTE 2020 PROGRAMA OPERACIONAL REGIONAL DO NORTE

PORTUGAL 2020

União Europeia

Fundo Europeu de Desenvolvimento Regional

U.PORTO

FEUP FACULDADE DE ENGENHARIA UNIVERSIDADE DO PORTO

EUROPEAN MECHANICS SOCIETY

Santander Universidades
Reitoria da U. Porto and Banco Santander

Preface

This book of proceedings contains the texts supporting the three invited lectures (IL) and forty three regular communications that constituted the program of *EUROMECH Colloquium 603*, *Dynamics of micro and nano electromechanical systems: multi-field modelling and analysis*, held from the 5th to the 7th of September, 2018, at the Faculty of Engineering, University of Porto, Portugal. Regular communications range from extended abstracts (EA) with two pages to short papers (SP) with four pages. In this book, EA and SP are ordered according to their number, which follows the submission sequence.

The colloquium was devoted to the discussion of analysis, characterization, modelling, application and design of electromechanical dynamical systems with dimensions of a few micro or nanometres. The following interconnected topics were addressed:

- modelling and analysis of small-scale structures, using non-classical continuum theories - as couple stress theories and non-local theories – or molecular dynamics;
- multi-field modelling at small length scales, where piezoelectric or electrostatic sensing/actuation, van der Waals forces, Casimir forces or fluid–structure interactions are considered;
- analysis of linear and non-linear dynamics of micro and nano electromechanical systems, including investigations addressing damping, modes of vibration, internal resonances, contact and non-smooth dynamics, stability and chaotic dynamics.

We are very grateful to the invited lecturers, authors, participants, members of the scientific committee, session chairs, local organiser and reviewers for their important contributions to the colloquium. We would also like to sincerely thank the institutions that supported or sponsored the event.

Pedro Ribeiro, Stefano Lenci and Sondipon Adhikari

Organisers and Committees

Chair

- Pedro Ribeiro, Faculdade de Engenharia da Universidade do Porto, Portugal

Co-chairs

- Sondipon Adhikari, Swansea University, UK
- Stefano Lenci, Università Politecnica delle Marche, Italy

Scientific Committee

- Adrian Bachtold, ICFO - The Institute of Photonic Sciences, Spain
- Alberto Corigliano, Politecnico di Milano, Italy
- Anil Bajaj, Purdue University, USA
- Eihab M. Abdel-Rahman, University of Waterloo, Canada
- Hiroshi Yabuno, University of Tsukuba, Japan
- Holm Altenbach, Otto von Guericke University Magdeburg, Germany
- J. N. Reddy, Texas A&M University, USA
- Narayana R. Aluru, University of Illinois at Urbana-Champaign, USA
- Olivier Thomas, ENSAM - Arts et Métiers ParisTech, France
- Romesh C. Batra, Virginia Tech, USA
- Slava Krylov, Tel Aviv University, Israel
- Ulrich Schmid, Technische Universität Wien, Austria
- Urs Staufer, Delft University of Technology, The Netherlands

Local Organizer

- Hamed Akhavan, INEGI, Portugal

Reviewers

- Adrian Bachtold, Spain
- Alberto Corigliano, Italy
- Anil Bajaj, USA
- Atanas Popov, UK
- Eihab M. Abdel-Rahman, Canada
- Emil Manoach, Bulgaria
- Hamed Akhavan, Portugal
- Hiroshi Yabuno, Japan
- Mohammad Younis, Saudi Arabia and USA
- Oded Gottlieb, Israel
- Olivier Thomas, France
- Pedro Ribeiro, Portugal
- Peter Steeneken, The Netherlands
- Rob Fey, The Netherlands
- Slava Krylov, Israel
- Stefano Lenci, Italy
- Ulrich Schmid, Austria
- Urs Staufer The Netherlands

Contents

Preface iii

Organisers and Committees iv

Contents v

Invited Lectures

Number	*Title and authors*	*Page*
01	Nonlinear Dynamics of Thermo-visco-elastic Nano-opto-mechanical Panel Resonators: a multi-scale continuum mechanics coupled fields approach; E. Hollander and Oded Gottlieb	2
02	Dynamics-based micro and nano devices; Mohammad I. Younis	4
03	Dynamics of Graphene and 2D Materials; P.G. Steeneken, D. Davidovikj, R.J. Dolleman, F. Alijani and H.S.J. van der Zant	6

Extended Abstracts/Short Papers

Number	*Title and authors*	*Page*
04	Dynamical instability of pressurized electrically-actuated circular micro-plates; Pierpaolo Belardinelli, Banafsheh Sajadi, Stefano Lenci and Farbod Alijani	11
05	Analysis of micro plates with a modified couple stress theory and RBF-FD meshless method; Carla Roque	14
06	Observation of amplitude-dependent nonlinear damping in MEMS micro mirrors; Ulrike Nabholz, Frank Schatz, Jan E. Mehner and Peter Degenfeld-Schonburg	17
07	Printed Circuit Boards Experimental and Numerical Characterization; Carlos Castro, Pedro Bastardo, Sérgio Tavares and Paulo T. de Castro	21
08	Simulation of the electromechanical properties and strain-sensing response of CNT polymer composites; Miguel A. S. Matos, Vito L. Tagarielli and Silvestre T. Pinho	25
09	Atomistic modelling of hydrocarbon nanostructure failure; Mat Tolladay, Neil L. Allan, Dmitry Ivanov and Fabrizio Scarpa	28
10	Effect of nonlinear feedback control on a coupled cantilevers; Takumi Nakamura, Masatoshi Yano and Hiroshi Yabuno	32
11	Semi-analytic modeling and experiments of a collapse-mode CMUT with fluid coupling; R.H.B. Fey, M. Pekař, S.H.M. van Nispen, S. Shulepov, N. Mihajlović and H. Nijmeijer	34
12	Theoretical Framework for modelling the fluid-structure interaction of complex MEMS/NEMS resonator eigenmodes; Daniel Platz, Georg Pfusterschmied and Ulrich Schmid	38
13	Experimental and theoretical investigation of a microbeam-based MEMS device with half electrode configuration; Laura Ruzziconi, Nizar Jaber, Lakshmoji Kosuru, Mohammed L. Bellaredj, Stefano Lenci and Mohammad I. Younis	41
14	On nonlinear vibrational properties of graphene-based structures; Reza Ghaffari, Aningi Mokhalingam, Shakti S. Gupta and Roger A. Sauer	43
15	Finite elements based reduced order models for nonlinear dynamics of piezoelectric and dielectric laminated micro/nanostructures; O. Thomas, A. Givois, A. Grolet, J.-F. Deü, C. Fuinel, F. Mathieu and B. Legrand, L. Nicu	47
16	Analysis of isolated solutions in a symmetric MEMS array during symmetry breaking event using NNM; C. Grenat, S. Baguet, R. Dufour and C-H. Lamarque	51
17	Dynamic response of a piecewise linear MEMS oscillator; Andrea Guerrieri, Attilio Frangi, Valentina Zega and Luca G. Falorni	55

18	Shock response of a ring-based coriolis vibrating gyroscope under nonlinear electrostatic excitation; B. Chouvion, S. McWilliam and A.A. Popov	59
19	Frequency modulated (FM) micro-gyroscopes: recent advances; Valentina Zega, Claudia Comi, Paolo Minotti, Giacomo Langfelder, Luca Falorni and Alberto Corigliano	63
20	Mechanical non-linearity effects in supported MEMS ring-based resonators; Violetta Di Napoli, Stewart McWilliam and Atanas A. Popov	67
21	Measured and simulated tri-stability in MEMS capacitive switches; Devin Kalafut, Anil Bajaj and Arvind Raman	71
22	Experiments on nonlinear characteristics of parametric resonance in microcantilever; Shouhou Tei and Hiroshi Yabuno	74
24	Array of nanostrings electromagnetically coupled through repelling Lorentz forces; Slava Krylov and Rivka Gilat	76
26	Feasibility study of a resonant accelerometer with bistable electrostatically actuated cantilever as a sensing element; Omer HaLevy, Naftaly Krakover and Slava Krylov	80
27	Pressure drop measurements in microchannels: influence of the tap design; Tomás R. Pinto and Laura Campo-Deaño	84
29	Electrostatic arch micro-tweezers; Ayman M. Alneamy, Mahmoud E. Khater, Ahmed K. Abdel Aziz, Glenn R. Heppler and Eihab M. Abdel-Rahman	88
30	Dynamic behaviour of two cantilevers partially immersed in glycerol; N.Wagner, S. Gutschmidt, and T. Sattel	92
31	Graphene-based broadband high-frequency ultrasound detector; Gerard J. Verbiest, Jan N. Kirchhof, Matthias Goldsche, Jens Sonntag, Tymofiy Khodkov and Christoph Stampfer	96
32	Dynamics of very viscous flow in deformable microchannels under impact loads; L. Parras and F.J. Galindo-Rosales	100
33	An overview on dynamical behavior and control of an atomic force microscopy (AFM) taking into account the forces of Van Der Walls and fractional-order; José M. Balthazar, Angelo M. Tusset, Rodrigo T. Rocha, Frederic C. Janzen and Átila M. Bueno	104
34	A note on dynamics and control of a MEMS oscillator with chaotic behavior; Angelo M. Tusset, Giane G. Lenzi, Stefania Specchia, Rodrigo T. Rocha and José M. Balthazar	108
35	Free, geometrically non-linear, periodic vibrations of non-local plates by a mixed model; Pedro Ribeiro and Tomás Chuaqui	112
36	Multiple scales analysis of MEMS resonators under the simultaneous excitation of subharmonic and primary resonances; Saad Ilyas, Feras K. Alfosail and Mohammad I. Younis	116
37	Investigating the phenomenon of mode localization in electrostatically and mechanically coupled MEMS resonators; Saad Ilyas and Mohammad I. Younis	118
38	Structure and properties of helical carbon nanotubes using MM simulations; Akshay Dahiya, Shakti S. Gupta and Romesh C. Batra	120
39	Toward electrostatic atomic force microscopy; Hamidreza Nafissi, Ayman Alneamy, Eihab Abdel-Rahman and Raafat Mansour	124
40	Squeeze film damping control of a piezoresistive micro accelerometer for neurological disease diagnosis, S. Biswas and A. K. Gogoi	129
41	Nonlinear interaction of a pair of nano/micromechanical resonators with different decay rates far away from internal resonance; Oriel Shoshani, StevenW. Shaw and Mark I. Dykman	133
42	Gas flow in a micro-channel with an elastic obstacle; Kiril Shterev, Emil Manoach and Stefan Stefanov	137

43	Free, periodic, large amplitude vibrations of small-scale piezoelectric beams by a modified couple stress theory; Batool Soleimani Roody, Hamed Akhavan, Pedro Ribeiro and Ali Reza Fotuhi	141
44	Ballistic thermal transport in two-dimensional MoSe2 lattices; Nicolas Morell, Slaven Tepsic, Antoine Reserbat-Plantey, Andrea Cepellotti, Marco Manca, Andreas Isacsson, Xavier Marie, Francesco Mauri and Adrian Bachtold	145
46	Vibrational analysis of functionally graded nano-mass sensor based on a nonlocal continuum theory; Omid Rahmani, Ali R. Mohammadi Niaei, Amir H. Hosseini and Mahdi Faisal	147
47	Parametric study on buckling behavior of piezoelectric nanobeams based on nonlocal elasticity theory; Mehdi Yarmohammad Tooski, Ali Akbar Jandaghian and Omid Rahmani	151
48	On the quasiperiodic motion in nonlinear graphene resonators; Pierpaolo Belardinelli, Robin J. Dolleman, Peter G. Steeneken and Farbod Alijani	155
49	Molecular dynamics for characterization of probe-sample interaction in atomic force microscopy; Pierpaolo Belardinelli, Abhilash Chandrashekar, Urs Staufer and Farbod Alijani	159
50	Application of modified LuGre friction model to the analysis of friction-induced oscillations; Danylo Pikunov and Andrzej Stefanski	163

Author Index 167

Invited Lectures

EUROMECH Colloquium 603
Dynamics of micro and nano systems
5 – 7 September 2018, Porto, Portugal

Nonlinear dynamics of thermo-visco-elastic nano-opto-mechanical panel resonators: a multi-scale continuum mechanics coupled fields approach

E. Hollander and O. Gottlieb

Technion – Israel Institute of Technology, Haifa Israel
oded@technion.ac.il

Summary. We formulate a continuum mechanics-based nonlinear thermo-visco-elastic model for a thin panel under the influence of an electromagnetic field. The exciting field is constructed by constraining the light-structure interaction to the classical first order scattering phenomenon modelled as a spatiotemporal perturbation around a time-harmonic field. This coupled fields approach enables a consistent formulation of a dynamical system which incorporates both bolometric heating and radiation pressure. A numerical investigation reveals an intricate self-excited bifurcation structure that includes coexisting periodic limit-cycles, quasiperiodic energy transfer between coupled modes, and non-stationary chaotic dynamics.

Keywords: nonlinear dynamics, nano-opto-mechanical panels, coupled fields.

1 Introduction

Nonlinear macro-, micro- and nano- optomechanical resonators (OMRs) have been extensively studied in recent years due to their promising potential for non-intrusive sensing, quantum computing and optical tweezing. In a free-space OMR, a thin mechanical membrane panel is coupled to an optical cavity through Lorentz forces and bolometric heating. In the absence of external modulation, the interaction with these forces leads can lead to self-excitation of the resonator, in which a response to a continuous wave (CW) laser culminates with periodic limit-cycle oscillations beyond an equilibrium state stability threshold [1]. These self-excited oscillations can in-turn lose their orbital stability culminating with period-doubled and nonstationary chaotic dynamics in regimes governed by radiation pressure [2] or bolometric effects [3]. Characterizing these thresholds is crucial in explaining observed phenomena such as hysteresis, mode-hopping and optical cooling. To date, nonlinear lumped-mass models [4] that do not incorporate the spatiotemporal complexity of the coupled thermo-visco-elastic and electromagnetic (EM) fields have described the dynamics of OMRs. In addition, most researches have focused on cases in which only one of the forces (i.e. bolometric or radiation effects) is active and in the close vicinity of an optical resonance [5].

2 Problem Formulation

We thus derive a continuum mechanics-based nonlinear thermo-visco-elastic model for a thin panel under the influence of an EM field. The latter is constructed by constraining the light-structure interaction to the classical first order scattering phenomenon modelled as a spatio- spatiotemporal perturbation around a time-harmonic field. We employ a Galerkin procedure on the resultant fields (Fig. 1) and replace them with their time-dependent modal counterparts.

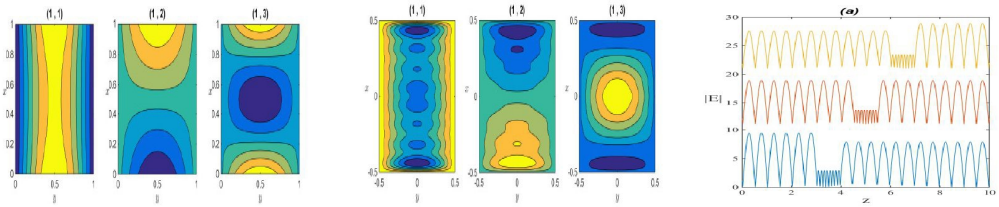

Figure 1. Mechanical (left), thermal (centre) and electric field (right) mode shapes.

3 Bifurcation Analysis

An investigation of a limiting planar bolometric case of an adiabatic EM field is used to validate experimental results [3], including hysteresis effects and mechanical mode-switching hopping that can lead to quasiperiodic torus breakdown and homoclinic chaos (Fig.2).

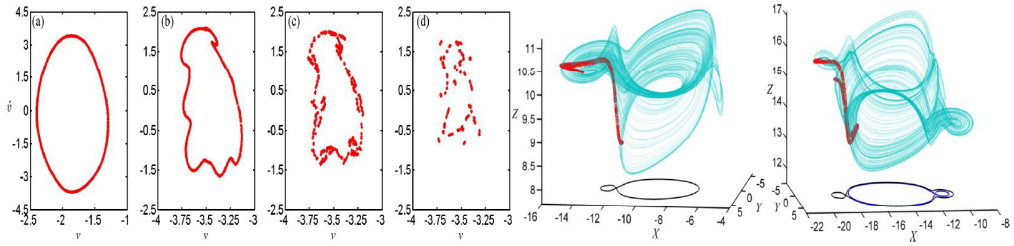

Figure 2. Poincare' sections demonstrating quasiperiodic torus breakdown (left), and a combined state-space and Poincare' map depicting two types of homoclinic chaos (right).

In regions governed by combined bolometric and radiation pressure induced oscillations, homoclinic connections ensue co-dimension two bifurcations including Bogdanov-Takens, and Zero-Hopf and saddle-node-homoclinic bifurcations. We show (Fig. 3) that for a range of control parameters a homoclinic loop of a saddle-focus elicit a global Shilnikov bifurcation which culminates with a distinct period-doubling route to chaos.

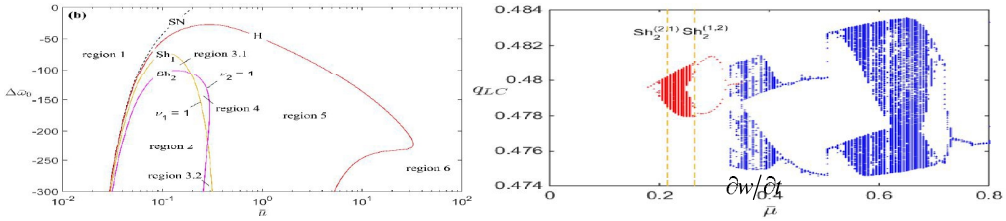

Figure 3. Co-dimension two stability map depicting Saddle-node (SN), Hopf (H) and Shilnikov (Sh) bifurcations (left), and a bifurcation diagram depicting a period-doubling route to chaos.

4 Closing Remarks

The results of this investigation reveal that a coupled fields approach enables a formulation of a dynamical system which consistently incorporates the effects of both bolometric heating and radiation pressure. A comprehensive bifurcation analysis reveals an intricate self-excited structure that includes coexisting periodic limit-cycles, quasiperiodic energy transfer between coupled modes, and non-stationary chaotic dynamics that may shed light on the discrepancies between experimental measurements and numerical simulations from qualitative lumped-mass models.

References

[1] S. Zaitsev, O. Gottlieb, E. Buks, Nonlinear dynamics of a microelectromechanical mirror in an optical cavity. Nonlinear Dynamics, **69**, 1589-1610, 2012.

[2] L Bakemeier, A. Alvermann, H. Fehske, Routes to chaos in optomechanics, Physical Review Letters, 114, 01360, 2015

[3] E. Hollander, O. Gottlieb, Self-excited chaotic dynamics of a nonlinear thermos-visco-elastic system that is subject to laser irradiation, Applied Physics Letters 101, 133507, 2012.

[4] D. Blocher, R.H. Rand, A.T. Zehnder, Multiple limit-cycles in laser interference transduced resonators, International Journal of Non-Linear Mechanics, 52, 119-126, 2013.

[5] D. Lee, M. Underwood, D. Mason, A.B. Shkarin, S.W. Hoch, J.G.E. Harris, Multimode optomechanical dynamics in a cavity with avoided crossings, Nature Communications, **6**, 6232, 2015.

Dynamics-based micro and nano devices

Mohammad I. Younis

Physical Sciences and Engineering Division, King Abdullah University of Science and Technology, Thuwal, Saudi Arabia
mohammad.younis@kaust.edu.sa

Department of Mechanical Engineering, State University of New York at Binghamton, Binghamton, 13902 NY, USA
myounis@binghamton.edu

Summary.

In this talk, we will demonstrate experimentally and theoretically several intriguing nonlinear dynamical phenomena at the micro and nano scale, including internal resonances, veering and modal coupling, escape phenomena, and fractal behaviours. Also, we will show that by developing a proper understanding and deep insight of the dynamics and nonlinear mechanics at the micro and nano scale, new technological solutions and innovative ideas can be realized leading to new generations of superior devices. Applications will be shown including combined smart sensors and actuators; band-pass filters, and logic and memory devices.

Keywords: nonlinear dynamics, mode coupling, escape, MEMS, NEMS

1 Introduction

Miniature structures and devices have captured the attention of the scientific community for several decades for their unprecedented attractive features. Today, several micro-electro-mechanical systems MEMS devices are being used in our everyday life, ranging from accelerometers and pressure sensors in automobiles, radio-frequency (RF) switches and microphones in cell phones, and inertia sensors in video games. With the quest to boost sensitivity, reduce power consumption, and increase integration density, the past decade has witnessed the emergence of Nano-electro-mechanical systems NEMS [1]. Along with their great promise, micro and nano devices have brought new challenges and wide spectrum of unexplained and less-understandable behaviours and phenomena. Because these devices employ moveable compliant structures, many of these challenges are related to their dynamical behaviour, which is mostly nonlinear. On the other hand, micro and nano systems have presented new opportunities to explore fundamental nonlinear dynamics phenomena through their well-controlled and highly flexible operating environment and experimental testing conditions.

2 Devices

This talk will feature several dynamically-based device concepts at the micro and nano scales. Examples based on linear dynamics principles include a tunable band pass filter based on electrothermal actuation [2] and electromechanical logic devices based on resonant structures, Figure 1 [3]. Also, nonlinear dynamics inspired micro and nano devices will be demonstrated, which include a smart microelectromechanical sensor and switch triggered by gas, Figure 2, [4], and band-pass filters of improved roll-off from the pass band to the stop band based on two separate nonlinear resonators [5] and based on a single resonator utilizing mode couple through the veering phenomenon [6].

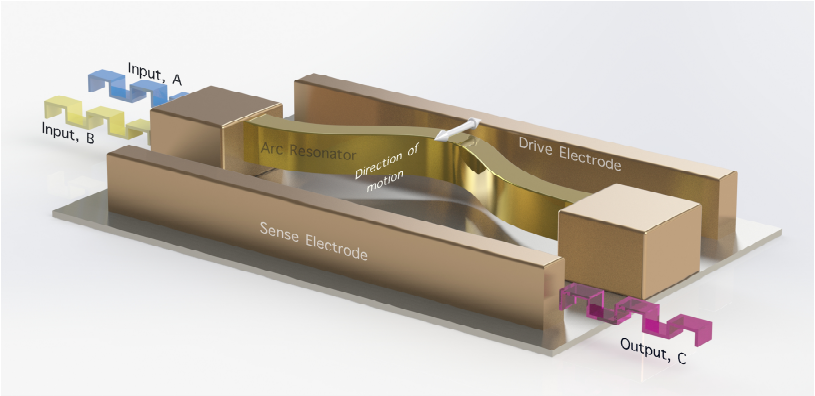

Figure 1. Schematic of an electromechanical logic device based on a micro resonant beam.

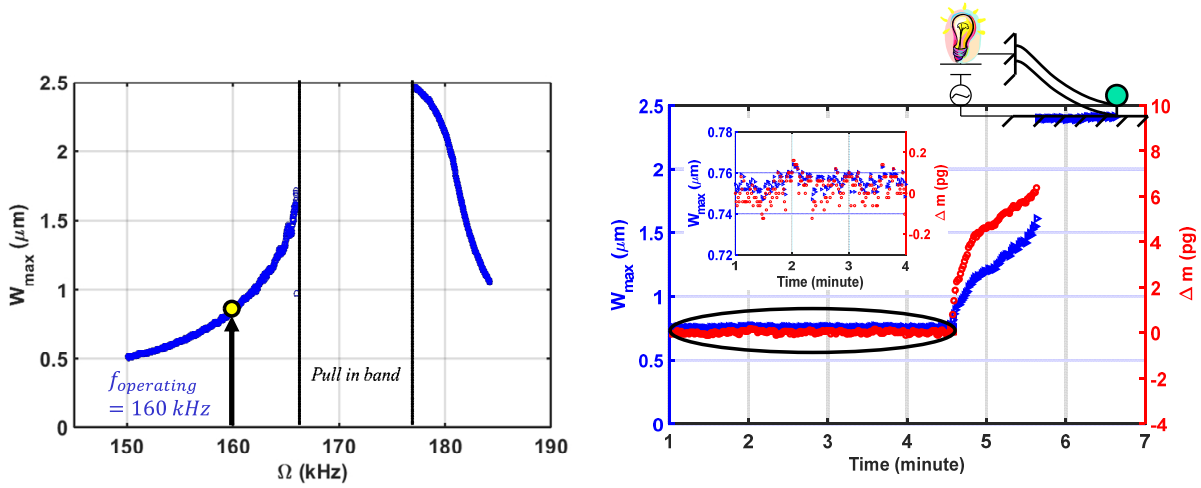

(a) (b)

Figure 2. (a) Frequency response near the first mode showing the softening behavior and the pull-in band. Also shown the operating point for the resonator before mass detection. (b) Real time measurement of the amplitude change due to water vapor exposure until pull in. Inset: the fluctuation due to noise.

References

[1] M. I. Younis, *MEMS Linear and Nonlinear Statics and Dynamics*, Springer, New York, 2011.
[2] M. A. A. Hafiz, L. Kosuru, A. Z. Hajjaj, and M. I. Younis, Highly Tunable Narrow Bandpass Filter Using MEMS resonators. *IEEE Transactions on Electron Devices*, **64**, 3392- 3398, 2017.
[3]M.A.A. Hafiz, L. Kosuru, M. I. Younis, Microelectromechanical reprogrammable logic device. *Nature Communications*, **7**:11137. doi: 10.1038/ncomms11137, 1-9, 2016.
[4] N. Jaber, S. Ilyas, O. Shekhah, M. Eddaoudi, and M. I. Younis, Resonant Gas Sensor and Switch Operating in Air with Metal-Organic Frameworks Coating. *Journal of Microelectromechanical systems*, **27**, 156-163, 2018.
[5] S. Ilyas, K. N. Chappanda, M. I. Younis, Exploiting nonlinearities of micro-machined resonators for filtering applications. *Applied Physics Letters*, **110**, 253508, 1-4, 2017.
[6] A. Z. Hajjaj, M. A. Al Hafiz, M. I. Younis, Mode Coupling and Nonlinear Resonances of MEMS Arch Resonators for Bandpass Filters. *Scientific Reports*, **7**, 41820, doi:10.1038/srep41820, 2017.

Dynamics of graphene and 2D materials

P.G. Steeneken[1,2], D. Davidovikj[2], R.J. Dolleman[2], F. Alijani[1] and H.S.J. van der Zant[2]

[1]Dept. of Precision and Microsystems Engineering, Delft University of Technology, The Netherlands
[2]Kavli Institute of Nanoscience, Delft University of Technology, The Netherlands
p.g.steeneken@tudelft.nl

Summary. Suspended graphene and 2D materials open up the possibility to study the dynamics of membranes of only one atom thick. The dynamics of these systems is governed by phenomena that are unique to the nanoscale: for large vibration amplitudes, graphene shows strong nonlinearities that result in spring hardening, nonlinear damping and parametric resonances. At small amplitudes, the dynamics of graphene becomes strongly interlinked with its thermodynamics, and is influenced by entropic effects. In this work, a short overview is given of our recent progress to elucidate these phenomena.

Keywords: Dynamics, graphene, 2D materials

1 Introduction

At first glance, the dynamics of membranes with a thickness of one atom does not seem that special. However, during the last decade, it has become apparent that the motion of graphene is clearly different from macroscopic membranes. These differences can be mainly accounted for by a combination of thermodynamics and the unique properties of graphene, including its low areal mass density ρ_A ~7.5 kg/m^2, low flexural rigidity D ~1 eV, high Young's modulus E_Y ~1 TPa and high breaking strain $\varepsilon_{\max}$ ~10%.

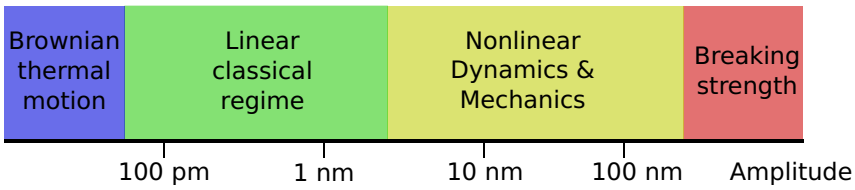

Figure 1. Typical regimes that can be distinguished in the dynamics of a 5 μm diameter circular graphene membrane at room temperature, as a function of the vibration amplitude of its fundamental mode.

Different regimes can be distinguished in the dynamics of circular graphene membranes at room temperature, depending on their vibrational amplitude (Fig. 1). Even in the absence of actuation forces, a 5 μm diameter membrane displays thermal vibrations of the order of 50 pm [1], due to its Brownian motion. For driving forces up to ~1 nN, the membrane is in the linear regime after which it enters the nonlinear dynamics regime at amplitudes of only a few nm. At even larger amplitudes the membranes might break, as has been demonstrated by static means using atomic force microcopy (AFM) [2], but which has not been directly observed yet in dynamics experiments. In the following sections we give an overview of our recent work studying the dynamics of 2D membranes in these different regimes.

2 Graphene membrane fabrication and imperfections

The prototype of a graphene resonator is a circular membrane. A circular membrane is ideal, because it avoids bending and folding of graphene at free edges and sharp corners that can result in folds and wrinkles; moreover it facilitates analytical studies. Ideally, structures as in Fig. 2 (left) are fabricated, however, when inspecting the surface of an actual circular graphene drum, imperfections are often found. As an example, the right side of Fig. 2 shows an AFM measurement of a suspended graphene drum with a diameter of 5 microns showing a large number of wrinkles and imperfections with amplitudes

up to 20 nm. Root causes for these wrinkles include non-uniform forces during the transfer process, height imperfections at the edge of the membrane cavity and particles/growth imperfections in and on the graphene itself. Normally, the membranes display tensile stress after fabrication, as is found from their resonance frequency. The source of the stress is partly the transfer process, however, we hypothesise that even if this source of stress can be eliminated, self-tensioning of the membrane, by edge adhesion forces, wrinkling or thermodynamic effects could prevent the membrane from buckling.

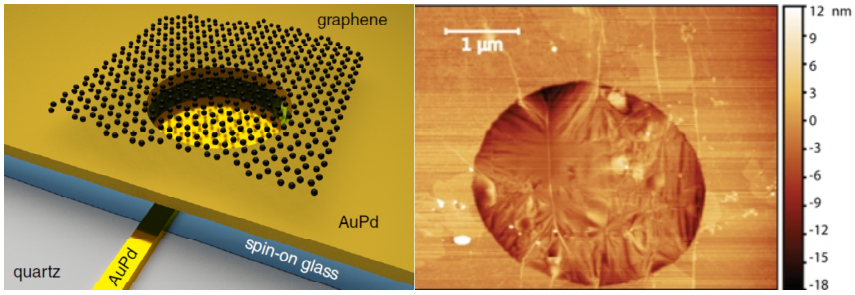

Figure 2. Left: A single layer of graphene is transferred and suspended over a hole in a substrate (adapted from [3]). Right: A false coloured AFM image highlighting the nanometer scale wrinkles and imperfections that can be found on a suspended CVD graphene membrane [4].

3 Linear dynamics and Brownian motion

Despite these imperfections and nanometer scale thicknesses, the dynamics of graphene membranes can still be described by classical dynamics. As shown in Fig. 3, the mode shapes of these devices [1] closely resemble the theoretical solutions of the membrane equation. Due to the low stiffness of the membrane, the amplitudes due to its Brownian motion are about 10 pm and can be detected using an interferometric technique. It is observed that imperfections do cause larger deviations at higher mode numbers. Better control over transfer techniques and graphene growth is needed to fabricate devices that resemble ideal membranes even more closely.

On top of the static tension applied during fabrication, it has been hypothesised that thermal fluctuations might also result in tension fluctuations in ultrathin strings and membranes [5]. This would result in random time variations of the membrane's resonance frequency and thus cause a broadening of the peak in a measurement of its frequency response curve. Potentially, this broadening can affect the value of the mechanical quality-factor Q determined from frequency response measurements. Comparisons between frequency-response and ring-down measurements of graphene resonators have not yet allowed discerning this effect.

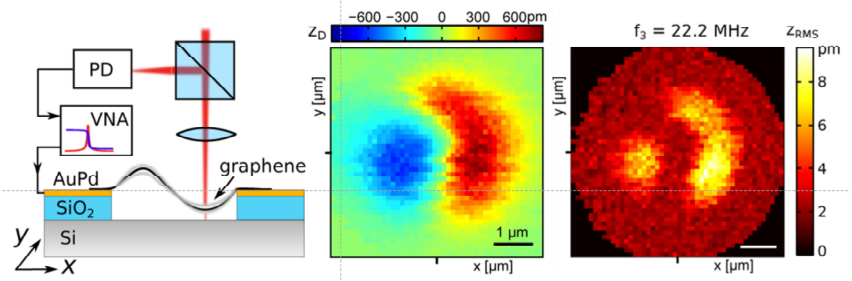

Figure 3. Using an interferferometric setup (left) the mode shapes of a graphene membrane can be visualized [1]using actuation by electrostatic force (middle) or by monitoring its intrinsic Brownian motion at room temperature (right).

4 The interplay between dynamics and thermodynamics in 2D materials

In general, the dynamics of graphene membranes cannot be studied separately from its thermodynamics at room temperature. Although it is experimentally difficult to study the deviations from classical behaviour caused by the tiny thermal fluctuations of the membrane in thermal equilibrium, molecular dynamics (MD) simulations can provide much insight. By MD, it has been shown that graphene's resonance frequencies deviate from that of an ideal membrane. Although the lowest resonance modes are relatively close to ideal membrane modes, already before the 10^{th} mode clear deviations from membrane behaviour can be observed. These deviations can be attributed to an effective bending rigidity of graphene, and have been extracted by analysis of the FFT of the MD simulations [6]. In contrast to macroscale systems, the bending rigidity is not constant, but depends strongly on membrane size and temperature. This is a consequence of entropic effects, where the bending of graphene does not only induce an increase in potential energy, but also causes a reduction in entropy, analogous to other entropic springs, like a rubber band, where the entropy reduction is due to the stretching of polymer changes.

Using a new method, that involves modulation of the laser intensity at high frequency [7], we also studied the dynamic heat transport in suspended graphene. The time-dependent temperature was monitored via its effect on the motion of the membrane, caused by thermal expansion. From a frequency scan, a thermal cut-off frequency can be determined. Above this frequency, which corresponds to a thermal time-constant τ_{th}, the membrane has no time to heat up completely. The thermal time-constant $\tau_{th} = R_{th}C_{th}$ is a product of an effective thermal resistance R_{th} and a thermal capacitance C_{th} and can thus be used to determine the heat capacitance of 2D materials [8]. Interestingly, the thermal time-constant of graphene appears to be significantly lower than expected from theory. This might be due to reduced phonon transmission at the membrane edges, but could also point towards a larger thermal capacitance, due to imperfections or contamination.

5 Nonlinear dynamics

Suspended 2D materials show geometric nonlinearities at driving forces of only a few picoNewtons (Fig. 4). Of course this is partly due to their extreme atomic thickness (t=0.335 nm for graphene), such that amplitudes of only a few nanometers already cause nonlinearities. Another cause for the strong nonlinearity is the high Young's modulus of graphene of the order of 1 TPa, which causes a small strain due to deflection, to be transformed into a large stress.

Although spring hardening nonlinearities in graphene resonators had been observed before, they have only recently been analyzed quantitatively [9]. The nonlinearities shown in Fig. 4 can thus provide a fast and non-contact method to determine the Young's modulus of graphene. In comparison to AFM this eliminates issues related to high stresses, deformations and adhesion effects near the AFM tip. Moreover, it allows distinguishing the high-frequency mechanics and damping from the static mechanical properties.

Besides direct actuation, graphene can also be very efficiently driven parametrically using optothermal methods [10]. When graphene is heated by a laser a large change in the tension is a result of the combination of the high Young's modulus with the membrane's thermal expansion. A temperature change of 1 K can thus result in a change in resonance frequency of 10-100 %. Thus, despite the relatively low Q-factor of the graphene membranes, a record of 14 parametric resonance modes have been excited. The shape of the nonlinear parametric response does not only provide information on the nonlinear stiffness, but also on the nonlinear damping in 2D materials.

6 Outlook and applications

Besides fundamental interest, the dynamics of 2D materials also provides a strong potential for new applications. Since the flexible membranes are extremely sensitive to small forces, they can be used for novel sensors. First steps in this direction have been set by using graphene as a pressure sensor and osmotic gas sensor [3, 11, 12]. The high flexibility also allows for an efficient force transduction as was demonstrated by high-frequency pneumatic actuation using graphene gas pumps [13]. The membranes

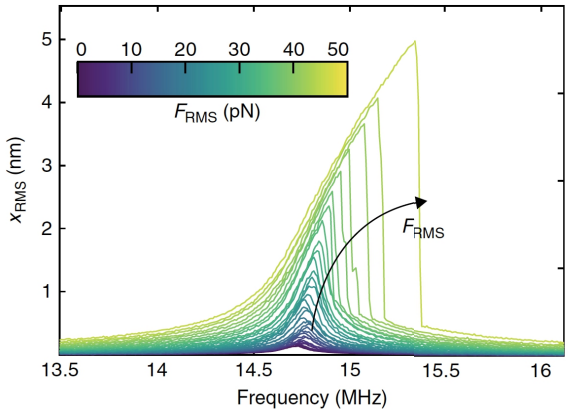

Figure 4. Nonlinear spring hardening of a 5 μm diameter graphene drum with a thickness of 5 nm, driven by electrostatic forces (adapted from [9]).

can also be actuated and tension modulated by on-chip heaters [14], and have been shown to function as arrays for optical modulation of light [15].

We hope to have shown, that the theory, characterization and application of the dynamics of 2D materials, offers interesting challenges and opportunities for scientific discovery and innovation. This work is funded by NWO (project 13307) and by the EU (grant 785219 Graphene Flagship).

Acknowledgments

We would like to acknowledge the contributions of many coworkers that have contributed to the referenced works in this overview.

References

[1] D. Davidovikj, J.J. Slim, S.J. Cartamil-Bueno, H.S.J. van der Zant, P.G. Steeneken and W.J. Venstra, Visualizing the Motion of Graphene Nanodrums. *Nano Letters*, Vol. 16, pp. 2768-2773, 2016.

[2] C. Lee, X. Wei, J.W. Kysar and J. Hone, Measurement of the Elastic Properties and Intrinsic Strength of Monolayer Graphene. *Science*, Vol. 321, pp. 385-388, 2008.

[3] D. Davidovikj, P.H. Scheepers, H.S.J. van der Zant and P.G. Steeneken, Static capacitive pressure sensing using a single graphene drum. *ACS Applied Materials and Interfaces*, Vol. 9, pp. 43205-43210, 2017.

[4] I.E. Roslon, MSc. thesis TU Delft, 2018.

[5] A.W. Barnard *et al.*, Fluctuation broadening in carbon nanotube resonators. *PNAS*, Vol. 109, pp 19093-19096, 2012.

[6] B. Sajadi, S. van Hemert, B. Arash, P. Belardinelli, P.G. Steeneken and F. Alijani, Size-and temperature-dependent bending rigidity of graphene using modal analysis. *Carbon*, Vol. 139, pp. 334-341, 2018.

[7] R.J. Dolleman, S. Houri, D. Davidovikj, S.J. Cartamil-Bueno, Y.M. Blanter, H.S.J. van der Zant and P.G. Steeneken , Optomechanics for thermal characterization of suspended graphene. *Physical Review B*, Vol. 96, 165421, 2017.

[8] R.J. Dolleman, D. Lloyd, J.S. Bunch, H.S.J. van der Zant and P.G. Steeneken, Transient thermal characterization of suspended monolayer MoS_2. *arXiv preprint*, 1806.10769, 2018.

[9] D. Davidovikj *et al.*, Nonlinear dynamic characterization of two-dimensional materials. *Nature Communications*, Vol. 8, pp. 1253, 2017.

[10] R.J. Dolleman, S. Houri, A. Chandrashekar, F. Alijani, H.S.J. van der Zant and P.G. Steeneken, Opto-thermally excited multimode parametric resonance in graphene membranes. *Scientific Reports*, Vol. 8, pp. 9366, 2018.

[11] R.J. Dolleman, D. Davidovikj, S.J. Cartamil-Bueno, H.S.J. van der Zant and P.G. Steeneken, Graphene squeeze-film pressure sensors. *Nano Letters*, Vol. 16, pp. 568, 2016.

[12] R.J. Dolleman, S.J. Cartamil-Bueno, H.S.J. van der Zant and P.G. Steeneken, Graphene gas osmometers. *2D Materials*, Vol. 4, 011002, 2017.

[13] D. Davidovikj, D. Bouwmeester, H.S.J. van der Zant and P.G. Steeneken, Graphene gas pumps. *2D Materials*, Vol. 5, 031009, 2018.

[14] D. Davidovikj, M. Poot, S.J. Cartamil-Bueno, H.S.J. van der Zant and P.G. Steeneken, On-chip Heaters for Tension Tuning of Graphene Nanodrums. *Nano Letters*, Vol. 18, pp. 2852, 2018.

[15] S.J. Cartamil-Bueno, D. Davidovikj, A. Centeno, A. Zurutuza, H.S.J. van der Zant, P.G. Steeneken and S. Houri, Graphene mechanical pixels for Interferometric MOdulator Displays (GIMOD). *arXiv preprint*, 1803.01883, 2018.

Extended Abstracts\ Short Papers

EUROMECH Colloquium 603
Dynamics of micro and nano systems
5 – 7 September 2018, Porto, Portugal

Dynamical instability of pressurized electrically-actuated circular micro-plates

Pierpaolo Belardinelli[1,2], **Banafsheh Sajadi**[1], **Stefano Lenci**[2] **and Farbod Alijani**[1]

[1]Precision and Microsystems Engineering, TU Delft, Delft, The Netherlands
p.belardinelli@tudelft.nl, b.sajadi@tudelft.nl, f.alijani@tudelft.nl

[2] DICEA, Polytechnic University of Marche, Ancona, Italy
lenci@univpm.it

Summary. This work presents an overview on the dynamic stability of electrically-actuated circular micro-plates by accounting for a differential pressure. The commonly observed pull-in instability evolves into a more complex scenario in which primary, secondary and ultimate saddle-node bifurcations characterize the device snap-through. The global dynamics of the micro-plate is investigated by making use of basins of attraction and integrity measures are accordingly evaluated. It is found that the device pressurization increases the complexity of the response in which flip bifurcations undermine the overall operational stability.

Keywords: Micro-plates, basins of attraction, bifurcation scenario, snap-through instability

1 Introduction

The fabrication of sensors and actuators based on Micro-Electro-Mechanical Systems (MEMS) [1, 2] requires a proper design for the realization of prototypes. Scientists and engineers are asked to provide insights and precise information regarding the final behaviour of the devices along with their characteristics and limitations. This is a stringent need because of the nonlinear response manifested by MEMS. The presence of nonlinearities, sometimes possible reason of failure status, is not always undesired. As a matter of fact, instability conditions can be exploited as driving mechanism to trigger switches and sensors [3].

Due to the complex response, the analysis of instability regions under a global perspective is of great importance. In details, bifurcation charts and basins of attraction represent tools to characterize the multistable behaviours and the evolution of a variety of attractors with respect to governing parameters [4].

The device analysed in this work behaves as the upper flexible electrode of a circular parallel-plate pressure sensor [5]. The combination of geometrical and elctrostatic-induced nonlinearities results in softening or hardening nonlinearity with configurations of instability (pull-in or snap-through) in which the electrode collapses to the ground reference. The micro-plate is subjected to differential pressure and is actuated with combined AC and DC voltages. This makes the overall dynamics close to bifurcation points very complex.

The governing equations of motion are obtained by using a Lagrangian approach. An accurate reduced order model is used to study the nonlinear dynamics of the device [6]. The numerical study is performed by making use of a pseudo arc-length continuation and collocation technique [7] to detect periodic solutions and instability points. The applied DC voltage and the device pressurization are shown to be the driven parameters for the device instability. Domains of attraction in the proximity of the pull-in are computed to evaluate the practical stability [8]. As a byproduct, this study uncovers the evolution of the global dynamics and how the applied load parameters significantly affect the pull-in mechanisms of the micro-plate. The method presented in this paper is to be used as a design tool for MEMS pressure sensors.

2 Problem formulation

A fully-clamped circular micro-plate is considered that is subjected to i) a positive outward differential pressure (P); ii) an electric potential (V) responsible for deformation in the opposing direction.

The total potential energy of the system is composed of: (i) the elastic deformation of the micro-plate (U_s) assuming the von Kármán plate theory [9], (ii) the electrostatic potential (U_e), (iii) and the potential due to the differential pressure (W).

Equations of motion are obtained by using a Lagrangian approach in which the Lagrangian of the system is $L = T - (U_s + U_e - W)$, with T being the kinetic energy of the plate. Assuming axisymmetric motion, Lagrange equations provide N algebraic equations in terms of the generalized radial coordinate and one nonlinear differential equation in terms of the axisymmetric transverse coordinate q. By means of a condensation procedure a single-degree-of-freedom equation can then be obtained as [10]:

$$\ddot{q}(t) + 2\zeta\omega_0\dot{q}(t) + \omega_0^2 q(t) = -\alpha_1 D q(t)^3 + \alpha_2 V(t)^2 \left(\frac{1-(q+1)F(q)}{2q(1+q)} \right) - \alpha_3 P, \tag{1}$$

in which ω_0 is the natural frequency of the circular clamped plate with bending stiffness D and ζ is the modal damping coefficient. The parameters $\alpha_{1,2,3}$ are the coefficients of geometric nonlinearity, the nonlinear electrostatic force and pressure, respectively. Finally, the term $F(q)$ arises from the integration of the electrostatic potential and it is approximated by a polynomial of 12^{th} order for the numerical analyses.

3 Numerical results

The micro-plate is assumed to be actuated by combined AC and DC voltages. The solution branches over a range of DC voltages are then obtained while keeping the AC component fixed. Moreover, the frequency of the excitation is set at the fundamental resonance of the non-pressurized plate.

In the absence of V_{AC} the system instability reduces to only a static pull-in. Conversely, the V_{AC} component undermines the stability of the device prior to the snap-through of the device. It also introduces a nonlinear resonance with a softening behaviour.

In the pull-in phenomenon the micro-plate collapses towards the reference electrode. This event occurs differently with respect to the shape of the deflection curve as a function of the DC voltage. In details, the plate can collapse directly to the fixed electrode or recover the stability over an additional stable state before the pull-in. The exact thresholds for the first, secondary, and ultimate instability points can be obtained only by means of pressure/voltage bifurcation charts. The analysis underlines the presence of lower and upper boundaries for the existence of a double snap-through of the micro-plate that is usually, characterized by a sole instability for low values of the differential pressure.

The micro-plate shows several period-doubling bifurcation points with the generation of stable period-2 branches. These undermine the continuity of the main stable response affecting the device integrity.

To illustrate the complexity induced by a progressive pressurization, Figure $1(a)$ presents secondary bifurcations of the period-doubled branch for the normalized deflection vs. V_{DC}. Additional bifurcations take place around the region with $P = 3140Pa$ in which a saddle (LP7) evolves towards a cross-shaped configuration. The figure shows three main saddle-nodes, namely LP7, LP9 and LP10. They are the vertexes of the cross-shaped bifurcation curve at $P = 3130Pa$. The stability of period-2 branch within LP7 and LP10 is broken with unstable and stable responses between the limit points LP13, LP14 and LP15. For a pressure of $3120Pa$ the response loses the cross-shaped configuration with only LP9 as the remaining saddle-node bifurcation.

In view of the intricate bifurcations scenario, the dynamical response cannot be assessed only by observing the local behaviour. In particular, the presence of the period-doubling bifurcations close to the primary instability modifies the dynamics of the system. For this reason, a proper global analysis based on basins of attraction has to be performed (see Figure $1(b)$). Figure $1(c)$ highlights the phase-space topology in proximity of the ultimate saddle-node point. The safe area shrinks and disappear leaving the device to an inevitable pull-in. Again it is observed that a period-2 attractor interrupts the evolution of the primary stable solution.

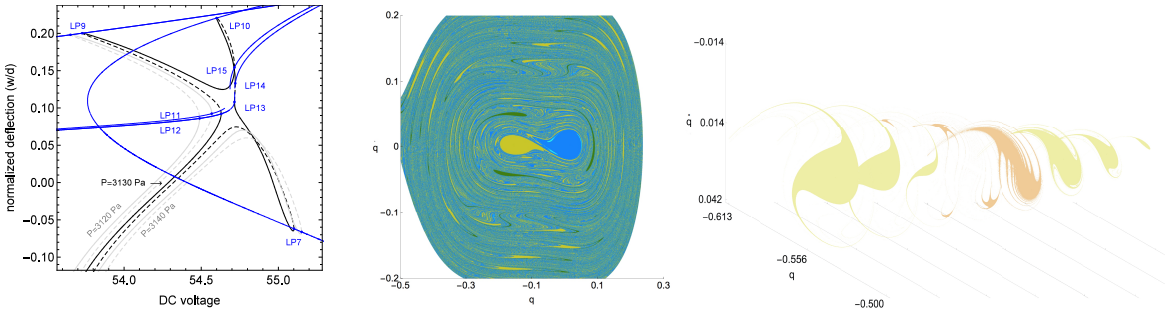

(a) (b) (c)

Figure 1: a) Complex bifurcation scenario for large values of the differential pressure. The figure show the deflection of the micro-plate normalized with respect to the gap d as function of the DC voltage (black lines). Dashed lines are unstable solutions. Blue lines sketch the loci of limit points (LP). b) Overall topology of the phase-space with the presence of multiple basins of attraction ($V_{DC} = 54.55V$, $P = 3300Pa$). c) Erosion of the safe basin in proximity of the micro-plate pull-in in presence of a flip bifurcation (yellow P-1 attractor, orange P-2 attractor). The sequence of the basins is with an increasing DC voltage.

4 Conclusions

The study of the dynamics of an electrically-actuated micro pressure sensor shows a complex scenario of multiple bifurcations in which, in particular, flip bifurcations are responsible for a severe degradation of the system stability. The global analysis performed with measure on basins of attraction highlights that small variations of the DC voltage can be responsible for a sensible reduction of the dynamical integrity.

References

[1] J. Sharma and A. Dasgupta. Effect of stress on the pull-in voltage of membranes for mems application. *Journal of Micromechanics and Microengineering*, **19**, 115021, 2009.

[2] H. Luo, G. Zhang, L. Carley, and G. Fedder. A post-CMOS micromachined lateral accelerometer. *J. Microelectromechanical Systems*, **11**, 188–195, 2002.

[3] J. F. Rhoads, S. W. Shaw, K. L. Turner, J. Moehlis, B. E. DeMartini, and W. Zhang. Generalized parametric resonance in electrostatically actuated microelectromechanical oscillators. *Journal of Sound and Vibration*, **296**, 797 – 829, 2006.

[4] S. Wiggins. *Introduction to Applied Nonlinear Dynamical Systems and Chaos*. Texts in Applied Mathematics. Springer, 2003.

[5] B. Sajadi, F. Alijani, H. Goosen, and F. van Keulen. Effect of pressure on nonlinear dynamics and instability of electrically actuated circular micro-plates. *Nonlinear Dynamics*, **91**, 21572170, 2018.

[6] G. W. Vogl and A. H. Nayfeh. A reduced-order model for electrically actuated clamped circular plates. *Journal of Micromechanics and Microengineering*, **15**, 684, 2005.

[7] E. J. Doedel, A. R. Champneys, T. F. Fairgrieve, Y. A. Kuznetsov, B. Sandstede, and X. Wang. Auto97, 1998.

[8] S. Lenci and G. Rega. Load carrying capacity of systems within a global safety perspective. Part II. Attractor/basin integrity under dynamic excitations. *International Journal of Non-Linear Mechanics*, **46**, 1240–1251, 2011.

[9] M. Amabili. *Nonlinear vibrations and stability of shells and plates*. Cambridge University Press, 2008.

[10] A. Nayfeh and P. Pai. *Linear and Nonlinear Structural Mechanics*. Wiley Series in Nonlinear Science. Wiley, 2008.

Analysis of micro plates with a modified couple stress theory and RBF-FD meshless method.

Carla M. Roque[1]

[1]INEGI, Porto, Portugal
croque@fe.up.pt

Summary. A modified couple stress theory and a meshless method is used to study the free vibration of simply supported micro isotropic plates. The modified couple stress theory involves only one length scale parameter and thus simplifies the theory, since experimentally it is easier to determine the single scale parameter. The numerical method is easy to implement and it provides accurate results that are in agreement with analytical solutions.

Keywords: Radial basis function, collocation method, finite differences.

1 Introduction

Experimental observations indicate that the mechanical behavior of micro and nano systems cannot be accurately simulated by using classical deformations theories. Due to the presence of scale effects, non classical models such the modified couple stress theory is used for analytical analyses. Unlike classical models, this theory contains an internal material length scale parameter that can capture size effects at the micro scale.

In the present work, the modified couple stress theory [1] and a meshless method is used to study the static behavior and free vibration of simply supported micro plates. The meshless method with collocation is used to solve the resulting boundary value problem, and the results are compared with Navier analytical solutions.

2 Modified Couple stress theory

The modified couple stress theory proposed by Yang has the advantage over the classical couple stress theory of involving only single scale parameter, l. A brief description of the modified couple stress theory is here presented. Further details can be found in [1] and [2, 3].

The strain energy for an isotropic linearly elastic material in domain Ω is:

$$\begin{aligned} U &= \int_\Omega \frac{1}{2}(\boldsymbol{\sigma} : \boldsymbol{\varepsilon} + \boldsymbol{m} : \boldsymbol{\chi}) dV \\ &= \int_\Omega \frac{1}{2}\lambda(tr\boldsymbol{\varepsilon})^2 + \mu(\boldsymbol{\varepsilon} : \boldsymbol{\varepsilon} + l^2\boldsymbol{\chi} : \boldsymbol{\chi}) dV \end{aligned} \tag{1}$$

where dV is the volume element, σ is the symmetric part of the Cauchy stress tensor, m is the deviatoric part of the couple stress tensor, χ is the symmetric curvature tensor, λ and μ are Lamé constants and l is a material length scale.

The kinematic relations are

$$\varepsilon = \frac{1}{2}[\Delta \boldsymbol{u} + (\Delta \boldsymbol{u})^T], \quad \chi = \frac{1}{2}[\Delta \boldsymbol{\theta} + (\Delta \boldsymbol{\theta})^T] \tag{2}$$

where $\boldsymbol{u}$ and $\boldsymbol{\theta}$ are the displacement and rotation vector, respectively, and $\boldsymbol{\theta} = \frac{1}{2}\text{curl}\, \boldsymbol{u}$.

Constitutive equations are given by

$$\boldsymbol{\sigma} = \lambda tr(\boldsymbol{\varepsilon})\boldsymbol{I} + 2\mu\boldsymbol{\varepsilon}, \quad \boldsymbol{m} = 2l^2\mu\boldsymbol{\chi} \tag{3}$$

where λ and μ are the Lamé constants

$$\lambda = \frac{E\nu}{(1+\nu)(1-2\nu)}; \mu = \frac{E}{2(1+\nu)} \tag{4}$$

3 The RBF-FD Method

The basic formulation of the RBF-FD method is here briefly presented [4]. Considering a set of N nodes where N represents the total number of points or nodes used for the spatial discretization, the multiquadric radial basis functions centred at x_j can be defined as:

$$g\left(x\right)|_{x_j} = \left(\|x - x_j\| + c^2\right)^{1/2} \tag{5}$$

where $\|x - x_j\|$ corresponds to the Euclidean norm and c denotes a shape parameter.

In classical finite difference formulas, nodes are equidistant and weights are computed using polynomial interpolation. This limits the spatial distribution of nodes, which is not desirable for more generic problems. However, using RBFs as an interpolant, a scattered distribution of nodes can be used. Radial basis functions basically depend on the distance between points. This property of RBFs adds flexibility to the method, since it is easy to compute distances between points, even for complex 2D/3D geometries.

The method can be viewed as an extension of classical FD methods, where a linear operator $\mathcal{L}$ at a location x_j is approximated as a linear combination of the values of the function at a defined subset of the grid, called stencil or support grid. The stencil is defined by the n closest nodes to the point x_j where $\mathcal{L}$ is being approximated:

$$\mathcal{L}u\left(x\right)|_{x_j} = \sum_{i=1}^{n} w_i u\left(x_i\right) \tag{6}$$

The weights w_i are calculated by enforcing the approximation (6) to each node of the entire domain and boundaries. For each point x_j a corresponding stencil-sized vector composed of the weights w_i is calculated. Rewriting in matrix form:

$$\begin{bmatrix} g(\|x_1 - x_1\|, c) & \cdots & g(\|x_1 - x_n\|, c) \\ \vdots & \ddots & \vdots \\ g(\|x_n - x_1\|, c) & \cdots & g(\|x_n - x_n\|, c) \end{bmatrix} \begin{bmatrix} w_i \\ \vdots \\ w_n \end{bmatrix} = \begin{bmatrix} \mathcal{L}g(\|x - x_1\|, c)|_{x_j} \\ \vdots \\ \mathcal{L}g(\|x - x_n\|, c)|_{x_j} \end{bmatrix} \tag{7}$$

The weight matrix defined by the radial basis functions is generally better conditioned than the interpolation matrix used in classical global RBF collocation methods since its size is considerably smaller, depending on the size of the stencil.

As an example, for static analysis, results for deformations are compared with Navier analytical solution.

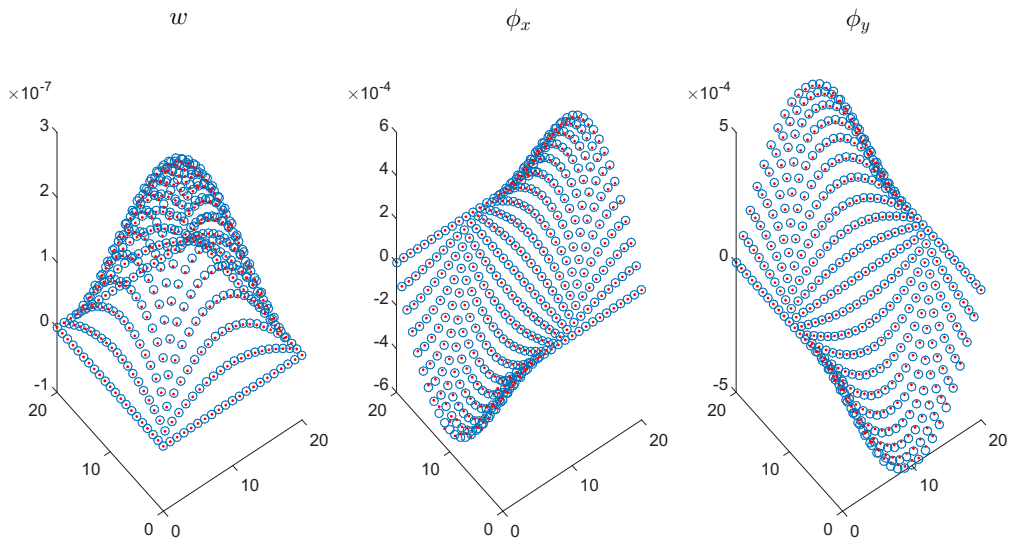

Figure 1. Bending analysis for a micro plate. Numerical RBF-FD and Navier analytical solutions for w, ϕ_x and ϕ_y.

4 Final Comments

A Modified Couple Stress Theory and a Meshless Method are used to study the static bending and free vibration analysis of a simply supported micro plate. The numerical method is easy to implement and provides accurate results.

Acknowledgments

The support of Ministerio da Ciencia Tecnologia e do Ensino Superior and Fundo Social Europeu (MCTES and FSE) under programs POPH-QREN and Investigador FCT from FSE are gratefully acknowledged.

References

[1] F. Yang, A. Chong, D. C.C. Lam, P. Tong, Couple stress based strain gradient theory for elasticity *International Journal of Solids and Structures*, **39**, 2731-2743, 2002.

[2] H. Ma, X.-L. Gao, J. Reddy, A non-classical Mindlin plate model based on a modified couple stress theory *Acta Mechanica*, **220**, 217-235, 2011.

[3] J. Reddy, Microstructure-dependent couple stress theories of functionally graded beams *Journal of the Mechanics and Physics of Solids*, 2011.

[4] A.I. Tolstykh, M.V. Lipavskii, D.A. Shirobokov, High-accuracy discretization methods for solid mechanics *Archives of Mechanics*, **55**, 531-533, 2003.

EUROMECH Colloquium 603
Dynamics of micro and nano systems
5 – 7 September 2018, Porto, Portugal

Observation of amplitude-dependent nonlinear damping in MEMS micro mirrors

Ulrike Nabholz[1], Frank Schatz[1], Jan E. Mehner[2] and Peter Degenfeld-Schonburg[1]

[1]Robert Bosch GmbH, Corporate Research, 71272 Renningen, Germany
ulrike.nabholz@de.bosch.com

[2] Chemnitz University of Technology, 09107 Chemnitz, Germany

Summary. A micro mirror constitutes a prominent example of an oscillatory silicon-based micro-electromechanical systems (MEMS). Typically, micro mirrors are designed with high quality factors to minimize energy consumption. Using a phase-locked loop (PLL), the system can be actuated at resonance despite the occurrence of frequency shifts. For such a sytstem, we expect the oscillation amplitude to scale linearly with the actuation input power. Here however, we observe amplitude depletion and thus the micro mirror deviates from linear behaviour. We are able to explain these experimental observations accurately by employing a single degree-of-freedom model including an amplitude-dependent nonlinear damping term.

Keywords: microelectromechanical devices, nonlinear dynamical systems, micro mirror, modeling

1 Introduction

Micro-electro-mechanical systems (MEMS) are small-scale devices in the micrometer range made up of mechanical and electrical components that rely on integrated circuit fabrication and micromachining technologies. Typical functions of MEMS include sensing, signal processing, actuation and control, among others [1].
Oscillatory MEMS are often actuated by an external periodic force where the frequency of excitation is electronically controlled by a phase-locked loop (PLL) that enables a fixed phase relation between drive and system response [1]. For a phase relation of $\phi = \frac{\pi}{2}$, a linear relation between oscillation amplitude and driving force is expected. MEMS micro mirrors have to reach high deflection angles [2] due to functional and performance requirements. A basic nonlinear single degree-of-freedom model, the Duffing oscillator [3], is widely used for resonant MEMS. Yet, it only takes into account linear damping and thus it cannot emulate nonlinear damping phenomena related to amplitude depletion. The underlying physical effects that lead to nonlinear damping are the subject of an ongoing field of study [4–6].
Here, we report on experimental observations in a MEMS micro mirror that exhibits nonlinear damping effects. The observed phenomena can be explained by a single degree-of-freedom (DOF) model developed in [7] for a different micro mirror design. The parameters of our model are extracted using laser doppler vibrometry as well as optical measurements of the micro mirror in operation.

2 Experimental setup

MEMS micro mirrors are scanning systems with a torsional degree of freedom [2] and dimensions in the millimetre range. During the operation of the mirror, a light beam is pointed onto its reflective, planar structure that oscillates around the resonant axis and is deflected by a defined angle.
Figure 1 shows a typical design [8]. The light grey area represents the reflective mirror structure and the red outline shows the simplified form of the springs and their attachment to the mirror. The location of the resonant axis around which the deflection occurs is indicated by the dashed vertical line and the frame connecting the mirror to its packaging is shown in dark grey.

The linear system parameters - the linear mode frequency of the drive mode and its quality factor - are geometry-dependent and can be extracted from the system using laser doppler vibrometry. Here, the MEMS micro mirror is actuated mechanically through noise in a broad frequency range. In an optical test setup, amplitude response curves of the system can be recorded: A laser beam is pointed on the reflective structure of the mirror and projected onto a screen where the deflection angle of the system can

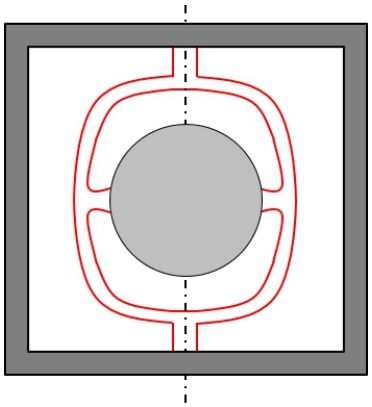

Figure 1: Schematic representation of the micro mirror design layout

be correlated to the length spanned by the deflected laser beam. The mirror is actuated using a frequency generator that provides a sinusoidal DC voltage. The frequency sweep is conducted using a fixed step-size of 1 Hz. Using results obtained from this second test setup, the nonlinear system parameters - the nonlinear quality factor and the Duffing coefficient - can be fitted to our model. They are expected to remain constant when the mirror is operated at ambient pressure and the corresponding physics is expected to influence the behaviour of the mirror significantly [7].

3 Methods

The single degree-of-freedom mechanical oscillator model proposed in [7] will be used. The equation of motion is given by

$$\ddot{q} + \omega_0^2 q + \frac{\omega_0}{Q}\dot{q} + \beta q^3 + \frac{\omega_0}{Q_{nl}} q^2 \dot{q} = F_0 \cdot \sin\left(\omega_d t\right). \tag{1}$$

Here, the basic Duffing oscillator [3] with a cubic nonlinearity and the Duffing coefficient β is expanded by a damping term. Two effective quality factors occur in the model: The (linear) quality factor Q and the nonlinear quality factor Q_{nl}.
$q = q\left(t\right)$ is the modal coordinate of the oscillation, F_0 is the amplitude of driving force. ω_0 and ω_d are the linear mode frequency of the drive and the drive frequency, respectively.
Exploiting the method of averaging [9] leads to an implicit equation for the steady-state oscillation amplitude a (proportional to the deflection angle Φ of the mirror) given by

$$a^2 = \frac{\left(\frac{F}{2\alpha\omega_0^2}\right)^2}{\left(\frac{\sigma}{2\alpha} + \frac{3\beta a^2}{8\alpha\omega_0^2}\right)^2 + \left(\frac{1}{2Q} + \frac{a^2}{8Q_{nl}}\right)^2}, \tag{2}$$

using the detuning factors $\alpha = \frac{\omega_d}{\omega_0}$ and $\sigma = \left(1 - \alpha^2\right)$.

4 Results

Using the optical test setup introduced in section 2, the amplitude response curve for four different input voltages (corresponding to input forces) is recorded. The tip of the amplitude response curve corresponds to a phase relation between drive and system response of $\phi = -\frac{\pi}{2}$. During normal operation, the mirror is driven using a PLL at this phase relation. Here, evaluation of the operating point at four different input voltages yields figure 2.

The measurements clearly diverge from the linear curve expected for a basic Duffing oscillator. Such phenomena can be explained using the nonlinear damping model introduced in section 3 as already shown for a similar MEMS micro mirror system in [7]. The parameters responsible for the system's nonlinearity, the Duffing coefficient β and the nonlinear quality factor Q_{nl}, are fitted to approximate the measurements. Since both are geometry parameters, they have to remain constant over the whole range of input voltages. Figure 3 shows that this is the case; the measurements (denoted by red and blue lines

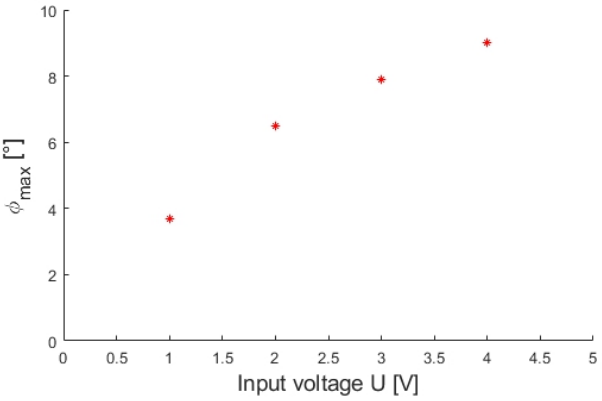

Figure 2: Peak deflection angle of amplitude response curves a range of input forces

that correspond to forward and reverse sweep) fit the model (displayed in black) well for all four input voltages. The deviation in Figure 3a can be attributed to the test setup: For only a small frequency shift, the fixed increment of 1 Hz during the frequency sweep in connection with measurement errors can lead to a premature exit from the bistable region onto the lower stable solution branch. In Figure 3d, the mirror is driven close to its maximum deflection angle which leads to visible distortions of the projected line, increasing the error margin. Here, the reverse sweep is missing since a fracture in the frame structure occurred before the test was completed.

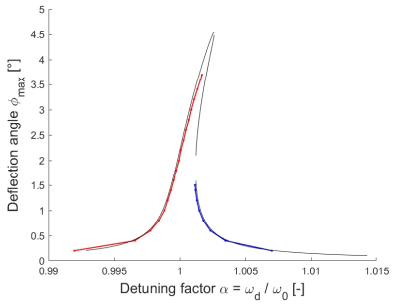

(a) Input voltage: 1V

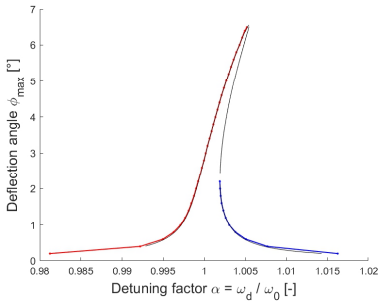

(b) Input voltage: 2V

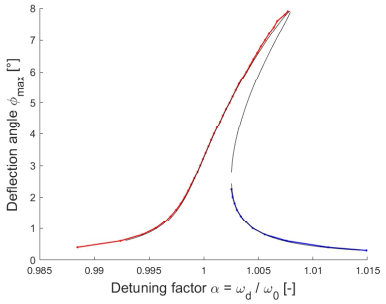

(c) Input voltage: 3V

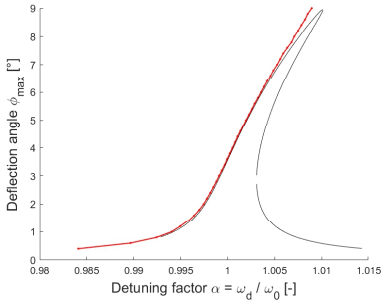

(d) Input voltage: 4V

Figure 3: Amplitude response curves obtained from frequency sweeps (forward: red, reverse: blue) compared to the model (black) for different input voltages

5 Conclusion

We reported on experimental observations that show depletion of the oscillation amplitude in a MEMS micro mirror. We modeled the observed phenomenon by including a nonlinear damping term in a single

degree-of-freedom model. The nonlinear system parameters were fitted from measurements of the systems amplitude response curve. Thus, we were able to emulate the measurements comprehensively. These nonlinear damping phenomena entail higher power consumption due to a disproportional increase in the required input voltage needed for a required deflection angle. Thus, it is of interest to investigate the physical origins of nonlinear damping.

References

[1] S.D. Senturia. *Microsystem Design*. Kluwer Academic Publishers, New York, 2002.

[2] M.E. Motamedi. *MOEMS: Micro-opto-electro-mechanical Systems*. SPIE Press, Bellingham, Washington, 2005.

[3] G. Duffing. Erzwungene Schwingungen bei veränderlicher Eigenfrequenz und ihre technische Bedeutung. *Sammlung Vieweg*, 41/42, 1918.

[4] Ron Lifshitz and M. C. Cross. *Nonlinear Dynamics of Nanomechanical and Micromechanical Resonators*, pages 1–52. Wiley-VCH, Weinheim, Germany, 2009.

[5] Stav Zaitsev, Oleg Shtempluck, Eyal Buks, and Oded Gottlieb. Nonlinear damping in a micromechanical oscillator. *Nonlinear Dynamics*, 67:859–883, 2012.

[6] A. Eichler, J. Moser, J. Chaste, M. Zdrojek, I. Wilson-Rae, and A. Bachtold. Nonlinear damping in mechanical resonators made from carbon nanotubes and graphene. *Nature Nanotechnology*, 6:339 – 342, 2011.

[7] U. Nabholz, W. Heinzelmann, J. E. Mehner, and P. Degenfeld-Schonburg. Amplitude- and gas pressure-dependent nonlinear damping of high-Q oscillatory MEMS micro mirrors. *Journal of Microelectromechanical Systems*, PP:1–9, 2018.

[8] U. Baran, D. Brown, S. Holmstrom, D. Balma, W. O. Davis, P. Muralt, and H. Urey. Resonant PZT MEMS scanner for high-resolution displays. *Journal of Microelectromechanical Systems*, 21:1303–1310, 2012.

[9] N. Kryloff, N.N. Bogoliubov, and S. Lefschetz. *Introduction to Non-linear Mechanics*. Princeton University Press, Princeton, 1947.

EUROMECH Colloquium 603
Dynamics of micro and nano systems
5 – 7 September 2018, Porto, Portugal

Printed Circuit Boards Experimental and Numerical Characterization

Carlos Castro[1,2], Pedro Bastardo[2], Sérgio Tavares[1] and Paulo T. de Castro[1]

[1] Faculdade de Engenharia da Universidade do Porto, Porto, Portugal
em12042@fe.up.pt
stavares@fe.up.pt
ptcastro@fe.up.pt

[2] Bosch Security Systems, Ovar, Portugal
pedro.bastardo@pt.bosch.com

Summary. Mechanical, thermal and vibration behaviour of printed circuit boards under different conditions are of interest for design purposes. An experimental and numerical study was carried out on a selected population of different specimens, with the main objective of characterizing their stiffness. Notwithstanding their diversity, it was possible to identify a typical range of practical values. In parallel, experimental thermal and vibration characterization was performed in order to gather data for use in future studies. The intention is to predict behaviour in service, without the need for manufacturing physical components or prototypes.

Keywords: PCBs characterization, Numerical Modelling, Mechanical Testing, Thermography, Vibration Analysis.

1 Introduction

Quality and durability of electronic systems require high and increasing levels of reliability assurance. The complexity of printed circuit boards (PCBs) morphology, schematically shown in Fig.1, explains the little information available about their mechanical, thermal and vibration characterization [1].

Although printed circuit boards' failure depends on many factors, the temperature is the parameter which has a bigger impact on their reliability. Therefore, and since the thermal effects lead to fracture of the components, efficient heat dissipation is required during every printed circuit board assembly (PCBA) operating conditions. To serve this purpose, thermal interface materials (TIMs) are potential candidates for the task – specifically gap pads [2], which have an influence on the PCBs' stiffness.

This communication intends to answer a preliminary problem – the identification of range of stiffness values for a diversity of common PCBs. In parallel, relevant issues of PCB design and use – that need to be addressed in industrial context – were reviewed, given the fact that design procedures are not widely available or generally agreed.

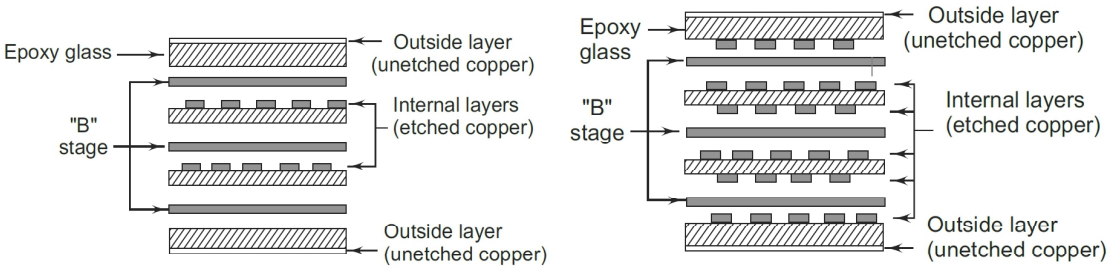

Figure 1. Multi-layer printed circuit boards stack-up details; B-stage: pre-preg; left, 4 Cu layers; right: 8 Cu layers. [1]

2 Tests and Models

A population of printed circuit board specimens was subjected to experimental tests – mechanical,

thermal and vibration. The mechanical tests were carried out in order to obtain the mechanical properties of the selected printed circuit board specimens, by submitting them to a series of three and four-point bending tests, 3PB and 4PB, respectively. Due to time constraints, geometric variability for each PCB model was not measured. No linear relation between the flexural stiffness and the number of copper layers or copper percentage of any PCB considered in the present work could be identified.

Numerical simulation was performed to model the mechanical tests' results and a parametric evaluation was carried out. For this purpose, material models of the tested specimens were created, under 3PB and 4PB test conditions, and were experimentally validated, Fig. 2. Thus, other parameters (*e.g.* stress and strain) could subsequently be obtained. Electronic components – BGAs (ball grid arrays), condensers, LEDs (light-emitting diodes), etc. – were not included in the numerical simulations. Therefore, the stiffness of the PCB alone was considered, without external contributions [3].

Only the static component of the PCB models' behaviour was evaluated, since the thermal considerations would imply large additional computational effort, due to the high level of detail of the material model. Fig. 3 shows the ABAQUS output for the stress analysis of a given PCB model. For one model (basis scenario), a parametric evaluation varying size, thickness and number of layers was performed.

The load *vs.* displacement relationship found in the numerical simulations was always greater than the experimental one. Since in industrial context the maximum displacement (or strain) are usually prescribed, this means that the numerical model will provide a conservative evaluation of the maximum load values acting on the PCB. This implies that numerical simulation will be associated to an enhanced safety margin, *i.e.* the numerical predictions of maximum load are higher than the real values.

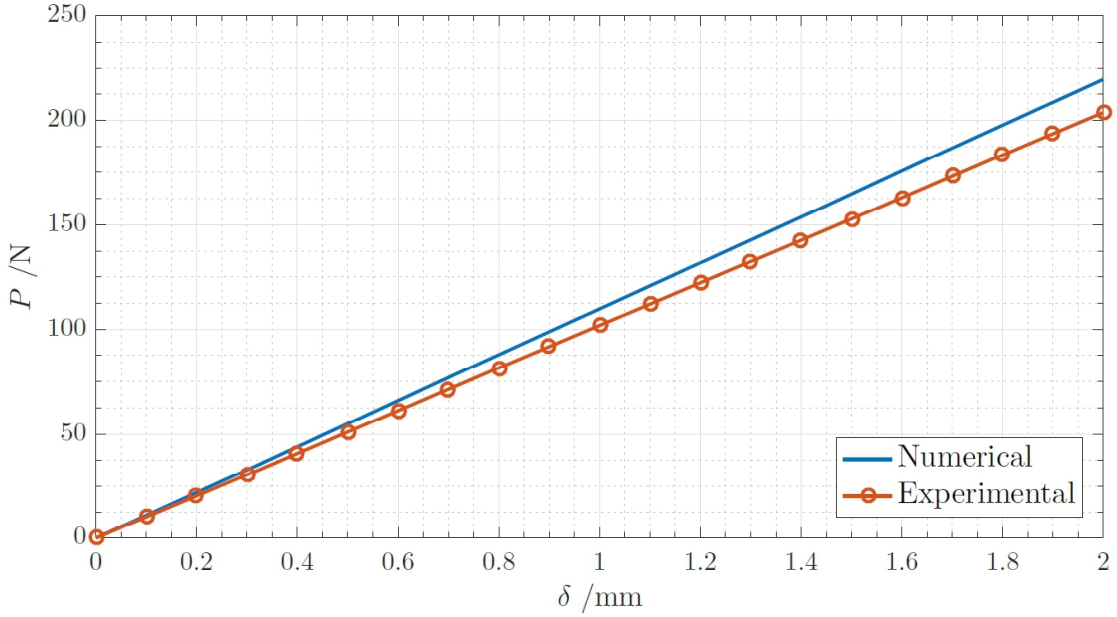

Figure 2. Comparison of numerical and experimental load-displacement curves, for one of the tested PCB models

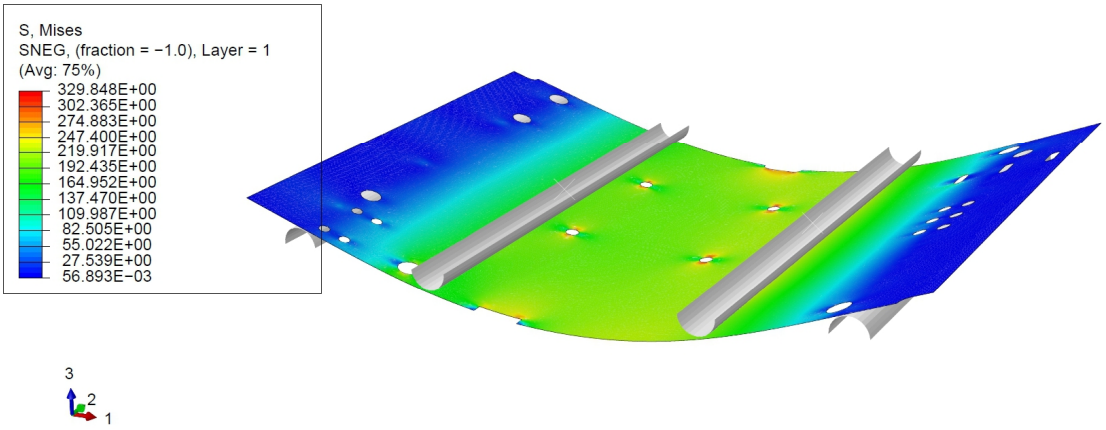

Figure 3. Von Mises stress distribution in a detailed geometry of a PCB material model

As mentioned before, the work intends to gather data for use in subsequent analyses of service behaviour of PCBs. For that purpose, the stiffness analyses must be complemented with thermal and vibration studies.

The thermal tests – thermography and digital shearography – allowed to clearly understand the critical temperature areas on a PCBA while powered on, provided useful information for gap pad dimensioning and knowledge of the gradient displacements fields caused by thermal loads [4,5]. The vibration tests confirmed the performance reliability of a printed circuit board assembly under normal and severe vibration conditions. Additionally, these are strongly dependent on the boundary conditions.

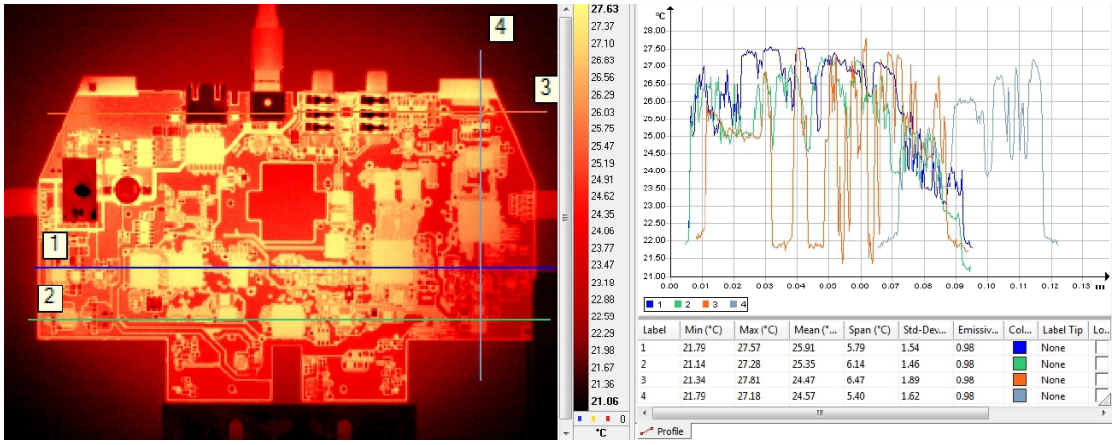

Figure 4. Temperature profile along sketched lines on a PCBA model's top surface, while powered on

3 Concluding Remarks

- Gap pads are the most feasible TIMs for efficient heat dissipation through printed circuit board components.
- For both experimental and numerical testing, it is crucial to have accurate knowledge of the material properties of a given printed circuit board to be analysed.
- It is important to measure specimen geometric variability, so that more uniform values for the geometric parameters – and also for the derived material properties – can be known, and flawed specimens can be discarded.

- The thickness is the geometric parameter with the biggest influence on the obtained material properties and correspondent material models' results. Therefore, the knowledge of its exact value is of great importance.
- The thermography, digital shearography and vibration tests greatly contributed to printed circuit boards thermal and vibration characterization, namely the knowledge of the maximum temperature differences (required for gap pad's dimensioning), displacement gradients fields and number of vibration cycles until electrical failure, respectively.

Acknowledgments

This communication is based upon the first author's master dissertation supervised at the Universidade do Porto by Professors Paulo Tavares de Castro and Sérgio Tavares, and at Bosch Security Systems Ovar, by Engineer Pedro Bastardo. Engineer Francisco Moreira gave the opportunity to develop this study and welcomed the first author to the ENI team of Bosch Security Systems Ovar. Also at the Universidade do Porto, the collaboration of Professors Mário Vaz and José Dias Rodrigues, in thermal and vibration tests, respectively, is acknowledged.

References

[1] R. Khandpur, Printed Circuit Boards: Design, Fabrication and Assembly. New Delhi: MCGraw-Hill, 2008.
[2] K. Bruzda, "Stress minimization during deflection of thermally conductive gap pads", in Twenty Third Annual IEEE Symposium Semiconductor Thermal Measurement and Management, SEMI-THERM 2007, IEEE, 2007, pp. 136-143.
[3] Y.-C. Lee, B.-T. Wang, Y.-S. Lai, C.-L. Yeh, and R.-S. Chen, "Finite element model verification for packaged printed circuit board by experimental modal analysis", Microelectronics Reliability, vol. 48, no. 11, pp. 1837-1846, 2008.
[4] J. M. Lloyd, Thermal imaging systems. Springer Science & Business Media, 2013.
[5] P. Bai, F. Zhu, and X. He, "Out-of-plane displacement field measurement by shearography", Optics & Laser Technology, vol. 73, pp. 29-38, 2015.

Simulation of the electromechanical properties and strain-sensing response of CNT-polymer composites

Miguel A. S. Matos, Vito L. Tagarielli and Silvestre T. Pinho

Department of Aeronautics, Imperial College London, South Kensington Campus,
London SW7 2AZ, United Kingdom
miguel.matos@imperial.ac.uk
v.tagarielli@imperial.ac.uk
silvestre.pinho@imperial.ac.uk

Summary. A novel approach to simulate elastic properties, bulk conductivity and strain sensing capabilities of carbon nanotube polymer composites using the finite element method is presented. The approach is based on coupled mechanical and electrical simulations of a representative volume element constructed based on measurable statistical descriptors of the microstructure. The models include the nanoscale tunnelling effect and its sensitivity to the imposed strain field through the implementation of a new user element. Monte Carlo analyses are performed for different nanotube and polymer properties. Predictions are found to be in good agreement with published data.

Keywords: Conductive polymers, nanocomposites, strain sensing, finite element model

1 Introduction

This work presents a novel framework to model the strain-sensing capabilities of Carbon Nanotube (CNT) reinforced polymer composites based on the Finite Element (FE) method. The models can simulate the electro-mechanical response of these materials by analysis of a Representative Volume Element (RVE).

The use of Carbon nanotubes as a polymer composite filler has been the target of numerous scientific studies owing to the outstanding combination of mechanical, electrical and thermal properties [1]. With small dimensions, very high aspect ratios and low density, CNTs enable the improvement of the composite properties at low concentrations [2]. Low concentrations, as small as 0.0025 wt% [3], have successfully enabled conductivity in otherwise insulating polymers. Due to their characteristics, these conductive composites display changes in conductivity when strained, operating as a self-sensing material that goes beyond some limitations of ordinary resistance strain gauges acting as an embedded and multidirectional sensor [4] with superior sensitivities [5].

2 Numerical modelling

We present a multi-scale numerical approach that can capture the main mechanisms responsible for the conductivity of CNT-polymer composites and their sensitivity to deformation, while reproducing the geometric details of CNT dispersions. The mechanical and electrical properties of the material are calculated based on RVEs constructed from statistical descriptors of the nanostructure. The developed framework considers both straight and curved CNTs in three-dimensional domains. Geometry periodicity is enforced, as shown in Figure 1**.** Two different FE analyses, mechanical and electrical, are sequentially performed on the RVEs using Abaqus [6], both with periodic boundary conditions. The model incorporates the nanoscale tunnelling effect and its sensitivity to the imposed applied strain field via a user-element developed for this purpose [7]. A converged size for the RVE is determined, and homogenized mechanical and electrical properties are calculated for a range of CNT concentrations. The results are compared against published data (Figure 2).

3 Results

The analyses capture the sensitivity of the electrical bulk conductivity to imposed strain, reproducing the piezoresistive behaviour of these composites [8] by modelling both the piezoresistive

response of CNTs and the evolution of the connectivity of the conductive network that they form in a polymeric matrix. Predictions are found in agreement with previously published experimental data, as presented in Figure 3.

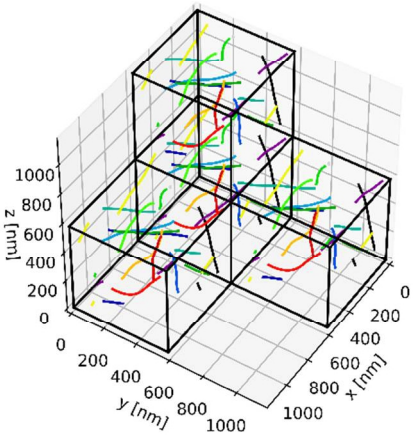

Figure 1. Example of a generated RVE illustrating the geometric periodicity

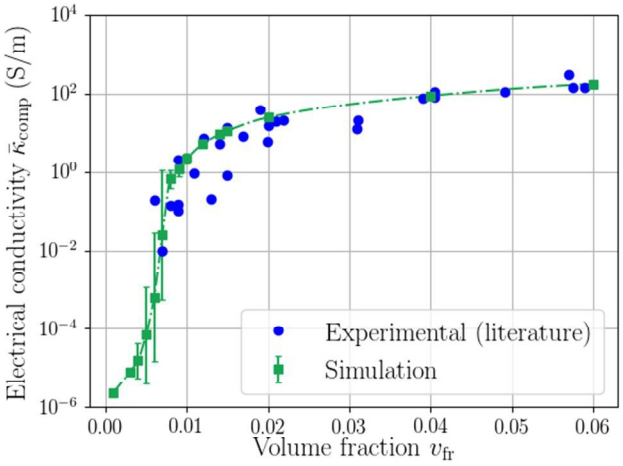

Figure 2. Homogenized electrical conductivity compared with experimental data reproduced from Hu et al. [9]

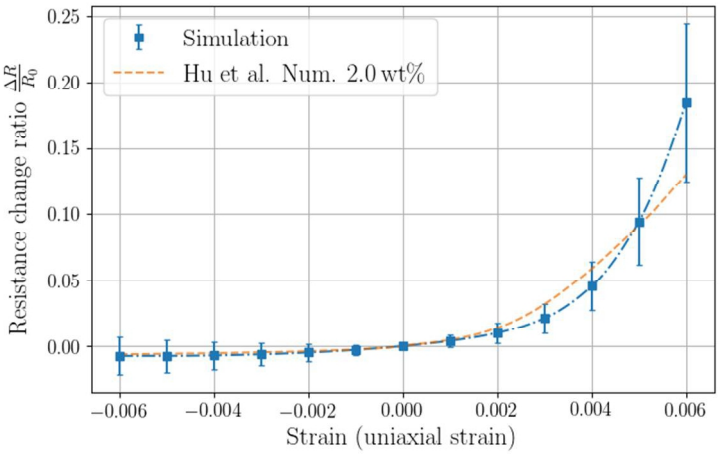

Figure 3. Simulated piezoresistivity of a multiwall CNT-epoxy composite with 1% volume fraction subject to uniaxial strain

Acknowledgments

This project has received funding from the European Union's Horizon 2020 research and innovation program under the Marie Skłodowska-Curie Grant Agreement no. 642890 (http://thelink-project.eu).

References

[1] J. N. Coleman, *et al.* Small but strong: A review of the mechanical properties of carbon nanotube-polymer composites, *Carbon,* **44** (9), 1624-1652, 2006.

[2] X. L. Xie, *et al.* Dispersion and alignment of carbon nanotubes in polymer matrix: A review, *Materials Science & Engineering R-Reports,* **49** (4), 89-112, 2005.

[3] J. K. W. Sandler, *et al.* Ultra-low electrical percolation threshold in carbon-nanotube-epoxy composites, *Polymer,* **44** (19), 5893-5899, 2003.

[4] W. Obitayo and T. Liu. A Review: Carbon Nanotube-Based Piezoresistive Strain Sensors, *Journal of Sensors*, 15, 2012.

[5] G. T. Pham*, et al.* Processing and modeling of conductive thermoplastic/carbon nanotube films for strain sensing, *Composites Part B-Engineering,* **39** (1), 209-216, 2008.
[6] D. S. Simulia, *Abaqus 2017 Documentation*, 2017.
[7] M. A. S. Matos*, et al.* Predictions of the electro-mechanical response of conductive CNT-polymer composites, *Journal of the Mechanics and Physics of Solids,* **114**, 84-96, 2018.
[8] Z. Yuan and Z. Lu. Numerical analysis of elastic–plastic properties of polymer composite reinforced by wavy and random CNTs, *Computational Materials Science,* **95**, 610-619, 2014.
[9] N. Hu*, et al.* Investigation on sensitivity of a polymer/carbon nanotube composite strain sensor, *Carbon,* **48** (3), 680-687, 2010.

EUROMECH Colloquium 603
Dynamics of micro and nano systems
5 – 7 September 2018, Porto, Portugal

Atomistic modelling of hydrocarbon nanostructure failure

Mat Tolladay[1], Neil L. Allan[1], Dmitry Ivanov[1] and Fabrizio Scarpa[1]

[1]University of Bristol, Bristol, U.K
Mat.Tolladay@Bristol.ac.uk
Neil.Allan@Bristol.ac.uk
Dmitry.Ivanov@bristol.ac.uk
F.Scarpa@Bristol.ac.uk

Summary. Atomistic simulation is a widely used technique for the modelling of nanostructures. This work examines mechanical material properties, such as strengths and strains to failure, and how they can be determined from atomistic simulations. The maximum restorative force of an atomic bond and the atomic separation at which it occurs are used as analogues for material strength and strain to failure. Different atomistic simulation methods are compared and the difficulty of capturing these important mechanical properties is discussed.

Keywords: Atomistic simulations, material failure, nanomaterials.

1 Introduction

Accurate modelling of material failure is difficult to achieve at any lengthscale. At larger lengthscales, upwards from the microscale, it is often most convenient to use some form of empirically based parametrisation combined with a continuum mechanics simulation. As the lengthscale gets shorter from the microscale the tendency is to use atomistic based simulations. Different simulation types can be applied to atomistic simulations varying from molecular mechanics potentials down to ab initio calculations. The choice of method requires the user to decide upon a balance between the accuracy and computational speed of a calculation. The methods can produce both qualitatively and quantitatively different results. Different ab initio methods will generate different values for important properties such as material strength and strain to failure.

The rise of planar materials, particularly graphene, has led to the development of two dimensional nanostructures to fulfil a variety of functions [1, 2, 3, 4, 5]. Graphene based structures are essentially large polyaromatic hydrocarbons (PAHs) with a hexagonal carbon lattice with edges terminated by hydrogen atoms. These structures often try to make use of the impressive mechanical properties of graphene such as its stiffness, strength and strain to failure. Imposing a specific geometry on a graphene sheet leads to stress concentrations, just as at the macroscale. At the macroscale the stress concentrators are normally corners and the concentration effect can be mitigated by increasing the corners radii. However, on the nanoscale corners become ill defined due to the discrete nature of the molecular structure; such a corner cannot be continuously curved. At the atomistic level, the stress in the structure will become concentrated on a bond between specific atoms. In order to determine the behaviour of a structure, including failure, any model must accurately describe the structure's atomic bonds and this requires an accurate representation of the electronic behaviour of the structure.

Strength and strain to failure can be related to the atomic scale by defining stress as

$$\sigma_x = \frac{1}{V_0}\frac{\partial E}{\partial \varepsilon_x}. \tag{1}$$

Where, σ_x is the stress in the x direction, V_0 the initial volume of the structure, E the energy of the system and ε_x is the strain in the x direction. The strength of a material is defined as the maximum stress a material can withstand, i.e. the point at which failure occurs. This occurs at the point when the derivative of the energy is at a maximum. From an atomistic point of view this occurs when the restorative force between two atoms is at a maximum [6]. The distance between the two atoms where

this peak occurs can be considered as the strain to failure of the bond. The challenge is to determine both the maximum restorative force and the bond elongation at which it occurs.

The work presented here highlights a number of issues with some popular methods for modelling nanoscale mechanics and highlights the difficulties facing those who wish to use simulations to predict mechanical strength and strain to failure.

2 Simulation methods

There are a number of different methods available for atomistic simulations and for each of these there are large numbers of variants. The computationally cheapest methods are molecular mechanics (MM) force fields which rely on analytical expressions for calculating the energy for an arrangement of atoms. The most popular force fields for modelling hydrocarbon structures are of the Tersoff Brenner type [7, 8]. The reactive empirical bond order potential (REBO) [9] is widely employed alongside derivatives thereof, such as the adaptive intermolecular REBO (AIREBO) [10] and the long-range carbon bond order potential (LCBOP) [11]. Such methods make no attempt to calculate the electronic behaviour and instead rely on fitted parameters to describe the forces between atoms. These force fields are computationally cheap and simulations involving very large numbers of atoms (> 1000) are possible.

The alternatives to molecular mechanics are electronic structure methods. In this approach the energy is determined by approximating solutions to the Schrödinger equation for a system of electrons in a potential generated by ionic cores. These methods require computing large numbers of integrals or using a parametrised method for estimating values of the integrals, so-called semi empirical methods. The most reliable methods available are ab initio post Hartree-Fock (post-HF) methods such as Møller Plesset perturbation theory, configuration interaction theory or coupled cluster theory. However, these methods scale very poorly with system size, limiting their applicability to molecules containing a dozen or so atoms. The most commonly used electronic structure method available is density functional theory (DFT) which is capable of handling systems up to a few hundred atoms. DFT and post-HF methods require a choice of basis set and in the case of DFT a choice of exchange-correlation functional. There are hundreds of basis sets and functionals to choose from and their choice impacts both the speed and accuracy of the calculation.

In nano-mechanical simulations accuracy is generally traded for lower computational cost, thus increasing the possible system size. Nanostructures of interest usually contain thousands of atoms forcing modellers to rely on MM methods but in many cases semi empirical methods may be an option. Another alternative is to employ QM/MM or QM/QM methods whereby different regions of the structure are simulated at different levels of theory.

3 Numerical experimental methods

In this work the problems of accurately modelling failure are investigated through simulations of small hydrocarbon molecules. MM, DFT and post-HF methods are employed to calculate interatomic forces over a range of bond lengths to determine the maximum restorative force and the bond length at which it occurs. These properties can be thought of as the chemical equivalent to the mechanical properties of strength and strain to failure.

Electronic structure calculations were performed in Gaussian09 [12] and AIREBO calculations were performed with LAMMPS [13]. For the AIREBO calculations the potential cut-off was set to 2.0 Å such that the cut-off function is removed. This is done to avoid spurious forces generated by the cut-off function in the region of the peak restoring force [14].

The B3LYP [15, 16] and PBE [17] exchange correlation functionals were used as they are the most popular functionals currently used in DFT calculations. The B2PLYPD3 [18] double hybrid functional was used as it has been shown to be more accurate than the B3LYP and PBE functionals [19]. This functional mixes Hartree-Fock exchange with the exchange from the functional as well as introducing a dispersion term and a MP2 correlation term calculated using the Kohn-Sham orbitals. Dunning's correlation consistent basis sets were used for the post-HF calculations and Ahlrichs polarisation optimised

Table 1: Results for bond failure for ethene. The failure strain is taken relative to the method's own equilibrium bond length.

Method	Parameters	$\lvert F_{\text{Max}}\rvert$ (nN)	Difference from CCSD(T)	R_{Failure} (Å)	Failure strain
MM	AIREBO	6.73	25%	1.60	22%
DFT	B3LYP/DGDZVP	9.73	8%	1.72	31%
DFT	PBE/DGDZVP	9.21	2%	1.72	31%
DFT	B2PLYPD3/DGDZVP	9.26	3%	1.73	29%
MP2	ccPTVZ	9.07	1%	1.72	29%
CCSD(T)	ccPTVZ	8.99	-	1.72	-

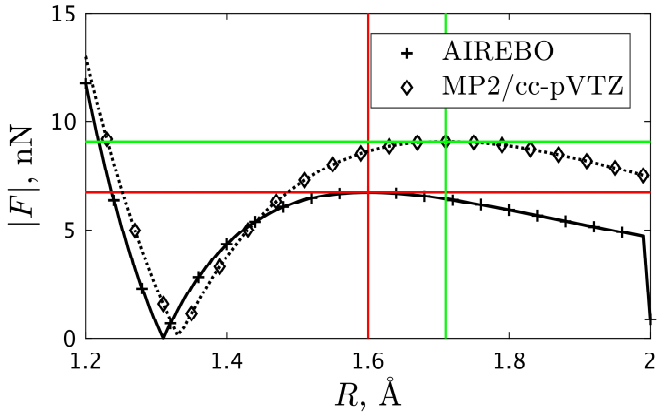

Figure 1: Plot showing the magnitude of the force for ethene as a function of the carbon-carbon bond length, R. The horizontal lines indicate the bond strength and the vertical lines the maximum bond strain for the two methods. The sudden drop in the AIREBO force at 2 Å is due to the applied cut-off radius.

split valence basis sets for the DFT calculations.

The coupled cluster (CCSD(T)) calculations were performed using single, double and pertubative triple excitations with the forces on the atoms calculated numerically. Due to the computational cost of the CCSD(T) calculations only single point energy calculations were performed using the MP2 geometries at carbon-carbon bond lengths of 1.71 Å, 1.72 Å and 1.73 Å. All other calculations used 0.01 Å steps from 0.8 Å to 3.3 Å.

4 Results and conclusions

Table 1 shows the results for different simulation methods arranged from computationally cheapest to most expensive. The CCSD(T) result is the highest order calculation performed here and is taken to be the benchmark. Figure 1 highlights the difference in bond strength and strain to failure for different simulation methods.

The results for the electronic structure methods show that they can overestimate the bond strength by up to 8% but will produce reliable strains to failure. The AIREBO results are significantly different from the electronic structure methods, which suggests the potential inaccurately describes failure related properties. Some experiments to measure bond rupture forces have been performed [20] but there are very few experimental values for the bond failure properties. As such, only high order electronic structure methods can be employed to validate lower order computational methods. From this point of view the electronic structure methods provide better results for the bond failure properties than those produced

using the REBO based potential but the parameters for the calculations must be chosen with care.

Acknowledgments

This work was supported by the Engineering and Physical Sciences Research Council through the EPSRC Centre for Doctoral Training in Advanced Composites for Innovation and Science [grant number EP/L016028/1]

References

[1] Y. W. Son, M. L. Cohen, and S. G. Louie. Half-metallic graphene nanoribbons. *Nature*, 444(7117):347–349, 2006.

[2] M. A. Rafiee, W. Lu, A. V. Thomas, A. Zandiatashbar, J. Rafiee, J. M. Tour, and N. A. Koratkar. Graphene Nanoribbon Composites. *ACS Nano*, 4(12):7415–7420, 2010.

[3] K. S. Mali, J. Greenwood, J. Adisoejoso, R. Phillipson, and S. De Feyter. Nanostructuring graphene for controlled and reproducible functionalization. *Nanoscale*, 7(5):1566–1585, 2015.

[4] M. K. Blees, A. W. Barnard, P. A. Rose, S. P. Roberts, K. L. McGill, P. Y. Huang, A. R. Ruyack, J. W. Kevek, B. Kobrin, D. A. Muller, and P. L. McEuen. Graphene kirigami. *Nature*, 524(7564):204–207, 2015.

[5] D. A. Bahamon, Z. Qi, H. S. Park, V. M. Pereira, and D. K. Campbell. Graphene kirigami as a platform for stretchable and tunable quantum dot arrays. *Physical Review B*, 93(23):235408, 2016.

[6] M. K. Beyer. The mechanical strength of a covalent bond calculated by density functional theory. *The Journal of Chemical Physics*, 112(17):7307–7312, 2000.

[7] J. Tersoff. New empirical approach for the structure and energy of covalent systems. *Physical Review B*, 37(12):6991–7000, 1988.

[8] D. W. Brenner. Empirical potential for hydrocarbons for use in simulating the chemical vapor deposition of diamond films. *Physical Review B*, 42(15):9458–9471, 1990.

[9] D. W. Brenner, O. A. Shenderova, J. A. Harrison, S. J. Stuart, B. Ni, and S. B. Sinnott. A second-generation reactive empirical bond order (REBO) potential energy expression for hydrocarbons. *Journal of Physics: Condensed Matter*, 14(4):783–802, 2002.

[10] S. J. Stuart, A. B. Tutein, and J. A. Harrison. A reactive potential for hydrocarbons with intermolecular interactions. *The Journal of Chemical Physics*, 112(2000):6472–6486, 2000.

[11] J. H. Los and A. Fasolino. Intrinsic long-range bond-order potential for carbon: Performance in Monte Carlo simulations of graphitization. *Physical Review B*, 68(2):024107, 2003.

[12] M. J. Frisch, G. W. Trucks, H. B. Schlegel, G. E. Scuseria, M. A. Robb, J. R. Cheeseman, G. Scalmani, V. Barone, B. Mennucci, G. A. Petersson, H. Nakatsuji, M. Caricato, X. Li, H. P. Hratchian, A. F. Izmaylov, J. Bloino, G. Zheng, J. L. Sonnenberg, M. Hada, M. Ehara, K. Toyota, R. Fukuda, J. Hasegawa, M. Ishida, T. Nakajima, Y. Honda, O. Kitao, H. Nakai, T. Vreven, J. A. Montgomery, Jr., J. E. Peralta, F. Ogliaro, M. Bearpark, J. J. Heyd, E. Brothers, K. N. Kudin, V. N. Staroverov, T. Keith, R. Kobayashi, J. Normand, K. Raghavachari, A. Rendell, J. C. Burant, S. S. Iyengar, J. Tomasi, M. Cossi, N. Rega, J. M. Millam, M. Klene, J. E. Knox, J. B. Cross, V. Bakken, C. Adamo, J. Jaramillo, R. Gomperts, R. E. Stratmann, O. Yazyev, A. J. Austin, R. Cammi, C. Pomelli, J. W. Ochterski, R. L. Martin, K. Morokuma, V. G. Zakrzewski, G. A. Voth, P. Salvador, J. J. Dannenberg, S. Dapprich, A. D. Daniels, O. Farkas, J. B. Foresman, J. V. Ortiz, J. Cioslowski, , and D. J. Fox. Gaussian 09, Revision D.01, 2013. Gaussian Inc. Wallingford CT.

[13] S. Plimpton. Fast Parallel Algorithms for Short-Range Molecular Dynamics. *Journal of Computational Physics*, 117(1):1–19, 1995.

[14] O. A. Shenderova, D. W. Brenner, A. Omeltchenko, X. Su, and L. H. Yang. Atomistic modeling of the fracture of polycrystalline diamond. *Physical Review B*, 61(6):3877–3888, 2000.

[15] C. Lee, W. Yang, and R. G. Parr. Development of the Colle-Salvetti correlation-energy formula into a functional of the electron density. *Physical Review B*, 37(2):785–789, 1988.

[16] A. D. Becke. Densityfunctional thermochemistry. III. The role of exact exchange. *The Journal of Chemical Physics*, 98(7):5648–5652, 1993.

[17] J. P. Perdew, K. Burke, and M. Ernzerhof. Generalized Gradient Approximation Made Simple. *Physical Review Letters*, 77(18):3865–3868, 1996.

[18] S. Grimme. Semiempirical hybrid density functional with perturbative second-order correlation. *The Journal of Chemical Physics*, 124(3):034108, 2006.

[19] L. Goerigk, A. Hansen, C. Bauer, S. Ehrlich, A. Najibi, and S. Grimme. A look at the density functional theory zoo with the advanced GMTKN55 database for general main group thermochemistry, kinetics and noncovalent interactions. *Physical Chemistry Chemical Physics*, 19(48):32184–32215, 2017.

[20] M. Grandbois, M. Beyer, M. Rief, H. Clausen-Schaumann, and H. E. Gaub. How strong is a covalent bond? *Science (New York, N.Y.)*, 283(5408):1727–30, 1999.

EUROMECH Colloquium 603
Dynamics of micro and nano systems
5 – 7 September 2018, Porto, Portugal

Effect of nonlinear feedback control on a coupled cantilevers

Takumi Nakamura[1], **Masatoshi Yano**[1] **and Hiroshi Yabuno**[1]

[1]University of Tsukuba, Tsukuba, Japan
s1720835@s.tsukuba.ac.jp
yabuno@esys.tsukuba.ac.jp

Summary. In order to enhance the measurement accuracy of mass sensing method based on mode localization in weakly coupled cantilevers, we propose an amplitude control method for them based on nonlinear feedback in addition to linear feedback. The steady-state amplitude of the cantilevers can be controlled to be sufficiently small so that the cantilevers oscillate with the first liner normal mode. We theoretically show that the high-gain nonlinear feedback realizes the steady state oscillation with sufficiently small amplitude. Experimental results using weakly coupled microcantilevers demonstrates the validity of the theoretically proposed amplitude control method.

Keywords: MEMS, coupled microcantilevers, nonlinear feedback control, self-excited oscillation

1 Introduction

Small mass detection using a microcantilever has attracted much interest [1–3]. In order to enhance the measurement accuracy, a method utilizing the linear mode localization in weakly coupled cantilevers is proposed [4]. Our research group proposed a way to use self-excitation of the coupled cantilevers by linear feedback control to keep the accuracy even in viscous measurement environments [5, 6]. In general, the amplitude of self-excited oscillation in linear systems grows with time. In practical systems, the growth is often suppressed by the inherent nonlinearity of the systems or in the environments. The power limit to self-excitation is also another reason for the suppression. The magnitude of the response amplitude in such a self-excited oscillation is uncertainty. For the high-accuracy measurement, the steady state oscillation with sufficiently small amplitude is required for the detection of the linear normal mode from the self-excited coupled cantilevers. To this end, we propose the application of nonlinear viscosity by nonlinear feedback control. The effect of nonlinear feedback control is analytically clarified by nonlinear analysis based on the method of multiple scales. Experiments with coupled microcantilevers demonstrates the steady state self-excited oscillation with sufficiently small amplitude.

2 Principal of amplitude control

According to the previous study [4], we employ two degree-of-freedom spring mass damper system. We introduce m, c, k and k_c: m is the equivalent mass of cantilevers, c is the viscous damping coefficient, k is the equivalent stiffness of the cantilevers, and k_c is the equivalent coupling stiffness between the cantilevers. We apply an external base excitation to the cantilevers according to the linear and nonlinear feedback $\Delta x = (\beta_{lin}/k)\dot{x}_1 + (\beta_{non}/k)x_1^2\dot{x}_1$. Dimensionless equations of motion are expressed as follows:

$$\ddot{x}_1 + \mu\dot{x}_1 + x_1 + \kappa(x_1 - x_2) = \beta_l\dot{x}_1 + \beta_n x_1^2\dot{x}_1 \tag{1}$$

$$\ddot{x}_2 + \mu\dot{x}_2 + x_2 + \kappa(x_2 - x_1) = \beta_l\dot{x}_1 + \beta_n x_1^2\dot{x}_1, \tag{2}$$

where $\mu = c/\sqrt{mk}$, $\kappa = k_c/k$, $\beta_l = \beta_{lin}/\sqrt{mk}$ and $\beta_n = \beta_{non}/\sqrt{mk}$. x_1 and x_2 are the dimensionless displacements of the cantilevers. Dot represents dimensionless time derivative. We introduce an order parameter ϵ $(0 < \epsilon \ll 1)$ and expand x_1 and x_2 as $x_1 = x_{10} + \epsilon x_{11}$ and $x_2 = x_{20} + \epsilon x_{21}$. We introduce the multiple time scales as $t_0 = t$ and $t_1 = \epsilon t$ and assume the order of the parameters as $\beta_l = \epsilon\hat{\beta}_l$, $\beta_n = \epsilon\hat{\beta}_n$, $\mu = \epsilon\hat{\mu}$ and $\kappa = \epsilon\hat{\kappa}$. Substituting these into Eqs. (1) and (2) and equating the coefficients of each power of ϵ, x_{10} and x_{20} are derived as $x_{10} = a(t_1)\cos(t_0+\phi_1(t_1))$ and $x_{20} = b(t_1)\cos(t_0+\phi_2(t_1))$ from the equations of $O(\epsilon^0)$, respectively. Substituting x_{10} and x_{20} into the equations of $O(\epsilon^1)$, secular terms are acquired. Conditions not to produce the secular terms in x_{11} and x_{21} are expressed as follows:

$$\frac{d}{dt}a = -\frac{1}{2}\mu a + \frac{1}{8}\beta_n a^3 + \frac{1}{2}\beta_l a + \frac{1}{2}\kappa b\sin\phi \tag{3}$$

$$\frac{d}{dt}b = -\frac{1}{2}\mu b + \frac{1}{8}\beta_n a^3\cos\phi + \frac{1}{2}\beta_l a\cos\phi + \frac{1}{2}\kappa b\sin\phi. \tag{4}$$

From Eqs. (3) and (4), we obtain steady state amplitude as follows:

$$\text{trivial solution}: \ a_{st} = b_{st} = 0, \quad \text{nontrivial solution}: \ a_{st} = b_{st} = \sqrt{\frac{4(\beta_l - \mu)}{-\beta_n}}.$$

In the region of $\beta_l - \mu > 0$, the trivial solution is unstable, and in the region of $\beta_l - \mu < 0$, the trivial solution is stable. In case of $\beta_n > 0$, the nontrivial solution is unstable and in case of $\beta_n < 0$, the nontrivial solution is stable. As a result, the cantilevers have the stable nontrivial steady state amplitude when nonlinear feedback control is applied. The nontrivial amplitude becomes smaller under the high-gain nonlinear feedback.

3 Amplitude control experiment

To confirm validity of the theoretically proposed method, we performed amplitude control experiments using weakly coupled microcantilevers in the air. A picture of the cantilevers with dimensions is shown in Fig. 1(a). The schematic of the experimental system is shown in Fig. 1(b). The velocity signal for feedback control is measured by a laser Doppler vibrometer and transferred to a feedback circuit. Feedback control Δx is applied by the piezoelectric attached to the cantilever case. We operate the parameter β_n via the resistor R_n in the feedback circuit.

Experimental results Fig. 1(c) confirmed that increasing the nonlinear feedback gain realizes response amplitude smaller.

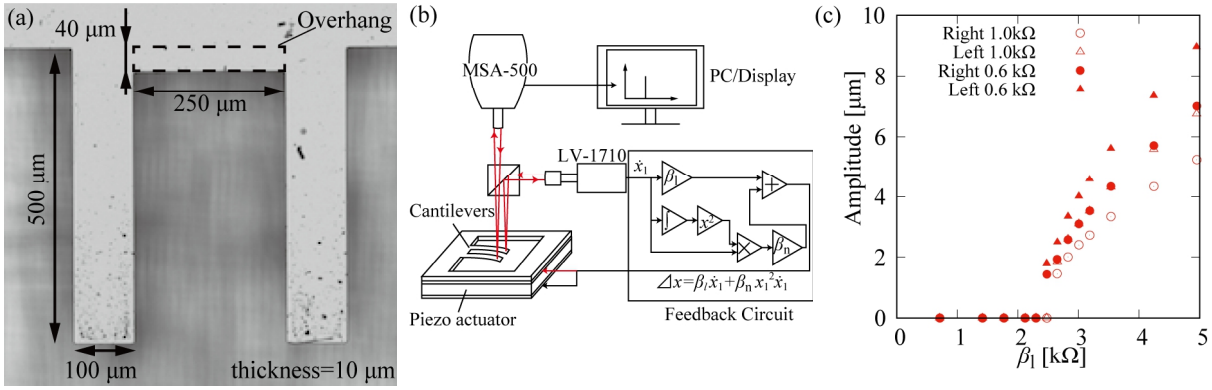

Figure 1. (a) Top view of the coupled microcantilevers. (b) Simplified experimental systems. β_l and β_n is controlled via the resistor in the circuit. (c) Variation of the amplitude depending on R_n.

The experimental results are in qualitatively good agreement with theoretical ones.

4 Acknowledgements

The authors acknowledge a Grant-in-Aid for Scientific Research A (Grant No. 16H02318) from the Japan Society for the Promotion of Science (JSPS).

5 Conclusions

In this research, we theoretically and experimentally confirm that the self-excited microcantilever has the steady-state amplitude that is controlled by changing the nonlinear feedback gain.

References

[1] Y. Aboelkassem, A. H. Nayfeh, and M. Ghommem. Bio-mass sensor using an electrostatically actuated microcantilever in a vacuum microchannel. *Microsystem technologies*, 16(10):1749–1755, 2010.

[2] K. Y. Gfeller, N. Nugaeva, and M. Hegner. Micromechanical oscillators as rapid biosensor for the detection of active growth of escherichia coli. *Biosensors and Bioelectronics*, 21(3):528–533, 2005.

[3] B. Ilic, D. Czaplewski, M. Zalalutdinov, H. G. Craighead, P. Neuzil, C. Campagnolo, and C. Batt. Single cell detection with micromechanical oscillators. *Journal of Vacuum Science & Technology B: Microelectronics and Nanometer Structures Processing, Measurement, and Phenomena*, 19(6):2825–2828, 2001.

[4] M. Spletzer, A. Raman, A. Q. Wu, X. Xu, and R. Reifenberger. Ultrasensitive mass sensing using mode localization in coupled microcantilevers. *Applied Physics Letters*, 88(25):254102, 2006.

[5] H. Yabuno, Y. Seo, and M. Kuroda. Self-excited coupled cantilevers for mass sensing in viscous measurement environments. *Applied Physics Letters*, 103(6):063104, 2013.

[6] D. Endo, H. Yabuno, K. Higashino, Y. Yamamoto, and S. Matsumoto. Self-excited coupled-microcantilevers for mass sensing. *Applied Physics Letters*, 106(22):223105, 2015.

EUROMECH Colloquium 603
Dynamics of micro and nano systems
5 – 7 September 2018, Porto, Portugal

Semi-analytic modeling and experiments of a collapse-mode CMUT with fluid coupling

R.H.B. Fey[1], M. Pekař[2], S.H.M. van Nispen[1], S. Shulepov[2], N. Mihajlović[2], and H. Nijmeijer[1]

[1]Eindhoven University of Technology, Eindhoven, the Netherlands
r.h.b.fey@tue.nl, h. nijmeijer@tue.nl

[2] Philips Research, Eindhoven, the Netherlands
martin.pekar@philips.com, sergei.shulepov@philips.com, nenad.mihajlovic@philips.com

Summary. A semi-analytic, reduced-order model of a fluid-loaded transmitting capacitive-micromachined ultrasound transducer (CMUT) operated in collapse mode is developed. A prototype of this CMUT has been used in an intracardiac catheter for preclinical imaging. Simulation of static deflections are validated with digital holography microscope measurements of a fabricated CMUT. The model accurately predicts the static response behavior. In addition, the dynamic responses of a detached single CMUT cell and an array of CMUT cells are analyzed for the effect of pressure radiation. Experiments show that the dynamic response and frequency-tunability of the CMUT array are modeled with satisfactory accuracy. The model is thus a powerful tool for CMUT pre-design.

Keywords: CMUT, collapse mode, semi-analytic model, simulations, experiments

1 Introduction

Collapse-mode operation of capacitive-micromachined ultrasound transducers (CMUTs) has shown potential for high performance medical imaging [1], [2]. A few hundred nanometer displacement of thousands of CMUT cells results in a pressure propagation up to tens of centimeters. State-of-the-art collapse-mode CMUT models utilize the intrinsically slow Finite Element Method or are based on an equivalent circuit approach giving limited physical insight. The objective of this paper[1] is to develop and experimentally validate an electro-mechanical, fluid-coupled, semi-analytic model that enables both thoroughly understanding the dynamic collapse-mode CMUT behavior and fast parameter studies to guide its pre-design. Static and dynamic (transmitting) response behavior of the CMUT will be studied.

2 Semi-analytic modeling

A schematic side-view of a circular CMUT cell in collapsed state is given in Fig. 1a. The clamped flexible top plate comprising the top electrode has radius a and thickness t_m. It is separated from the rigid bottom plate comprising the bottom electrode by two insulation layers, each having a thickness $t_i/2$, and a vacuum gap of height t_g. The DC bias voltage V_{bias} causes the center part of the top plate to collapse onto the bottom plate. Then the AC voltage $V_{AC}(t)$ causes vibrations in the free part of the top plate, which generate pressure waves (ultrasound) in the fluid above the top plate. Assuming axisymmetric motion of the circular top plate, the governing equation for the transversal displacement $w(r,t)$, with r the radial coordinate, is

$$\rho_{tp} t_m \ddot{w} + D\nabla_r^4 w = -\frac{\epsilon_0 V^2(t)}{2\left(t_{eff}+w\right)^2} + \frac{H_{ab}}{2}\mathrm{erfc}\left(\frac{t_g+w}{\sigma\sqrt{\pi}}\right) + \frac{\tau t_m}{r}\frac{\partial}{\partial r}\left(r\frac{\partial w}{\partial r}\right) - P_a - P_s - P_m. \tag{1}$$

The CMUT parameters are defined in Table 1. The left-hand side of (1) contains the classical terms describing the flexural deformations of a thin, isotropic vibrating plate. The right-hand terms model respectively the electrostatic pressure, the contact pressure of the collapsed part of the top plate, the biaxial residual stress, atmospheric pressure, pressure due to self-radiation, and pressure due to mutual radiation. Self-radiation pressure describes the effect that the emitted pressure to the surrounding fluid

[1]This work is for the first time presented orally to the scientific community. This paper is a summary of [3].

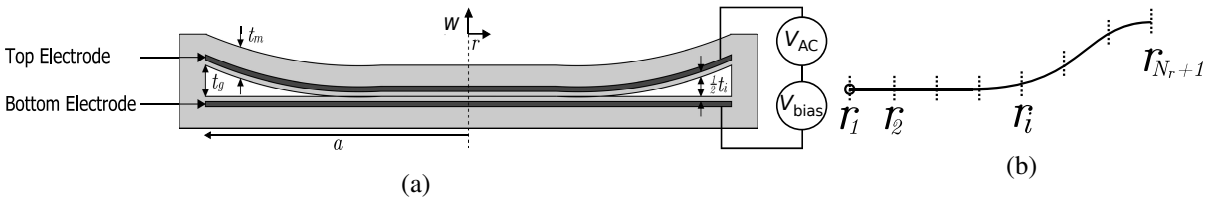

Figure 1: Schematic side-view of the geometrical parameters of a CMUT in collapsed state (a). Equidistant element mesh in radial direction (b).

from a point on the top plate of the cell influences the top-plate motion of the cell itself. In case of $N_c > 1$ cells, in addition pressure radiation of one cell influences the motion of other cells (mutual radiation effect). For calculating the radiation pressures, each cell surface is meshed into $N = N_r N_\theta$ elements, where $N_r = 101$ and $N_\theta = 64$ are the numbers of elements in radial (see Fig. 1b) and circumferential direction, respectively. Self-radiation pressure is calculated by

$$P_s(r,t) = \sum_{i=1}^{N_r} \sum_{m=1,m\neq i}^{N} \frac{\rho_{fl} A_m \ddot{w}_m(r,t)\ \delta\left(t - \frac{d_{m,i}}{c_{fl}}\right)}{2\pi d_{m,i}} \mathrm{BF}_i(r)\,, \tag{2}$$

where A_m is the area and $\ddot{w}_m$ is the acceleration of the emitting element, $d_{m,i}$ is the distance from the emitting to the receiving element, and $\mathrm{BF}_i(r)$ is 1 if $r_i \leq r < r_{i+1}$ and 0 otherwise; ρ_{fl} and c_{fl} are defined in Table 1. The mutual radiation pressure for receiving cell l is calculated by

$$P_{m,l}(r,t) = \sum_{k=1,k\neq l}^{N_c} \sum_{i=1}^{N_r} \sum_{m=1}^{N} \frac{\rho_{fl} A_m \ddot{w}_m(r,t)\ \delta\left(t - \frac{d_{mk,il}}{c_{fl}}\right)}{2\pi d_{mk,il}} \mathrm{BF}_i(r)\,. \tag{3}$$

A reduced order (RO) model is obtained by applying Galerkin discretization to (1). Displacement field

Table 1: CMUT parameters; τ and σ have been identified experimentally.

Parameter	Value	Unit	Description
a	$30{\cdot}10^{-6}$	m	Plate radius
ϵ_0	$8.85{\cdot}10^{-12}$	F/m	Dielectric permittivity of vacuum
ϵ_r	4.3	–	Relative dielectric permittivity of insulator
t_g	$230{\cdot}10^{-9}$	m	Gap height
t_i	$450{\cdot}10^{-9}$	m	Insulator thickness
t_{eff}	$3.347{\cdot}10^{-7}$	m	Effective gap height ($= t_g + t_i/\epsilon_r$)
t_m	$1.565{\cdot}10^{-6}$	m	Plate thickness
D	$4.092{\cdot}10^{-8}$	Nm	Effective flexural rigidity of plate
P_a	$101.325{\cdot}10^{6}$	Pa	Atmospheric pressure
τ	$-100{\cdot}10^{6}$	Pa	Uniform residual biaxial plane stress
σ	$4{\cdot}10^{-9}$	m	Combined surface roughness standard deviation
H_{ab}	$1{\cdot}10^{9}$	Pa	Effective indentation hardness
ρ_{tp}	3290	kg/m^3	Combined mass density of the top plate
c_{fl}	1483	m/s	Speed of sound in water
ρ_{fl}	1000	kg/m^3	Mass density of water

$w(r,t)$ is approximated by a linear combination of the 6 lowest undamped axisymmetric eigenmodes of the clamped circular plate. A convergence study showed a remaining inaccuracy of 2 nm in w.

The dynamic response of a single cell in an array of cells (see the next section) can be calculated now. For computational efficiency it is assumed that all cells show the same response, i.e. an infinite array is assumed. In simulations, to meet the infinite array assumption, the array size is chosen in accordance with the response time interval of interest.

The pressure at an arbitrary point in the fluid is calculated by summing pressures originating from all the surface accelerations predicted by the RO model, which is similar to the pressure calculation in (3).

3 Prototype

Fig. 2a shows the fabricated CMUT prototype. The array consists of 932 30-μm-radius CMUT cells arranged on a rectangular grid in an octagonal shape. The spacing between neighboring cells is 3.6 μm. All CMUT cells are driven in parallel. Fig. 2b shows the material layers of the CMUT stack.

The modeling assumption of an axisymmetric response of a single cell is compromised by the rectangular grid, resulting in a mutual radiation pressure profile for each cell which is only rotationally symmetric over 90°. The mutual radiation profile is calculated for a radial line connecting the centers of two adjacent cells. Furthermore, the (infinite array) assumption that all cells move identical may be inaccurate for cells near the edge of the array, which will receive different mutual radiation pressures than cells near the center of the array. These assumptions were made, however, to keep the model simple.

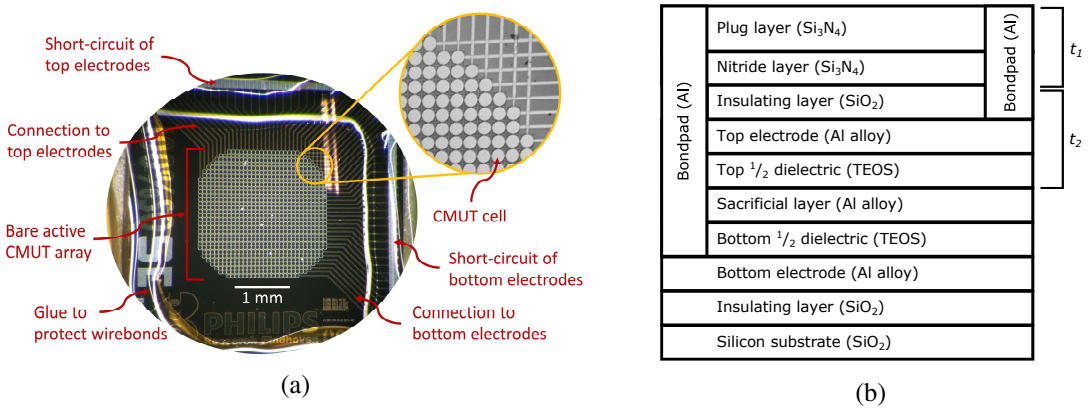

Figure 2: Photograph of the fabricated CMUT prototype (a) used for the experimental model validation and material layers (b); t_1 and t_2 represent the first and second effective layer of the top electrode.

4 Static and dynamic response results

A digital holography microscope (DHM; R2100, Lyncée Tec SA) is utilized (radial resolution 1.15 μm, accuracy $\pm$ 3 nm) to validate the static behavior of a CMUT cell in air predicted by the RO model. Fig. 3a shows that the RO model accurately predicts the static response for three bias voltages. The maximum deviation is 10 nm for a bias voltage of 140 V.

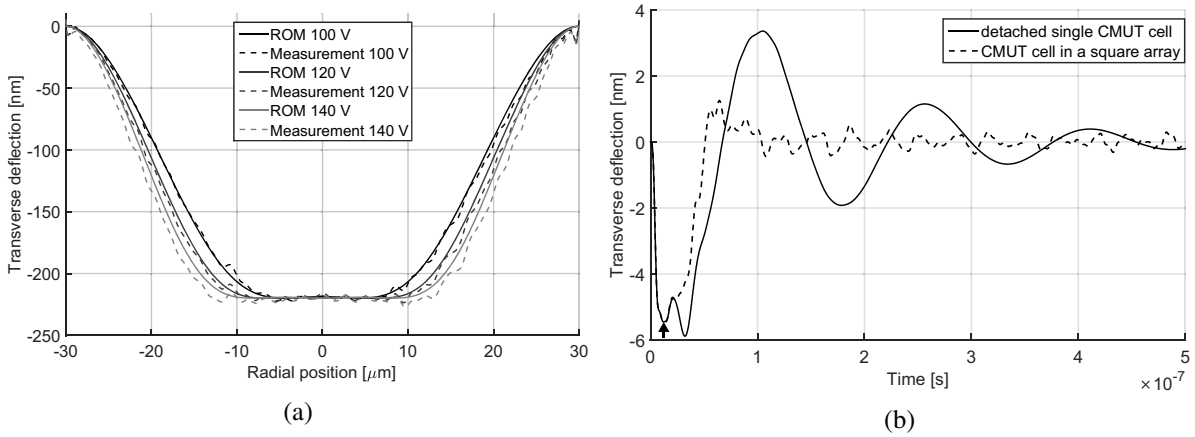

Figure 3: Static response (a) of the reduced-order model (ROM) validated towards measurements in air with a DHM. Simulated impulse response in water (b) of a point at 15 μm radius on a CMUT cell biased at 120 V, and excited with half a period of a 100-MHz 60-V squared sine. The arrow indicates the time at which the first mutual radiation forces reach the chosen radial position.

Static deflection profiles are used as initial conditions for dynamic simulations in water. Fig. 3b shows simulated time histories of the transversal displacement at $r = 15\mu$m, where $V_{AC}(t) = 60\ \sin^2(2\pi \cdot 10^8 \cdot t)$, with $0 \leq t \leq 5 \cdot 10^{-9}$s, is used as the dynamic excitation signal. The solid line shows the response of a single detached CMUT cell, whereas the dashed line shows the response of a CMUT cell in the center of the array. During the first few nanoseconds, only self-radiation is active and the responses are similar. For the CMUT array, after 12.5 ns (time indicated by the arrow), the first mutual radiation pressure wave reaches the chosen radial position. The mutual radiation forces significantly affect the dynamic response, which is damped and shows less overshoot.

Unfortunately, the DHM could not be used in water. To validate the dynamic behavior of the RO model of the CMUT array with fluid coupling, in a water tank, a needle hydrophone (Ø 0.2 mm, Precision Acoustics) is placed at a distance of 10.8 mm from the center of the CMUT array prototype. A bias voltage of 160 V and half a period of a 60-MHz 45-V sine is used as the excitation signal. Fig. 4a shows that the overall shape of the simulated pressure response is in satisfactory agreement with the measurement. The amplitude, however, is overestimated by the RO model. Fig. 4b shows the corresponding frequency spectra with peaks near 16.5 MHz. The difference in amplitude between the simulated and measured responses may be explained by the earlier discussed simplifying modeling assumptions that every CMUT cell shows 1) an identical and 2) an axisymmetric response. Another bias voltage of e.g. 100 V results in peaks near 12 MHz, which demonstrates the frequency tunability of the device.

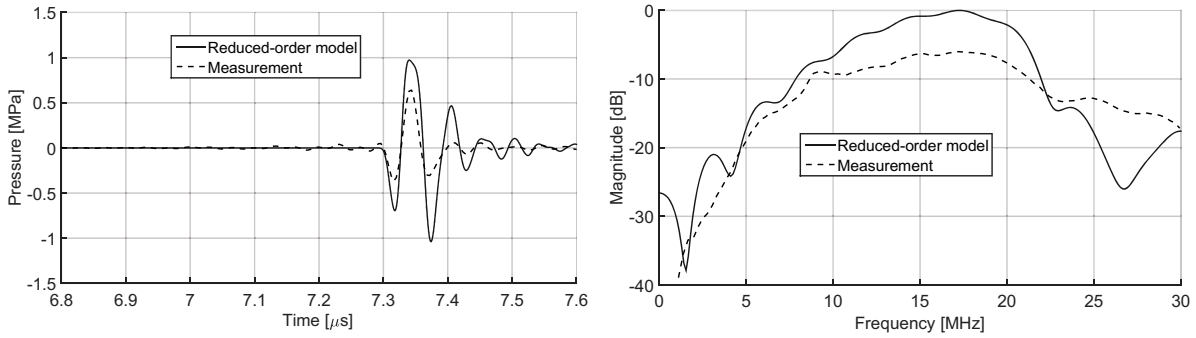

(a) (b)

Figure 4: Acoustic impulse response (a) and frequency response (b) of the simulated and measured CMUT array excited with half a period of a 60-MHz 45-V sine and biased at 160 V. The reference pressure corresponding to the 0 dB magnitude equals to 13.1 kPa.

5 Conclusions and recommendations

A semi-analytic RO model of a CMUT(-array) operated in collapse mode has been developed and validated with static and dynamic measurements. The model allows fast parameter studies and is therefore a powerful tool for CMUT pre-design. It is recommended to further study the effect of simplifying modeling assumptions and to interface the model with an ultrasound image simulator, which could then demonstrate the frequency tunable capability of the device enabling a trade-off between penetration depth and image resolution.

References

[1] K.K. Park et al., A Comparison Between Conventional and Collapse-Mode Capacitive Micromachined Ultrasonic Transducers in 10-MHz 1-D Arrays. *IEEE Trans Ultrason Ferroelectr Freq Control*, **60**, pp. 1245-1255, 2013.

[2] M. Pekař et al., Preclinical Testing of Frequency-Tunable Capacitive Micromachined Ultrasonic Transducer Probe Prototypes. *Ultrasound Med Biol*, **43**, pp. 2079-2085, 2017.

[3] M. Pekař, S.H.M. van Nispen, R.H.B. Fey, S. Shulepov, N. Mihajlović, H. Nijmeijer, A fluid-coupled transmitting CMUT operated in collapse mode semi-analytic modeling and experiments. *Sens Actuator A-Phys*, **267**, pp. 474-484, 2017.

EUROMECH Colloquium 603
Dynamics of micro and nano systems
5 – 7 September 2018, Porto, Portugal

Theoretical Framework for modelling the fluid-structure interaction of complex MEMS/NEMS resonator eigenmodes

Daniel Platz[1], Georg Pfusterschmied[1] and Ulrich Schmid[1]

[1] Institute of Sensor and Actuator Systems, TU Wien, A-1040 Vienna, Austria

daniel.platz@tuwien.ac.at
georg.pfusterschmied@tuwien.ac.at
ulrich.e366.schmid@tuwien.ac.at

Summary: The quality factor is an important figure of merit for evaluating the performance of MEMS/NEMS devices. Recently, it has been demonstrated that complex non-conventional eigenmodes exhibit extraordinary high quality factors in liquids. Here, we present a theoretical framework for the analysis of the interaction between a fluid and complex eigenmodes. We compare the modelling assumptions of two- and three-dimensional flows and discuss the damping of a two-dimensional plate mode shape in a fluid environment as an application of the presented framework.

Keywords: Fluid-structure interaction, damping, quality factor, plate eigenmodes

1 Introduction

Micro- and nanoelectromechanical systems (MEMS/NEMS) are increasingly more widespread used in both engineering and scientific measurement applications. Typically, MEMS/NEMS devices are operated in either a gaseous or a liquid environment which interacts with the device. This interaction strongly affects the performance of MEMS/NEMS devices and thus controlled operation and quantitative measurement require accurate knowledge of this interaction. Most prominently the resonance frequency and the quality factor (Q factor) are modified by the interaction.

The interaction is commonly described as the continuum mechanical interaction between a solid structure and a fluid. This fluid-structure interaction has been extensively studied for standard MEMS/NEMS structures like cantilevers[1–4]. These studies are restricted to the simplest geometries which is sufficient for many applications. Recently, it has been demonstrated that complex mode shapes of plate-like MEMS resonators exhibit extraordinary high Q factors[5–9]. However, the exact physical origin of this observation remains elusive.

In this talk we will present a theoretical framework for the analysis of the fluid-structure interaction for complex eigenmodes and will discuss the experimental observations in the context of this theory.

2 Theory

Conventional eigenmodes of MEMS/NEMS devices as depicted in figure 1a have been studied extensively. They occur in cantilever-like systems which can be described as one-dimensional objects. In contrast non-conventional complex eigenmodes as shown in figure 1b exhibit a two-dimensional spatial structure. Modelling of these modes thus requires a two-dimensional approach like the Kirchhoff-Love plate theory for which the equation of motion for a plate in the xy plane is given by

$$D\nabla^2\nabla^2 w(x,y,t) + 2\rho_p h\frac{\partial^2 w(x,y,t)}{\partial t^2} + F(x,y,t) = 0\,, \tag{1}$$

where w is the deflection of the plate in z direction depending of both the spatial coordinates x and y and on time t , D is the bending stiffness, ρ_p is the density of the plate, h is the thickness of the plate and F is an external force acting on the plate. This external force couples the plate to the surrounding fluid which is represented in the limit of small deflections with the linearized Navies-Stokes equations for an incompressible fluid

$$\rho \frac{\partial \mathbf{u}}{\partial t} - \mu \nabla^2 \mathbf{u} + \nabla p = \mathbf{0}\,, \tag{2}$$

$$\nabla \cdot \mathrm{u} = \mathbf{0}\,, \tag{3}$$

where $\mathbf{u}$ is the velocity of the fluid, p is the pressure, ρ is the density of the fluid and μ its viscosity. A common approach is to model the force F as a linear response relation in Fourier space such that

$$\hat{F}(x,y,\omega) = \Gamma(\omega)\hat{w}(x,y,\omega)\,, \tag{4}$$

where the hat denotes the Fourier transformation with respect to time and ω is the corresponding frequency. Γ is called the hydrodynamic function and describes the geometry-dependent interaction between device and fluid[2].

3 Results

For simple geometries approximations of the hydrodynamic function are readily obtained. However, for complex mode shapes such expressions have been missing. We derive the hydrodynamic functions using a boundary integral method based on a Green's function approach for the fluid flow for a complex mode shape[11].

While the boundary integral approach is well established for two dimensional flows, three dimensional flows around simple MEMS structures have been considered recently[12]. The approach is based on Fourier expanding the fluid velocity field in the spatial coordinates and determining the expansion amplitudes by the boundary conditions. We extend this approach to complex mode shapes. By comparing the results of the two-dimensional and the three-dimensional approach we study the limits of validity of both methods.

As an application we discuss how the computed flow fields can be used to investigate the influence of mode geometry and the damping of complex plate eigenmodes in inviscid and viscous fluids.

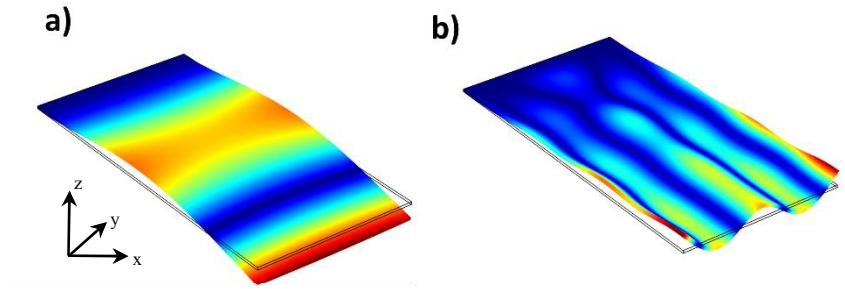

Figure 1: Simulated mode shapes of a cantilevered plate. (a) A conventional mode shape. (b) A complex mode shape exhibiting a two-dimensional spatial pattern.

References

1. Elmer, F. & Dreier, M. Eigenfrequencies of a rectangular atomic force microscope cantilever in a medium. *J. Appl. Phys.* **81,** 7709–7714 (1997).

2. Sader, J. E. Frequency response of cantilever beams immersed in viscous fluids with applications to the atomic force microscope. *J. Appl. Phys.* **84,** 64–76 (1998).

3. Green, C. P. & Sader, J. E. Torsional frequency response of cantilever beams immersed in viscous fluids with applications to the atomic force microscope. *J. Appl. Phys.* **92,** 6262–6274 (2002).

4. Van Eysden, C. A. & Sader, J. E. Frequency response of cantilever beams immersed in viscous fluids with applications to the atomic force microscope: Arbitrary mode order. *J. Appl. Phys.* **101,** 44908 (2007).

5. Kucera, M. *et al.* Characterization of a roof tile-shaped out-of-plane vibrational mode in aluminum-nitride-actuated self-sensing micro-resonators for liquid monitoring purposes. *Appl. Phys. Lett.* **104,** 233501 (2014).

6. Pfusterschmied, G. *et al.* Temperature dependent performance of piezoelectric MEMS resonators for viscosity and density determination of liquids. *J. Micromechanics Microengineering* **25,** 105014 (2015).

7. Pfusterschmied, G. *et al.* Multi roof tile-shaped vibration modes in mems cantilever sensors for liquid

monitoring purposes. in *2015 28th IEEE International Conference on Micro Electro Mechanical Systems (MEMS)* **2015–Febru,** 718–721 (IEEE, 2015).

8. Pfusterschmied, G. *et al.* Roof tile-shaped modes in quasi free–free supported piezoelectric microplate resonators in high viscous fluids. *Sensors Actuators B Chem.* **237,** 999–1006 (2016).

9. Toledo, J. *et al.* Comparison of in-plane and out-of-plane piezoelectric microresonators for real-time monitoring of engine oil contamination with diesel. *Microsyst. Technol.* **22,** 1781–1790 (2016).

10. Kucera, M. *et al.* Characterisation of multi roof tile-shaped out-of-plane vibrational modes in aluminium-nitride-actuated self-sensing micro-resonators in liquid media. *Appl. Phys. Lett.* **107,** 53506 (2015).

11. Tuck, E. O. Calculation of unsteady flows due to small motions of cylinders in a viscous fluid. *J. Eng. Math.* **3,** 29–44 (1969).

12. Van Eysden, C. A. & Sader, J. E. Small amplitude oscillations of a flexible thin blade in a viscous fluid: Exact analytical solution. *Phys. Fluids* **18,** 123102 (2006).

Experimental and Theoretical Investigation of a microbeam-based MEMS device with Half Electrode Configuration

Laura Ruzziconi[1], Nizar Jaber[2], Lakshmoji Kosuru[2], Mohammed L. Bellaredj[2], Stefano Lenci[3] and Mohammad I. Younis[2]

[1] eCampus University, Faculty of Engineering, 22060 Novedrate, Italy
laura.ruzziconi@uniecampus.it

[2] King Abdullah University of Science and Technology (KAUST), Physical Science and Engineering Division, 23955-6900 Thuwal, Saudi Arabia
nizar.jaber@kaust.edu.sa
Mohammad.Younis@kaust.edu.sa

[3] Polytechnic University of Marche, Department of Civil and Building Engineering, and Architecture, via Brecce Bianche, 60131 Ancona, Italy
lenci@univpm.it

Summary. The present work deals with a MEMS device consisting of a clamped-clamped microbeam electrically actuated with half electrode configuration. Many experimental frequency sweeps are acquired. After introducing a Galerkin reduced-order model, systematic local and global simulations are preformed. The model is observed to catch the main aspects of the device response, both at low and at higher frequency values.

Keywords: MEMS, experimental data, nonlinear dynamics.

1 Introduction

The present work is motivated by the increasing attention toward describing and predicting the nonlinear phenomena in MEMS, which is essential for their proper design, performance analysis, and calibration [1]. Numerous studies explore the complex non-linear scenario that may arise in a MEMS device [2-4]. In the present work we focus on the device of Figs. 1, which is an electrically actuated clamped-clamped microbeam with half electrode configuration, fabricated by surface micromachining process. An extensive experimental investigation is conducted and systematic simulations are developed to analyze the nonlinear phenomena arising in its response.

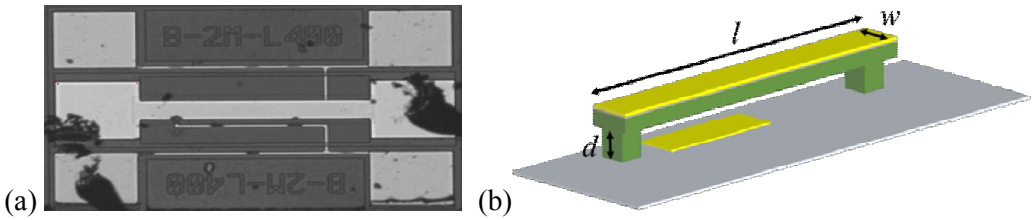

Figure 1. Electrically actuated microbeam-based MEMS device with half electrode configuration. (a) Optical image. (b) Schematic representation.

2 Experimental Data and Theoretical Predictions

After identifying the first three experimental natural frequencies, the nonlinear dynamics are explored at increasing values of electrodynamic excitation in a neighborhood of the first symmetric resonance. Several backward and forward frequency sweeps are acquired. Two of them are reported in Fig. 2, at V_{AC} = 4.0 V and V_{AC} = 14.4 V. A Galerkin reduced-order model is derived. The device response is

characterized by the presence of both the non-resonant branch (at right) and the resonant one (at left). They exhibit bending toward higher frequencies, which is not particularly common in MEMS. At low electrodynamic voltages, when a branch disappears there is jump to the other branch; at higher values, instead, at disappearance the system undergoes dynamic pull-in. Increasing the electric voltage excitation, the range of coexistence of the non-resonant and the resonant branches initially increases, then it decreases and finally vanishes, resulting in an interval where no one of the attractors exist.

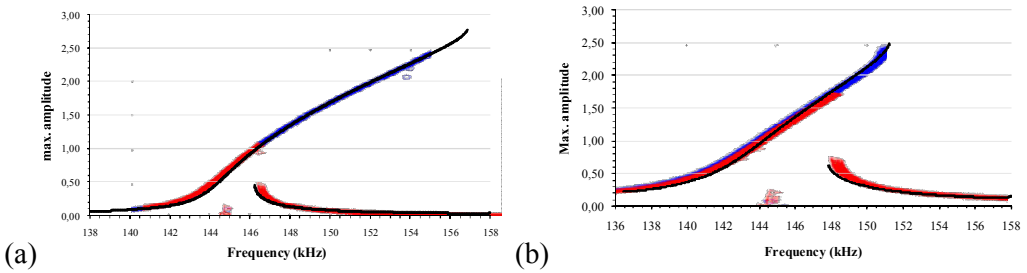

(a) (b)

Figure 2. Frequency response diagrams at (*a*) $V_{AC} = 4.0\ V$ and (*b*) $V_{AC} = 14.4\ V$. Experimental data obtained by forward and backward sweeps are in blue circles and red triangles, respectively. Theoretical simulations are in black solid line.

Developing a global investigation, we can observe that at low voltages the two basins are close to each other and form a large and compact safe region; at higher ones, instead, the escape penetrates inside the core of the potential well and separates the two basins, preventing any safe jump between them. This is confirmed by the experimental data.

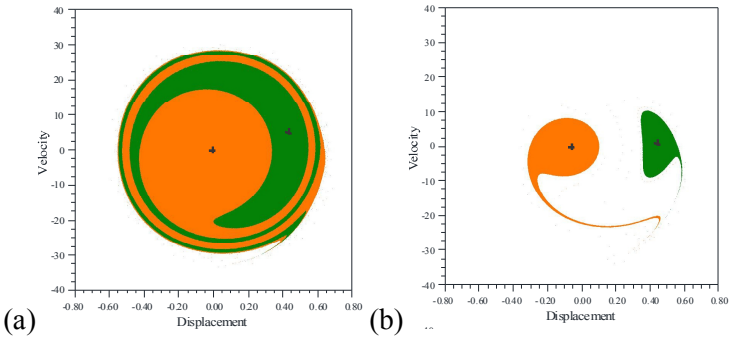

(a) (b)

Figure 3. Attractor-basins phase portraits. (a) $V_{AC} = 4V$ and $\Omega = 153$Hz; (b) $V_{AC} = 15V$ and $\Omega = 150$Hz

3 Conclusions

In the present study an experimental and theoretical investigation has been conducted on a MEMS device. The model has been shown to provide valuable information on the MEMS dynamics and catch all the main nonlinear features of the device response.

Acknowledgments

Mohammad I. Younis acknowledges KAUST funding to support this project.

References

[1] M. I. Younis, *MEMS Linear and Nonlinear Statics and Dynamics*, Springer, New York, 2011.

[2] L. Ruzziconi, A. M. Bataineh, M. I. Younis, W. Cui, S. Lenci, Nonlinear dynamics of an electrically actuated imperfect microbeam resonator: experimental investigation and reduced-order modeling, *Journal of Micromechanics and Microengineering*, **23**(7), 075012-1 – 075012-14, 2013.

[3] A. Z. Hajjaj, A. H. Ramini, N. Alcheikh, M. I. Younis, Electrothermally tunable arch resonator, *Journal of Microelectromechanical Systems*, **26**(4), 837 - 845, 2017.

[4] L. Ruzziconi, M. I. Younis, S. Lenci, An electrically actuated imperfect microbeam: dynamical integrity for interpreting and predicting the device response, *Meccanica*, **48**(7), 1761-1775, 2013.

EUROMECH Colloquium 603
Dynamics of micro and nano systems
5 – 7 September 2018, Porto, Portugal

On nonlinear vibrational properties of graphene-based structures

Reza Ghaffari[1], **Aningi Mokhalingam**[2], **Shakti S. Gupta**[2] **and Roger A. Sauer**[1]

[1]Aachen Institute for Advanced Study in Computational Engineering Science (AICES),
RWTH Aachen University, Templergraben 55, 52056 Aachen, Germany
ghaffari@aices.rwth-aachen.de
sauer@aices.rwth-aachen.de

[2] Department of Mechanical Engineering, IIT Kanpur, Kanpur - 208016, India
aningi@iitk.ac.in
ssgupta@iitk.ac.in

Summary. In this paper frequencies of transverse vibrations of radially stretched circular graphene sheets are studied using two approaches; atomistic simulations and quantum mechanics data based continuum model. The atomistic simulations are carried out employing MM3 and REBO+LJ potentials. The continuum formulation uses an anisotropic hyperelastic material model in the finite element framework. The changes in frequencies with increasing the radial stretch are determined from these two approaches and are found to be almost identical up to the surface stretch J= 1.2. However, beyond this value frequencies obtained from MM3 potential and REBO+LJ are found to be either higher or lower, respectively, for those computed using the continuum model.

Keywords: Anisotropic hyperelastic material model, graphene sheets, nonlinear modal analysis, molecular mechanics and dynamics.

1 Introduction

All edges clamped circular/rectangular graphene sheets or clamped-clamped graphene ribbons are the potential candidate for making highly sensitive mass sensors. Further, applying in-plane stretch in these structures can significantly increase the frequencies of transverse vibrations [1], [2] and [3] thus, further increasing their sensitivity. It has been reported in the literature that graphene can be elastically deformed up to 25% [4], [5]. For this, in the continuum framework a reliable material model which can predict frequencies of transverse vibrations at large value of stretches is most desirable. The available classical linear material models are limited to infinitesimal strains and an anisotropic hyperelastic material model is needed to capture nonlinear and anisotropic behavior of graphene-based structures. Also, one must be able to benchmark the results from the developed model with those obtained from molecular simulations or experiments. Towards this Ghaffari et al. [6, 5] propose nonlinear anisotropic hyperelastic shell material models over the membrane material model given by Kumar and Parks [7]. The shell material models are implemented in the curvilinear rotation-free finite element shell formulation of [8].
In this paper we compare the results from the continuum material model of Ghaffari et al. [5] and those from molecular simulations. The paper is arranged as follows. Section 2 describes the details of molecular simulations employing MM3 and REBO+LJ potentials. A brief introduction to continuum framework and the numerical procedure adopted is given in Section 3. Results and discussions appear in Section 4 followed by conclusions in Section 5.

2 Molecular simulations

In this study we use two different potentials; MM3 and REBO+LJ for simulation of vibrations in a circular graphene sheet to check consistency of the results. It is noted that both the potentials in their own right have been successful in predicting mechanical behavior of carbon based nanomaterials in the small deformation regime.

2.1 Molecular mechanics (MM)

In MM simulation MM3[9] potential is used to define the interactions between the atoms of the graphene sheet. The potential is described as

$$U_{\text{MM3}} = \sum_i \sum_j (U_{\text{s}} + U_\theta + U_\phi + U_{\text{s}\theta} + U_{\phi\text{s}} + U_{\theta\theta'}) + \sum_i \sum_k U_{\text{vdW}} \,, \tag{1}$$

where U_{s}, U_θ and U_ϕ are account for the energies assosiated with changes in bond, angle and dihedral respectively. $U_{\text{s}\theta}$, $U_{\theta\theta'}$ and $U_{\phi\text{s}}$ are accounts for cross-term interactions among stretching (s), bending (θ), torsional (ϕ) and out-of-plane bending $\left(\theta'\right)$ respectively. U_{vdW} defines the van der Waals (vdW) potential and is different than the standard 12-6 form and has the terms $(r_{\text{c}}/r)^6$ and $\exp(-12r/r_{\text{c}})$ with r_{c} as cut-off distance.

For simulations the graphene sheet is first relaxed to the minimum energy configuration within root mean square gradient of 0.001 Kcal/mol-Å, without employing any constraints. Then, the outer edge atoms are displaced radially with an increment of 0.1Å till the required stretch is obtained. At each incremental radial displacement the system is relaxed by fixing the outer edge atoms. The frequencies are found out by using the VIBRATE module in Tinker[10]. VIBRATE essentially finds the eigenvalues (frequencies) and eigenvectors (modeshapes) of mass weighted Hessian of the system.

2.2 Molecular Dynamics (MD)

In MD simulations REBO+LJ potential in LAMMPS [11] is used. The interactions between the atoms are defined as follows

$$U = U^{\text{REBO}} + U^{\text{LJ}} \,, \tag{2}$$

where

$$U^{\text{REBO}} = \sum_i \sum_{j=i+1} \left[E_{\text{R}}(r_{ij}) - b_{ij} E_{\text{A}}(r_{ij}) \right] , \tag{3}$$

with E_{R} and E_{A} as the repulsive and attractive terms, respectively, r_{ij} is the distace between the pair of atoms and b_{ij} is a many-bond empirical bond-order term. The vdW forces are described by U^{LJ} and has the standard 12-6 form.

In MD simulations the graphene sheet at the minimum energy configuration is equilibrated using Nose-Hoover thermostat at 0.1 K for 50 ps with a timestep of 1fs. The temperature of the system is maintained at the desired level by employing three Nose-Hoover chains. The outer edge atoms of the sheet are pulled radially with a velocity of 0.1Å. After obtaining the desired stretch, the sheet is deformed into the mode shape correspond the first frequency and then allowed to vibrate freely enforcing the total mechanical energy of the system to be constant. Said differently, NVE simulations are performed. The time history of the atoms at the center is recorded to calculate the frequencies of vibration using fast Fourier transform (FFT).

3 Equivalent continuum model

Employing the improved material model available in [5], the circular graphene sheet in this paper is modelled as a shell in the finite element frame work. The discretized weak form can be written as

$$\mathbf{M}\,\ddot{\mathbf{u}} + \mathbf{f}_{\text{int}} = \mathbf{f}_{\text{ext}} \,, \tag{4}$$

where $\mathbf{M}$ is the mass matrix and $\mathbf{f}_{\text{int}}$ and $\mathbf{f}_{\text{ext}}$ are the internal and external force vectors. Using Taylor expansion around $\hat{\mathbf{u}}$ such that $\mathbf{u} = \hat{\mathbf{u}} + \mathrm{d}\mathbf{u}$, the linearized equations of motion are as follows

$$\mathbf{M}\,\mathrm{d}\ddot{\mathbf{u}} + \mathbf{K}\,\mathrm{d}\mathbf{u} = -(\mathbf{f}_{\text{int}} + \mathbf{M}\,\ddot{\hat{\mathbf{u}}} - \mathbf{f}_{\text{ext}}) \,, \tag{5}$$

where $\mathbf{K} := \partial(\mathbf{f}_{\text{int}} - \mathbf{f}_{\text{ext}})/\partial\mathbf{u}$ is the stiffness matrix (see [3] for details). Next, to explore harmonic response of the system we assume

$$\mathrm{d}\mathbf{u} := \mathrm{d}\bar{\mathbf{u}}\, e^{-i\omega t} \,, \tag{6}$$

where $\mathrm{d}\bar{\mathbf{u}}$ are ω are the mode shape and frequency of the structure, respectively. Using (3) the eigenvalue problem can be written as

$$\mathbf{K}\,\mathrm{d}\bar{\mathbf{u}} = \omega^2\,\mathbf{M}\,\mathrm{d}\bar{\mathbf{u}} \,. \tag{7}$$

4 Results and Discussions

The modal analysis for a circular graphene sheet with the radius of 4.4 nm is conducted and results are compared with atomistic simulations. The variation of the first frequency against the surface change J is shown in Fig. 1. In finite element solution simply-supported boundary condition is considered which in atomistic simulations is achieved by constraining all the three translation degrees of freedom. Variation in frequency of first mode from molecular simulations and that from finite element simulations are in good agreement for up to $J = 1.2$. We also note mismatch in the predicted frequency at $J = 1$ among all three simulations. This mismatch between results of REBO+LJ and MM3 is attributed to different potential parameters used. However, the difference between the results at $J = 1$ from continuum model and molecular simulations can be due to built in stresses in atomistic simulations in the minimum energy configuration which is not present in the continuum model. Beyond $J = 1.2$ the frequency computed from continuum model and from both the potentials show deviation in the frequency with increasing J. For REBO+LJ simulations could not be carried out beyond $J = 1.4$ due to breakage of bonds.

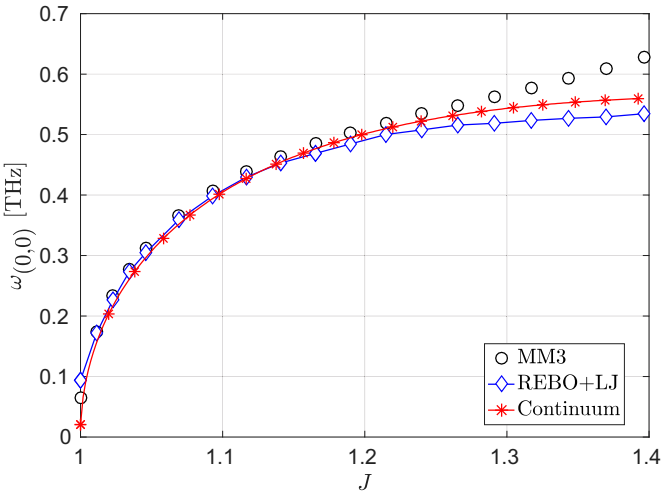

Figure 1. Variation in the first mode frequency against surface change computed from three different methods.

5 Conclusions

The nonlinear modal analysis of a circular graphene sheet is considered and results are compared with molecular simulations employing MM3 and REBO+LJ potentials. For up to $J = 1.2$ the results are in good agreement from all the three approaches. The divergence in frequency from molecular simulations and the continuum model at large value of J are under investigation.

Acknowledgments

Financial support from the German Research Foundation (DFG) through grant GSC 111 is gratefully acknowledged.

References

[1] S. S. Gupta and R. C. Batra. Elastic properties and frequencies of free vibrations of single-layer graphene sheets. *Journal of Computational and Theoretical Nanoscience*, **7**(10):2151–2164, 2010.

[2] Deepti Verma, S. S. Gupta, and R. C. Batra. Vibration mode localization in single- and multi-layered graphene nanoribbons. *Computational Materials Science*, **95**:41–52, 2014.

[3] Reza Ghaffari and Roger A. Sauer. Modal analysis of graphene-based structures for large deformations, contact and material nonlinearities. *Journal of Sound and Vibration*, **423**:161–179, 2018.

[4] Changgu Lee, Xiaoding Wei, Jeffrey W Kysar, and James Hone. Measurement of the elastic properties and intrinsic strength of monolayer graphene. *Science*, **321**(July):385–388, 2008.

[5] R. Ghaffari and R. A. Sauer. A new efficient hyperelastic finite element model for graphene and its application to carbon nanotubes and nanocones. *ArXiv e-prints*, February 2018.

[6] Reza Ghaffari, Thang X. Duong, and Roger A. Sauer. A new shell formulation for graphene structures based on existing ab-initio data. *International Journal of Solids and Structures*, **135**:37–60, 2018.

[7] Sandeep Kumar and David M. Parks. On the hyperelastic softening and elastic instabilities in graphene. *Proc. Royal Soc. Lond. A: Math. Phys. Eng. Sci.*, **471**(2173), 2014. DOI: 10.1098/rspa.2014.0567.

[8] Thang X. Duong, Farshad Roohbakhshan, and Roger A. Sauer. A new rotation-free isogeometric thin shell formulation and a corresponding continuity constraint for patch boundaries. *Comput. Methods in Appl. Mech. Eng.*, **316**:43–83, 2017. Special Issue on Isogeometric Analysis: Progress and Challenges.

[9] Norman L. Allinger, Young H. Yuh, and Jenn Huei Lii. Molecular Mechanics. The MM3 Force Field for Hydrocarbons. 1. *Journal of the American Chemical Society*, **111**(23):8551–8566, 1989.

[10] J.W. Ponder. Users guide computer code tinker molecular modelling package 4.2, 2004.

[11] Steve Plimpton. Fast parallel algorithms for short-range molecular dynamics. *Journal of Computational Physics*, **117**(1):1–19, 1995.

EUROMECH Colloquium 603
Dynamics of micro and nano systems
5 – 7 September 2018, Porto, Portugal

Finite elements based reduced order models for nonlinear dynamics of piezoelectric and dielectric laminated micro/nanostructures

O. Thomas[♯], A. Givois[♯,♭], A. Grolet[♯], J.-F. Deü[♭], C. Fuinel[♮], F. Mathieu[♮], B. Legrand[♮], L. Nicu[♮]

[♯] Arts et Métiers ParisTech / LISPEN, Lille, France
olivier.thomas@ensam.eu, arthur.givois@ensam.eu

[♭]Laboratoire de Mécanique des structures et des systèmes couplés, Cnam, Paris, France
jean-francois.deu@cnam.fr

[♮]CNRS, LAAS, Toulouse, France
bernard.legrand@laas.fr, liviu.nicu@laas.fr

Summary. This paper presents a general methodology to predict the dynamics of geometrically nonlinear Micro/Nano Electro-Mechanical Systems (M/NEMS) with piezoelectric and dielectric transducers, modelled as laminated thin structures. Modal Reduced Order Models (ROM) are built using finite-element software thanks to a non-intrusive strategy. The resulting system of coupled oscillators is solved with the Harmonic Balance Method (HBM) coupled to an Asymptotic Numerical Method (ANM). The present study focuses on the computation of the ROM, that include the geometrical nonlinear terms and the direct and converse electromechanical couplings. Then, frequency responses and nonlinear modes, including possible internal resonances, are proposed for some particular beams and circular plates M/NEMS architectures.

Keywords: Geometrical nonlinearities, electromechanical coupling, piezoelectric, dielectric, M/NEMS, finite elements.

1 Introduction

Geometrical nonlinearities, due to large transverse displacements of thin structures, are involved in a large range of applications. Among them, Micro-Electro Mechanical Systems (MEMS) developments has been the focus of numerous studies, whose purpose is to master and use the geometrically nonlinear behaviour (among others, see [7, 11, 14, 17]). Recent advances in non-intrusive reduced-order finite element modeling of nonlinear geometric structures offer new perspectives for massive nonlinear prediction in structural computation [8]. An application on piezoelectric nanobridges of such a method has been proposed in [6], with a home made finite element code. The purpose of this paper is to extend this approach to a wider range of MEMS architectures with thin geometries, including beams with complex cross section [16] and laminated beams/plate structures [2, 4, 5].

Two examples of structures are shown on Fig. 1. They are both constituted of a base structure (a silicon / silicon oxide stack) which has been etched through the material to pattern a beam/plate thin structure, with clamped boundary conditions. The electromechanical transducers are constituted of multilayer stacks of an active layer surounded by two electrodes (top and bottom). On Fig. 1, both structures are equipped with two transducers (one at each end of the clamped/clamped beam; an annular one at the edge of the circular plate and another circular one at its center). The structures are at a nanometer (thickness of $\simeq 350$ nm for the beam) or micrometer (thickness $\simeq 2.5$ μm for the plate) scale, with a thin geometry (aspect ratio of 0.012: $0.35/30$ for the beam and $2.5/200$ for the plate). Two electromechanical transduction schemes are considered. The first one is the well known piezoelectric material, and the second one is based on the use of dielectric layers, as introduced in [5]. In this latter case, the excitation results from the electrostatic force created between the charged electrodes which causes a transverse deformation of the dielectric film and a bending of the multilayer structure; the detection of the vibration is capacitive, based on the fluctuation of the capacitance due to the deformation of the dielectric film. In the case of thin layers, both effects can be modelled in the same way [13]. The modelling proposed here thus includes: (i) the geometrical nonlinearities (ii) the laminated structure and (iii) the electromechanical transduction with both converse and direct effects.

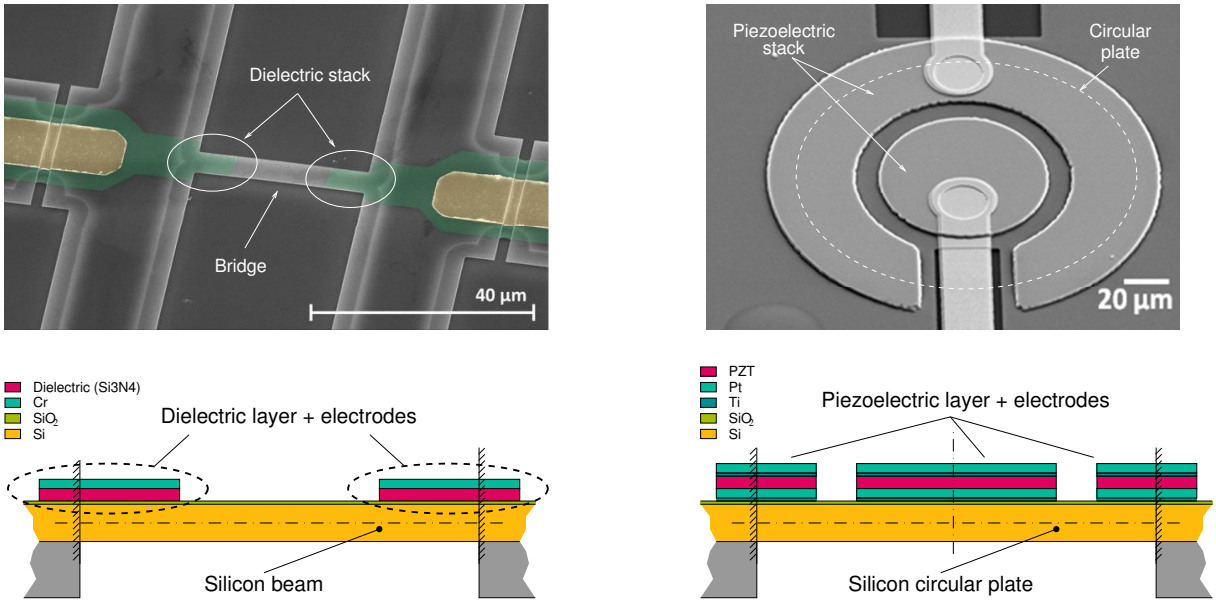

Figure 1. Scanning Microscope Images and cutaway view of some M/NEMS devices: a clamped/clamped beam and a clamped circular plate. Beam dimensions: 5×30 μm, thickness 320 nm, dielectric stack thickness: 35 nm. Plate dimensions: diameter 200 μm, thickness 1 μm, piezoelectric stack thickness: 1.6 μm

2 Finite element reduced-order model

We consider an elastic structure equipped with $P \in \mathbb{N}^*$ thin transducers composed of multilayer stacks including an active layer (piezoelectric/dielectric, Fig. 1). Following the ideas of [12] for the linear case and [6] for the case with geometrical nonlinearities, the governing equations can be written:

$$\begin{cases} \boldsymbol{M}_m \ddot{\boldsymbol{U}} + \boldsymbol{K}_m \boldsymbol{U} + \boldsymbol{f}_{nl}(\boldsymbol{U}) + \sum_{p=1}^{P} \left[\boldsymbol{f}_c^{(p)} + \boldsymbol{P}_c^{(p)} \boldsymbol{U} \right] V^{(p)} = \boldsymbol{F}, & \text{(1a)} \\ C^{(p)} V^{(p)} - \left[\boldsymbol{f}_c^{(p)} + \boldsymbol{P}_c^{(p)} \boldsymbol{U} \right]^{\mathrm{T}} \boldsymbol{U} = Q^{(p)}, \qquad \forall p \in \{1, \dots P\}. & \text{(1b)} \end{cases}$$

In the above equations, $\boldsymbol{U}$ is the vector containing the mechanical degrees of freedom (of size N), $\boldsymbol{F}$ is the mechanical forcing vector (of size N), $V^{(p)}$ is the voltage applied to the p-th. active layer and $Q^{(p)}$ is the electric charge contained in one of its electrodes. $\boldsymbol{M}_m$ and $\boldsymbol{K}_m$ are the mechanical mass and stiffness matrices (of size $N \times N$), $\boldsymbol{f}_{nl}(\boldsymbol{U})$ is the nonlinear part of the internal mechanical forces vector (coming from the geometrical nonlinearities, of size N). All those mechanical quantities are related to the structure with all active layers short-circuited ($V^{(p)} = 0 \ \forall p$). $C^{(p)}$ is the electrical capacitance of the p-th. active layer with the elastic structure in blocked state ($\boldsymbol{U} = \boldsymbol{0}$). Finally, $\boldsymbol{f}_c^{(p)}$ is the electromechanical forcing vector (the one introduced in [12], of size N), which couples the p-th active layer to the mechanical dofs and $\boldsymbol{P}_c^{(p)}$ is an electromechanical coupling matrix, related to the geometrical nonlinearities, responsible in particular of parametric excitation effects in thin structures [14].

As shown in [6], we consider $K < N$ eigenmodes $(\boldsymbol{\Phi}_k, \omega_k)$ of the structure with all active layers short circuited ($V^{(p)} = 0 \ \forall p$). They are solution of:

$$\left(\boldsymbol{K}_m - \omega^2 \boldsymbol{M}_m \right) \boldsymbol{\Phi} = \boldsymbol{0}. \tag{2}$$

and normalized with respect to the mass matrix:

$$\boldsymbol{\Phi}_k^{\mathrm{T}} \boldsymbol{M}_m \boldsymbol{\Phi}_k = 1 \quad \forall k \tag{3}$$

The displacement $\boldsymbol{U}(t)$ is written:

$$\boldsymbol{U}(t) = \sum_{k=1}^{K} \boldsymbol{\Phi}_k q_k(t), \tag{4}$$

with the modal coordinate $q_k(t)$ that verify:

$$\begin{cases} \ddot{q}_k + 2\xi_k\omega_k\dot{q}_k + \omega_k^2 q_k + \sum_{i,j=1}^{K} \beta_{ij}^k q_i q_j + \sum_{i,j,l=1}^{K} \gamma_{ijl}^k q_i q_j q_l \\ \qquad + \sum_{p=1}^{P} \chi_k^{(p)} V^{(p)} + \sum_{p=1}^{P}\sum_{i=1}^{N} \Theta_{ik}^{(p)} q_i V^{(p)} = F_k, \qquad \forall k = 1, \dots K \qquad (5a) \\ C^{(p)}V^{(p)} - \sum_{k=1}^{K} \chi_k^{(p)} q_k - \sum_{i,j=1}^{K} \Theta_{ij}^{(p)} q_i q_j = Q^{(p)}, \qquad \forall p = 1, \dots P \qquad (5b) \end{cases}$$

The idea of a non-intrusive method is to use the standard static and modal analyses procedures of finite-elements commercial codes to evaluate the coefficients of the above reduced order model, especially β_{ij}^k, γ_{ijl}^k, $\chi_k^{(p)}$ and $\Theta_{ik}^{(p)}$.

As explained in [9], the nonlinear stiffness coefficients β_{ij}^k and γ_{ijl}^k are computed by prescribing a series of displacement expanded to some linear modes, evaluating nonlinear direct static problems and solving an algebraic linear system. For the electromechanical coupling coefficients $\chi_k^{(p)}$ and $\Theta_{ik}^{(p)}$, several strategies are tested. The first one is to use a standard elastic finite-elements code and to use a thermal analogy: prescribing a given voltage V is equivalent, to some assumptions, to prescribe a given temparature field. It enables in a straighforward manner to compute the linear coefficients $\chi_k^{(p)}$. The nonlinear ones $\Theta_{ij}^{(p)}$ can be evaluated with the same method, the only difference being that the displacement fields result from a geometrically nonlinear thermoelastic static problem. Another one is to use a finite element code with piezoelectric finite elements and geometrical nonlinearities.

3 Computation of frequency responses

The obtained reduced order model (5) can be treated in several manners. If it is reduced to very few oscillators (with normal form for instance [15]), analytical perturbation methods can be used (see [10]). Here, we are interested in numerical methods, which enables to consider more oscillators in (5) and compute accurately frequency responses. We use here a combination of the Harmonic Balance Method (HBM), to compute periodic solutions, and an Asymptotic Numerical Method (ANM) to follow the solution branches [1, 3]. It requires to rewrite (5) in the state space and under a quadratic form, which is done by introducing the modal velocities $v_k = q_k$ and new slave variables $S_{ij} = q_i q_j$.

We compute frequency responses, when the structure is subjected to an harmonic forcing (for instance by prescribing the voltage in one of the transducer stacks $V(t) = V_0 \cos \Omega t$) or nonlinear modes, which correspond to the periodic solutions of Eq. (5) in free/conservative vibrations. The latter case conducts to compute backbone curves, which are very interesting in practice since they constitute the skeleton of the forced vibrations responses. However, since the system is conservative in this case, numerous internal resonances are computed which increases the computation time. An example is shown on Fig. 2 on which some responses of a homogeneous isotropic circular plate are presented. The four first NNM have been computed by assuming that the axisymmetric and asymmetric problems are separated. Numerous modal interactions at high vibration amplitudes are obtained, for which harmonics of order $3, 7, 9, 10$ emerge in the free response of the plate around the first mode. The asymmetric modes are subject to a 1:1 internal resonance, well computed by the algorithm.

References

[1] R. Arquier, S. Karkar, A. Lazarus, O. Thomas, C. Vergez, and B. Cochelin. Manlab 2.0: an interactive path-following and bifurcation analysis software. Technical report, Laboratoire de Mcanique et d'Acoustique, CNRS, http://manlab.lma.cnrs-mrs.fr, 2005-2011.

[2] C. Ayela, L. Nicu, C. Soyer, É. Cattan, and C. Bergaud. Determination of the d_{31} piezoelectric coefficient of $pbzr_xti_{1-x}o_3$ thin films using multilayer buckled micromembranes. *Journal of Applied Physics*, 100:054908, 2006.

[3] B. Cochelin and C. Vergez. A high order purely frequential harmonic balance formulation. *Journal of Sound and Vibration*, 324(1-2):243–262, 2009.

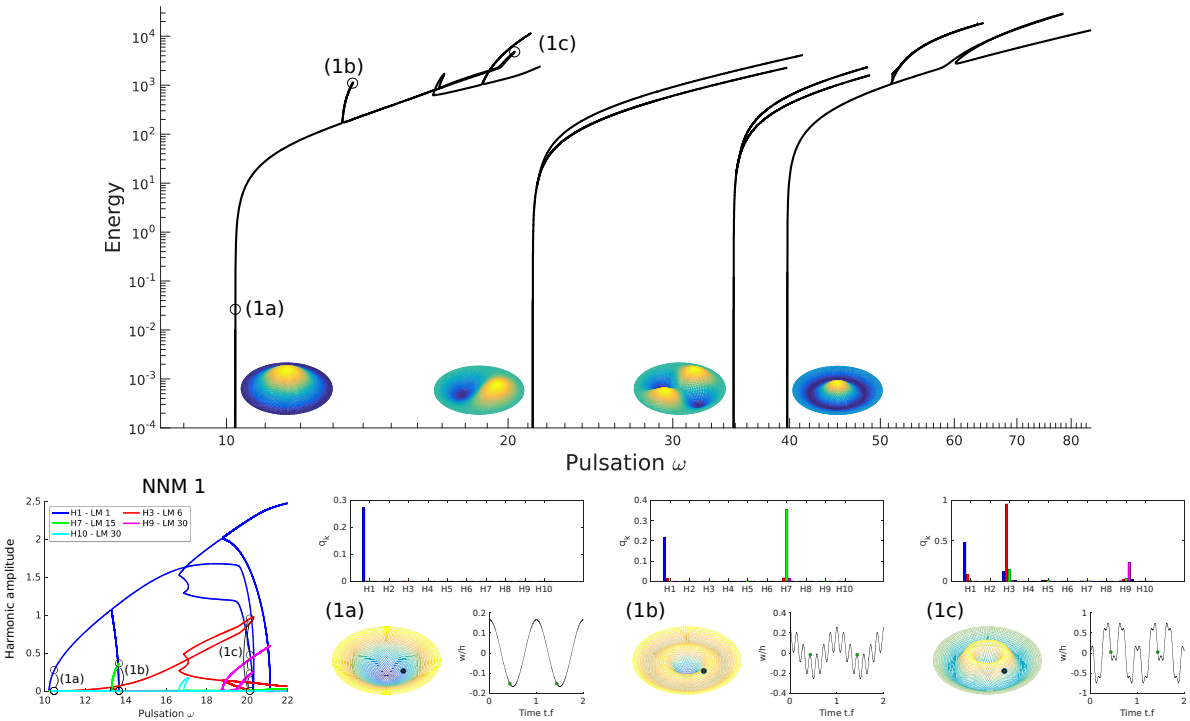

Figure 2. Nonlinear modes of an elastic clamped circular plate.

[4] D. Dezest, O. Thomas, F. Mathieu, L. Mazenq, C. Soyer, J. Costecalde, D. Remiens, J.-F. Deü, and L. Nicu. Wafer-scale fabrication of self-actuated piezoelectric nanoelectromechanical resonators based on lead zirconate titanate (pzt). *Journal of Micromechanics and Microengineering*, 25(3):035002, 2015.

[5] C. Fuinel, K. Daffé, A. Laborde, O. Thomas, L. Mazenq, L. Nicu, T. Leichlé, and B. Legrand. High-K thin films as dielectric transducers for flexural M/NEMS resonators. In *Proc. of the 29th. IEEE international conference on micro electro mechanical systems (MEMS 2016) conference*, Shanghai, China, January 2016.

[6] A. Lazarus, O. Thomas, and J.-F. Deü. Finite elements reduced order models for nonlinear vibrations of piezoelectric layered beams with applications to NEMS. *Finite Elements in Analysis and Design*, 49(1):35–51, 2012.

[7] M. H. Matheny, L. G. Villanueva, R. B. Karabalin, J. E. Sader, and M. L. Roukes. Nonlinear mode-coupling in nanomechanical systems. *Nano Letters*, 13(4):1622–1626, 2013.

[8] M. P. Mignolet, A. Przekop, S. A. Rizzi, and S. M. Spottswood. A review of indirect/non-intrusive reduced order modeling of nonlinear geometric structures. *Journal of Sound and Vibration*, 332(10):2437–2460, 2013.

[9] A. A. Muravyov and S. A. Rizzi. Determination of nonlinear stiffness with application to random vibration of geometrically nonlinear structures. *Computers and Structures*, 81(15):1513–1523, 2003.

[10] A. H. Nayfeh and D. T. Mook. *Nonlinear oscillations*. John Wiley & sons, inc., New-York, 1979.

[11] O. Shoshani, D. Heywood, Y. Yang, T. W. Kenny, and S. W. Shaw. Phase noise reduction in an mems oscillator using a nonlinearly enhanced synchronization domain. *Lournal of Microelectromechanical Systems*, 25(5):870–876, 2016.

[12] O. Thomas, J.-F. Deü, and J. Ducarne. Vibration of an elastic structure with shunted piezoelectric patches: efficient finite-element formulation and electromechanical coupling coefficients. *International Journal of Numerical Methods in Engineering*, 80(2):235–268, 2009.

[13] O. Thomas, B. Legrand, and C. Fuinel. Optimization of length and thickness of smart transduction layers on beam structures for control and m/nems applications. In *Proceedings of SMASIS 2015 (ASME 2015 Conference on Smart Materials Adaptive Structures and Intelligent Systems*, Colorado Springs, USA, September 2015. Paper 8857.

[14] O. Thomas, F. Mathieu, W. Mansfield, C. Huang, S. Trolier-McKinstry, and L. Nicu. Efficient parametric amplification in mems with integrated piezoelectric actuation and sensing capabilities. *Applied Physics Letters*, 102(16):163504, 2013.

[15] C. Touzé, O. Thomas, and A. Chaigne. Hardening/softening behaviour in non-linear oscillations of structural systems using non-linear normal modes. *Journal of Sound Vibration*, 273(1-2):77–101, 2004.

[16] L. G. Villanueva, R. B. Karabalin, M. H. Matheny, D. Chi, J. E. Sader, and M. L. Roukes. Nonlinearity in nanomechanical cantilevers. *Physical Review B*, 87:024304, 2013.

[17] L. G. Villanueva, E. Kenig, R. B. Karabalin, M. H. Matheny, R. Lifshitz, M. C. Cross, and M. L. Roukes. Surpassing fundamental limits of oscillators using nonlinear resonators. *Physical Review Letters*, 110(17):177208, 2013.

EUROMECH Colloquium 603
Dynamics of micro and nano systems
5 – 7 September 2018, Porto, Portugal

Analysis of isolated solutions in a symmetric MEMS array during symmetry breaking event using NNM

C. GRENAT[1], **S. BAGUET**[1], **R. DUFOUR**[1] **and C-H. LAMARQUE** [2]

[1]Univ Lyon, INSA-Lyon, CNRS UMR5259, LaMCoS, F-69621, France
clement.grenat@insa-lyon.fr
sebastien.baguet@insa-lyon.fr
regis.dufour@insa-lyon.fr

[2] Univ Lyon, ENTPE, CNRS UMR5513, LTDS , F-69518, France
claude.lamarque@entpe.fr

Summary. These works analyze isolated solutions in a symmetric 2-beam MEMS array designed for mass detection using Nonlinear Normal Modes (NNM) during symmetry breaking event. While symmetric, the system present two pure NNM and one mixed NNM. Then an added mass is dropped onto the MEMS array, the symmetry is broken and an isolated NNM is appearing. Particular behaviors on the isolated solutions depend on which type of NNM the isolated solution are linked to. The originality lies in the detection and analysis of isolated solution and NNM before and after symmetry breaking in a MEMS array using bifurcation calculation and continuation methods.

Keywords: MEMS array, isolated solutions, NNM, symmetry breaking, mass detection

1 Introduction

Current researches on mass sensing are essentially focused on an single MEMS resonator. A study by Nguyen et al. investigates alternatives mass-sensing techniques using nonlinearities [1]. The multistability and frequency sweep, the resulting hysteresis cycle are used to provide a new mass sensing technique. Nevertheless array of resonant MEMS present complex dynamical behavior due to the nonlinear couplings induced by electrostatic forces. A paper by Gutschmidt and Goettlieb [2] analyzed an arrays with electrical coupling. They focused on the n-beam dynamic behavior in the region of internal one-to-one, parametric and several internal three-to-one resonances corresponding to low, medium and large DC voltages. These nonlinear behavior are complex to analyze and researches are currently working on methods that simplify the understanding of such phenomena. Hill et al. [3] analyze analytically the apparition of isolated solutions on backbone curves (NNMs). They show that symmetry breaking can generate isolated solutions supported by an isolated NNM. Kuether et al. worked on the Energy balance method [4] that allows to know the amplitude of forcing required to pass by the wanted point of a NNM. In this work, a symmetric 2-beam array is considered for mass detection purpose. When an added mass drops onto one of the moving beam of the MEMS array, the symmetry of the system is broken. This symmetry breaking event have been used in [5] for mass detection. Our work proposes to analysis the change in the nonlinear dynamics behavior of the MEMS array before and after symmetry breaking event using NNM, bifurcation analysis and continuation of bifurcation points in parallel with standard response curve. For some configuration of the system, isolated solutions, isolated and mixed NNM appear. Parametric methods of continuation that allows to catch the various isolated solutions and isolated NNM are presented. Moreover the results shows that the merging behavior of the isolated solutions with the response curve depend greatly on which type of NNM the isolated solutions are found onto.

2 Array of two nanomechanical resonators

A 2-moving-beam array is considered, as represented in Fig. 1. The two beams 0 and 3 located at the ends of the array are clamped and serve only as electrostatic actuator. The two others beams 1 and 2 are clamped-clamped. All 4 beams are identical. l, b, h, I, g are respectively length, width, height, moment

of inertia of the beams, gap between two adjacent beams. Let E, ρ be the Young's modulus and the mass density.

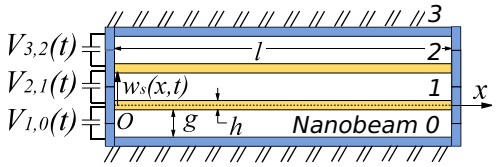

Figure 1: Array of two clamped-clamped M/NEMS beams.

Each beam is an electrostatic actuator for its adjacent beams. $V_{s,s+1} = V_{dcs,s+1} + V_{acs,s+1}\cos(\Omega t)$ is the voltage applied between the successive beams s and $s+1$ with V_{dc}, V_{ac} the continuous and alternative voltages. The equation of the beam s in bending is written as follows.

$$EI\frac{\partial^4 \tilde{w}_s(\tilde{x},\tilde{t})}{\partial \tilde{x}^4} + \rho bh\frac{\partial^2 \tilde{w}_s(\tilde{x},\tilde{t})}{\partial \tilde{t}^2} + \delta_i(s)\,\delta_{x0}(x)\,m\frac{\partial \tilde{w}_s}{\partial \tilde{t}^2} + c\frac{\partial \tilde{w}_s}{\partial \tilde{t}} - \Big[\tilde{N} + \frac{Ebh}{2l} \int_0^l \Big(\frac{\partial \tilde{w}_s(\tilde{x},\tilde{t})}{\partial \tilde{x}}\Big)^2 \mathrm{d}\tilde{x}\Big]\frac{\partial^2 \tilde{w}_s(\tilde{x},\tilde{t})}{\partial \tilde{x}^2} = \frac{\epsilon_0 bC_n}{2}\left[\frac{V_{s,s+1}^2}{\big(g+\tilde{w}_{s+1}-\tilde{w}_s\big)^2} - \frac{V_{s-1,s}^2}{\big(g+\tilde{w}_s-\tilde{w}_{s-1}\big)^2}\right] \quad (1)$$

with $s = 1, 2$. Small added mass m is dropped on the beam i at the location $x0$. Let ϵ_0, C_n be the dielectric constant and fringing the coefficient respectively. $\tilde{N}$ represents the lineic load along the x-axis. The following voltages are taken, see Tab. 1.

Vdc_{10}	Vac_{10}	Vdc_{21}	Vac_{21}	Vdc_{32}	Vac_{32}
3	0.1	3	0	3	-0.1

Table 1: Applied voltages.

Since the resonators of the 2-beams-array are identical, the beams $1, .., 2$ have the same eigenmodes. Therefore Galerkin method is used to withdraw the spatial dependence from the equation of motion, see Eq. (1). To compute the solution of the MEMS array, the Harmonic Balance Method (HBM) is used which consists in researching a periodic solution as a truncated Fourier series. Then the alternate frequency-time (AFT) is used for the calculation of nonlinear part of the equation of motion. The NNM are then computed on a conservative equation of motion [6]. This equation being autonomous, a phase condition is added and the equation of motion regularized to ensure the computation of an unique solution. Then the stability and bifurcation points of the NNM is calculated using a regularized quadratic eigenvalue problem and augmented system. An Energy balance is performed to calculate the corresponding amplitude of the force necessary to pass by the corresponding point of the NNM [4].

2.1 Before symmetry breaking event

The NNM and the response curve of the system are computed for a null added mass, see Fig. 2. The denomination pure and mixed NNM below are defined as in [7] [8]. The system exhibit two pure NNMs initialized using the Linear Normal Modes frequency and modal shape. One can see, on the NNM that a Branch Point (BP) appears on the second pure NNM initialized at the Frequency 22.35. The Branch point, also known as symmetry breaking point, is symptomatic of a symmetric system. Beyond the BP, the pure NNM becomes unstable and two new stable mixed NNM, that does not respect the symmetry of the system, appear. A mixed NNM has a modal shape mixing modal shapes of the pure NNM of the system. The given voltages (see Table 1), excite the first pure NNM and the two mixed NNM. One can see on the response curve that the first pure NNM behaves as expected, while the second pure NNM does not react at all. Additionally, isolated solutions are present on each mixed NNM. They are found and initialized using the energy balance method. The two mixed NNM being isolated from the excited

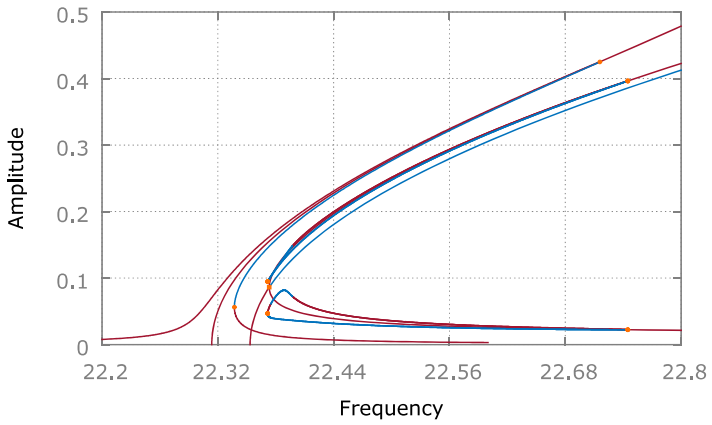

Figure 2: Beam 1 and 2 for an null added mass, Stable (red), Unstable (blue), Bifurcation (orange).

NNM, the merging of the isolated solutions with the response curve can not occur with the current shape of excitation 1.

2.2 After symmetry breaking event

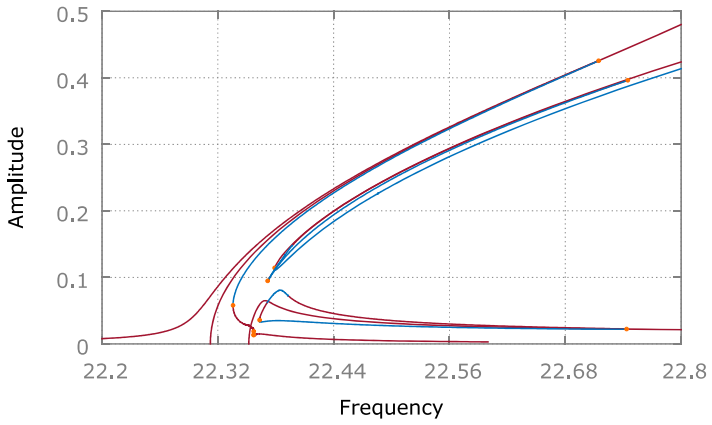

Figure 3: Beam 1 for an dimensionless added mass of $1e-4$, Stable (red), Unstable (blue), Bifurcation (orange).

After the drop of a dimensionless added mass of $1e-4$ onto the beam 1, the symmetry of the system is broken. The corresponding NNM of the system are computed in Figs. 3,4. The dynamical behavior of the system is modified, the BP onto the second pure NNM does no longer exist. The drop of the added mass has broken the symmetry and therefore the BP becomes an imperfect bifurcation point. The second pure NNM and the two mixed modes existing before the symmetry breaking event become one pure NNM and one isolated NNM. Such a behavior for beam 1 can be seen in Fig. 3. Moreover the system now being non-symmetric has different modal shape on each beam. The second pure NNM is composed by the previous lower energy part of the second pure NNM and lower energy mixed NNM. While the upper part of the second pure NNM and mixed NNM form now the isolated NNM. On the second beam 4, the left part of the previous second pure NNM and the mixed NNM form the second pure NNM after symmetry breaking. In the same way, the right part of the previous second pure NNM and mixed NNM compose the isolated NNM. The isolated NNM are found and initialized using Limit Point continuation of NNM. Moreover, the second pure NNM, now composed partially by a previous mixed NNM, responds to the current excitation. Therefore the isolated solution found onto the second

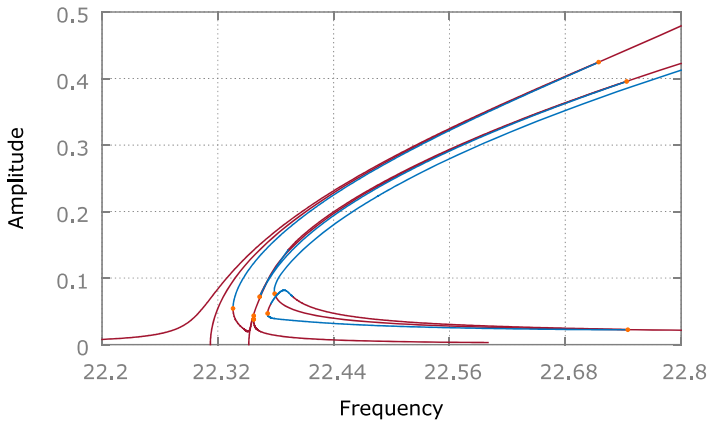

Figure 4: Beam 2 for a dimensionless added mass of $1e-4$, Stable (red), Unstable (blue), Bifurcation (orange).

pure NNM is supported by an excited NNM. Consequently, for a high enough amplitude of voltages with respect to the current shape of excitation, the isolated solution supported by the second pure NNM will merged with the response curve. On the other hand, the isolated solution found onto the isolated NNM is totally isolated from any excited NNM. Hence, the isolated solution will remain isolated even for other amplitude and shape of excitation. The analysis of the complex dynamical behavior of an array of two nanomechanical resonators beams explain well the symmetry breaking phenomena used for mass detection in [5].

3 Conclusion

Multiple complex dynamical behavior, such as isolated NNM and isolated solutions with different merging behaviors, have been found in the considered array of two nanomechanical resonators. The merging of isolated solutions present in such system have been characterized depending on which NNM it can be found. Method that allows to find and initialize isolated solutions and isolated NNM are presented. As a conclusion, the results found with the presented method explain and analysis complex dynamical behavior found in a 2-beam MEMS before and after symmetry breaking used for mass detection. This research represents an increment towards the comprehension and modeling of resonator arrays for application in mass sensing.

References

[1] Van Nghi Nguyen, Sébastien Baguet, Claude-Henri Lamarque, and Régis Dufour. Bifurcation-based micro-/nanoelectromechanical mass detection. *Nonlinear Dynamics*, 79(1):647–662, January 2015.

[2] S. Gutschmidt and O. Gottlieb. Nonlinear dynamic behavior of a microbeam array subject to parametric actuation at low, medium and large dc-voltages. *Nonlinear Dynamics*, 67(1):1–36, 2012.

[3] TL Hill, SA Neild, and A Cammarano. An analytical approach for detecting isolated periodic solution branches in weakly nonlinear structures. *Journal of Sound and Vibration*, 379:150–165, 2016.

[4] Robert J Kuether, Ludovic Renson, Thibaut Detroux, Chiara Grappasonni, Gaëtan Kerschen, and Mathew S Allen. Nonlinear normal modes, modal interactions and isolated resonance curves. *Journal of Sound and Vibration*, 351:299–310, 2015.

[5] C. Grenat, S. Baguet, R. Dufour, and C-H. Lamarque. Mass detection through parametric analysis and symmetry-breaking in a mems array. In *ENOC 2017, 9th European Nonlinear Dynamics Conference*, Budapest, Hungary, June 2017.

[6] C Grenat, S Baguet, R Dufour, and C-H Lamarque. Bifurcation analysis of nonlinear normal modes with the harmonic balance method. In *ENOC 2017, 9th European Nonlinear Dynamics Conference*, Budapest, Hungary, June 2017.

[7] Martin Golubitsky and David G Schaeffer. *Singularities and groups in bifurcation theory*, volume 1. Springer Science & Business Media, 2012.

[8] Martin Golubitsky, Ian Stewart, and David G Schaeffer. *Singularities and groups in bifurcation theory*, volume 2. Springer Science & Business Media, 2012.

Dynamic response of a piecewise linear MEMS oscillator

Andrea Guerrieri[1], Attilio Frangi[1], Valentina Zega[1] and Luca G. Falorni[2]

[1] Politecnico di Milano, Milano, Italy
andrea.guerrieri@polimi.it
attilio.frangi@polimi.it
valentina.zega@polimi.it

[2] STMicroelectronics, Cornaredo, Italy
luca.falorni@st.com

Summary. This work presents the results obtained from the analysis of the dynamic response of a MEMS oscillator impacting on a one-sided elastic constraint. The experimental results are compared with the mathematical model of a non-smooth single-dof oscillator with piecewise linear stiffness. The model, though very simple, predicts accurately the behaviour of the actual device. The focus is on the dynamic behaviour of the device forced near resonance, when impacts have a strong effect on the dynamic response. As the forcing amplitude grows the time response shows an increasing superposition of different frequency contributions induced by period doubling bifurcations, up to chaotic behaviour. Interesting is the analysis of these frequency components, as the FFT of the time response shows a regularly but non-symmetric energy distribution on different tones.

Keywords: Impact oscillator, chaos, period doubling, MEMS.

1 Introduction

In the literature, an extensive list of references focuses on the numerical modelling and experimental testing of non-smooth systems. The dynamic behaviour of these systems is generally complex, leading to a very rich and interesting time response. Consequently, a lot of effort has been devoted in the past to find the proper mathematical model [1] and to implement a numerical algorithm to treat these systems with all their difficulties. Hence, experimental tests are of great importance to validate and compare such unusually complex numerical predictions.
On piecewise linear systems, an exhaustive work has been done in the past with great focus on the classification of all the possible type of bifurcation that such systems can exploit [3] and in finding the best normal form able to capture their large amplitude dynamic response [2].
In the present paper, a periodically forced system with non-symmetric bilinear restoring force and linear damping is analysed. A single-dof lumped mass model is used to predict the dynamic response of a test device, ad hoc designed, consisting in an oscillating mass impacting on a clamped-clamped beam. As strong contact occurs, both the numerical and experimental time response spectrum shows a rich composition of different tones

2 Mathematical model

The model depicted in Fig.1(a) shows a lumped mass m attached to a linear spring k_1 and a linear viscous damper c. A second linear spring k_2 increase the overall stiffness of the systems when the displacement x exceeds the contact distance $x_0 > 0$. This results in a piecewise linear stiffness Fig.1(b). For simplicity the contact distance x_0 is not time or amplitude dependent.
The non-dimensional equation of motion of the bilinear system excited by a harmonic force is written as

$$x'' + \frac{1}{Q}x' + H(x) = \beta \sin(\omega t) \tag{1}$$

where

$$H(x) = \begin{cases} x, & x < x_0 \\ \widetilde{\omega}^2 x + (1 - \widetilde{\omega}^2) x_0, & x \geq x_0 \end{cases} \tag{2}$$

$\widetilde{\omega}^2$ the stiffness ratio $(k_1 + k_2)/k_1$, Q the quality factor, β and ω the forcing static amplitude and circular frequency, $(\cdot)' = d(\cdot)/d\tau$ with $\tau = \omega_0 t$ the dimensionless time, ω_0 the system's circular eigenfrequency.

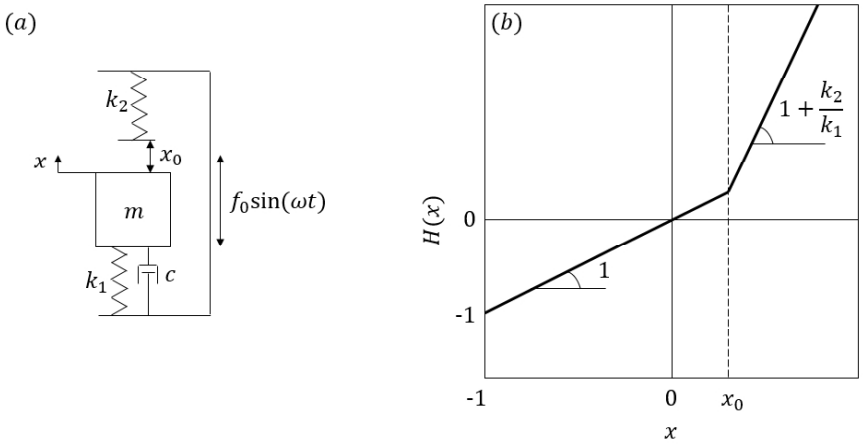

Figure 1. (a) physical model, (b) bilinear restoring force vs displacement.

The equation of motion has been integrated in time by means of both an explicit central difference scheme and implicit unconditionally stable Newmark scheme (with $\beta = 1/4$ and $\gamma = 1/2$).

3 Experimental setting

A set of ad-hoc designed MEMS device has been fabricated by STMicroelectronics laboratories with Thelma surface micromachining process. The geometry, sketched in Fig.2, represents half of the complete device. The latter consists of a stiff frame supported by four springs, each made by folded beams anchored to the substrate, with total stiffness k_1. In the bottom part of the frame, a hammer head impacts the second spring with stiffness k_2 (a clamped-clamped beam) as the displacement of the frame exceeds $x_0 = 4.73\mu m$. The moving mass, the clamped-clamped beam and the second set of sense comb-fingers have a constant bias voltage V_{dc}. The device is actuated by comb-fingers in a push-pull configuration so that just the pure harmonic signal $4V_{dc}V_{ac}\sin(\omega t)$ survives. The output voltage V_{out} measured from the remaining set of sensing comb-fingers is collected for post-processing. The device is sealed at a pressure close to $0.75mbar$ to minimize viscous dissipation.
The dimensions of the device are not reported, instead the equivalent parameters to be used in Eq.1 are equal to $Q = 730$, $\widetilde{\omega}^2 = 19.96$, $\beta = 0.43\mu m$ and $\omega_0 = 0.023470 rad/\mu s$.

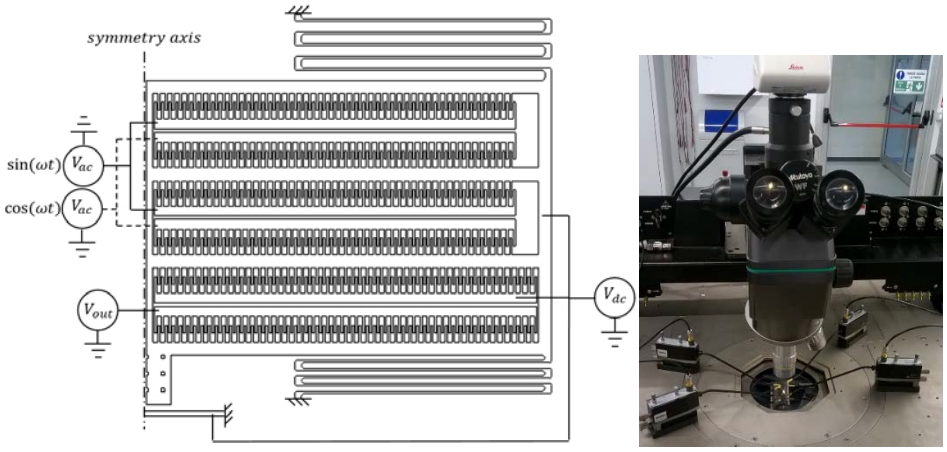

Figure 2. layout of the device and probe setup.

4 Dynamic response analysis

The goal of the experimental campaign was to observe an unusual behaviour in the dynamic response of the device when forcing is high enough to induce contact. Increasing gradually the magnitude of the forcing sinusoidal signal (at resonance $\omega = \omega_0$), we observed numerically a cascade of period doubling bifurcation that can even led to chaotic response of the device. Hence, we tune the driving voltages V_{dc} and V_{ac} such that the device strongly enters the nonlinear (bilinear) regime but not enough to show a chaotic behaviour.

With the above parameter settings, the phase space diagram shows in Fig.3 that the device impacts the second spring k_2 not every cycle but with a certain periodicity. Notice that amplitudes can be greater than the distance x_0 being the clamped-clamped beam deformable (soft impact or contact). This cyclic impact behaviour has been deeply studied by other authors [3] and seems to be closely related to period doubling bifurcations, in which the periodic response of the system is represented by more than one complete cycle in the phase space. When contact does not occur, the system remains in the linear regime and the phase space is a single elliptic cycle repeated periodically.

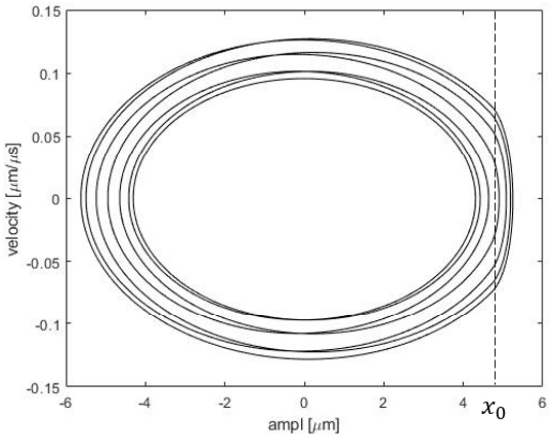

Figure 3. Phase space plot.

Here we are interested in the time response of the system, depicted in Fig.4, that clearly shows a sort of beating behaviour. The main high frequency tone at resonance with ω_0 is modulated by a low frequency ($\approx 500Hz$) signal. The numerical model and the experimental time response are quite similar. Performing the Fast Fourier Transform of the above signal we get the single side amplitude spectrum in Fig.5 revealing that the energy is collected in clusters of tones where the central one has always the largest magnitude. Focusing on the group close to resonance, we notice that the two tones immediately next to the main harmonic has both almost the same distance from the latter and the frequency shift is approximately equal to the modulation frequency observed in the time response of Fig.4. Further it is evident that the energy stored in the tone on the right of the resonance frequency is higher than the left one. The reason of this asymmetry could be that the system has a unilateral constraint, hence it reaches higher amplitudes when it moves away from the second spring k_2 as we can see from Fig.4.

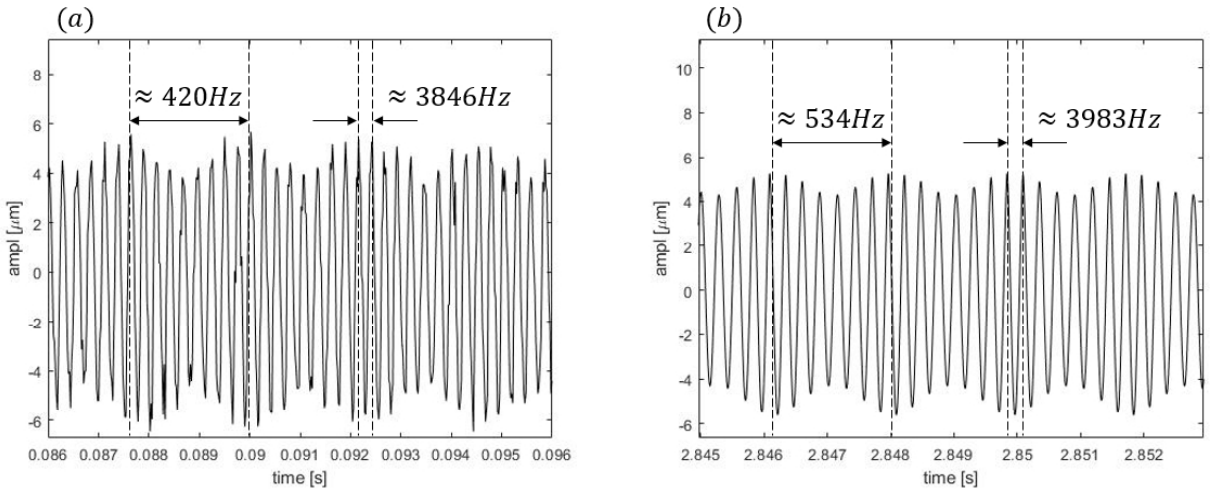

Figure 4. Time response (a) experimental and (b) numerical.

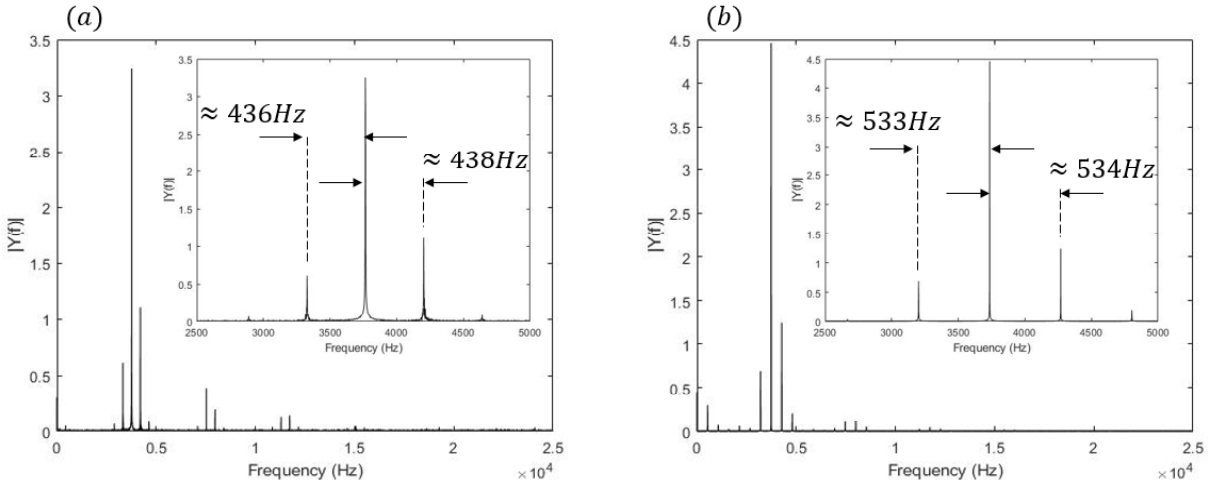

Figure 5. Single side amplitude spectrum (FFT) (a) experimental and (b) numerical.

5 Conclusions

In this work the resonant dynamic response of a MEMS device is studied in presence of non-smooth non-symmetric contact. The single-dof numerical model and the test performed on the device agrees on the fact that for certain level of external forcing the device enters in strong nonlinear regime, where period doubling bifurcation governs the device response.

The analysis of the FFT revealed an unusual energy distribution, where tones are grouped around different central frequencies. In each group, tones are characterized by having symmetric frequency shift from the central one but non-symmetric magnitudes.

References

[1] S. W. Shaw, P. J. Holmes, A periodically forced piecewise linear oscillator. *Journal of Sound and Vibration*, **90(1)**, 129-155, 1983.

[2] S. R. Hsieh, S. W. Shaw, C. Pierre, Normal modesfor large amplitude vibration of a cantilever beam. *Int. J. Solids Structures*, **31(4)**, 1981-2014, 1994.

[3] E. Pavlovskaia, J. Ing, S. Banerjee, M. Wiercigroch, Strange dynamics of bilinear oscillator close to grazing. *I. J. Bifurcations and Chaos*, **20**, 3801-3817, 2010.

EUROMECH Colloquium 603
Dynamics of micro and nano systems
5 – 7 September 2018, Porto, Portugal

Shock response of a ring-based Coriolis Vibrating Gyroscope under nonlinear electrostatic excitation

B. Chouvion[1], **S. McWilliam**[2] **and A.A. Popov**[2]

[1]Ecole Centrale de Lyon, LTDS, CNRS UMR 5513, 69 130 Ecully, France
benjamin.chouvion@ec-lyon.fr

[2] Faculty of Engineering, University of Nottingham, University Park, Nottingham NG7 2RD, UK
stewart.mcwilliam@nottingham.ac.uk
atanas.popov@nottingham.ac.uk

Summary. In this work, a general analytical model is developed to investigate the dynamic behaviour of a capacitive ring-based Coriolis Vibrating Gyroscope (CVG) under shock conditions. The electrostatic force is described as a Taylor series expansion and the in-plane vibration of the multi-supported ring is expressed with a modal approach. For severe shock occurring under operating conditions, it is shown that the nonlinear effect of the electrostatic force introduces mode coupling which has potential to reduce sensor performance. Under particular rigid-body motion damping conditions, it is also found that severe shock can cause the steady vibrating state to jump to a lower amplitude stable state.

Keywords: Vibrating ring gyroscope, electrostatic forcing, shock response, nonlinear dynamics.

1 Introduction

Micro-Electro-Mechanical Systems (MEMS) "Coriolis Vibrating Gyroscopes" (CVG) are used to measure speed angle of a body around a particular axis according to the harmonic response of a resonator subjected to Coriolis forces. Practically employed because of their small size and low manufacturing cost, these sensors must be designed to operate in harsh environmental conditions [1] and it is important to make sure that external shocks do not affect the accuracy of the measurements made.

Under normal operating conditions, the gap between the resonator and the electrodes, used to excite and detect the vibratory response of capacitive type MEMS sensors is constant to a first approximation, and the system dynamics operate in the linear regime. In this regime, sensors based on axisymmetric resonators, such as rings and slotted discs [2], are advantageous because the flexural modes of vibration occur in degenerate pairs and external shock induces no coupling between the modes. However in the event of severe shock, the gap between the resonator and the electrodes varies considerably and the electrostatic forces become strongly non-linear.

The purpose of this study is to gain understanding into the influence of electrostatic nonlinearity on the flexural response of an axisymmetric resonator subjected to severe shock. Previous work [3, 4] has already investigated this effect under pure shock conditions. The existing model involves expressing the ring response in terms of the modes for an unsupported ring and expanding the electrostatic force as a Taylor series. In this paper the model is generalised to consider a severe shock applied to a resonator initially driven at resonance under normal operating conditions based on [5]. After briefly introducing the general ideas of the resonator modelling, with some more detailed insights on the nonlinear electrostatic force, a systematic study is presented into the nonlinear response of ring resonators under severe shock conditions for a device recently reported in the literature [1].

2 Modelling of a ring resonator and its electrostatic forcing

Figure 1 shows a schematic diagram of the gyroscope studied where the vibrating ring is surrounded by electrodes for driving and sensing purposes, and the ring is supported by legs connected to a fixed rigid hub. We propose here a general model of devices of this kind that could include inner and outer electrodes and any number of supporting legs.

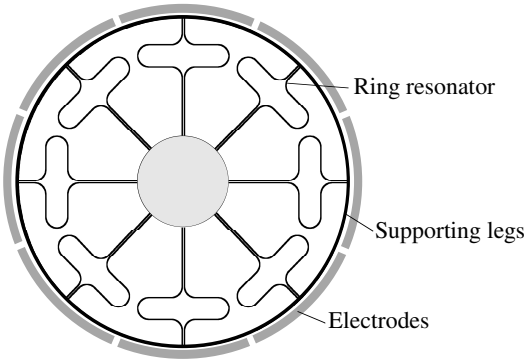

Figure 1: Schematic view of the studied vibrating ring gyroscope [1]

The ring is assumed thin and in-extensible and its in-plane radial displacement is defined using a Ritz approach:

$$w(\theta) = \sum_{n=1}^{N_R} q_n^{(1)} \cos n\theta + q_n^{(2)} \sin n\theta, \tag{1}$$

where $q_n^{(1)}$ and $q_n^{(2)}$ are pairs of generalised coordinates associated with orthogonal shape functions having n nodal diameters. These shape functions are commonly referred to as the $n\theta$-modes. N_R defines the number of generalised coordinate pairs used to describe the flexural ring deformation. It is assumed there are 8 identical support legs uniformly spaced around the ring circumference and each support leg provides constant stiffness restoring forces in the radial and tangential directions and a point mass inertia. The overall stiffness matrix that results from the strain energy of the system is generally not diagonal but off-diagonal terms are neglected in the simulations. Possible linear coupling is negligible because the frequencies for different modes of unsupported rings are normally well separated; higher order modal responses decay quickly; and there is no linear coupling between the first ring modes.

As the mean radius of the electrodes is large compared to the nominal capacitor gap size, the electrode capacitors are approximated as parallel plate capacitors. The differential electrostatic energy stored $\mathrm{d}E_{c_o}$ by the outer capacitor is given by

$$\mathrm{d}E_{c_o} = \frac{\epsilon_0 \epsilon V_o^2}{2(d_0 - w(\theta))} l r_o \, \mathrm{d}\theta, \tag{2}$$

where ϵ is the relative permittivity of the ring material, ϵ_0 is the absolute permittivity, V_o is the electrical potential across the outer electrode-ring capacitor, d_0 is the nominal gap size between the capacitor and the ring, r_o is the outer capacitor mean radius, and l is the axial length of the ring. A similar expression can be found for the energy stored by the inner electrode. The total electrostatic energy stored E_c is obtained by: 1) expanding the term $1/(d_0 - w(\theta))$ of Eq. (2) as a Taylor series in terms of $w(\theta)/d_0$, 2) summing the energy from both electrodes, and 3) integrating the result over the ring circumference with the assumption that the circumferential gaps between electrodes can be neglected [4]. The outcome is:

$$E_c = \frac{\epsilon \epsilon_0 l}{2 d_0} \sum_{k=0}^{N_T} \left(\frac{r_o V_o^2 + (-1)^k r_i V_i^2}{{d_0}^k} \int_0^{2\pi} w^k \, \mathrm{d}\theta \right), \tag{3}$$

where subscript i relates to the inner capacitor. Using the Ritz expansion of radial displacement (1), Eq. (3) provides a polynomial expansion for the electrostatic energy in terms of generalised coordinates $q_n^{(1)}$, $q_n^{(2)}$ up to order N_T.

The equation of motion for the $n\theta$-mode is determined using Lagrange's equation, and can be expressed as:

$$\ddot{q}_n^{(1)} + \frac{\omega_n}{Q_n} \dot{q}_n^{(1)} + \omega_n^2 q_n^{(1)} + F_{\mathrm{nl}_{q_n^{(1)}}} = F_{\mathrm{ext}_{q_n^{(1)}}} \tag{4}$$

A similar equation can be found for the companion $n\theta$ orthogonal mode. The modal damping Q_n is expressed via the Q-factor. It is either given by experimental measurements made in [1] or calculated

with the assumption that thermoelastic damping is dominant and using an extension of Zener's theory [6] to supported ring structures [7]. The linear natural frequencies ω_n are calculated using a commercial FE package. The external force $F_{\text{ext}_{q_1^{(1)}}}$ corresponds to external shock and only excites the 1θ-modes. Standard operating conditions for a Coriolis vibrating ring based gyroscope can be replicated by applying an harmonic force to one of the 2θ-modes (for instance $F_{\text{ext}_{q_2^{(1)}}} = \cos\omega t$). The only source of nonlinearity is provided by the electrostatic force. The polynomial order of the nonlinear force $F_{\text{nl}_{q_n^{(1)}}}$, derived from the electrostatic energy, is $N_T - 1$ and including these nonlinear forces introduces a physical mechanism for mode coupling to occur. Depending on the selected value of N_T, coupling can occur between several generalised coordinates.

3 Shock simulations

Numerical results presented here are obtained for a recently reported device, manufactured and tested by Yoon et al. [1]. The applied shock, assumed to be a half-sine pulse, corresponds to an imposed acceleration of the base of the sensor and is represented as an applied external force on the 1θ rigid body mode.

A preliminary study on the convergence of the number of modes to keep in the model (N_R-value) shows that the effect of the modes with $n > 3$ is negligible on the global dynamic of the sensor. Only the rigid body motion and the 2θ and 3θ flexural modes are considered. Furthermore, as the applied shock is severe, with a maximum amplitude of deformation of approximately 60% of the nominal gap size, strong nonlinear effects are expected and we show that the polynomial nonlinear force in (4) must be of order at least 9 to accurately predict these effects.

Under operating conditions, one of the 2θ-modes of the gyroscope is driven at resonance. We then investigate the conditions when an applied shock significantly affects the forced vibration of the 2θ-mode via inter-modal coupling. In the following simulations, the 2θ-mode is driven at a frequency close to the peak of the nonlinear resonance. As the response is nonlinear, several stable solutions may co-exist over some particular frequency range, and initially the system is maintained at a steady state that corresponds to the maximum amplitude of the top stable branch solution ($q_2 \approx 0.39\mu$m at $t < 0$s in Fig. 2). A shock is then applied to the 1θ-mode, at $t = 0$s. The shock causes the ring to vibrate as a rigid body but also influences the flexural vibration of the 2θ-mode because of the coupling provided by the nonlinear electrostatic forces. Time-histories of the positive envelopes for the modal displacements are plotted in Fig. 2. These envelopes encapsulate local maxima in short duration windows of the multi-frequency time-history. The results presented are obtained using different values of shock excitation amplitude and 1θ damping (Q_1).

Figure 2 shows different possible behaviours of the resonator after a shock. If the shock amplitude is small (Fig. 2.a), the system returns relatively quickly to its initial conditions where q_2 is at its top stable branch. With a large shock amplitude and low 1θ damping ($Q_1 = 120\ 000$), Fig. 2.b shows that q_2 displays particularly interesting dynamic behaviour. After an initial transient response (up to approximately $5s$), q_2 appears to stabilise on another stable branch $q_2 \approx 0.03\mu$m. However, while q_1 displacement slowly decays due to damping, q_2 returns to its initial condition on the top stable branch. Finally, if one increases the damping on the 1θ-mode to $Q_1 = 40\ 000$ (Fig. 2.c), q_1 displacement more rapidly reduces so it becomes negligible at around 7s. Also, after an initial transient q_2 stabilises and remains on the bottom stable branch. These results demonstrate the jump phenomenon from one branch to the other: q_2 jumped from $q_2 \approx 0.39\mu$m to $q_2 \approx 0.03\mu$m while being driven harmonically at the same frequency. Further investigations on the influence of damping confirm this finding where q_2 solution jumps to the bottom branch when the 1θ damping is high (low Q_1-value) but returns to the top branch after a sufficient stabilisation time when the 1θ damping is low (high Q_1-value).

4 Conclusions

A mathematical model has been developed and used to investigate the dynamic behaviour of ring resonators subjected to combined operating harmonic forcing and severe shock excitations. The model

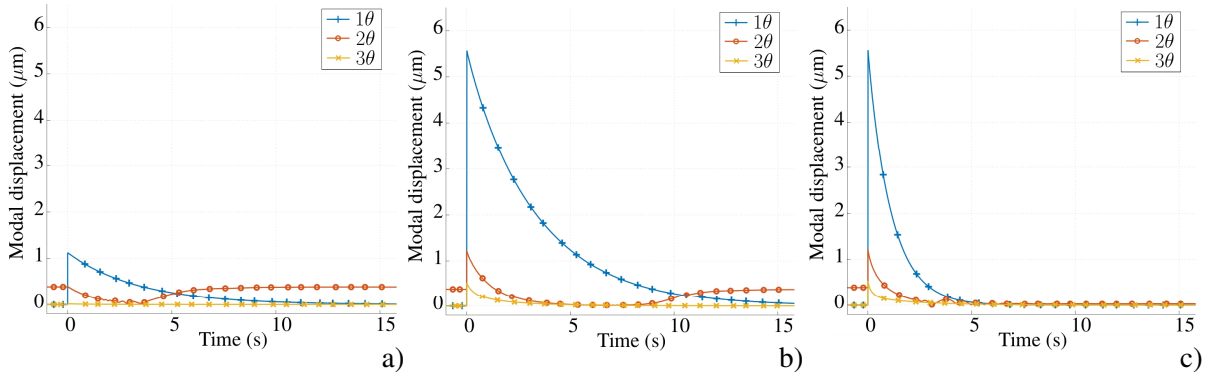

Figure 2: Positive envelope of the modal displacements (q_1 in blue, q_2 in red and q_3 in yellow) as a function of time after: a) a small shock, b) a severe shock, and c) a severe shock with high 1θ damping.

describes the ring response in terms of the modes of a perfect ring, and approximates the nonlinear electrostatic force using a Taylor series expansion. The simulation results obtained demonstrate the presence of mode coupling created after the shock occurs and suggest the possibility of jump phenomenon when the ring is driven hard under particular conditions of shock amplitude and rigid-body motion damping. The very rich dynamics created by the nonlinear effects after shock also makes possible the existence of modal interaction between a mode and the harmonics or combination of harmonics of other modes. These coupling all have potential to diminish sensor performance momentarily compared to the linear case (without coupling).

Acknowledgments

The authors acknowledge the International Exchanges Scheme - Cost Share Programme - between the CNRS (PRC1088) in France and the Royal Society of London (IE150531) in the U.K. for funding this study.

References

[1] S. Yoon, U. Park, J. Rhim, and S. S. Yang. Tactical grade mems vibrating ring gyroscope with high shock reliability. *Microelectronic Engineering*, **142**, pp. 22–29, 2015.

[2] A. D. Challoner, H. H. Ge, and H. Y. Liu. Boeing disc resonator gyroscope. *2014 IEEE/ION Position, Location and Navigation Symposium - PLANS 2014*, Monterey, USA, pp. 504-514, 2014.

[3] S. Sieberer, A. A. Popov, and S. McWilliam. Shock-induced electrostatic coupling of modes of vibration in the response of a MEMS ring sensor. *Proceedings of the ASME Design Engineering Technical Conference, IDETC/CIE 2012, Chicago, USA*, Vol. 5, pp. 111-118, 2012.

[4] S. Sieberer. *In-plane shock response of capacitive MEMS ring-rate senors*. PhD thesis, The University of Nottingham, 2014.

[5] B. Chouvion, S. McWilliam, and A. A. Popov. Effect of nonlinear electrostatic forces on the dynamic behaviour of a capacitive ring-based Coriolis Vibrating Gyroscope under severe shock. *Mechanical Systems and Signal Processing*, **106**, pp. 395–412, 2018.

[6] C. Zener. Internal friction in solids I. theory of internal friction in reeds. *Physical Review*, **52**, pp. 230–235, 1937.

[7] S. T. Hossain. *Thermoelastic damping and support loss in MEMS ring resonators*. PhD thesis, The University of Nottingham, UK, 2016.

EUROMECH Colloquium 603
Dynamics of micro and nano systems
5 – 7 September 2018, Porto, Portugal

Frequency modulated (FM) micro-gyroscopes: recent advances

Valentina Zega[1], Claudia Comi[1], Paolo Minotti[2], Giacomo Langfelder[2], Luca Falorni[3] and Alberto Corigliano[1]

[1]Department of Civil and Environmental Engineering, Politecnico di Milano, Italy
valentina.zega@polimi.it
claudia.comi@polimi.it
alberto.corigliano@polimi.it

[2] Department of Electronics, Information and Bioengineering, Politecnico di Milano, Italy
paolo.minotti@polimi.it
giacomo.langfelder@polimi.it

[2] STMicroelectronics, AMG R&D
luca.falorni@st.com

Summary. MEMS gyroscopes are micro-devices able to measure the external angular rate through the exploitation of different physical phenomena among which the Coriolis force is the most common one. A new working principle based on the frequency modulation (FM) has been recently proposed for micro-gyroscopes and the authors are currently working on the design and experimental verification of pitch and three-axial devices. The recent advances will be presented at the colloquium.

Keywords: micro-gyroscope, frequency modulation, MEMS

1 Introduction

Micro-gyroscopes, enabling the measurement of external angular rates at low cost, have a variety of applications especially in the consumer market. The need of stability against environmental fluctuations, such as temperature, is a key factor in order to avoid expensive calibration procedures of these sensors. Frequency Modulation (FM) has been recently proposed by the Berkley Sensors and Actuators Center (BSAC) as an innovative working principle for MEMS gyroscopes (see [1]) and as the desired solution in terms of stability against environmental fluctuations.

The main difference between the Amplitude Modulated (AM) and the Frequency Modulated (FM) pitch gyroscopes is related to the actuation and detection schemes. While AM operation relies on controlling *y*-axis displacement (the drive axis) and measuring the *z*-axis displacement variation (the sense axis) due to the Coriolis force, FM operation controls both *y*- and *z*-axis velocities (in amplitude and phase) and measures the frequency variation due to the Coriolis force. The FM working principle is here described with reference to a pitch gyroscope.

Recently, the authors proposed the first designs of pitch and three-axial FM gyroscopes (see [2] - [4]), the recent advances in this topic will be presented at the colloquium.

2 Working principle

A FM pitch gyroscope can be schematized as in Fig. 1: an inertial mass m is forced to oscillate in two orthogonal directions with velocities $\dot{y}$ and $\dot{z}$ respectively and when an external angular rate Ω_x is applied, the Coriolis force, with components $F_{cy} = 2m\Omega_x\dot{z}$ and $F_{cz} = -2m\Omega_x\dot{y}$, acts on the mass. An electronic circuit (see [5] for more details) controls the velocities along the two directions both in amplitude ($v_y = v_z$) and phase. Depending on the imposed phase difference $\Delta\Phi_{yz}$ between the driving velocities of the two axes, there are two different FM schemes (see [1] for more details):

- Quadrature Frequency Modulation (QFM): the phase difference between the oscillations is controlled to be equal to +90 or -90 degrees. The two axes of motion are in quadrature and the proof

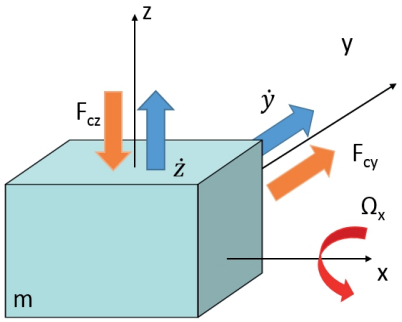

Figure 1. Schematic view of a single-mass FM pitch gyroscope.

mass follows a circular trajectory (see Fig. 2a). The natural frequencies of the two driven modes (along the y- and z- axis) of the mechanical structure are the same and the gyroscope operates in a mode-match condition.

- Lissajous Frequency Modulation (LFM): the phase difference between the oscillations is controlled to be linearly increasing with time ($\Delta\Phi_{yz} = \omega_{LFM}t$). The proof mass follows a 2D Lissajous trajectory (see Fig. 2b) and the natural frequencies of the two driven modes (along the y- and z- axis) of the mechanical structure differ from a fixed quantity called mismatch in the MEMS language.

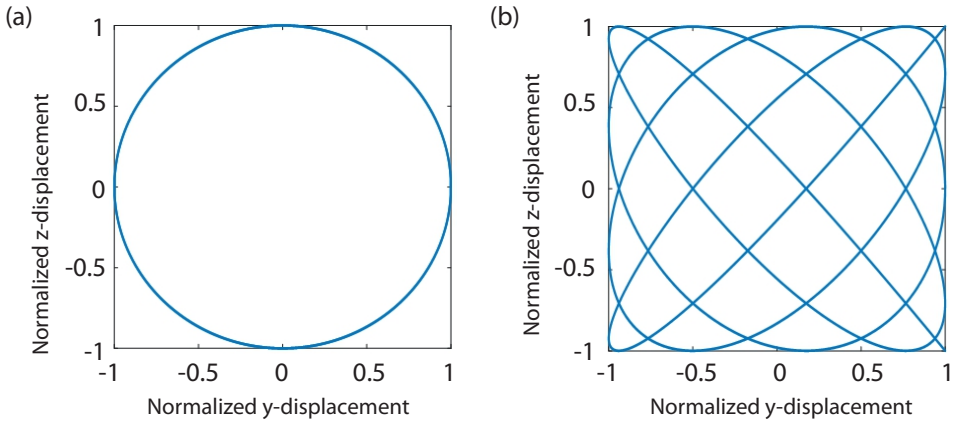

Figure 2. Orbits that the proof mass of the FM pitch gyroscope follows according to the a) QFM scheme and the b) LFM scheme.

By solving through the phasor method (see [4] for more details) the equations of motions describing the behavior of a FM pitch gyroscope under an external angular velocity Ω_x, the expressions for the natural frequencies of the two driven modes read:

$$\omega_y = \omega_{0y} - \alpha_x^{yz}\Omega_x, \quad \omega_z = \omega_{0z} - \alpha_x^{zy}\Omega_x \tag{1}$$

for the QFM operation scheme and

$$\omega_y = \omega_{0y} - \alpha_x^{yz}\Omega_x \sin(\Delta\Phi_{yz}), \quad \omega_z = \omega_{0z} - \alpha_x^{zy}\Omega_x \sin(\Delta\Phi_{yz}) \tag{2}$$

for the LFM operation scheme. Note that ω_{0y} and ω_{0z} represent the natural frequencies of the two modes without external angular rate, α_x^{yz} and α_x^{zy} the angular gains (each one equal to one for a point mass) and $\Delta\Phi_{yz}$ the phase difference between the velocities of the two axes in the LFM operation scheme.

From equation (1) and (2) after a proper demodulation (see [5]), one obtains a scale factor ($\partial\omega/\partial\Omega_x$) of the FM gyroscope equal to the angular gain, α_x^{yz} (or α_x^{zy}), a pure geometric quantity that takes into

account the coupling between the modal masses of the two drive modes due to the Coriolis' force. Summing up, the scale factor of the proposed FM micro-gyroscopes does not depend on environmenatal fluctuations and remains stable in operation as whished.

Note that in Equations (1)-(2) cross-stiffness and cross-damping terms are neglected for the sake of simplicity, the complete expressions can be found in the authors work [4].

3 Mechanical design

From the working principle explained in the previous section, it is clear that the mechanical structure of a FM pitch gyroscope must be able to translate along the y- and the z- directions simultaneously. Proper flexural springs must then be designed to allow such kinds of motions of the gyroscope' proof mass. Moreover, all the fabrication process constraints (e.g. fixed out-of-plane thickness) must be taken into account during the design: a trade off between the maximization of the scale factor and the feasibility of the device is then a key issue from the designer point of view.

In Fig. 3, a possible mechanical design of a pitch gyroscope is shown: two elongated springs allow the pure translational motions of the proof mass along the y- and z- directions. It represents the simplest implementation of a FM pitch gyroscope being the proposed mechanical structure very close to a point-mass structure suspended through two springs (scale factor close to one). Depending on the designed

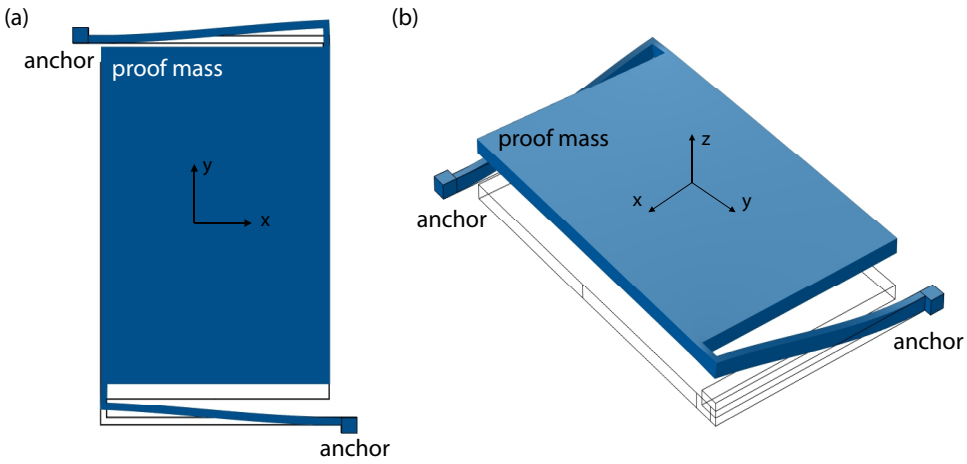

Figure 3. Preliminary mechanical design of a FM pitch micro-gyroscope. a) y-axis mode, b) z-axis mode.

natural frequencies of the proposed device (mode-match or mode-mismatch), it is able to work according to both the QFM and the LFM schemes. Proper electrodes must also be designed to allow the driving and the sensing. Preliminary experimental results have been already published in [2] while improved designs in terms of decoupling between the modes and differential readout are under study.

3.1 Conclusions

In this work, the new FM working principle for micro-gyroscopes is presented. A preliminary mechanical design is also shown while further improved designs are under study and will be presented at the colloquium.

References

[1] M.H. Kline, Y.-C- Yeh, B. Eminoglu, H. Najar, H. Daneman et al., Quadrature FM gyroscope. *MEMS 2013, Taipei, Taiwan*, pp. 604-608, 2013.

[2] V. Zega, P. Minotti, G. Mussi, A. Tocchio, L. Falorni et al., The first frequency-modulated (FM) pitch gyroscope. *Proceedings Eurosensors 2017, Paris, France*, vol. 1, pp. 1-4, 2017.

[3] V. Zega, C. Comi, P. Minotti, L. Falorni, A. Tocchio et al., Mechanical design of a fully-differential triaxial frequency modulated MEMS gyroscope. *AIMETA 2017, Salerno, Italy*, 2017.

[4] V. Zega, C. Comi, P. Minotti, G. Langfelder, L. Falorni and A. Corigliano , A new MEMS three-axial frequency-modulated (FM) gyroscope: a mechanical perspective. *European Journal of Mechanics, A/Solids*, **70**, 203-212, 2018.

[5] P. Minotti, S. Dellea, G. Mussi, A. Bonfanti, S. Facchinetti et al., High scale-factor stability frequency-modulated mems gyroscope: 3-axis sensor and integrated electronics design. *IEEE Transactions on Industrial Electronics*, **65**(6), 5040-5050, 2018.

EUROMECH Colloquium 603
Dynamics of micro and nano systems
5 – 7 September 2018, Porto, Portugal

Mechanical non-linearity effects in supported MEMS ring-based resonators

Violetta Di Napoli, Stewart McWilliam, Atanas A. Popov

Faculty of Engineering, University of Nottingham, Nottingham, United Kingdom
violetta.dinapoli@nottingham.ac.uk
stewart.mcwilliam@nottingham.ac.uk
atanas.popov@nottingham.ac.uk

Summary. An analytical model is developed to investigate the 2θ in-plane flexural response of supported ring-based resonators used in Coriolis Vibrating Gryroscopes (CVGs) when the ring is driven into large amplitude vibration. The model includes geometric non-linearity arising from ring inextensibility and characterises each support as discrete masses and non-linear springs acting in the radial and tangential directions. The non-linear equations of motion for the generalised coordinates describing the 2θ modes are solved using the method of averaging and numerical simulation to investigate the effect of non-linearity on the frequency backbone curve and frequency split. For ring resonators having 8 support legs the frequencies are equal in the linear regime. However, as the amplitude increases the model predicts that the supports cause the degenerate frequency pair to split, which has potential to affect sensor performance.

Keywords: ring-based resonators, mechanical non-linearity, frequency splitting.

1 Introduction

Micro-Electro-Mechanical Systems (MEMS) ring-based Coriolis Vibrating Gyroscopes (CVGs) are devices used to measure angular rate in a wide variety of applications such as autonomous vehicles and robotics [1, 2]. The vibrating element is a thin ring supported by support spokes (or legs) anchored to a fixed frame; Figure 1 presents a common configuration for this type of devices. In operation, the primary 2θ mode (referred to as the drive mode) is excited harmonically at resonance and Coriolis forces arising from the rotation of the device about the ring polar axis induce a response in the secondary 2θ mode (sense mode) the vibration amplitude of which is proportional to the angular rate experienced by the device. Primary and secondary 2θ modes are oriented 45 degrees from each other, as shown in Figure 2.

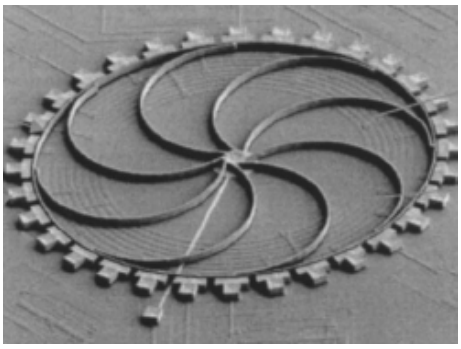

Figure 1. Ring-based Coriolis MEMS gyroscope

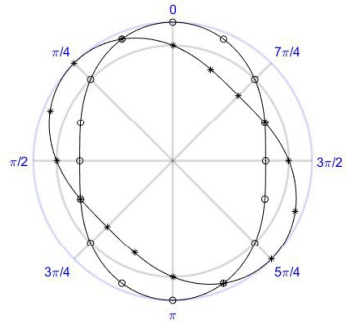

Figure 2. Primary and secondary 2θ modes

To maximise coupling and increase sensitivity of the device it is important to ensure that the drive and sense modes have the same frequency [3] and 8 support legs are used to maintain the symmetry of the resonator relative to the drive and sense modes. In practice, coupling between drive and sense modes is weak [4] and the sense response amplitude is much smaller than the drive amplitude. To magnify the sense response it is beneficial to force the drive mode into large amplitude vibration. The aim of this paper is to investigate the effect of increasing the amplitude of the drive mode on the dynamic behaviour of the resonator and frequencies. An analytical model is developed for a supported ring resonator having 8 uniformly spaced supports that includes geometric non-linearity in the ring [5] arising from ring

inextensibility and support legs based on discrete mass and cubic non-linear springs acting in the radial and tangential directions. The model is used to predict the non-linear frequency response and frequency backbone curves as the sensor is driven into large amplitude vibration. It is shown that geometric non-linearity in the ring and support structures has potential to affect performance by inducing frequency splits between the modes as the resonator is driven into large amplitude vibration.

2 Analytical model

The supported ring is modelled as an inextensible curved beam where the radial and tangential displacements of the ring centre line are expressed in terms of generalised coordinates $Q_1(t)$ and $Q_2(t)$, representing the radial antinode responses of the drive and sense modes, and non-linear breathing mode [5] is taken into account. All 8 supports are modelled as lumped masses with cubic nonlinear springs having different inertia and stiffness properties in the radial and tangential directions, and are calculated using a Finite Element model of a single support. Coriolis effects are also included in the model to take account of ring rotation.

Lagrange's equation is used to determine the governing equation of motion for the generalised coordinates $Q_1(t)$ and $Q_2(t)$ when the drive mode is excited by a harmonic force applied midway between two adjacent support spokes. As the sense response amplitude is normally much smaller than the drive, all nonlinear terms in Q_2 (including derivatives and combinations) are assumed negligible and backwards coupling from the sense mode to the drive mode is assumed weak. Under these assumptions, the equations of motion for the drive and sense modes can be expressed as:

$$\ddot{Q}_1\left(1+\eta_1 Q_1^2\right)+\frac{\omega_0}{Q_f}\dot{Q}_1\left(1+\eta_2\dot{Q}_1 Q_1\right)+\omega_0^2 Q_1\left(1+\sigma_1 Q_1^2+\sigma_2 Q_1^4\right)=\bar{F}_D\cos\Omega t \tag{1}$$

$$\begin{aligned}&\ddot{Q}_2\left(1+\eta_3 Q_1^2\right)+\frac{\omega_0}{Q_f}\dot{Q}_2\left(1+\eta_4\dot{Q}_1 Q_1\right)+\omega_0^2 Q_2\left(1+\eta_5\ddot{Q}_1 Q_1+\eta_6\dot{Q}_1^2+\sigma_3 Q_1^2+\sigma_4 Q_1^4\right)=\\ =&\eta_7\left(\ddot{Q}_1 Q_1^2+\dot{Q}_1^2 Q_1\right)+\sigma_5 Q_1^3+\sigma_6 Q_1^5-2\Omega_z\dot{Q}_1\end{aligned} \tag{2}$$

where ω_0 is the undamped natural frequency of vibration of the 2θ modes, Q_f is the quality factor; Ω_z is the applied angular velocity around the ring polar axis; $\bar{F}_D$ is the magnitude of the applied modal force dividied by the resonator modal mass. η coefficients govern the non-linear inertia coefficients for the ring and supports, while σ coefficients govern the non-linear stiffness coefficients for the ring and supports. When these terms are zero, the equations of motion are linear, the natural frequencies are equal and the modes have no preferred orientation. The non-linear inertia and stiffness coefficients depend on the mass and stiffness properties of the support and ring as well as the location of the supports relative to the applied force. It is worth noting that the small sense amplitude assumption ensures drive mode equation (1) is independent of Q_2 with sense equation (2) externally excited by the drive response.

2.1 Solution methods

Equations of motion (1) and (2) are solved in two ways: i) using the method of averaging and ii) using numerical simulation.

Appying the method of averaging to equation (1) is simplified because it is independent of Q_2 and yields a polynomial expression in F_D, Ω and drive averaged amplitude q_1 that can be solved for q_1. When the resonator is driven into large amplitude vibration, the drive amplitude has three possible solutions while the phase of the drive response can be expressed as a function of q_1, F_D and Ω. By combining the amplitude and phase responses, the drive frequency response curve (amplitude and phase) can be calculated. The sense response is analysed in a second step by averaging (2) with analytical expressions obtained for the averaged sense amplitude q_2 and phase based on the drive response, allowing the sense frequency response curve to be determined.

Runge-Kutta numerical time-integration is applied to the fully nonlinear equations of motion, without making any assumptions about sense amplitude and backward coupling intensity. This simulation

method is used to generate time-history responses for the drive and sense modes which are analysed to determine the steady-state amplitude and phase for each excitation frequency. This process is repeated to determine the frequency response curves for different levels of excitation force.

3 Numerical results

Figure 3 shows the calculated frequency response curves obtained for the supported ring resonator analysed by Serandour et al. [6] with a quality factor of 1000 and an angular velocity Ω_z of 60 degrees per second. Results obtained using the method of averaging and numerial simulation are shown when the drive mode is excited to have a maximum amplitude of ~ 20 microns. It is worth noting that the resonator does not exhibit jump behaviour because the damping has been chosen to be large to ensure the numerical simulation results are obtained efficiently.

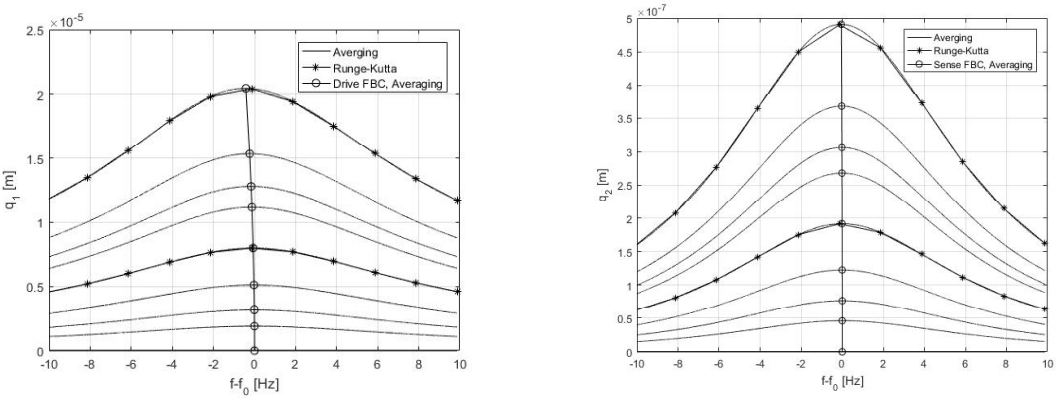

(a) Drive (b) Sense

Figure 3. Frequency response curves

The results obtained for the frequency response curves using the averaging method and numerical simulation are in excellent agreement. For the case considered the sense amplitude is two orders of magnitude smaller than the drive, so the small sense amplitude and weak backward coupling assumptions are valid in this case. Figure 3 also includes the pseudo-resonant frequencies (drive and sense) for different drive amplitudes q_1. The drive pseudo-frequency is calculated based on the drive excitation frequency that produces a drive response having a 90 degree phase lag from the applied force, while the sense pseudo-frequency is calculated based on the drive excitation frequency corresponding to the peak sense response q_2. The results indicate that geometric non-linearity arising from the ring and supports produce a softening behaviour compared to the linear system. As the drive amplitude increases the drive frequency reduces more than the sense frequency.

Figure 4 shows a plot of the frequency backbone curves for the resonator with no support (i.e ring only) and the supported resonator, where the frequency shift from the linear case is plotted against drive amplitude. For the ring only case the drive and sense frequencies remain equal and exhibit softening behaviour as the drive amplitude increases. Adding supports causes the drive and sense frequencies to split, with the drive mode frequency less than and the sense mode frequency greater than the ring only frequency. As the drive amplitude increases the frequency split increases. These resuts indicate that the frequency split is induced by the support.

4 Conclusions

A model is developed to investigate the effect of mechanical geometric non-linearity for a supported ring-based CVG as it is driven into large amplitude vibration. Frequency response curves were obtained using the method of averaging, based on the assumption of small sense response and weak back coupling,

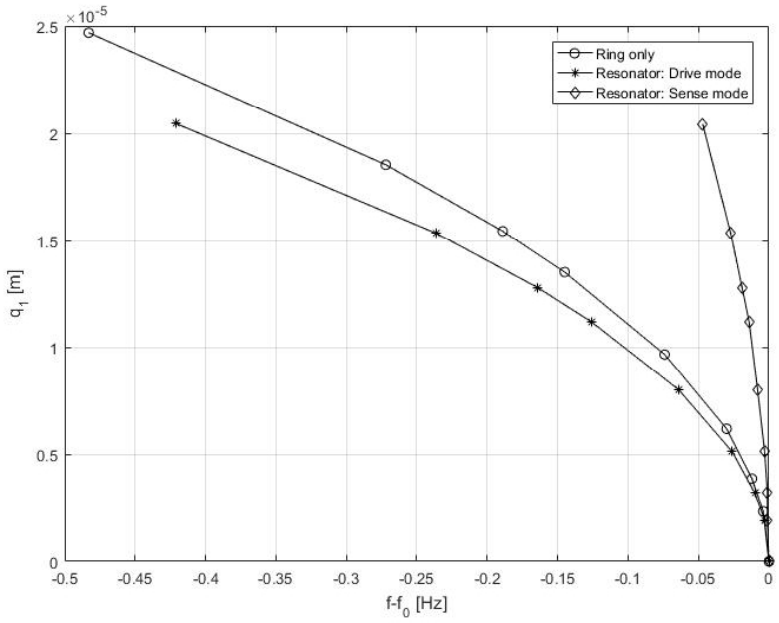

Figure 4. Frequency backbone curves

and simulation was used to verify the results. The results indicate that non-linearity in the ring produces a softening behaviour and that the supports induce a frequency split that can affect sensor performance. The conference presentation will include additional insights into the origins and causes of non-linear frequency splitting in ring-based CVGs.

References

[1] M. Armenise, C. Ciminelli, F. DellOlio, V. Passaro, *Advances in Gyroscope Technologies*. Springer Science & Business Media, 2010.

[2] C. Acar, A. Shkel, *MEMS Vibratory Gyroscopes: Structural Approaches to Improve Robustness*. Springer, 2008.

[3] V. Apostolyuk, *Coriolis Vibratory Gyroscopes: Theory and Design*. Springer, 2015.

[4] M. Bao, *Analysis and Design Principles of MEMS Devices*. Elsevier, 2005.

[5] D.A. Evensen, Non-linear flexural vibrations of thin circular rings. *Journal of Applied Mechanics*, **33 (3)**, 553-560, 1966.

[6] G. Serandour, C.H.J. Fox, S. McWilliam, Modelling geometric nonlinearity in a MEMS resonator. *Proceedings of the IX International Conference on Recent Advances in Structural Dynamics/RASD06, Southampton, England, 2006*.

EUROMECH Colloquium 603
Dynamics of micro and nano systems
5 – 7 September 2018, Porto, Portugal

Measured and simulated tri-stability in MEMS capacitive switches

Devin Kalafut, Anil Bajaj and Arvind Raman

Purdue University, West Lafayette, United States of America
kalafut@purdue.edu
bajaj@purdue.edu
raman@purdue.edu

Summary. Cantilever capacitive switches, a subset of radio frequency (RF) microelectromechanical systems (MEMS), continue to see application in automotive and biological sensing, high-performance wireless communication, and military weaponry. Many of these industries may benefit from novel implementations of switches with more than two capacitive states. Herein, experimental measurements and finite element simulations of such devices complement prior theoretical frameworks by exhibiting the existence of tri-stable behaviour and improving modelling efforts to predict instability thresholds.

Keywords: MEMS, bifurcation, multistability, FEM, experimental measurements.

1 Introduction

Mechanical multistability has been previously explored in micro- and nanosystems in hopes of exploiting nonlinearity for improved device performance, with some going as far as employing novel latching designs to force this behaviour [1]. In recent work [2], mono-, bi-, and tri-stable static equilibrium behaviour was found to be intrinsic to a simple model for a standard representation of cantilever switches. These features arose from the presence of turning point instabilities, or saddle-node bifurcations, along the static equilibrium solution branches. Early capacitance-voltage measurements of similar devices indicated the possibility of tri-stability [3], but thorough experimentation and advanced modelling approaches are required for full device characterization.

2 Experimental measurements

Five RF MEMS cantilever capacitive switches previously fabricated at the PRISM Center of Purdue University are used to conduct experimental measurements. The configuration is a nickel cantilever suspended over a (silicon nitride) dielectric-coated gold electrode. An additional gold electrode is connected to the cantilever via its fixed anchor to provide a voltage bias to the beam, while the dielectric-coated gold electrode is kept at ground. A top-down view of an example device with components labelled can be found in Figure 1(a).

Devices are first examined using a Bruker optical microscope to determine the undeflected cantilever profile with respect to the rest of the device components. Additionally, dielectric thickness is measured for a single representative device using an Asylum Research MFP-3D-BIO. Next, the wafer is mounted inside a Suss PLV50 ProbeStation, whose chamber is pumped down to high vacuum and pressurized back to 1 atm with dry nitrogen gas. This step reduces capillary forces and dielectric charging due to ambient humidity during device performance. With the aid of a Piezo Systems linear amplifier, a 90 V amplitude triangular waveform at a frequency of 50 Hz is provided to the actuation probe/electrode, while a Polytec MSA-400 laser Doppler vibrometer system is aligned to measure the velocity of a point on the device at a sampling frequency of 102.4 Hz. Successive velocity measurements are taken at each of the 105 scan points (7x15 grid) defined on the top surface of the cantilever beam. Finally, this velocity data is numerically integrated and combined with the optical microscope data to reconstruct a representation of the cantilever profiles throughout an actuation cycle.

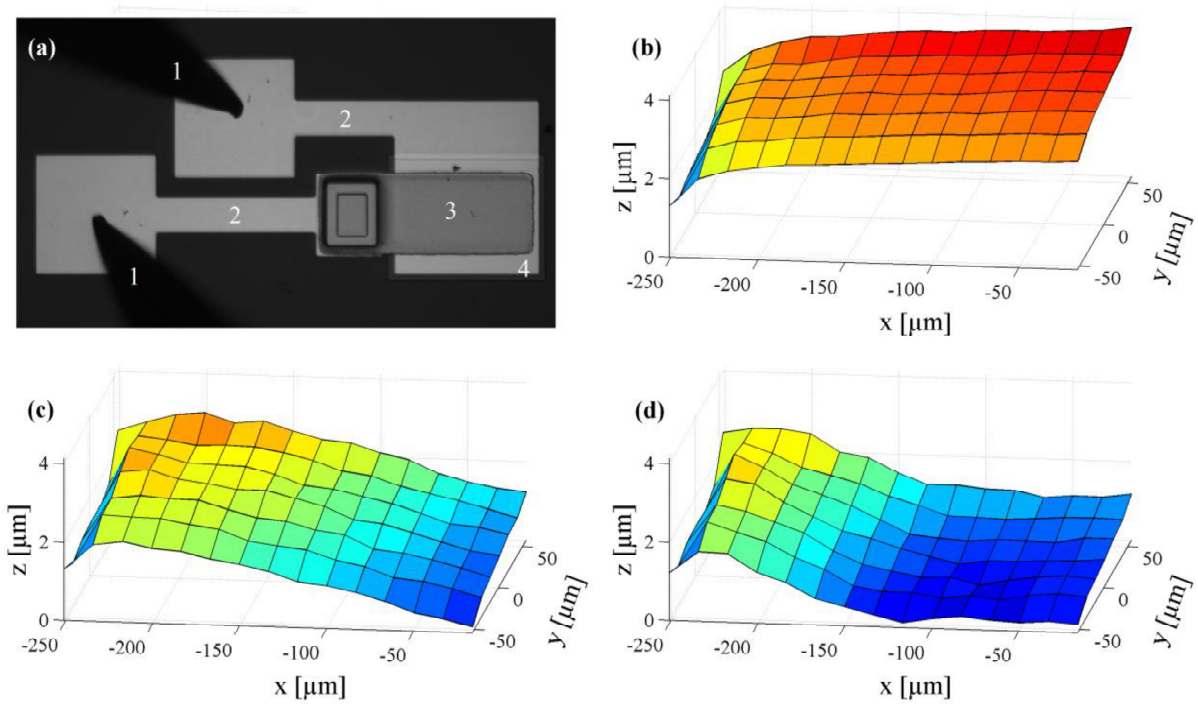

Figure 1. (a) Top view of an example device, with the actuation probes (1), gold electrodes (2), nickel cantilever (3), and silicon nitride dielectric (4), labelled. Cantilever profile reconstructions from experimental data for (b) low, (c) medium, and (d) high voltage actuation.

3 Computational modelling

As a companion to the experimental measurements, the use of COMSOL Multiphysics 5.3® software extends the prior theoretical model to incorporate realistic device geometry, stress and strain fields, and electrostatic field effects via finite element modelling. A continuation study is conducted for each device, following static equilibrium paths stemming from the original undeflected configuration. Material properties used are the default software values for the device components listed in Figure 1(a), with nitrogen as the surrounding simulation medium. Studies are conducted using a 2D cross-section representation, with an assumed out-of-plane depth corresponding to the device geometries.

For reference, a simulation constructed from nominal design parameters and a flat beam profile is first run to predict ideal instability thresholds. These nominal values, with quantities given in parenthesis, are the beam width (110 μm), beam thickness (2 μm), beam length (240 μm), uniform gap between the beam and dielectric (2 μm), and dielectric thickness (~300 nm). In an effort to improve the predictions, a unique simulation is run for each device in the experimental set using measured geometries, providing an updated beam width, length, and top surface profile, along with the dielectric thickness, directly. The beam thickness is identified indirectly at the cantilever tip while it is in contact with the dielectric, and is further assumed to be uniform along the length of the beam. These updated simulations are as close to matching individual device geometries as is reasonable to achieve using only non-destructive measurement techniques.

3.1 Results and discussion

The actuation cycle reconstructions themselves are of great interest, as they experimentally showcase the same three cantilever shapes of tri-stability found theoretically in literature. An example of floating, arc-shaped, and s-shaped beam configurations for a device is shown in Figure 1(b)-(d), respectively, using terminology from Kalafut et al. [2]. Figure 2 depicts the actuation voltages of transitions between successive switching states, and provides a comparison of these instabilities between experimental results and those of COMSOL Multiphysics 5.3®. With the exception of device 3, the predictions of instabilities from updated simulations are clearly improvements over their nominal design counterparts.

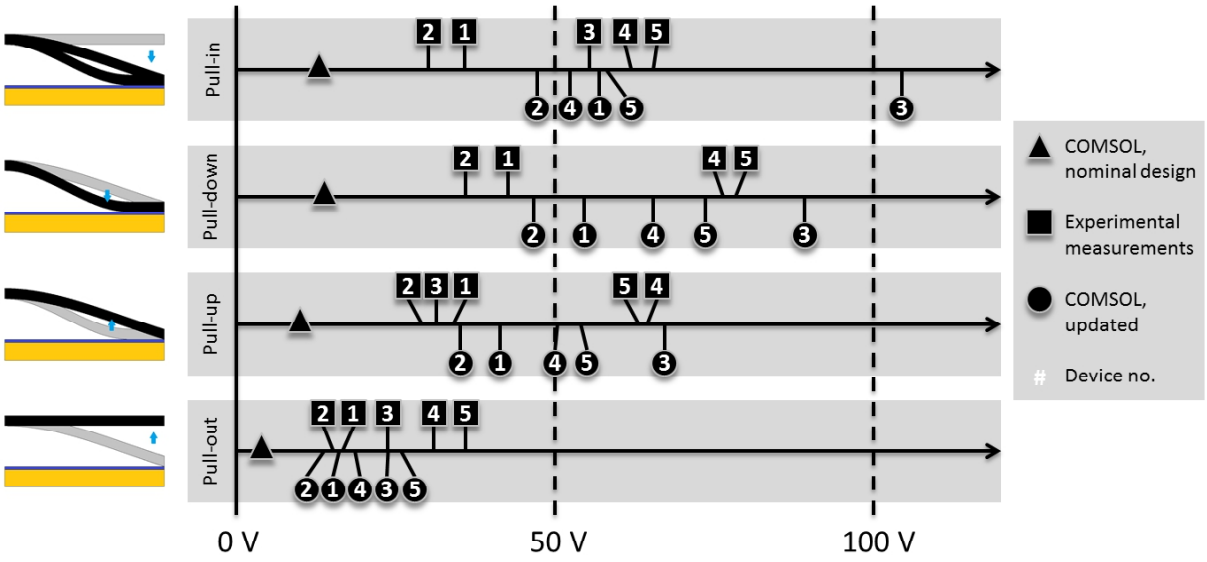

Figure 2. Schematics of transitions across instabilities, with initial beam shape in grey, final beam shape(s) in black, dielectric layer in indigo, and electrode in gold (left); associated comparisons of simulations and experiments for five devices (centre); and corresponding legend (right).

4 Conclusions

Cantilever profiles, reconstructed from direct measurements combined with numerical processing, are qualitatively consistent with tri-stability predicted by simple models of physical phenomena. COMSOL Multiphysics 5.3® simulations updated with newly-obtained device measurements provide quantitative improvement to predictions made from nominal design values, making tri-stable cantilever capacitive switches more attractive for novel uses.

References

[1] J. Oberhammer, M. Tang, A.-Q. Liu, G. Stemme, Mechanically tri-stable, true single-pole-double-throw (SPDT) switches. *Journal of Micromechanics and Microengineering*, **16**, 2251-2258, 2006.

[2] D. Kalafut, A. Bajaj, A. Raman, Multistability of cantilever MEMS/NEMS switches induced by electrostatic and surface forces. *International Journal of Non-Linear Mechanics*, **95**, 209–215, 2017.

[3] E. K. Chan, K. Garikipati, R. W. Dutton, Characterization of contact electromechanics through capacitance-voltage measurements and simulations. *Journal of Microelectromechanical Systems*, **8**, 208–217, 1999.

EUROMECH Colloquium 603
Dynamics of micro and nano systems
5 – 7 September 2018, Porto, Portugal

Experiments on nonlinear characteristics of parametric resonance in microcantilever

Shouhou Tei[1], **Hiroshi Yabuno**[1]

[1]University of Tsukuba, Tsukuba, Japan
s1720900@s.tsukuba.ac.jp
yabuno@esys.tsukuba.ac.jp

Summary. In this study, the nonlinear characteristics of parametric resonance in a microcantilever are experimentally investigated. In general, it is desirable in the frequency response curve of band-pass filter not to have a bistable reigion in any input frequencies. In this study, the experimental frequency response curve in a parametrically excited cantilever is shown which does not include a bistable region in any input frequencies.

Keywords: MEMS, parametric resonance, microcantilever, nonlinear characteristics

1 Introduction

Recently, with the development of MEMS technology, many kinds of resonances including self-excited oscillation, parametric resonance, subharmonic resonance, and so on have attracted for their application to the enhancement of measurement accuracy. The parametric resonance is proposed for the application to band-pass filter because the trivial steady state in the oscillator is resonated in the region that the input excitation frequency is in the neighborhood of twice the natural frequency of the resonator [1, 2, 3]. However, in general, the frequency response curve is bent due to the nonlinearity of the resonator or the environment and the overhang of frequency response curve caused from the bending produces a bistable region for an input frequency region. For the application of parametric resonance to band-pass filter, such a characteristics must be avoided. By the way, it is known for parametrically excited macro beam that the frequency response curve has no bistable region due to the quadratic damping effect[4, 5]. In this study, experiments of parametrically excited microcantilever are conducted. The occurrence of parametric resonance is confirmed from the frequency in the resonated cantilever. It is reported that the desirable frequency response without bistable region is experimentally observed in a parametrically excited microcantilever.

2 Parametrically excited microcantilever

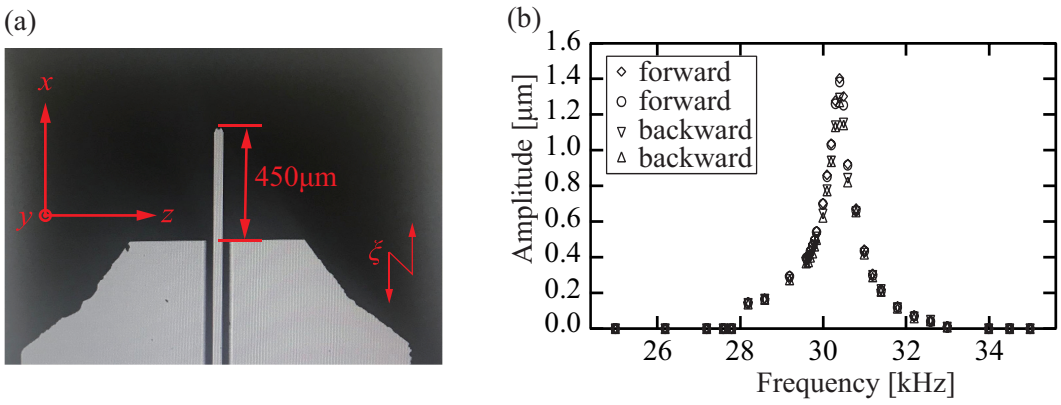

Figure 1. (a) Parametrically excited microcantilever; (b) Experimental frequency response curve.

Figure 1(a) shows the microcantilever which oscillates on x-y plane under the parametric excitation in x-direction. A piezo actuator is attached to the base and provides a base excitation in x-direction. The parameters of the microcantilever are the length 450 μm, width 50 μm, thickness 2 μm and the first natural frequency 15.2 kHz.

3 Experimental results

Figure 1(b) shows the experimentally obtained frequency response curve. The vertical axis is the magnitude of a half the excitation frequency component in the response and the horizontal axis is the excitation frequency. $\diamondsuit$ and $\bigcirc$ denote the largest and smallest steady amplitude for a given excitation frequency in forward sweep, respectively. $\bigtriangledown$ and $\bigtriangleup$ denote the largest and smallest steady amplitude in backward sweep, respectively. The frequency response curve has the desired shape that there is no bistable region. At the bifurcation points from the trivial steady state, the slope of the frequency response curve is not infinite but finite. Therefore, the bifurcation is not pitchfork, but regarded as trans-critical bifurcation, which is produced by the quadratic nonlinear damping effect[6].

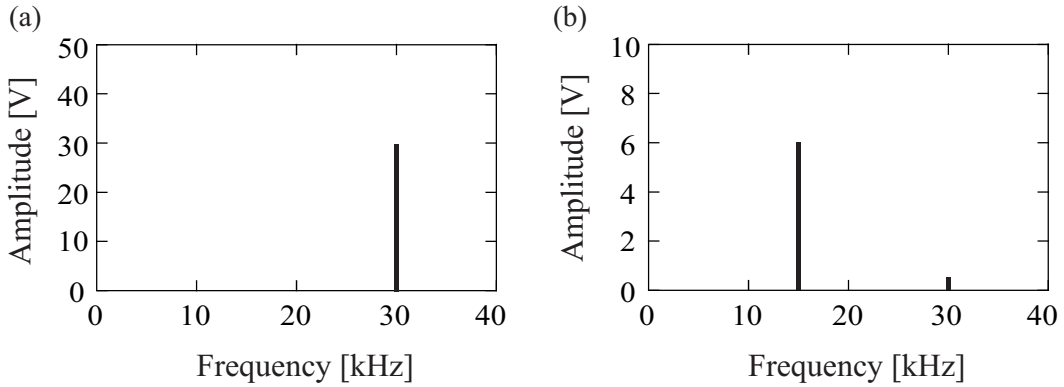

Figure 2. (a) Spectrum diagram of input voltage; (b) Spectrum diagram of response of microcantilever.

Figure 2(a) and (b) show the spectrum diagram of input voltage and response of the microcantilever in which the excitation frequency is 30 kHz, respectively. Therefore, the experimentally observed response is due to the parametric resonance.

4 Conclusion

This study, the frequency response curve without bistable region is reported that is the desired shape for the application to the band-pass filter. The bifurcation is regarded as the trans-critical bifurcation from the slope at the bifurcation point due to the quadratic damping. The experimental identification of the quadratic damping effect and the comparison with the theoretical results are in a near future work.
Acknowledgements: The authors acknowledge a Grant-in-Aid for Scientific Research A (Grant No. 16H02318) from the Japan Society for the Promotion of Science (JSPS).

References

[1] K. Moran, C. Burgner, S. Shaw, K. Turner, A review of parametric resonance in microelectromechaniacl systems. *NOLTA*, **4-3**, 198-224, 2013.

[2] B. E. DeMartini, J. F. Rhoads, K. L. Turner, S. W. Shaw, J. Moehlis, Linear and nonlinear tuning of parametrically excited MEMS oscillators. *J. Microelectromech. S.*, **16-2**, 310-318, 2007.

[3] S. M. Shahruz, Design of mechanical band-pass filters for energy scavenging. *Berkeley Engineering Research Institute*, **14-5**, 753-768, 2008.

[4] T. J. Anderson, A. H. Nayfeh, B. Balachandran, Experimental verification of the importance of the nonlinear curvature in the response of a cantilever beam. *Journal of Vibration and Acoustics-Transactions of the ASME*, **6-6**, 339-342, 2011.

[5] A. Shibata, S. Ohishi, H. Yabuno, Passive method for controlling the nonlinear characteristics in a parametrically excited hinged-hinged beam by the addition of a linear spring. *Journal of Sound and Vibration*, **350**, 111-122, 2015.

[6] H. Yabuno, Y. Ide, N. Aoshima, Nonlinear analysis of a parametrically excited cantilever beam(effect of the tip mass on stationary response). *JSME International Journal Series C Mechanical Systems, Machine Elements and Manufacturing*, **41-3**, 555-562, 1998.

EUROMECH Colloquium 603
Dynamics of micro and nano systems
5 – 7 September 2018, Porto, Portugal

Array of nanostrings electromagnetically coupled through repelling Lorentz forces

Slava Krylov[1] **and Rivka Gilat**[2]

[1]School of Mechanical Engineering, Faculty of Engineering, Tel-Aviv University, Ramat Aviv 69978, Israel
krylov@post.tau.ac.il

[2] Department of Civil Engineering, Faculty of Engineering, Ariel University, Ariel 44837, Israel
gilat@eng.tau.ac.il

Summary. The behavior of an array of conductive nanostrings actuated by electromagnetic interaction forces is studied. The stimulating current in each two adjacent strings is in the opposite directions inducing a repelling Lorentz force. This force is solely due to interaction between the array elements, with no external magnets incorporated in the setting. Under a critical current value, a push-out instability occurs transforming the ideal initial planar array architecture into an out-of-plane configuration. The latter exhibits inherent nonlinear post buckling behavior due to the interaction between the elastic and electromagnetic fields.

Keywords: Critical current, Pull-in, Push-out, NEMS.

1 Introduction

The buckling phenomenon, which was traditionally considered as a failure which should be avoided, is recently found to be beneficial [1]. In the realm of micro and nanoelectromechanical systems the buckling behavior of mechanical devices has various applications, one of which is performance enchantment of bifurcation based sensors. Such devices, mainly consisting of a single beam/string or an array of mechanical elements, are often actuated by configuration dependent electrostatic forces, inducing instabilities such as the electrostatic pull-in or nonlinear dynamics [2, 3]. Magnetic rather than electrostatic interactions were considered as well. Actuation of a microcantilever resonator by a current-carrying metallic wire loop placed in a permanent magnetic field has been demonstrated in [4]. Actuation of a three parallel conductive nanolayers by parallel currents provoking attracting Lorentz force between the layers, was suggested in [5] where the in-plane symmetric and asymmetric bifurcations and equilibrium pathes were studied. In the present work, the behavior of a planar array of conductive nanostrings interacting through repelling Lorentz force, is studied. The actuating force is induced exclusively by the electric current in the strings without the usage of external magnets. This force, which depends on the array deformation, yields bifurcation into an out-of-plane configuration.

2 Formulation

Consider an array of weightless strings stretched in the $\hat{y}$ direction between two immovable parallel electrically insulating supports located at a distance H from each other, as shown in Fig.1. The distance between the strings is g_0. The structure can be realized by patterning a conductive layer to form a folded wire and then by etching a cavity in the electrically insulating substrate. Due to an electric current in the strings there is a distributed Lorentz force acting along the strings, which may deform each of them to a curve described by a function $\hat{w}_n(\hat{y})$. The behavior of each of the strings is governed by the equilibrium equation [6, 7],

$$-\hat{T}_n \frac{\hat{w}_{n,\hat{y}\hat{y}}}{(\sqrt{1+(\hat{w}_{n,\hat{y}})^2})^3} = \hat{f}_L \tag{1}$$

accompanied by the boundary conditions $\hat{w}_n = 0$ at the ends of the string. The tensile force $\hat{T}_n(\hat{w}_n)$, which is constant along the string since the Lorentz force is perpendicular to it [6], contains a deflection-independent component, $\hat{T}_{n0} = \hat{T}_0$, and a variable deflection-dependent component, $\hat{T}_{ne}$, resulting from

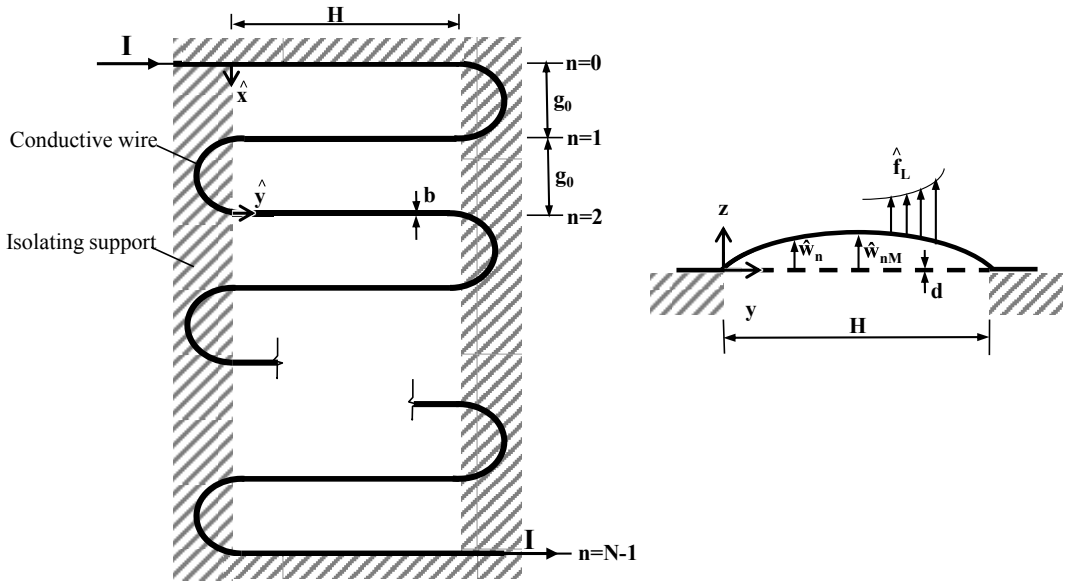

Figure 1. The nanostrings array architecture (a) and the single n^{th} string in its initial (dashed line) and deformed (continuous line) states. The stings deflect only in he out of plane z direction.

the stretching of the string during actuation. The deflection-independent component is associated with the fabrication related residual stress as well as with the thermal stress appearing due to the Joule's heating caused by the electric current. In this work we neglect the influence of the Joule's heating and assume a constant T_0. Our calculations show that this assumption is valid for the case of nano scale strings made of highly conductive materials such as metals. However, in larger devices, with a distance of several micrometers between the strings, the current required for actuation is high and the thermal buckling can be dominant.

Due to the pattern of the current, namely due to the fact that the current in each two adjacent strings is in the opposite directions, the Lorentz force is repelling and is $\hat{f}_L = \mu_0 I^2/(2\pi\hat{r})$, where μ_0 is permeability and $\hat{r}$ is the distance between the strings. For the sake of simplicity, we limit our consideration to the case of a local interaction and assume that each of the strings interacts only with its closest neighborhoods. As a result, the vertical z component of the force (per unit length) acting on each of the strings is given by the expression

$$\hat{f}_L = \frac{\mu_0 I^2}{2\pi}\left[\frac{\hat{w}_n - \hat{w}_{n-1}}{g_0^2 + (\hat{w}_n - \hat{w}_{n-1})^2} - \frac{\hat{w}_{n+1} - \hat{w}_n}{g_0^2 + (\hat{w}_{n+1} - \hat{w}_n)^2}\right] \tag{2}$$

For convenience, we introduce non-dimensional quantities

$$\begin{aligned} w &= \frac{\hat{w}}{g_0}, \quad x = \frac{\hat{x}}{g_0}, \quad y = \frac{\hat{y}}{H}, \quad \delta = \frac{g_0}{H}, \\ T_n &= \frac{\hat{T}_n}{EA} \equiv \frac{\sigma}{E}, \quad \beta = \frac{\mu_0\, I^2\, H^2}{2\pi g_0^2\, EA}, \quad \lambda_n = \frac{2\beta}{T_n} \end{aligned} \tag{3}$$

where $A = bd$ is the string cross-section area ($b > d$), and the configuration-dependent parameter λ_n is referred as a modified current parameter. In the case of small aspect ratio δ, the effect of finite slope and curvature, which are of the order of δ^2, can be neglected such that the non-dimensional counterpart of Eq. (1) is reduced to

$$w_{n,yy} - \frac{\lambda_n}{2}\,\frac{(w_{n+1} - 2w_n + w_{n-1})(1 - (w_n - w_{n-1})(w_{n+1} - w_n))}{(1 + (w_n - w_{n-1})^2)(1 + (w_{n+1} - w_n)^2)} = 0 \tag{4}$$

3 Results

3.1 Critical push-out current parameter

In the case of small deflections, $w_n \ll 1$, the nonlinear stretching can be neglected. Thus we can assume $T_n = T,\ \lambda_n = \lambda$, and Eq. (4) takes the following linearized form

$$w_{n,yy} - \frac{\lambda}{2}\left(w_{n+1} - 2w_n + w_{n-1}\right) = 0 \tag{5}$$

representing an eigenvalue problem which defines the critical current inducing bifurcation of the initial equilibrium configuration consisting of aligned straight strings. As the form of Eq.(5) implies variables separation, we let

$$w_n = X_n Y(y) \tag{6}$$

namely assume that all strings have the same buckled form ($Y_n = Y$), such that Eq. (5) is separated into two equations

$$Y_{,y\,y} + \Omega^2 Y = 0 \tag{7}$$

$$(X_{n-1} - 2X_n + X_{n+1}) + \omega^2 X_n = 0 \tag{8}$$

where $\Omega^2 = \omega^2\lambda/2$. For an array consisting of N strings ($n = 0, 1, ...N-1$) with the external ones, $n = 0, N-1$, fixed, the solution of these coupled eigenvalue problems provides the lowest push-out current parameter in the following form

$$\lambda_{PO} = \frac{2\pi^2}{\omega^2} = \frac{\pi^2}{1 - \cos(\frac{(N-2)\pi}{N-1})} \tag{9}$$

Note that for $N = 3$, namely when only one string is free to move and the two adjacent strings are fixed, $\omega^2 = 2$ and the lowest push-out value of the modified current parameter is $\lambda_{PO} = \pi^2$. For infinite number of strings, the push-out modified current value reduces to $\lambda_{PO} = \frac{\pi^2}{2}$, with a corresponding "zig-zag" eigenvector reflecting a buckled form characterized by $w_n = -w_{n-1}$.

It is interesting to note that Eq. (5), in conjunction with the finite differences approximation, can be considered to be represented by the following quasi continuous equation

$$w_{,yy} - \frac{\lambda}{2}\, w_{,xx} = 0 \tag{10}$$

which resembles the string free vibrations equation or a wave equation. However, replacing Eq.(8) by its quasi continuous representation yields a critical modified current parameter which is smaller than that predicted by the discrete formulation.

3.2 Nonlinear behavior

While the derivation of the nonlinear behavior of the array, which is governed by the set of coupled differential equations, Eq.(4), requires application of an approximate solution strategy (e.g. the Galerkin decomposition, the finite differences method), the special case of three strings with only the middle one free to move can be solved analytically. In this case, $n = 1,\ w_{n-1} = w_{n+1} = 0,\ w_n = w,\ \lambda_n = \lambda$ in Eq. (4)

$$w_{,yy} + \lambda\,\frac{w}{1 + w^2} = 0 \tag{11}$$

which is an equation of a string on a nonlinear elastic foundation with a negative stiffness parameterized by the modified current parameter λ.

Using the first integral of Eq.(11), while employing the requirement of zero slope at the string midpoint, and subsequent further integration between the string midpoint and its end, where the deflection is monotonous, yields the following relation

$$\lambda = 4\left(\int_{w_M}^{0} \frac{dw}{\sqrt{\ln\left(\frac{1+w_M^2}{1+w^2}\right)}}\right)^2 \tag{12}$$

This equation defines the dependence between the modified current parameter λ and the non-dimensional midpoint deflection of the string w_M. This dependence is presented in Fig.2. It is noted that the critical value of Eq. (12) is equal to $\lambda_{PO} = \pi^2$.

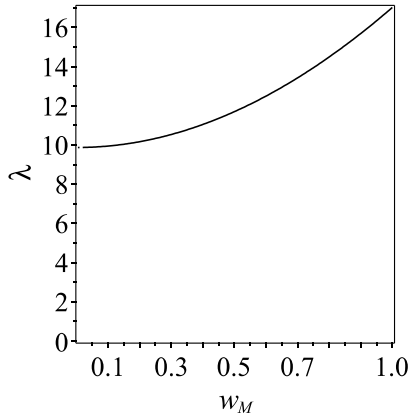

Figure 2. Non-dimensional buckling curve of a single string, modified current parameter vs. string midpoint z location.

4 Conclusions

- Repelling Lorentz force, stimulated exclusively by direct current in nanostrings arranged in a planar array configuration, induce push-out instability which manifests itself in an out-of-plane deformation of the strings. The buckled array configuration is of a short wavelength "zig-zag" pattern.
- The value of the critical current depends on the deflection-independent component of the axial force.
- The electromagnetically actuated interacting strings exhibit geometrically inherent nonlinear behavior.
- The representation of the discrete algebraic form governing the array buckling by its quasi continuous counterpart, did not provide a reliable result.
- The dynamic behavior of the nanostrings array under alternating current is presently under examination.

Acknowledgments

The research is supported by Israel Ministry of Science, Technology and Space, and by the Israel Science Foundation (ISF, grant no. 1272/16).The first author acknowledges support from the Henry and Dinah Krongold Chair of Microelectronics.

References

[1] N. Hu, R. Burgueo, Buckling-induced smart applications: recent advances andtrends. *Smart Mater. Struct.*, **24**, 1-20, 2015.
[2] W-M. Zhang, H. Yan, Z-K. Peng, g. Meng, Electrostatic pull-in instability in MEMS/NEMS: a review. *Sensors and Actuators A: Physical*, **214**, 187-218, 2014.
[3] S. Krylov, S. Lulinsky, B. R. Ilic, I. Schneider, Collective dynamics and pattern switching in an array of parametrically excited micro cantilevers interacting through fringing electrostatic fields. *Applied Physics Letters*, **105**, 071909, 2014.
[4] A. B. Sabater, V. Kumar, A. Mahmood, J. F. Rhoads, On the Nonlinear Dynamics of Electromagnetically Transduced Microresonators. *Journal of Microelectromechanical Systems*, **22**, 1020-1031, 2013.
[5] A. V. Lukin, I. A. Popov, D. Yu. Skubov, L. V. Shtukin, Equilibrium forms branching of a nanolayers system. *Vibroengineering PROCEDIA*, **8**, 517521, 2016.
[6] J. A. Pelesko, D. H. Bernstein *Modeling of MEMS and NEMS*. Chapman and Hall: CRC Press, 2002.
[7] S. Krylov, S. Seretensky, Higher order correction of electrostatic pressure and its influence on the pull-in behavior of microstructures. *J Micromech Microeng*, **16**, 13821396, 2006.

EUROMECH Colloquium 603
Dynamics of micro and nano systems
5 – 7 September 2018, Porto, Portugal

Feasibility Study of a Resonant Accelerometer with Bistable Electrostatically Actuated Cantilever as a Sensing Element

Omer HaLevy, Naftaly Krakover and Slava Krylov

School of Mechanical Engineering, Faculty of Engineering, Tel Aviv University,
Ramat Aviv, Tel Aviv, Israel 69978

Summary. We report on a feasibility study of a resonant accelerometer, based on a vibrating bistable cantilever, serving as a sensing element. Using reduced order (RO) Galerkin model and numerical coupled electromechanical finite elements (FE) analysis, we show that the initially planar cantilever actuated by appropriately tailored fringing electrostatic field, may bring the cantilever to a bistability threshold where frequency sensitivity to the beam's deflection is enhanced. The reported approach allows the achievement of a bistable behavior in a simple, manufacturable, cantilever device distinguished by robustness and low sensitivity to thermal and residual stress. In addition, we show, by means of the model, that by integration of the bistable cantilever with a proof mass, it is possible to design a highly sensitive resonant accelerometer.

Keywords: MEMS; Bistable Cantilever; Inertial Sensor; Resonant Accelerometer; Fringing Electrostatic Fields

1 Introduction

Resonant accelerometers play a vital role in the development of future high end inertial sensors, among the numerous advantages of these decides, one can mention, high sensitivity, frequency resolution being independent on the amplitude measurement device resolution, wide bandwidth, robustness and reduced $1/f$ noise [1]. Most of the designs exploit frequency modulation in axially loaded ties, where the axial stretching is associated with the inertial force applied to the tie by a proof mass. To overcome high axial stiffness of the ties, complex force amplification mechanisms are often implemented [2], which complicates design of these devices and introduces undesired mechanical coupling. Another approach is based on the reduction of the overall dimensions of the vibrating sensing elements to nanometric scale, in which case fabrication is challenging. One of the recent alternatives is based on the use of electrostatic softening and of the electrostatic coupling between the proof mass and the resonator, which both act as the electrodes of a parallel-capacitor transducer. In these devices, the displacement of the proof mass under an external inertial force changes the gap between the mass and the resonator. This gap variation is followed by a change in the resonators effective spring constant and frequency [3]. Electrostatic softening near pull-in results in higher sensitivity but has a danger of pull-in collapse as its drawback. Bistable curved micro beams [4] or offset clamped beams [5] allow reversible contactless operation near instabilities, but are sensitive to temperature and residual stress. A solution for this problem could be incorporation of cantilever devices, which by fringing field related electrostatic forces could be brought to a bistable state [6]. However, in these devices the problem arises related to the large displacement and therefore large actuating voltages needed in order to bring the beam to the working point near instabilities.

Here we report on a design of a simple, robust and manufacturable bistable cantilever device, which allows to overcome this limitation. The concept is based on a particular design of the side electrodes, such that the beam in its initial undeformed configuration is already positioned at the working point, close to the point of highest frequency sensitivity.

2 Model

Our device is a cantilever of length L, width h and thickness d designed to bend in the out-of-plane (z) direction, Fig. 1(a). A planar side electrode of length L_S and thickness d_S is located at the distance g_S from the beam and is a source of the actuating electrostatic force F_{ES}, Fig. 1(b), [7]. Combination of the electrostatic fringing field force acting in a transverse z direction and pulling the beam towards the

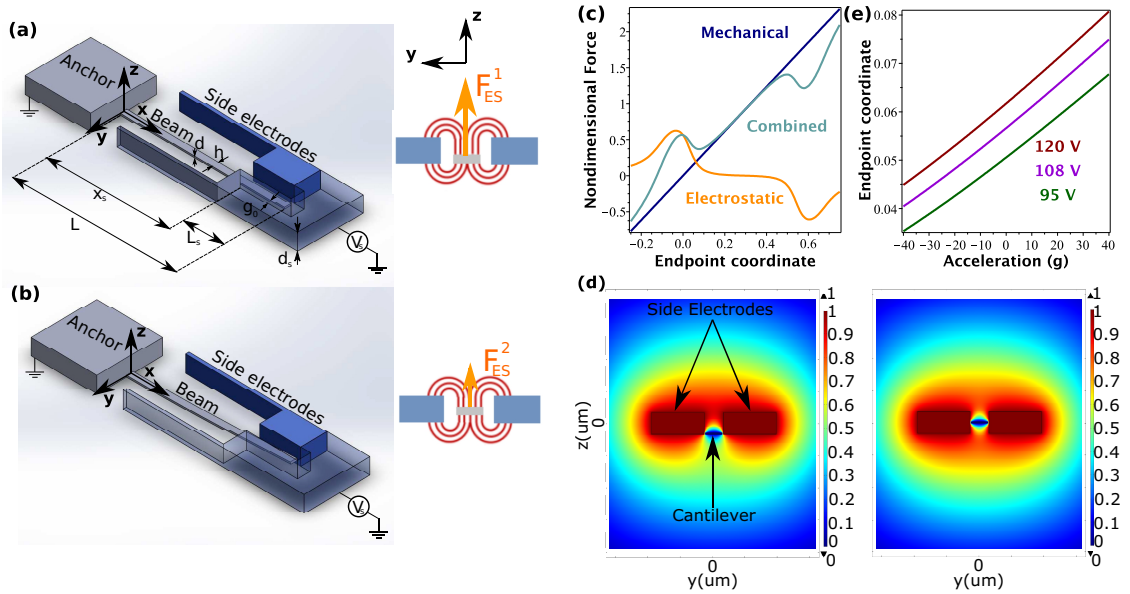

Figure 1: (a) Schematics of an undeformed cantilever under non-symmetric fringing fields emerging from the side (fringing) electrode. (b) Deformed beam at its working point, where the electrostatic force from the side electrodes connected to the voltage V_S and the mechanical force as a result of the cantilever's stiffness are equilibrated. Insets show schematically the fringing fields and electrostatic force for each case. (c) Schematic representation of the various forces as a function of the beams non-dimensional endpoint coordinate: elastic mechanical (dark blue), fringing field (side electrode) electrostatic restoring (orange) and the combined electrostatic and mechanical force (light blue). (d) 2D Finite Elements solution: electric potential around the beam (grounded) and side electrodes (unit voltage) in the yz plane, for two endpoint locations: on the left the beam is at the initial position and on the right the beam is at the middle of the side electrodes thickness. (e) The equilibrium non-dimensional endpoint coordinate as a function of the acceleration, for different values of the side electrode voltage V_S (numbers).

middle of the side electrodes thickness, with the restoring mechanical forces, may result in an equilibrium curve corresponding to the bistable behavior, Fig. 1(c).

The beam was described in the framework of the Euler-Bernoulli theory. The electrostatic forces incorporated into the RO Galerkin model were obtained by curve fitting of the results of the two-dimensional (2D) FE electrostatic analysis results, Fig. 1(d). In the framework of this approach the non-dimensional electrostatic force per unit length of the beam is given by the expression

$$\begin{aligned}\phi = a_2 - \arctan\left(a_3\left(\frac{w}{2d_s} - a_4\right)\right) + \arctan\left(a_5\left(\frac{w}{2d_s} - a_6\right)\right) \\ + \arctan\left(a_7\left(\frac{w}{2d_s} - a_8\right)\right) - \arctan\left(a_9\left(\frac{w}{2d_s} - a_{10}\right)\right)\end{aligned} \tag{1}$$

where $a_2 - a_{10}$ are non-dimensional constants and w is the displacement in the z axis. Since the fitting function (1) is written in a non-dimensional form, it is necessary to multiply it by a scaling factor a_1 in order to obtain the actual fit for the dimensional force per unit length of the beam.

Due to non-linear electrostatic coupling between the proof mass and the cantilever, the motion of the device is governed by two coupled equations associated with the dynamics of the cantilever and the proof mass. In the device under consideration, the side electrodes, which are the source of the fringing fields related electrostatic force acting on the cantilever, are attached to the movable proof mass. The clamped root of the cantilever is attached to an unmovable anchor. The deflection of the proof mass due to the inertial force results in disturbance of the fringing fields and modulation of the effective stiffness of the cantilever and its natural frequency. The geometric parameters of the cantilever and of the two fringing electrodes are shown in Figure 1(a). Because of the interest in the variation of the cantilever frequency as a result of the inertial force acting on the proof mass, a working point was calculated for multiple values

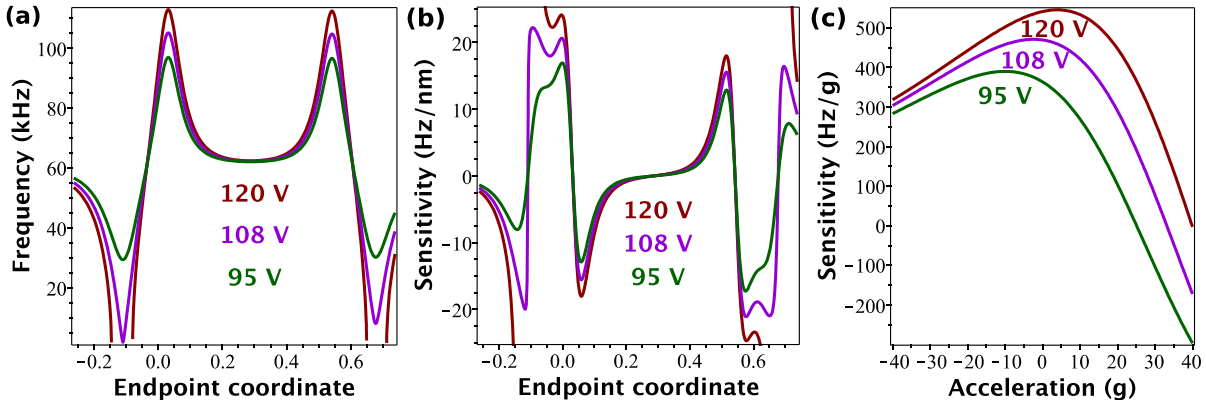

Figure 2: (a) The change in the cantilevers frequency, as a function of the non-dimensional coordinate of the endpoint of the beam, for different values of the side electrode voltage V_S (numbers). (b) The change in the cantilevers frequency with displacement, as a function of the non-dimensional coordinate of the endpoint of the beam, for different V_S (numbers). The curves corresponding to $V_S = 120$ V, reflect a bistable behavior, where instabilities are observed in two locations: between 0 and 0.1, and between 0.5 and 0.6. (c) Frequency sensitivity as a function of the acceleration, for different V_S (numbers).

of the acceleration, as suggested by Fig 1(e). Around this working point all relevant sensitivity values, regarding acceleration, were calculated.

3 Model Results

Calculations were carried out for $L = 150$ μm long, $h = 16$ μm wide and $d = 1$ μm thick beams assumed to be made from single crystal silicon with the Young's modulus $E = 169$ GPa. The side electrodes were $L_S = 37$ μm long and $d_S = 20$ μm thick. The bottom faces of the beam and of the side electrodes were coplanar and the lateral distance between the beam and each electrode was $g_S = 3$ μm. The proof mass used in these calculations was a 4 mm$\times 4$ mm square of the same thickness, $d_S = 20$ μm, as the side electrodes and made of the same device layer of the silicon on insulator (SOI) wafer.

The resonant frequency of the cantilever, as a function of its non-dimensional displacement (the displacement normalized by the side electrodes thickness, where zero displacement corresponds to the initial configuration of the beam) is shown in Fig. 2(a). Curves corresponding to $V_S = 108$ V and $V_S = 120$ V, Fig. 2(a), show typical behavior below and above the bistability threshold, respectively. Fig. 2(a) shows that for both cases the frequency at the working point (around zero displacement) is higher than the cantilevers mechanical (unactuated) resonance frequency. This is a very important and beneficial feature of the proposed configuration. Due to this feature, the increase in sensitivity does not sacrifice the bandwidth of the sensor, as in other reported devices, where electrostatic softening is usually exploited [3, 6].

Fig. 2(b) displays the dependence of the change of the frequency of the resonator as a function of the non-dimensional displacement, for differing values of V_S. Here the advantage of working near zero displacement is clearly observed. In the case of a non-bistable structure (purple and green curves) the highest sensitivity is obtained. Working in the vicinity of zero cantilever displacements is convenient, since it allows the use of a relatively simple fabrication process, as opposed to more complex devices [8]. In addition, this approach also solves issues regarding large displacements and pre-loading required in order to achieve bi-stability [6]. For V_S slightly below the bistability threshold, (purple line in Fig. 2) the equilibrium curve contains an inflection point where the slope of the curve can be tailored to be low and the effective stiffness and the natural frequency of the device are reduced. In the vicinity of the inflection point the sensitivity of the natural frequency to loading is significantly higher than in an undeformed cantilever. In addition, in contrast to the case where snap-through occurs (red lines in Fig. 2), a smooth continuous operation can be achieved. The main result concerning the use of the bistable cantilever-based sensing in an inertial accelerometer is presented in Fig. 2(c). This figure presents the

sensitivity of the device which includes the coupled cantilever and mass, in Hz/g units. This result is obtained by initially examining the mass displacement, and extracting the natural frequency from it.

$$w_m = \frac{a_{\max} M}{k_m} \rightarrow f_m = \frac{1}{2\pi}\sqrt{\frac{a_{\max}}{w_m}} \tag{2}$$

We set the maximal mass displacement as $w_m = 1$ μm thus obtaining for a maximal acceleration range of $a_{\max} = 392.4\,\mathrm{m}/s^2$ and a mass natural frequency of $f_m = 3150\,\mathrm{Hz}$. Note that in addition to the movement as a result of the acceleration, the mass moves also as a result of the voltage difference between the mass and the cantilever

$$w_m^{el} = 2h\frac{|a_1 V^2 \phi|}{k_m} \tag{3}$$

For the given configuration, with a voltage of $V = 108\,V$, and k_m as the proof mass supporting beams stiffness, the displacement is $w_m^{el} = 0.63$ nm which is negligible. We are planing to account for this electrostatic coupling correction at the further stages of the research.
After defining the mass' frequency we calculate the systems' sensitivity to acceleration

$$S_g = \left(\frac{a}{(2\pi f_m)^2}\right)\left.\frac{df}{dw}\right|_{w_p} \tag{4}$$

For the given system we use $a = 1$ g and the minimal frequency change for a given acceleration, at its work point. The relevant acceleration in this case is the maximal acceleration $a = 392.4\,\mathrm{m}/s^2$, where $df/dw \approx -1.2 \times 10^{10}$ Hz/m, from which we get a minimal sensitivity value of $S_g = 388$ Hz/g.

Turning our attention back to Fig. 2(c), one observes that the sensitivity increases with the voltage, and it is higher for higher acceleration. No visible differences in the character of the curves was observed, when comparing the cantilevers which don't exhibit snap-through (green and purple curves) and those which do (red curve). While relatively high sensitivity more than 500 Hz/g is observed, it varies with acceleration. This dependence can be eliminated by implementing close loop control of the proof mass position.

References

[1] G. Stemme. Resonant silicon sensors. *Journal of Micromechanics and Microengineering*, 1(2):113, 1991.

[2] Y. Wang, H. Ding, X. Le, W. Wang, and J. Xie. A mems piezoelectric in-plane resonant accelerometer based on aluminum nitride with two-stage microleverage mechanism. *Sensors and Actuators A: Physical*, 254:126–133, 2017.

[3] C. Comi, A. Corigliano, A. Ghisi, and S. Zerbini. A resonant micro accelerometer based on electrostatic stiffness variation. *Meccanica*, 48(8):1893–1900, 2013.

[4] N. Krakover, B.R. Ilic, and S. Krylov. Displacement sensing based on resonant frequency monitoring of electrostatically actuated curved micro beams. *Journal of Micromechanics and Microengineering*, 26(11):115006, 2016.

[5] J. Su, H. Yang, P. Fay, W. Porod, and G.H. Bernstein. A surface micromachined offset-drive method to extend the electrostatic travel range. *Journal of Micromechanics and Microengineering*, 20(1):015004, 2009.

[6] N. Krakover and S. Krylov. Bistable cantilevers actuated by fringing electrostatic fields. *Journal of Vibration and Acoustics*, 139(4):040908, 2017.

[7] A. Seleim, S. Towfighian, E. Delande, E. Abdel-Rahman, and G. Heppler. Dynamics of a close-loop controlled mems resonator. *Nonlinear Dynamics*, 69(1):615–633, 2012.

[8] M. Pallay, M. Daeichin, and S. Towfighian. Dynamic behavior of an electrostatic mems resonator with repulsive actuation. *Nonlinear Dynamics*, pages 1–14, 2017.

EUROMECH Colloquium 603
Dynamics of micro and nano systems
5 – 7 September 2018, Porto, Portugal

Pressure Drop Measurements in Microchannels: Influence of the Tap Design

Tomás R. Pinto and Laura Campo-Deaño

Centro de Estudos de Fenómenos de Transporte (CEFT), Departamento de Engenharia Mecânica,
Faculdade de Engenharia da Universidade do Porto, Rua Dr. Roberto Frias, 4200-465, Porto, Portugal
up201303703@fe.up.pt
campo@fe.up.pt

Summary. Microfluidics techniques have been recently used for the characterization of the complex flow dynamics around microbot prototypes to be used in biomedicine. For a complete fluid flow characterization, the determination of the pressure drop induced by the presence of these prototypes as they swim through the circulatory system is of key importance. The design of suitable microchannels able to mimic the main features of the circulatory system, including also pressure taps, constitutes a challenging task, due to the inherent difficulties in finding a proper configuration. The specific objective of this research is to study the influence of various shape parameters in the design of pressure taps, so that an optimal configuration is achieved.

Keywords: Microbots, microchannels, pressure taps, complex fluid flows.

1 Introduction

Microbots have come to be developed for, among other purposes, industrial applications and biomedicine [1, 2]. In the biomedicine field, once the technology matures, microbots will allow for precise and delicate minimally invasive procedures throughout the human body. As a matter of fact, the use of these microdevices as surgical tools will most certainly revolutionize areas such as cancer-fighting [3], drug delivery [4] and intraocular oxygen-sensing [5]. Moreover, several patient-oriented benefits are to be expected given the minimally invasive character of this surgical system. Some of the expected benefits are related to the reduction of recovery time, risk of infection and medical complications [6, 7].

In order to push the development of this concept forward, the dynamic efficiency and flow performance of microbots inside the human body are key topics that need to be fully understood. Therefore, the determination of the pressure drop originated by their presence in blood-vessels and other similar capillaries is a notoriously important matter that will undoubtedly add to this ongoing worldwide project that is microbots, contributing to its materialization in years to come.

Measuring pressure drops at microscale is not an easy task though, and several problems have been reported, mainly associated with tap design issues. Problems such as air bubbles trapped in the sub-channels leading to the taps are very common and have a negative impact on the accuracy of the readings, affecting the sensitivity of the overall measuring process and distorting the measurement itself. Surface tension issues have also been reported. They distort the reading in excess, by adding a residual pressure, associated with the surface tension phenomena, to the intended pressure drop that is being measured. Problems like these are closely related to poorly designed, long and narrow sub-channels, that promote such undesired effects.

This study aims to eradicate such difficulties when measuring pressure drops in microchannels, by developing guidelines on correct pressure tap design and proposing an optimal tap configuration for precise and problem-free readings.

2 Pressure measurement within microfluidic devices

Besides commercially available external pressure transducers, the most straightforward means of obtaining pressure data with little to no design modifications, several other methods for determining pressure drops in microchannels have been reported, differing from each other in measuring technique.

For instance, the base material from which the microchannels are made, thanks to its inherent properties, might allow for specific pressure measuring methods. This is the case of silicon based microchan-

nels, a rather decaying solution for microdevice fabrication thanks to the much practical and cheaper PDMS alternative. Several research groups [8, 9] have been using silicon based microchannels, since these can be routinely etched, allowing for several sensing elements to be incorporated. But as mentioned before, even though silicon is a good alternative from which to fabricate precise microfluidic devices, it has its drawbacks. It comes at a high cost, the whole fabrication process is time consuming and has some intricate steps along the way, and the fact that it is an opaque material, not allowing for the straightforward visualization of the devices, doesn't come in handy either.

As an alternative, microchannels made of polydimethylsiloxane (PDMS) are commonly used. They come at a lower cost and their fabrication process is less time consuming, while keeping the same step structure and technology requirements. Moreover, PDMS is optically transparent, which is good for quick first look impressions. When it comes to pressure sensing with PDMS, several research groups [10, 11] have used its elastic nature to their advantage, relating the deflection of the walls to the channel's pressure by means of imaging tools such as microscopes. However, this method and others alike often require additional fabrication steps in order to incorporate extra channel layers onto the main PDMS flow channels, fluorescent particles, or even to introduce separate probing fluids.

In the present study, the most practical solution for pressure drop measuring will be used, external pressure transducers. This is the best way to measure pressure drops in PDMS microchannels without the hassle of having to do major design modifications [12]. In addition to only requiring an external sensor and no design or extra microfluidic device incorporation requirements, pressure transducers can easily be coupled with a data acquisition card, allowing for real-time dynamic measurements.

3 Device design and fabrication

In this study, microchannels were fabricated in close resemblance to the blood-vessels that comprise the vast capillary network that is the human circulatory system. In this system one can find a wide range of flow conditions, deeply related to the proximity of the heart. The further away from the heart, the more variations the blood flow will present. The flow can range from larger vessels with a 2-3 mm characteristic diameter, where Re ~ 3000 having a strong pulsating component, to the smallest capillaries with a 20-30 μm characteristic diameter, where Re ≤ 1 and the flow is almost constant [13]. Taking into consideration that the smaller the vessel, the greater the non-Newtonian properties of the blood flow are, this work focuses on the medium to small scale (diameter < 1 mm) conduits of the human body.

Straight rectangular microchannels, with 270 μm across and 100 μm in depth, were designed, each one with a 2D microbot prototype in the center of the channel. The microchannels are all 10 mm long and the prototypes are located ~ 2.9 mm away from the inlet, in order to avoid any entry effects and ensure that enough space is left for the flow to fully develop again, downstream from the microbot, hence avoiding exit effects also. Two different prototypes were considered: a circular one and an elliptical one, with an aspect ratio of 1:4. Also, reference microchannels with no prototype inside were conceived for validation purposes.

In order to assess the pressure drop originated by the presence of the microbots, a couple of pressure taps, placed up and downstream and equally distant from their centroid, leading from the main flow channel were added. These taps provide the fluidic connection to the external pressure transducer, via the transducer ports inserted in them. The fluid flows through the main channel, via inlet and outlet ports.

Table 1. Shape parameters and respectively assigned values

	w (μm)	R (μm)	α ($^\circ$)
1	54	50	15
2	108	250	45
3	162	500	75

Aiming for the determination of the optimal tap design, a parametric study was conducted. In that sense, three variables were considered in the design of these taps and the secondary sub-channels con-

necting them to the main flow channel (Table 1): width of the sub-channel (w), radius of curvature between the sub-channel and the tap (R) and angle between the sub-channel and the tap (α).

Up to 18 different combinations can be arranged with these shape parameters. Which leads to a total of 54 microchannels, considering the two microbot shapes tested (squared and elliptical), as well as the reference channels. Figure 1 shows a microchannel with some of the pressure tap configurations possible.

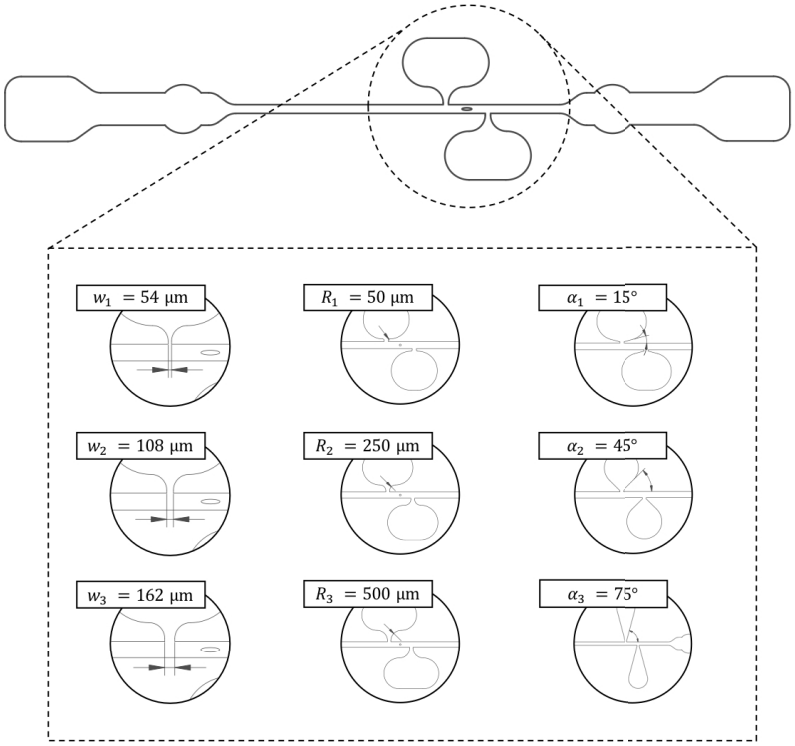

Figure 1. CAD designs for different pressure tap configurations.

PDMS microchannels were made using soft lithography techniques [14], and afterwards, bonded to glass microscope slides, that had been previously PDMS spin coated. Two different methods were used for the fabrication of the microchannel molds: on one hand, silicon substrate SU-8 coated master molds using photolithography; and, on the other hand, 3D printed molds were fabricated, in order to assess the degree of resolution of this technology and whether it can be used as an alternative for SU-8 molds. Two distinct 3D printing methods were used, both laser-based: stereolithography (SLA) and digital light processing (DLP).

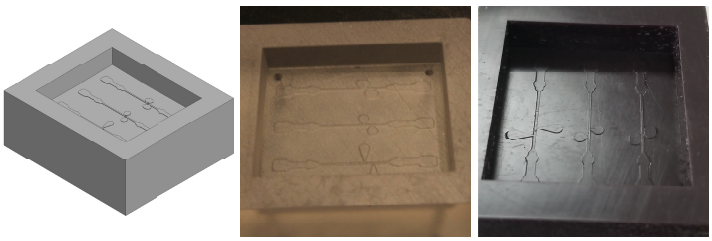

Figure 2. From left to right, the 3D CAD model and resulting 3D printed SLA and DLP molds.

The stereolithography printer's (Formlabs® Form 2) X:Y resolution is set at 150 μm (it has a laser spot size of 140 μm), while the digital light processing one (Creative CADworks® MiiCraft μMicrofluidics Edition) is capable of producing pieces with an X:Y resolution of up to 30 μm, making it more adequate for intricately detailed pieces (Figure 2).

4 Pressure drop measurements

Two blood analogues were used as working fluids, a Newtonian one and a non-Newtonian one. They are considered blood analogues in the sense that they are able to reproduce the viscosity curve and the elastic character of the whole human blood as a bulk [1, 15], making them adequate for this work.

Before carrying out any pressure measurements, the external transducers were calibrated. The calibration curves obtained were later used to relate the transducers's measured voltage output at a specific flow rate to a differential pressure drop measurement.

Once the transducers were calibrated, the tests were conducted and the pressure readings plotted in relation to flow rate. The experimental data gathered from the reference plain microchannels, which have no microbot prototype inside, was compared to pressure drop-flow rate curves obtained analytically for rigid walls rectangular cross section microchannels.

5 Final remarks

An optimal configuration for the shape of pressure taps in microchannels was achieved and several guidelines on how to correctly design them were developed. More experimental work is still needed for a complete characterization of the pressure drop obtained with the different configurations. Nevertheless, it is possible to conclude that 3D printing technology does not yet have the resolution required for the level of detail most microfluidic devices demand. Instead, it can be seen as a simple and fast way of materializing and prototyping microdevices before a final manufacturing. The overall surface roughness of the SLA molds looked smooth, but a closer look under the microscope revealed a much different reality. The layer interface inherent to the layer deposition process, characteristic of the fabrication technique and barely distinguishable at first, provoked a clear distortion of the microchannels. Regarding the DLP molds, the level of detail achieved was clearly higher when placed side by side with the SLA ones.

Acknowledgments

Authors acknowledge Dr. F. J. Galindo-Rosales for invaluable guidance in the experimental techniques.

References

[1] S. Martínez-Aranda, F. J. Galindo-Rosales, L. Campo-Deaño, Complex flow dynamics around 3D microbot prototypes. *Soft Matter*, **12**, 2334-2347, 2016.

[2] B. J. Nelson, I. K. Kaliakatsos, J. J. Abbott, Microrobots for minimally invasive medicine. *Annu. Rev. Biomed. Eng.*, **12**, 55-85, 2010.

[3] S. Martel, Magnetic Microbots to Fight Cancer, http://spectrum.ieee.org/robotics/medical-robots/magnetic-microbots-to-fight-cancer.

[4] W. Zhu, J. Li, Y. J. Leong, I. Rozen, X. Qu, R. Dong, Z. Wu, W. Gao, P. H. Chung, J. Wang, S. Chen, 3D-printed artificial microfish. *Adv. Mater.*, **27**, 4411-4417, 2015.

[5] O. Ergeneman, G. Chatzipirpiridis, J. Pokki, M. Marín-Suárez, G. A. Sotiriou, S. Medina-Rodríguez, J. F. Sánchez, A. Fernández-Gutiérrez, S. Pané, B. J. Nelson, In vitro oxygen sensing using intraocular microrobots. *IEEE Trans. Biomed. Eng.*, **59**, 3104-3109, 2012.

[6] M. J. Mack, Minimally invasive and robotic surgery. *J. Am. Med. Assoc.*, **285**, 568-572, 2001.

[7] M. C. Carrozza, P. Dario, L. P. S. Jay, Micromechatronics in surgery. *Trans. Inst. Meas. Control*, **25**, 309-327, 2003.

[8] M. Kohl, S. Abdelkhalik, S. Jeter, D. Sadowsk, A microfluidic experimental platform with internal pressure measurements. *Sens. Actuators, A*, **118**, 212-221, 2005.

[9] D. A. Ateya, A. A. Shah, S. Z. Hua, Impedance-based response of an electrolytic gas bubble to pressure in microfluidic channels. *Ses. Actuators, A*, **122**, 235-241, 2005.

[10] C. Y. Wu, W. H. Liao, Y. C. Tung, Integrated ionic liquid-based electrofluidic circuits for pressure sensing within polydimethylsiloxane microfluidic systems. *Lab Chip*, **11**, 1740-1746, 2011.

[11] K. Hosokawa, K. Hanada, R. Maeda, A polydimethylsiloxane (PDMS) deformable diffraction grating for monitoring of local pressure in microfluidic devices. *J. Micromech. Microeng.*, **12**, 1-6, 2002.

[12] P. Cheung, K. Toda-Peters, A. Q. Shen, In situ pressure measurement within deformable rectangular polydimethylsiloxane microfluidic devices. *Biomicrofluidics*, **6**, 026501, 2012.

[13] S. A. Berger, W. Goldsmith, E. R. Lewis, *Introduction to Bioengineering*, Oxford Univ. Press, Oxford, UK, 1996.

[14] Y. Xia, G. M. Whitesides, Soft Lithography. *Annu. Rev. Mater. Sci.*, **28**, 153-184, 1998.

[15] L. Campo-Deaño, M. S. N. Oliveira, F. T. Pinho, A review of computational hemodynamics in middle cerebral aneurysms and rheological models for blood flow. *Appl. Mech. Rev.*, **67**, 030801, 2015.

EUROMECH Colloquium 603
Dynamics of micro and nano systems
5 – 7 September 2018, Porto, Portugal

Electrostatic Arch Micro-Tweezers

Ayman M. Alneamy[1,2], Mahmoud E. Khater[3], Ahmed K. Abdel Aziz[4], Glenn R. Heppler[1] and Eihab M. Abdel-Rahman[1]

[1]Systems Design Engineering, University of Waterloo, Waterloo, On, Canada
[2]Department of Mechanical Engineering, Jazan University, Jazan, Saudi Arabia
[3]Mechanical Engineering Department, KFUPM, Dahran, Saudi Arabia
[4]Electrical and Computer Engineering, University of Waterloo, Waterloo, On, Canada

Summary. This paper reports on a novel micro-tweezers that can manipulate particles with diameters less than $14\,\mu$m. The tweezers are compact (largest dimension < 1 mm). It can manipulate a significant range of object diameters $[5-13]\,\mu$m with a maximum actuation voltage of 135 V. The tweezer arms are mounted to an electrostatically actuated initially curved micro-beam. It exploits the snap-through and pull-in instabilities to close the gap between the two rigid arms. This mechanism offers further controllability via electrostatic actuation, beyond the snap-through point, and allows for increasing pressure on an object or grasping of smaller objects. The tweezers were fabricated using a two-mask SOI process. During characterization, we observed a chaotic attractor in the vicinity of the tweezers' fundamental natural frequency that can be used for object release and cell lysis.

Keywords: Arch, Snap-through, Tweezers, Electrostatic.

1 Introduction

Micro-tweezers are important tools for micromanipulation and microassembly of tiny objects, such as biological cells, DNA strands, micro-particles, etc. Different actuation methods have been deployed to drive micro-tweezers including electromagnetic, piezoelectric, shape memory alloys (SMAs), optical, electrothermal and electrostatic actuation. Among these methods, electrostatic tweezers are attractive because of low power consumption and low temperature.

Tweezers have been designed using both parallel-plate and comb-finger electrostatic actuators. Beyeler *et al.* [1] designed a micro-tweezers driven by comb-finger actuators integrated with a capacitive force sensor to control the grip force. Their translational grippers achieved a stroke of $100\,\mu$m at 150 V. Xu [2] designed a similar micro-tweezers with a rotational grip mechanism allowing him to reduce voltage requirements to 72 V over a stroke of $63\,\mu$m. Varona *et al.* [3] used a parallel-plate actuator to reduce the micro-tweezers size. However, it escalated voltage requirement to the point where the needed 45 V to close a gap of $2\,\mu$m. In this paper, we present a novel compact electrostatic micro-tweezers that uses the snap-through instability to reduce actuation voltage requirements.

2 Micro-tweezers Design and Model

The micro-tweezers consist of an initially curved beam with two rigid arms mounted to it and a side-wall electrode for electrostatic actuation, Fig. 1(a). The beam has a length of l_b=1000 µm, a width of b=30 µm, a thickness of h_b=3 µm and an initial elevation of $h_\circ$=3.5 µm. The arms have a length of l_a=250 µm and thickness of h_a=4 µm. The nominal capacitive gap between the electrode and x-axis is d=11 µm, and the initial distance between grip arms is $14\,\mu$m. The device was fabricated using a p-type Silicon on Insulator (SOI) wafer. SEM pictures of the fabricated device are shown in Fig.1(b) and (c).

The initial beam curvature, Fig. 2, was designed according to the following expression:

$$\hat{w}_\circ(\hat{x}) = \frac{h_\circ}{2}[1 - \cos(\frac{2\pi\hat{x}}{l_b})]$$

where $\hat{x}$ is the position along the axis extending between the centroids of the beam sections at the anchors and $\hat{w}_\circ(\hat{x})$ is the distance between the beam's neutral axis and the x-axis. As a first-order approximation, we assume that the grip arms are rigid and that their effect on the beam response is negligible. The

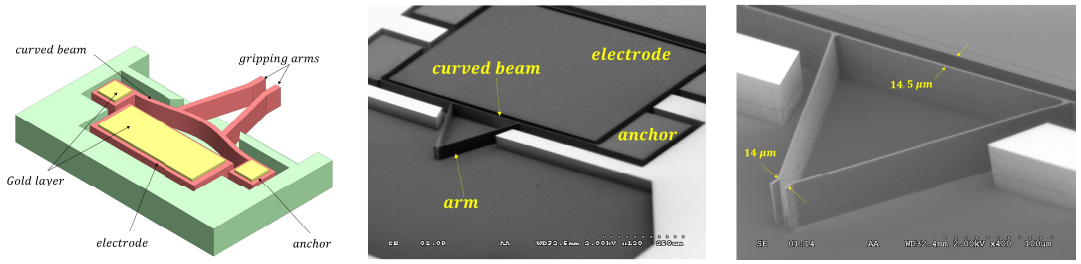

(a) (b) (c)

Figure 1: (a). A 3D drawing schematic of the micro-tweezers. SEM pictures of (b) the fabricated device and (c) a close-up on the grip arms.

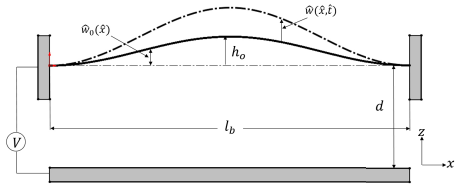

Figure 2: A schematic diagram of an electrostatically actuated curved beam.

equation of motion governing the micro-beam transverse deflection $\hat{w}$ under a distributed electrostatic load was formulated following Euler-Bernoulli beam theory as [4, 5]:

$$EI\frac{\partial^4\hat{w}}{\partial\hat{x}^4}+\rho A\frac{\partial^2\hat{w}}{\partial\hat{t}^2}+\hat{c}\frac{\partial\hat{w}}{\partial\hat{t}}=\Big(\frac{d^2\hat{w}_\circ}{d\hat{x}^2}+\frac{\partial^2\hat{w}}{\partial\hat{x}^2}\Big)\frac{EA}{2l_b}\int_0^{l_b}\Big(\big(\frac{\partial\hat{w}}{\partial\hat{x}}\big)^2+2\frac{\partial\hat{w}}{\partial\hat{x}}\frac{d\hat{w}_\circ}{d\hat{x}}\Big)d\hat{x} - \frac{\varepsilon\, b\, V(t)^2}{2(d+\hat{w}_\circ+\hat{w})^2} \tag{1}$$

To solve Eq. (1), a reduced order model (ROM) based on a Galerkin approximation was utilized to discretize the equation of motion in terms of a finite number of degrees-of-freedom describing the amplitude of the mode shapes. For simplicity, we chose to utilize the mode shapes of a straight beam instead of curved beam.

3 Static Analysis

We non-dimensionalize and eliminate the time-varying terms in Eq. (1) to obtain an equilibrium equation describing the non-dimensional static deflection $w_s(x)$ of the curved beam under a static load V_{dc}:

$$\frac{\partial^4 w_s}{\partial x^4}=\alpha_1\Big(\frac{d^2w_\circ}{dx^2}+\frac{\partial^2 w_s}{\partial x^2}\Big)\int_0^1\Big[\big(\frac{\partial w_s}{\partial x}\big)^2+2\frac{dw_\circ}{dx}\frac{\partial w_s}{\partial x}\Big]dx-\alpha_2\frac{V_{dc}^2}{2(1+w_\circ+w)^2} \tag{2}$$

where $w_s(x)$ is the deflection of the neutral axis measured from its initially curved configuration $w_\circ(x)$ and α_1 and α_2 are non-dimensional parameters. Convergence analysis showed that five symmetric modes were required in the Galerkin expansion of $w_s(x)$ in order for the solution to converge.

Figure 3(a) shows the static displacement of the beam mid-point $w_s(0.5)$. A snap-through bifurcation occurs as voltage increases and reaches V_s=108 V. It leads to a jump-up from a lower stable branch of solutions, corresponding to the initial beam curvature, to an upper stable branch of solutions, corresponding to the counter beam curvature. Decreasing voltage after snap-through causes a snap-back bifurcation at V_s=90 V leading to a jump-down from the upper stable branch to the lower stable branch. An intermediate branch of unstable solutions connects the two branches of stable equilibria. The traditional pull-in bifurcation occurs at a voltage of V_p=135 V. The bifurcation point represents the end of the upper stable branch where it meets an upper branch of unstable solutions. No stable equilibria exist beyond the pull-in point. The jump-up caused by snap-through is used to close the gap between the two grip arms.

The accuracy of the five-modes ROM is validated by comparing its static displacement results (lines in Fig. 3(a)) to those obtained from a FEM model including the arms (dotes in Fig. 3(a)). The figure shows no discernible difference between the two approaches, thereby confirming that the arms' contribution to

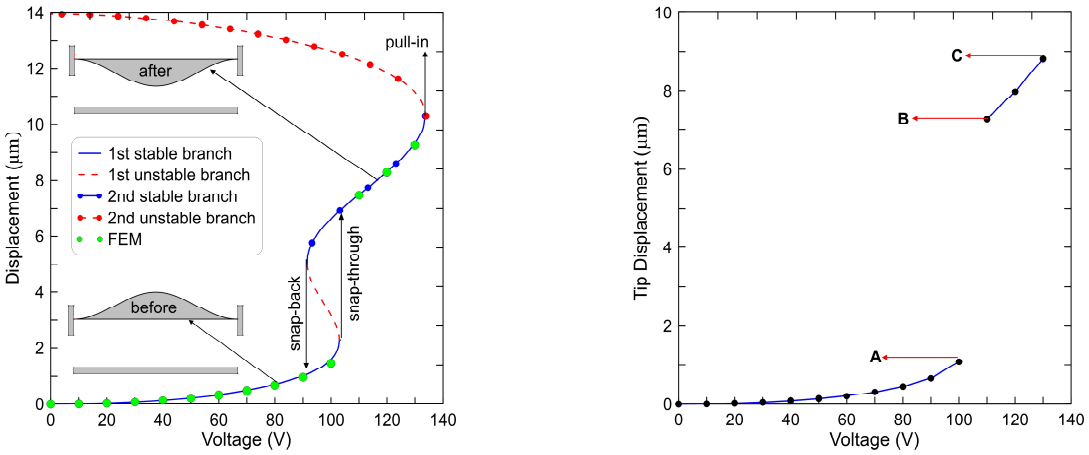

(a) Mid-point displacement (b) Arms' tip displacement

Figure 3: (a) The static displacement of the beam mid-point obtained analytically (solid lines) and numerically (dots) and (b) the displacement of the of the gripper tips obtained from an FEM model as functions of dc voltage.

static response is negligible. The FEM model was also used to calculate the arms' tip displacement as a function of dc voltage. Figure 3(b) shows a discontinuity in the object sizes that can be handled by the tweezers. Before snap-through, point A, the tweezers are able to pick particles with a minimum diameter of $11.5\,\mu$m. After snap-through, at point B, the object diameter is $7.2\,\mu$m, while the minimum diameter on that branch is $5\,\mu$m at point C (pull-in).

4 Dynamic Analysis

The dynamic response of the curved beam can be used as a release mechanism or to break (lysis) cell walls. The fundamental natural frequency of the curved beam was found experimentally by applying a pulse train to the beam with an amplitude of 22.5 V, a frequency of f=1 kHz and a duty cycle of 0.8%. It was found to be f_n=30.5 kHz as shown in the FFT of the measured mid-point velocity, Fig. 4(a). The

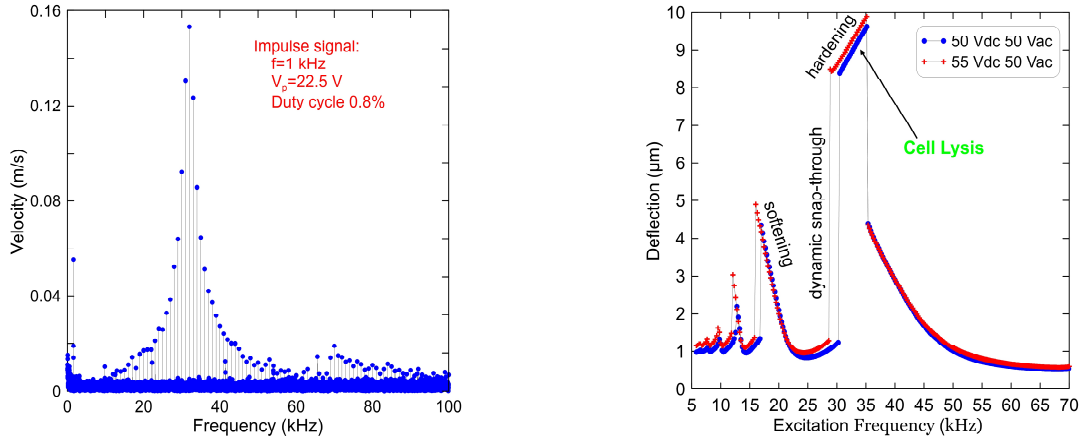

(a) FFT of the measured velocity (b) Frequency-response curves

Figure 4: (a) The FFT of the measured mid-point velocity under a pulse train and (b) ROM predicted frequency-response curves.

frequency-response curves of the mid-point displacement were numerically obtained by integrating the ROM for 500 excitation periods. The RMS of the mid-point displacement $w(0.5)$ was then evaluated over the last 200 excitation periods to observe the steady-state response. The frequency of excitation was swept up in the range of [5–70] kHz at two excitation levels, V_{dc}=V_{ac}=50 V, and V_{dc}=55 V and

V_{ac}=50 V. A train of super-harmonic resonances of orders two, three and four and a dynamic snap-through within a small frequency band of [28–38] kHz in the vicinity of primary resonance were observed. The effective nonlinearity is softening as indicated by the response in Fig. 4(b).

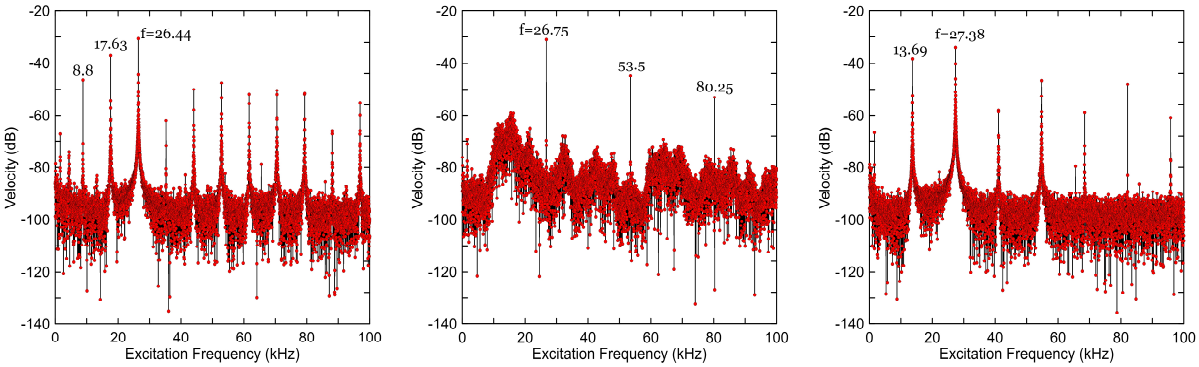

(a) f=26.44 kHz (b) f=26.75 kHz (c) f=27.38 kHz

Figure 5: FFTs of the mid-point velocity under an excitation signal of V_{dc}=30 V and V_{ac}=15 V.

The curved beam dynamic response was measured experimentally under the waveform of V_{dc}=30 V and V_{ac}=15 V at three different excitation frequencies. The FFTs of the mid-point velocity $\dot{w}(0.5)$ was measured in dB scale (0dB=1 m/s). The FFT at an excitation frequency of f=26.44 kHz, Fig. 5(a), shows peaks at f, $\frac{2}{3}f$, and $\frac{1}{3}f$ which indicates a period-three (P-3) orbit. Increasing the excitation frequency to f=26.75 kHz, a chaotic attractor was observed indicated by an elevated noise floor in Fig. 5(b). A period-two (P-2) orbit was observed at an excitation frequency of f=27.38 kHz, Fig. 5(c), suggesting that the chaotic attractor shown in Fig. 5(b) results from a cascade of period-doubling bifurcations and that the P-3 orbit shown in Fig. 5(a) is a periodic window within the chaotic attractor.

5 Conclusion

We presented a novel electrostatic MEMS micro-tweezers that consists of two rigid arms mounted to an initially curved beam. The tweezers can pick objects with diameters less than 14 µm. The grip mechanism uses the bistability of an initially curved beam to close the distance between the rigid arms. Target particles may be hard, such as uniform polystyrene beads, or soft, such as biological cells in aqueous media. A reduced-order model was developed to demonstrate the fundamental tweezers mechanism in the absence of the rigid arms. The micro-tweezers were fabricated using an SOI process. We found experimentally interesting dynamic phenomena in the vicinity of the fundamental natural frequency that can be used for object release and cell lysis.

6 Acknowledgment

The first author would like to acknowledge the financial support of Jazan University, Saudi Arabia.

References

[1] F Beyeler, A Neild, S Oberti, D J Bell, Y Sun, J Dual, and B J Nelson. Monolithically fabricated microgripper with integrated force sensor for manipulating microobjects and biological cells aligned in an ultrasonic field. *Journal of microelectromechanical systems*, **16**(1):7–15, 2007.

[2] Q Xu. Design, fabrication, and testing of an mems microgripper with dual-axis force sensor. *IEEE Sensors Journal*, **15**(10):6017–6026, 2015.

[3] J Varona, E Saenz, S Fiscal-Woodhouse, and AA Hamoui. Design and fabrication of a novel microgripper based on electrostatic actuation. In *Circuits and Systems, 2009. MWSCAS'09. 52nd IEEE International Midwest Symposium on*, pages 827–832. IEEE, 2009.

[4] A Hasan Nayfeh. *Nonlinear interactions: analytical, computational and experimental methods*. Wiley, 2000.

[5] S Krylov, B R Ilic, D Schreiber, S Seretensky, and H Craighead. The pull-in behavior of electrostatically actuated bistable microstructures. *Journal of Micromechanics and Microengineering*, **18**(5):055026, 2008.

EUROMECH Colloquium 603
Dynamics of micro and nano systems
5 – 7 September 2018, Porto, Portugal

Dynamic behaviour of two cantilevers partially immersed in glycerol

N. Wagner[1], **S. Gutschmidt**[2], **and T. Sattel**[1]

[1]Technische Universität Ilmenau, Ilmenau, Germany
niclas.wagner@tu-ilmenau.de
thomas.sattel@tu-ilmenau.de

[2] University of Canterbury, Christchurch, New Zealand
stefanie.gutschmidt@canterbury.ac.nz

Summary. The following work comprises of an experimental study on the dynamics of two beams partially immersed in glycerol. The cantilevers are mechanically decoupled and investigations emphasize on the fluid-coupling between the beams for varying parameters such as gap size between cantilevers, the distance to the wall and the actuation amplitude. One beam is actuated while the other is kept passive. There are two different cases investigated, far from as well as close to a rigid wall. The purpose of this work is to observe and understand fundamental fluid-related phenomena between mechanical resonators which dominate the overall dynamic behaviour of a small-size mechanical array. The outcomes of this initial investigation will benefit our ongoing work on the development of Atomic Force Microscopy Array technology for living biological samples, where not-well understood fluid-interactions currently generate undesired artifacts. One of our main findings from this experimental work is the identification of critical parameter ranges for gaps and wall distances for which the fluid coupling determines the dynamics of the otherwise decoupled mechanical system. In our presentation we will elaborate on the origin and underlying physics of observed variations of frequencies and amplitudes.

Keywords: Experimental fluid coupling, immersed resonators, coupled cantilevers.

1 Introduction

The Atomic Force Microscope (AFM) was initially invented to visualize the topology of rigid, sub-atomic objects by measuring force interactions. Today, AFM has found a wide range of applications [1–4] and is a promising technology to investigate soft, living biological samples in the near future. Current scan rate limitations of the technology can be overcome by introducing an AFM-array concept (see Fig. 1) [5–7]. While the desired design suggests rather small gaps between resonators to achieve

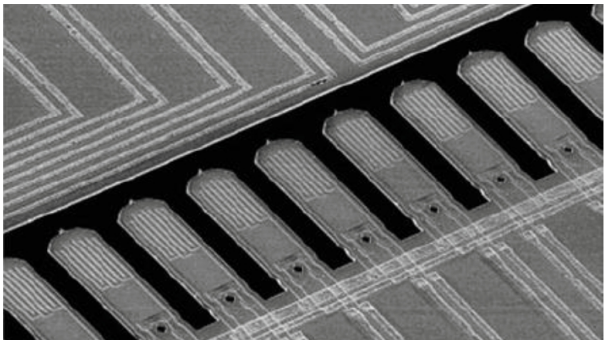

Figure 1. Self-actuated and self-sensing PRONANO AFM array [**?**]

a high throughput, observed coupling phenomena such as mechanical, electrical, thermal and fluidic, generate artifacts in the image formation which can be tracked back to the underlying dynamics of the system, especially for soft samples in a fluidic environment. To date, samples in fluid are imaged using the single resonator AFM contact mode [1, 2], which is impractical to be used for imaging biological processes and/or soft biological samples.

Recent research investigations have focused on a single cantilever in fluid, analytically [8, 9] and experimentally [10, 11]. An equivalent array configuration has not been investigated yet. This work

investigates two cantilevers immersed in glycerol with focus on underlying fluid-related coupling phenomena that dominate the overall dynamics of small array. The reasons for considering a macro-scale rather than a micro-scale test-rig are time, cost and complexity related. Equivalent macro-scale test setups have been proven useful in the past for studying micro-scale systems phenomenologically [12, 13], whose research approach we are following here to investigate the fluid-coupling effects between two mechanical resonators.

2 Experimental Investigations: Set-up & Analysis

Experiments are conducted with the macro-scale test-rig as depicted in Fig. 2. The test-rig consists of an aluminium bridge from which the cantilevers hang down, partially immersed into the basin of glycerol. The aluminium cantilevers (with dimensions $160\mathrm{mm} \times 40\mathrm{mm} \times 1.5\mathrm{mm}$) are mechanically decoupled by an especially designed clamp mechanism (not shown) [14]. Each cantilever can be actuated by an piezo-electric film actuator which is glued to one side of the beam. Four strain gauges, mounted in a full Wheatstone bridge configuration, measure the beam's deflection. The sample surface is mimicked by a plane, rigid aluminium plate attached to stepper motors which can be used to adjust distances, even individually (not done in this work). The test-rig is operated by NI modules and controlled by an embedded FPGA controller. LabVIEW is used as operating software [14, 15].

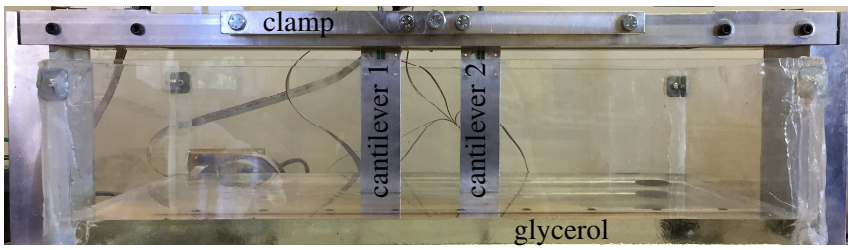

Figure 2. Macro-scale array test-rig [14]; two beams partially immersed in glycerol; length scale: beam width is 40 mm.

The resonance frequencies of each cantilever as well as the two-cantilever system are determined applying harmonic sweeps (up and down). In the case far from the wall and with large gaps between the cantilevers the resonance frequencies are about $f_{res} \approx 30$ Hz (cantilever 2 having a slightly higher frequency). To investigate the fluid-related coupling effects, cantilever 1 (active cantilever) is actuated at three different amplitudes and near its resonance frequency while cantilever 2 is kept passive. The experiment is repeated for several gaps ($2 - 15$ mm) far ($36 - 100$ mm) and close ($1 - 36$ mm) to the wall. The excitation frequency of the active cantilever is set according to the natural frequency which is decreasing with decreasing distances from the wall.

2.1 Analysis Far from the Wall

Figure 3 shows the ratio of displacement of the passive to the actuated cantilever over the gap size. It is observable that the most significant interaction occurs between a gap size of 1 mm and 20 mm. For gaps bigger than 20 mm the interaction is less than 1% and hence negligible. The effect stays the same for different actuation amplitudes. As expected the influence of the fluid-coupling increases the closer the two cantilevers are assembled together, eventually acting as one cantilever with double width.

2.2 Analysis Close to the Wall

Figure 4 shows the experimental results of the active cantilever and the amplitude ratio between active and passive cantilevers for a selected range of gaps and distances to the rigid wall. While the amplitudes of the active cantilever are constant over most of the gap range they decrease for smaller gap sizes (see left panel of Fig. 4). The right panel of Fig. 4 shows the amplitude ratio for selected gap and distance ranges. It is observed that for a normalised (with respect to the beam width) gap larger than 0.25 (10 mm) the behaviour does not vary much and shows a linear decrease (namely $7 - 1$ %) with increasing

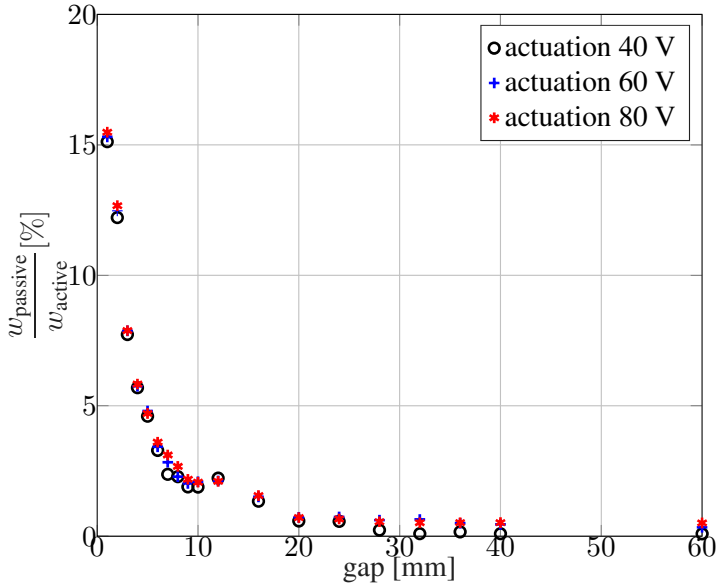

Figure 3. Amplitude ratios of active cantilever 1 to passive cantilever 2 for various gaps.

distance. However, different observations are made for gap sizes below 0.25 (10 mm), showing a small peak of 8.86 % at gap of 0.125 (5 mm) for the smallest distance from the wall of 2 mm. Furthermore, we observe a dip of the amplitude ratio (to 0.24 %) at a gap of 0.025 (1 mm) and 4 mm distance to the wall.

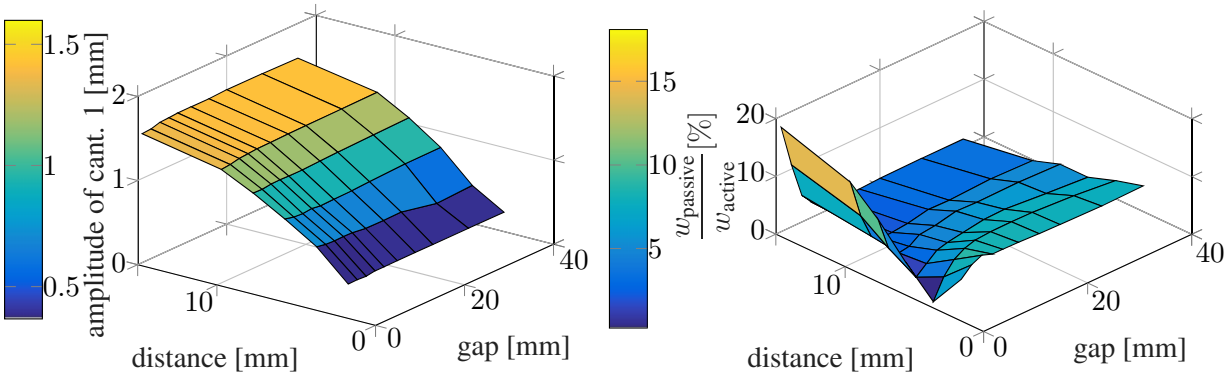

Figure 4. [Left panel] Amplitude of active cantilever 1 and [Right panel] amplitude ratio between passive and active cantilevers for varying gaps and distances.

3 Conclusions

Experimental results suggest that there are distinct parameter domains, even for very closely assembled resonators and wall distances, at which the two-beam array decouples i.e. the overall dynamics of the system are not influenced by fluid effects. There are also other parameter domains where fluid effects are significantly contributing to the dynamic behaviour of the system and thus cannot be neglected. Identified maxima and cancellation of fluid-coupling effects are observed for gap sizes smaller than half the width of the beam. Furthermore, the results show a clear coupling of the parameters 'gap' and 'distance', which means that they cannot be investigated separately.

Our conference presentation will also include an analysis of the beam system in air. We will compare and discuss these results against existing literature and our own theoretical findings.

Acknowledgments

The research work was conducted under the framework of an ongoing exchange program between the University of Canterbury, Christchurch, New Zealand and the Technische Universität Ilmenau, Germany. The first author would like to thank both supervisors and departments for having had this unique opportunity to be part of this collaboration for this project.

References

[1] T. Ando, T. Uchihashi, and T. Fukuma. High-speed atomic force microscopy for nano-visualization of dynamic biomolecular processes. *Progress in Surface Science*, 83(7):337 – 437, 2008.

[2] T. Ando. High-speed atomic force microscopy coming of age. *Nanotechnology*, 23(6), 2012.

[3] D. Y. Abramovitch, S. B. Andersson, L. Y. Pao, and G. Schitter. A tutorial on the mechanisms, dynamics, and control of atomic force microscopes. In *Proceedings of the 2007 American Control Conference*, pages 3488–3502, July 2007.

[4] T. Ando, T. Uchihashi, and N. Kodera. High-speed afm and applications to biomolecular systems. *Annuual Review Biophysics*, 42(1):393–414, 2013.

[5] A. Ahmad, N. Nikolov, T. Angelov, T. Ivanov, A. Reum, I. Atanasov, E. Guliyev, V. Ishchuk, M. Kaestner, Y. Krivoshapkina, S. Lenk, C. Lenk, I.W. Rangelow, and M. Holz. Large area fast-afm scanning with active quattro cantilever arrays; large area fast-afm scanning with active quattro cantilever arrays. *Journal of Vacuum Science and Technology B: Microelectronics and Nanometer Structures*, 34(26):6–3, 2016.

[6] T. Angelov, A. Ahmad, E. Guliyev, A. Reum, I. Atanasov, T. Ivanov, V. Ishchuk, M. Kaestner, Y. Krivoshapkina, S. Lenk, C. Lenk, I.W. Rangelow, M. Holz, and N. Nikolov. Six-axis afm in sem with self-sensing and self-transduced cantilever for high speed analysis and nanolithography. *Journal of Vacuum Science and Technology B: Microelectronics and Nanometer Structures*, 34(10):6–1, 2016.

[7] T. Michels and I.W. Rangelow. Review of scanning probe micromachining and its applications within nanoscience. *Microelectronic Engineering*, 126:191–203, 2014.

[8] W. Abassi, A.E Baroudi, and F. Razafimahery. Vibration analysis of euler-bernoulli beams partially immersed in a viscous fluid. *Physics Research International*, ID 6761372:1–14, 2016.

[9] M. Bardosova and T. Wagner. *Nanomaterials and nanoarchitectures: A complex review of current hot topics and their applications*. Springer Science + Business Media Dordrecht, 2015.

[10] E. Grimaldi, M. Porfiri, and L. Soria. Finite amplitude vibrations of a sharp-edged beam immersed in a viscous fluid near a solid surface. *Journal of Applied Physics*, 112(10):104907, 2012.

[11] C.M. Harwood, A.J. Stankovich, Y.L. Young, S.L. Ceccio, S.Y. Mpo, and R.O. Tatin. Combined experimental and numerical study of the free vibration of surface-piercing struts. In *16th International Symposium on Transport Phenomena and Dynamics of Rotating Machinery, ISROMAC 2016*, April 2016.

[12] M.J. Kim, M.J. Kim, J.C. Bird, J. Park, T.R. Powers, and K.S. Breuer. Particle image velocimetry experiments on a macro-scale model for bacterial flagellar bundling. *Experimental Fluids*, 37(6):782–788, 2004.

[13] I. Chakraborty and B. Balachandran. Noise influenced elastic cantilever dynamics with nonlinear tip interaction forces. *Nonlinear Dynamics*, 66(3):427–439, 2011.

[14] M.P.T. Raeder. *Design, analysis and fabrication of a test-rig to investigate dynamics of an array in fluidic media*. Bachelor's thesis, TU-Ilmenau, 2016.

[15] S. Jackson. *Modelling and control of coupled AFM arrays for parallel imaging verified through a macro scale experiment.* PhD thesis, University of Canterbury, 2017.

EUROMECH Colloquium 603
Dynamics of micro and nano systems
5 – 7 September 2018, Porto, Portugal

Graphene-Based Broadband High-Frequency Ultrasound Detector

Gerard J. Verbiest[1], **Jan N. Kirchhof**[1,*], **Matthias Goldsche**[1,2], **Jens Sonntag**[1,2], **Tymofiy Khodkov**[1,2,†] **and Christoph Stampfer**[1,2]

[1]RWTH Aachen University, Aachen, Germany
verbiest@physik.rwth-aachen.de
goldsche@physik.rwth-aachen.de
jens.sonntag@physik.rwth-aachen.de
stampfer@physik.rwth-aachen.de

[2]Forschungszentrum Jülich, Jülich, Germany

Summary. Ultrasound detection is one of the most important nondestructive subsurface characterization tools of materials. In recent years, graphene resonators attracted attention as loudspeaker and ultrasound radio. Here we use a graphene resonator to detect ultrasound propagating through the substrate on which it was fabricated. We achieve a sensitivity of 400 pm/nA and a resolution of 20 pm in ultrasound amplitude at frequencies up to 90 MHz. Thanks to a strong nonlinearity in the mechanical restoring force, the resonance frequency itself can also be used for ultrasound detection with a with a resolution of 25 pm in ultrasound amplitude. This work puts forward a sensor design that fits onto an atomic force microscope cantilever.

Keywords: Graphene, ultrasound detection, NEMS, resonator, scanning probe microscopy.

1 Introduction

Graphene resonators led to ultra-sensitive sensors, due to their high stiffness and low mass density (1). The unique electromechanical coupling in graphene allows for electrical read-out of its resonator properties, which is preferred for the integration into electronic circuits. This, in combination with a resonance frequency of tens of MHz, makes graphene an interesting material for ultrasound microphones and radios. For applications such as nondestructive material testing and medical imaging, the ultrasound propagates through a solid medium and is detected at the surface. The ultrasound detectors in these applications usually suffer from the diffraction limit, which prevents their application at the nanoscale. Yet, it is the nanoscale that gets increasingly important due to the ever ongoing miniaturization of electrical and mechanical components. This problem was partly overcome by introducing ultrasound into an atomic force microscope (AFM) (2). Here, the ultrasound detection relies on large ultrasound amplitudes (~ 0.1 to ~ 1 nm) and the nonlinear interaction between the cantilever-tip and the sample. This makes quantitative measurements tedious (3). Consequently, nondestructive material testing and medical imaging with an AFM would greatly benefit from a linear detection scheme for the ultrasound vibration of the sample.

Here we show a graphene resonator that detects ultrasound sent through the substrate on which it was fabricated (4). We compare the responds of the graphene resonator to ultrasound with that to the standard capacitive actuation (see Fig. 1). The vibration amplitude is measured with an amplitude modulated down-mixing technique. We show that both the vibration amplitude away from the resonance frequency and the resonance frequency itself can be used for ultrasound detection with a resolution of 20-25 pm.

2 Methods

We fabricated graphene resonators on a standard $\mathrm{Si}/\mathrm{SiO}_2(285\ \mathrm{nm})$ substrate by mechanically exfoliating graphene and using electron beam lithography to pattern the electrical contacts. The contacts consist of 5 nm Cr and 120 nm Au and also serve as clamps for the graphene resonator. Finally, the graphene membrane is suspended by etching the SiO_2 away in a 1% hydrofluoric acid solution followed by a

*Current address: Freie Universität Berlin, Berlin, Germany, e-mail: jan.kirchhof@fu-berlin.de
†ICFO, Barcelona, Spain, e-mail: tymofiy.khodkov@icfo.eu

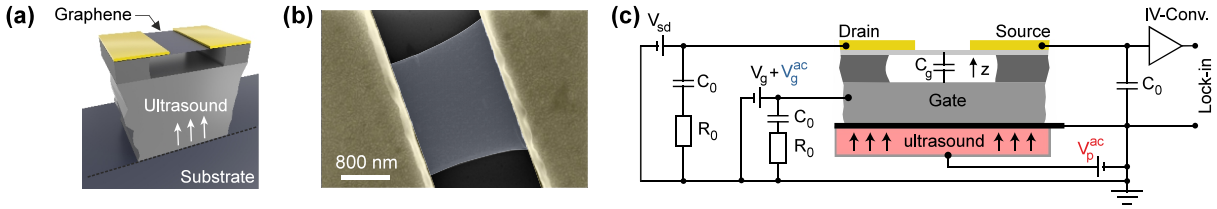

Figure 1. (a) Illustration of a graphene-based ultrasound detector and (b) a false-color scanning electron microscope image of a fabricated graphene resonator. (c) The detection circuit measures the resonance frequencies of the graphene resonator by an amplitude modulated down-mixing technique. The resonator is actuated either capacitively with a small potential $V_{\mathrm{g}}^{\mathrm{ac}}$ at frequency $\omega/2\pi$ on the gate or with ultrasound that is induced via a piezoelectric element that is placed underneath the substrate holding the resonator. We isolate the piezoelectric element electrically from the gate and actuate it at frequency $\omega/2\pi$ with a potential $V_{\mathrm{p}}^{\mathrm{ac}}$. A signal V_{sd} at frequencies $\omega/2\pi \pm \Delta\omega/2\pi$ is applied to the drain contact of the graphene and the current at frequency $\Delta\omega/2\pi$ flowing out of the source contact is measured with an IV-converter and a lock-in amplifier. The resistances $R_0 = 50\ \Omega$ and capacitances $C_0 = 100$ nF are for impedance matching and reducing the noise on the input of the IV-converter.

critical point dryer step to prevent the graphene membrane from collapsing due to capillary forces. From the scanning electron microscope image in Figure 1b, we extract a width W of 2.2 µm and a distance L between the clamps of 1.6 µm. The SiO_2 is spaced 140 nm underneath the graphene membrane, which results in a parallel plate capacitance C_{g} for the gate of 0.18 fF. This results in a lower bound of the carrier mobility of 1.500 (1.000) $\mathrm{cm}^2/\mathrm{Vs}$ for holes (electrons) from the conductance G and transconductance $\partial G/\partial V_{\mathrm{g}}$ tuning with gate potential V_{g}. The average pre-strain in the resonator is 0.24%.

In addition to the standard capacitive actuation of the resonator with a potential $V_{\mathrm{g}}^{\mathrm{ac}}$ on the gate, we use a piezoelectric element with a resonance frequency of 4.5 MHz to mechanically shake the substrate. The actuation frequency $\omega/2\pi$ is swept around the mechanical resonance frequency of the suspended graphene membrane. In both cases, a small modulation potential $V_{\mathrm{sd}} = 10$ mV at frequency $\omega/2\pi \pm \Delta\omega/2\pi$ is applied across the graphene membrane to generate a current $I_{\Delta\omega}$ at frequency $\Delta\omega/2\pi$ (see Fig. 1c). We tune $V_{\mathrm{g}}^{\mathrm{ac}}$ such that we have approximately the same $I_{\Delta\omega}$ in both actuation schemes. All experiments were performed in vacuum of 10^{-5} mbar at room temperature.

3 Results and discussion

Figure 2a and 2b show $I_{\Delta\omega}$ as a function of $\omega/2\pi$ and V_{g} for the standard capacitive actuation and the purely mechanical actuation. We observe in both schemes the resonance frequencies as dips and peaks in $I_{\Delta\omega}$ at approximately the same positions. The current $I_{\Delta\omega}$ is described by (1):

$$I_{\Delta\omega} = \frac{1}{2} V_{ds} \frac{\partial G}{\partial V_{\mathrm{g}}} \left(V_{\mathrm{g}}^{\mathrm{ac}} + V_{\mathrm{g}} \frac{\partial_z C_{\mathrm{g}}}{C_{\mathrm{g}}} \delta z \right), \tag{1}$$

in which δz is the displacement of the graphene membrane that also includes the time-dependent displacement δz_c of the contacts. In case of the purely mechanical actuation, the modulation potential $V_{\mathrm{g}}^{\mathrm{ac}}$ is zero, hence $I_{\Delta\omega}$ is directly proportional to δz.

To extract δz_c, we consider $I_{\Delta\omega}$ far away from a mechanical resonance of the graphene and assume that δz_c does not depend on V_{g} as well as that C_{g} and $\partial_z C_{\mathrm{g}}$ are well described by the parallel plate approximation for the capacitance such that their ratio is equal to 140 nm. Then, δz_c remains the single fitting parameter for $I_{\Delta\omega}$ (see Eq. 1). We find a vibration amplitude δz_c of 110 and 60 pm at 66 MHz and 84 MHz, respectively (Fig. 2d). At $V_{\mathrm{g}} = -5$ V, this translates into a sensitivity of 1100 pm/nA at 66 and of 400 pm/nA at 84 MHz. Considering the noise of ∼50 pA in $I_{\Delta\omega}$ (see figures 1c-1e), we have a detection resolution in ultrasound amplitude of 20 pm.

In the case of the standard capacitive actuation, δz_c is also the only unknown parameter, as $V_{\mathrm{g}}^{\mathrm{ac}}$ is fixed. However, the nonzero $V_{\mathrm{g}}^{\mathrm{ac}}$ results in a large background current that covers the signal coming of the vibrating contacts. This results in an upper bound for δz_c of $\sim$ 50 pm at 66 and 84 MHz (Fig. 2e). It is not surprising that the vibration amplitude in the purely mechanical actuation case is larger than in the

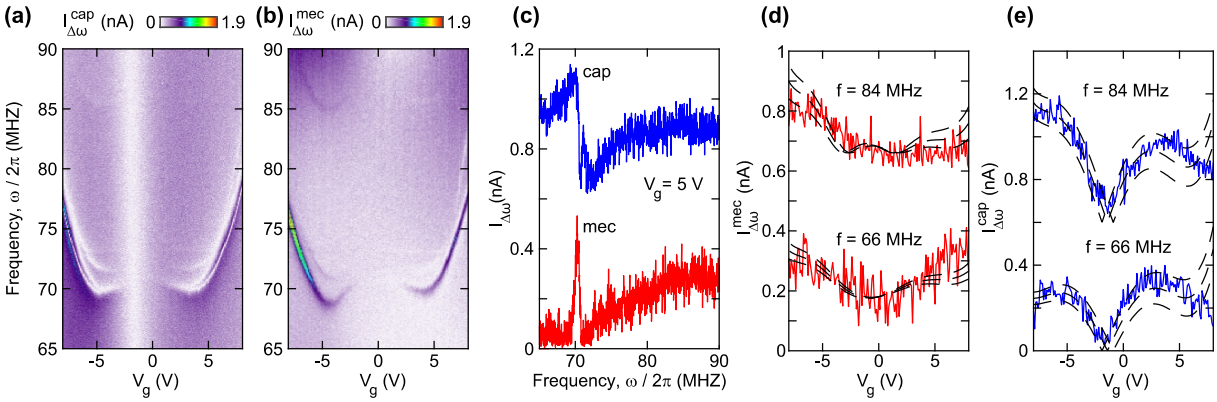

Figure 2. Unprocessed down-mixing current $I_{\Delta\omega}$ as a function of $\omega/2\pi$ and V_g in case of (a) standard capacitive actuation $I^{\mathrm{cap}}_{\Delta\omega}$ and (b) purely mechanical actuation $I^{\mathrm{mec}}_{\Delta\omega}$. The line traces in (c) show $I_{\Delta\omega}$ at $V_\mathrm{g} = 5$ V for the standard capacitive actuation (blue) and the purely mechanical actuation (red) scheme. The resonance frequency of the graphene resonator is approximately the same in both actuation schemes. By analyzing $I_{\Delta\omega}$ as a function of V_g far away from the resonance frequency of the graphene resonator, we observe a background current. In the purely mechanical actuation scheme (d), this current allows us to quantify the ultrasound vibration of the contacts (see text). This contribution is completely covered by a background current in the standard capacitive actuation scheme (e). The black lines in (d) and (e) correspond to the fit of $I_{\Delta\omega}$ to Eq. 1 including the confidence interval due to the uncertainty in $\partial G/\partial V_\mathrm{g}$.

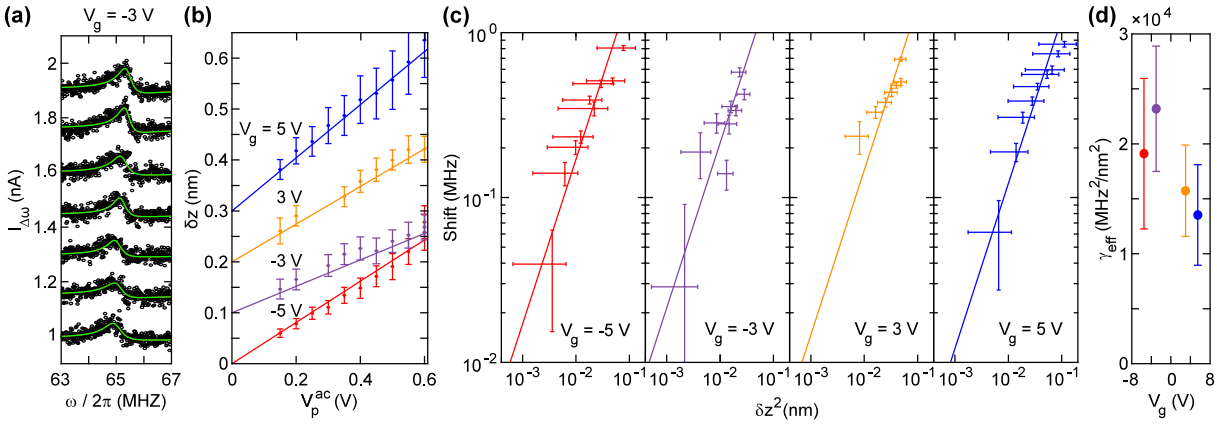

Figure 3. (a) $I_{\Delta\omega}$ for increasing drive amplitudes from bottom to top with the corresponding fit to a nonzero phase Lorentzian (green). The curves are offset with 0.15 nA for clarity. (b) The vibration amplitude δz as a function of $V_\mathrm{p}^{\mathrm{ac}}$ used for the mechanical actuation. The curves are offset by 0.1 nm for clarity. (c) The resonance frequency linearly shifts to higher frequencies scaling with the vibration amplitude squared. The slopes of these curves define the nonlinearity γ_{eff} (d). Within error bars, the nonlinearity does not depend on the applied V_g.

standard capacitive actuation, but what is really striking is their magnitude.

Let us now consider the vibration amplitude at the resonance frequency of the graphene resonator. If the graphene membrane is pulled down by V_g, the inversion symmetry is broken. The tension in the resonator gets reduced when moving the membrane away from the gate, whereas the tension is increased when the membrane is moved towards the gate. This symmetry breaking is described by the nonlinear restoring force $m\beta z^2$. In addition to this term, we take into account the well-known Duffing nonlinearity $m\gamma z^3$. Here, β and γ are constants quantifying the strength of the symmetry breaking effect and the Duffing nonlinearity in the equation of motion ($m\ddot{z}^2 + m\Gamma\dot{z} + kz + m\beta z^2 + m\gamma z^3 = F_\mathrm{d}$, where Γ is the linewidth quantifying the damping and F_d is the effective drive force). The nonlinear terms containing β

and γ lead to a vibration amplitude dependent frequency shift (5):

$$\Delta\omega_0 = \frac{3}{8}\frac{\gamma_{\text{eff}}}{\omega_0}\delta z^2, \tag{2}$$

in which $\Delta\omega_0/2\pi$ is the shift in $\omega_0/2\pi$ and $\gamma_{\text{eff}} = \gamma - \frac{10}{9}\frac{\beta^2}{\omega_0^2}$.

To quantify γ_{eff}, we measured $\omega_0/2\pi$ as a function of δz at a fixed V_{g} by varying the ultrasound drive potential V_{p}^{ac} (Fig. 3a and 3b). The resonance frequency is extracted by fitting the current $I_{\Delta\omega}$ with a nonzero phase Lorentzian (1). From the linear dependence of $\omega_0/2\pi$ on δz^2 (Fig. 3c), we find that $\gamma_{\text{eff}} = 18.000 \pm 5.000\ \text{MHz}^2/\text{nm}^2$ (Fig. 3d). The nonlinearity γ_{eff} is positive and thus the resonance frequency increases with increasing vibration amplitude. We conclude that the Duffing nonlinearity γ dominates over β due to the relatively large pre-strain ($\sim 0.24\%$) in the graphene resonator (5).

We can also make use of the nonlinearity γ_{eff} for ultrasound detection. The nonlinearity γ_{eff} is so strong that even a small vibration amplitude of 100 pm shifts the resonance frequency by 120 kHz. This suggest that after calibrating the nonlinearity, one can measure the ultrasound amplitude impinging on the resonator by monitoring its resonance frequency. In our measurements, the uncertainty on the extracted resonance frequencies is 29 kHz, which corresponds to resolution of 25 pm.

4 Conclusions

We investigated the feasibility of detecting ultrasound with a graphene resonator by introducing a purely mechanical actuation scheme. This new actuation scheme is also applicable to other two-dimensional resonators and even provides a method for actuating nonconductive resonators. Using this actuation scheme, we are able to sense the ultrasound vibration amplitude of the electrical contacts up to at least 90 MHz with a sensitivity of 400 pm/nA at 84 MHz. Alternatively, we use the mechanical nonlinearity $\gamma_{\text{eff}} = 14.800 \pm 2.300\ \text{MHz}^2/\text{nm}^2$ of the graphene resonator to detect ultrasound. With this nonlinearity, we detect ultrasound via resonance frequency monitoring with a resolution of 25 pm. We showed that graphene resonators can directly pick-up ultrasound at frequencies inaccessible for near field probes. Our work paves the way for ultrasound detection at the nanoscale using graphene.

Acknowledgments

Support by the ERC (GA-Nr. 280140), the Helmholtz Nanoelectronic Facility at the Forschungszentrum Jülich, and the Deutsche Forschungsgemeinschaft (SPP-1459) are gratefully acknowledged. G.V. acknowledges funding by the Excellence Initiative of the German federal and state governments.

References

[1] C. Chen, S. Rosenblatt, K.I. Bolotin, W. Kalb, P. Kim, I. Kymissis, H.L. Stormer, T.F. Heinz, J. Hone, Performance of monolayer graphene nanomechanical resonators with electrical readout. *Nature Nanotechnology*, **4**, 861-867, 2009.

[2] R. Garcia, E. Herruzo, The emergence of multifrequency force microscopy. *Nature Nanotechnology*, **7**, 217226, 2012.

[3] G.J. Verbiest, T.H. Oosterkamp, M.J. Rost, Subsurface contrast due to friction in heterodyne force microscopy. *Nanotechnology*, **28**, 085704, 2017.

[4] G.J. Verbiest, J.N. Kirchhof, M. Goldsche, T. Khodkov, J. Sonntag, C. Stampfer, Graphene-Based Broadband High-Frequency Ultrasound Detector. arxiv:1802.01906, 2018.

[5] A. Eichler, J. Moser, M. Dykman, A. Bachtold, Symmetry breaking in a mechanical resonator made from a carbon nanotube. *Nature Communications*, **4**, 2843, 2013.

EUROMECH Colloquium 603
Dynamics of micro and nano systems
5 – 7 September 2018, Porto, Portugal

Dynamics of very viscous flow in deformable microchannels under impact loads

L. Parras[1] **and F.J. Galindo-Rosales**[2]

[1]E. T. S. Ingeniería Industrial, Universidad de Málaga, Dr Ortiz Ramos s/n, 29071, Málaga, Spain
lparras@uma.es

[2]Centro de Estudos de Fenómenos de Transporte (CEFT). Faculdade de Engenharia da Universidade do Porto, Rua Dr. Roberto Frias s/n, 4200-465 Porto, Portugal
galindo@fe.up.pt

Summary. CorkSTFluidics composites consists of cork pads sandwiches with embedded microfluidic patterns filled with a shear thickening fluid, whose mechanical performance under impact loads is determined by the microfluidic pattern and the rheological properties of the fluid. From the experimental results it is impossible to decouple the fluid contribution from the solid contribution to the force-time response of the composite. With this work we aim at developing a model of the fluid-flow dynamics able to predict the fluid contribution in the energy dissipation of the CorkSTFluidic composites under impact loads.

Keywords: CorkSTFluidics composites, Fluid-Structure Interaction, Impact tests.

1 Introduction

CorkSTFluidics composites are among the most promising recent developments of passive smart materials for energy dissipation (or absorption) applications [1, 2, 3]. They consists of micro agglomerated cork pads reinforced with a shear thickening fluid, which is embedded by means of microfluidic patterns. When subjected to an impact, the energy will be dissipated by the combined effects of the cork elasticity, the complex fluid confined in the microchannels and the fluid-structure interaction. Cork is a natural cellular material with outstanding mechanical properties, particularly able to absorb considerable amounts of energy with almost total reversibility and exhibiting a nearly zero Poisson's ratio; however, it is still far from fulfilling stringent regulatory requirements when intended as a substitute of EPS in helmets for instance, and a reinforcement with a complex fluid having engineered properties allows overcoming this limitation. Shear Thickening Fluids (STFs) are commonly used for the development and fabrication of passive dissipative devices, such as ballistic fabric composites, due to their viscous damping and elastic stiffness capabilities spontaneously activated under stress [4] and enhanced under confinement [5]. The microfluidic patterns are designed based on the concept of microfluidic rectifiers, whose flow resistance depends on the direction of flow and nonlinear flow behaviour under creeping flow conditions of complex fluids; they allow controlling the dissipation of energy by controlling the pressure drop in the fluid. Thus, in order to optimize their mechanical performance under impact conditions modeling the fluid-flow dynamics is a must.

2 Experimental setup

Low velocity impact tests were performed at 20 °C using a drop weight impact test machine (ROSAND Instrument Falling Weight). The normal force in response to the impact was measured by means of a piezo-electric 1-component force sensor (Kistler 9031A) attached to striking mass. The energy of the impact is determined by $E_i = mgh$, where m is the total mass dropped (4.042 kg) from the height h, and g is the gravitational acceleration. As the mass was kept constant in all the experiments, the impact energy was increased by increasing the dropping height. The impactor has a rectangular shape of 65 mm in the z direction and 15 mm in the x direction. The composites considered for the impact tests consist of a sandwich of two different micro-agglomerated cork sheets: the one in the bottom holds engraved the microfluidic patterns and has a 2 mm thickness, hereafter named as 'bottom lamina'; and the one which closes the microfluidic pattern is a 1.2 mm thick self-adhesive pad, hereafter named as 'cover

lamina'. The microfluidic patterns consisted of straight microchannels having the following dimensions (Figure 1): $H \sim 0.75$ mm, $L = 50$ mm, $W = 2.55$ mm, and $E = 12.8$ mm. The microchannels were fully filled with a concentrated dispersion of precipitated calcium carbonate in glycerol at 55 % wt, having a shear thickening behavior. It has been recently observed that when this kind of complex fluid is suddenly impacted, undergoing shear stresses above the critical value, the internal microstructure is lead to a thickened state from which it is not able to return as the shear load decreases. Consequently, once the fluid is thickened, during the impact time-scale, its viscosity does not depend of the shear rate anymore and it can be consequently considered as constant with a very high value for the whole process [6].

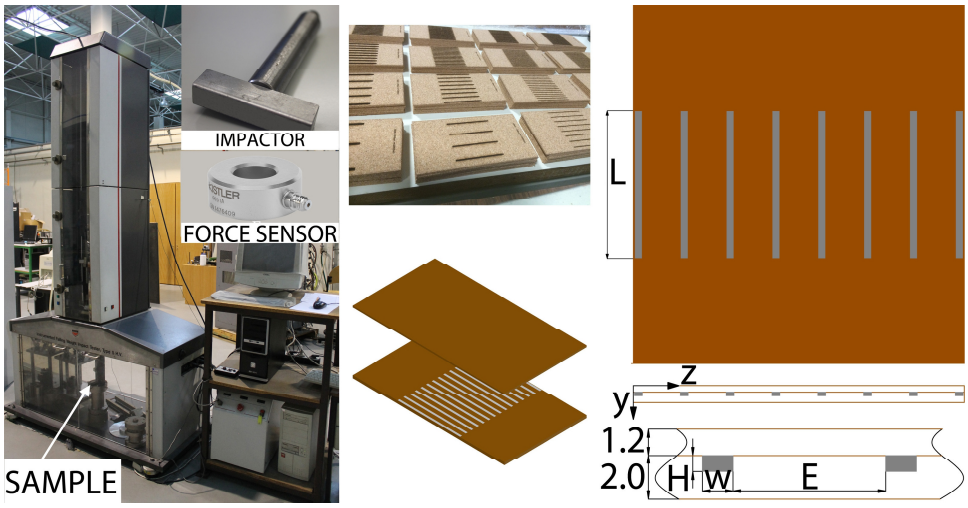

Figure 1. Experimental setup. Drop weight impact test machine (left), cork pads engraved with different straight microchannels (center-top), design of the cork composite (center-bottom), and key dimensions of the microfluidic pattern (right).

The curve force-time was measured and, from that, different parameters can be used to characterize the mechanical performance of the sample, i.e. impulse, incipient damage and peak force (Figure 2), as well as determining the time evolution of the velocity of the impactor, the deformation of the composite and the energy. Although, the elastic contribution in the energy can be considered due to the cork elasticity, it is not possible to determine the amount of energy dissipated by the cork and the fluid, since it is known that cork is a viscoelastic material and the impact conditions undergone stresses beyond its elastic limit. In this work, we aim at determining the contribution of the fluid to the energy dissipated in the system.

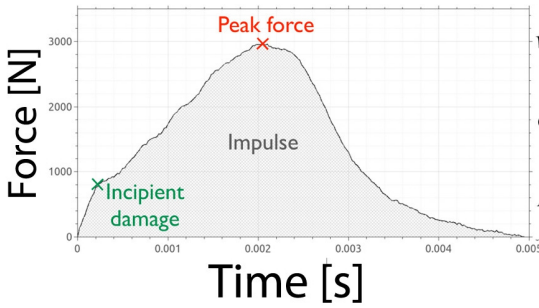

$$v(t) = v_0 + \int_0^t (9.81 - F(t)/m)\,dt$$

$$\delta(t) = \int_0^t v(t)dt$$

$$Energy(t) = \int_0^t \delta(t)F(t)dt$$

Figure 2. Typical force-time curve measured in the experiments (top) and the calculated time evolution of velocity (bottom-left), deformation (bottom-middle) and normalized energy (bottom-right).

3 Modeling

To model this problem we suppose that there is a rectangular duct of height $h(x,t)$ and constant width W and length L fully filled with thickened fluid exhibiting a constant viscosity with a very high value for the

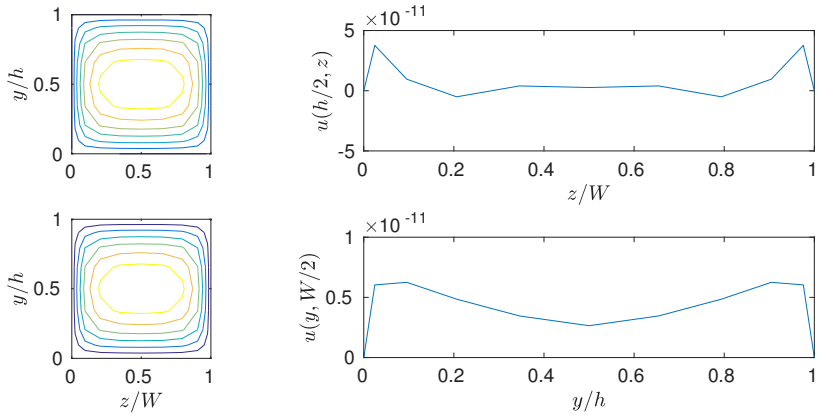

(a) (b)

Figure 3. (a) Numerical solution (up) and analytical solution (down) of the equation (1) with $dp/dx = 1$. (b) The errors at $y = h/2$ (up) and at $z = W/2$ (down).

whole process. Taking into account that $L \gg W, h$, the fluid velocity is unidirectional $\mathbf{v} = u(y,z)\mathbf{e}_x$. If $h_0^2/(t_0\nu) \ll 1$, being h_0 the initial height, t_0 the time for the channel to collapse and ν the kinematic viscosity, one can neglect the temporal variation on the velocity u. These hypothesis allows to solve at each section,

$$\mu\left(\frac{\partial^2 u}{\partial y^2} + \frac{\partial^2 u}{\partial z^2}\right) = \frac{\partial p}{\partial x}, \tag{1}$$

$$y = 0, H, \quad u = 0, \tag{2}$$

$$z = 0, W, \quad u = 0, \tag{3}$$

with $dp/dx \neq 0$ only if $h(t)$ depends on time. Finally, the velocity u will depend on t due to the variation of height with time $h(t)$ and on x due to the values of dp/dx.

3.1 Analytic solution at each section

The solution of the homogeneous problem can be easily obtained by separation of variables,

$$u(x,y,z,t) = \frac{1}{\mu}\frac{\partial p}{\partial x}\sum_{n,m=1}^{\infty} a_{m,n}\sin\left(\frac{n\pi y}{h}\right)\sin\left(\frac{m\pi z}{W}\right). \tag{4}$$

Projection on the whole domain we can get the value of $a_{m,n}$,

$$a_{m,n} = \frac{4((-1)^n - 1)((-1)^n - 1)}{nm\pi^2\left[\left(\frac{n\pi}{h}\right)^2 + \left(\frac{m\pi}{W}\right)^2\right]} \tag{5}$$

To check the validity of the analytical solution we solve the problem (1)-(3) numerically. The analytical solution is basically the same obtained before and we represent for n and m up to 50 terms, and the numerical solution has been obtained by using a pseudospectral method based in Chebyshev points ($N = 11$, being N the number of Chebyshev polynomials used). The results are shown in Figure 3 and the errors in the solution at $y = 0$. It can be observed how the analytical solution is very accurate using the 50 first terms of the series.

3.2 Force and energy calculation

First, the flow rate is calculated by integrating the velocity at each section,

$$q = \int_0^W \int_0^h u(x,y,z,t)dydz = \frac{1}{\mu}\frac{\partial p}{\partial x}\, q^* = \tag{6}$$

$$\frac{1}{\mu}\frac{\partial p}{\partial x} \sum_{n,m=1}^{\infty} a_{m,n}\frac{hW}{mn\pi^2}((-1)^n - 1)((-1)^m - 1). \tag{7}$$

Using the continuity equation

$$\frac{\partial u}{\partial x} + \frac{\partial v}{\partial y} = 0, \tag{8}$$

and integrating in the whole section we get,

$$\frac{\partial}{\partial x}\left(\frac{1}{\mu}\frac{\partial p}{\partial x}q^*\right) + W\frac{\partial h}{\partial t} = 0. \tag{9}$$

This equation is solved considering the following boundary conditions:

$$x = 0, L, \quad p = p_a. \tag{10}$$

To calculate the resulting force in the y coordinate we perform the following integral

$$F_y = W\int_0^L p dx, \tag{11}$$

and the total energy dissipated by the fluid is given by:

$$E_T = \int_0^T \left(W\int_0^L p\,\frac{\partial h}{\partial t}dx\right)dt. \tag{12}$$

4 Remarks

In order to compare between experiments and model, we need to solve the full fluid-structure interaction problem, by coupling the model described above for the fluid dynamics with the model for the solid mechanics of the micro agglomerated cork pads[7]. This is currently an ongoing work that we expect to finish in the near future.

Acknowledgments

FJGR would like to acknowledge the financial support from FCT, COMPETE and FEDER through grant IF/00190/2013 and project IF/00190/ 2013/ CP1160/CT0003.

References

[1] F.J. Galindo-Rosales, L. Campo-Deaño, Composite layer material for dampening external load, obtaining process, and uses thereof. PCT/IB2015/057399

[2] F.J. Galindo-Rosales, S. Martínez-Aranda, L. Campo-Deaño, CorkSTFμfluidics A novel concept for the development of eco-friendly light-weight energy absorbing composites. *Materials & Design*, **82**, 326-334, 2015.

[3] F.J. Galindo-Rosales, Complex Fluids in Energy Dissipating Systems. *Applied Sciences*, **6(8)**, 206, 2016.

[4] C. Fischer, A. Bennani, V. Michaud, E. Jaquelin, J-A.E. Manson, Structural damping of model sandwich structures using tailored shear thickening fluid compositions. *Smart Materials and Structures*,**19(3)**, 035017, 2010.

[5] S. Majumdar, R. Krishnaswamy, A.K. Sood, Discontinuous shear thickening in confined dilute carbon nanotube suspensions. *Proceedings of the National Academy of Sciences of United States of America*, **108**(22), 8996-9001, 2011.

[6] F.J. Galindo-Rosales, R.S. Duarte, P. Bourrianne, R.A. Lima, G.H. McKinley, Impact rheometry: A new approach for the rheological characterization of shear thickening fluids on real time under low velocity impact tests *In preparation*, 2018.

[7] F.A.O. Fernandez, R.T. Hardin, A.B. Pereira, R.J. Alves de Sousa, Comparing the mechanical performance of synthetic and natural cellular material. *Materials & Design*, **82**, 335-341, 2015.

An overview on dynamical behavior and control of an atomic force microscopy (AFM) taking into account the forces of Van Der Walls and fractional-order

José M. Balthazar[1], Ângelo M. Tusset[1], Rodrigo T. Rocha[1], Frederic C. Janzen [1] and Átila M. Bueno[2]

[1] Federal University of Technology - Paraná (UTFPR), Ponta Grossa, Brazil.
jmbaltha@gmail.com.br
tusset@utfpr.edu.com
digao.rocha@gmail.com
fcjanzen@hotmail.com

[2] UNESP - São Paulo State University, Sorocaba, Brazil
atila@sorocaba.unesp.br

Summary. This work overviews the analysis of the influence of damping, the nonlinear stiffness term and the squeeze film damping in the fractional-order dynamics of an AFM system operating in tapping mode. Additionally, it is attempted to study the State Dependent Ricatti Equation (SDRE) controller design with the goal to avoid chaotic behavior.

Keywords: Atomic Force Microscopy, Chaos, Control, Sensibility Analysis.

1 Introduction

It is well known that the nonlinear dynamics of the Atomic Force Microscope (AFM) is an emerging topic of research and is a widely used tool for atomic level surface analysis ([1-3], undeserved of others). In addition, it has become an important equipment in the industry for developing nanotechnology, being used to develop substances, compounds, artefacts, and Nano chips.

The AFM is generally composed of a cantilever and the achievable sensitivity and resolution of AFM depending largely on the geometry of the micro cantilever. The cantilever interacts with the sample via a probe tip that is mounted on the cantilever. Several studies have been developed on the dynamics of a probe, which is responsible for the process of image magnification and therefore must be constantly improved.

As an example, several authors have studied the cantilever of the atomic force microscopy based on its nonlinear dynamics, which observed the existence of chaos through Lyapunov exponent analysis, basins of attraction and their erosions [4]. In addition, bifurcations techniques are very important to study the topology of the dynamics of the AFM, making possible to design optimized controls to AFM in contact [5], non-contact [6], and tapping mode [7-10]. Furthermore, the influence of parametrical errors may be included in order to investigate the parametrical sensitivity, carrying out simulations of the frequency modulated–atomic force microscope (FM-AFM) nonlinear control system [11].

Recently, in [12] the authors studied the nonlinear dynamics of an Atomic Force Microscope (AFM) operating in tapping mode, considering the influence of a squeeze film damping in fractional-order. It has been noted that it played an important role, and because of the nonlinear dynamics of the AFM, different responses could be obtained, i.e., periodic and chaotic motions, specially the influence of the derivative order when in fractional-order. In a way to characterize the type of behavior, the 0–1 test [13] was used, given that this is a good tool to characterize fractional-order differential systems. Moreover, the linear feedback control technique for fractional-order systems was applied to control the chaotic behaviors. Therefore, the results showed a nonlinear behavior

presented by the AFM system. The feedback control technique was efficient to control the chaotic motion of the micro cantilever of the AFM, including the results of the variation of parameters of the fractional derivative of the squeeze film damping. In [14] both 0-1 test and Wavelet-Based Scale Index were applied to investigate the nonlinear dynamics of the AFM micro cantilever deflection, considering the influence of the Van der Waals forces, between various surface analyses, variation of the tip geometry, influence of the spring constant, and the variation of amplitude set point of AFM cantilever. The obtained numerical results shown that the analysis of the parameters can be very significant for the chaotic or periodic behavior. The reconstruction of the state-space was perfomed [15] with the theory of mutual information and false nearest neighbors observing different phase portraits for different distances between sample and tip.

Next, the influence of the damping, nonlinear stiffness term and squeeze film damping in fractional-order will be investigated in the dynamics of the AFM system in tapping mode, as an example, and in an extension of [8].

2 Fractional dynamics and control of an (AFM) tapping mode vibrating problem

The AFM in tapping mode, illustrated in Fig. 1, consists of a cantilever base-excited by a piezoelectric actuator, whose displacement is given by a harmonic force. Mathematically, the cantilever is represented as a mass-spring-damper system vibrating closely to the surface of a sample. The tip is considered as a sphere of radius R and the distance between the sample and the cantilever is z_0 (distance between an equilibrium position of the cantilever and the sample) when only the gravity force acts on it. The position of the cantilever is given by x, measured from the equilibrium position.

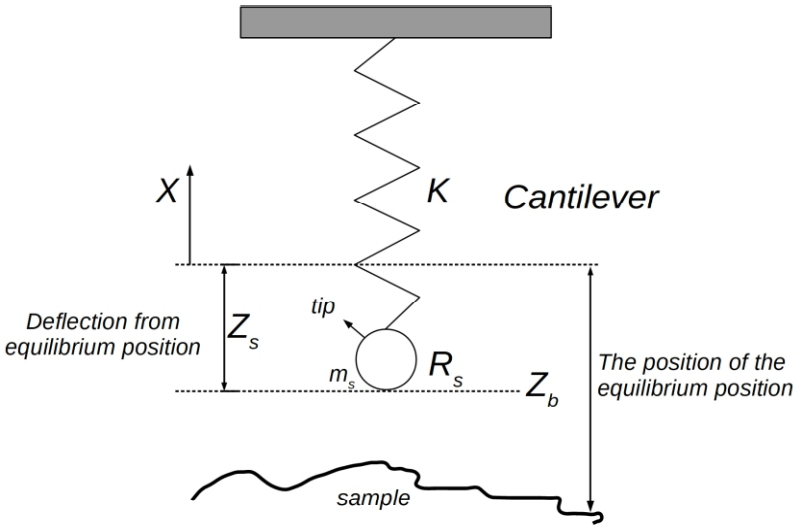

Figure 1. Simplified model of an AFM.

The behavior of the sample related to the damping is taken as viscoelastic. Therefore, the use of fractional-order derivatives to analyze the dynamic behavior of the system is possible. Using the Riemann-Liouville differential operators of fractional-order $q > 0$, the squeeze film damping becomes, in fractional order, as Eq. (1) neglecting U_s, where $0 < q_1, q_2, q_3 \leq 1$ and q_i is the order of the equation.

Additionally, the 0-1 test [13] is directly applied to the time series data of the system, based on the statistical properties of a single coordinate (variable x_1 of Equation (1)). Basically, the 0-1 test consists of estimating a single parameter K. If its value is close to 0 the system is periodic, on the other hand, if K is close to 1 the system is chaotic

$$\frac{d^{q_1}u_1}{dT^{q_1}} = x_2$$
$$\frac{d^{q_2}x_2}{dT^{q_2}} = -rx_2 - cx_1^{\,3} - \frac{d}{\left(a+x_1\right)^2} + g\cos\Omega\tau - \frac{p}{\left(a+x_1\right)^3}\frac{d^{q_2}x_3}{dT^{q_3}} + U_s \qquad (1)$$
$$\frac{d^{q_3}x_3}{dT^{q_3}} = x_2$$

3 Numerical results and discussions

The obtained results are showed in Figure 2. Figure 2a shows the K variations of the derivative order of $q_1 = q_2 = 1$ and $0.5 \leq q_3 \leq 1$. The behavior of the system is chaotic along the variation of q_3 as K is very near 1, in which represents the viscoelastic behavior of the squeeze film damping. However, when $q_3 < 1$, the value of K is the highest of the interval (for $q_3 = 0.76$, $K = 0.94$, for $q_3 = 1$, $K = 0.66$), which indicates a change in the chaotic behavior to a higher level of it. The time history of displacement and phase plane when $q_1 = q_2 = 1$ and $q_3 = 0.76$ is illustrated in Figs. 2b. In order to control the chaotic behavior of the AFM system, the SDRE control [16] is proposed as $U_s = u_{sf} + u_s$, where u_{sf} is the feedback control and u_s is the feedforward control, which is applied as a sum to the second equations of Eq. (1), with $x(t_0) = x_0$, as the initial conditions. Therefore, Fig. 2c shows the chaotic phase plane in blue and the controlled phase plane in red, whose control showed to be very useful to the fractional order case.

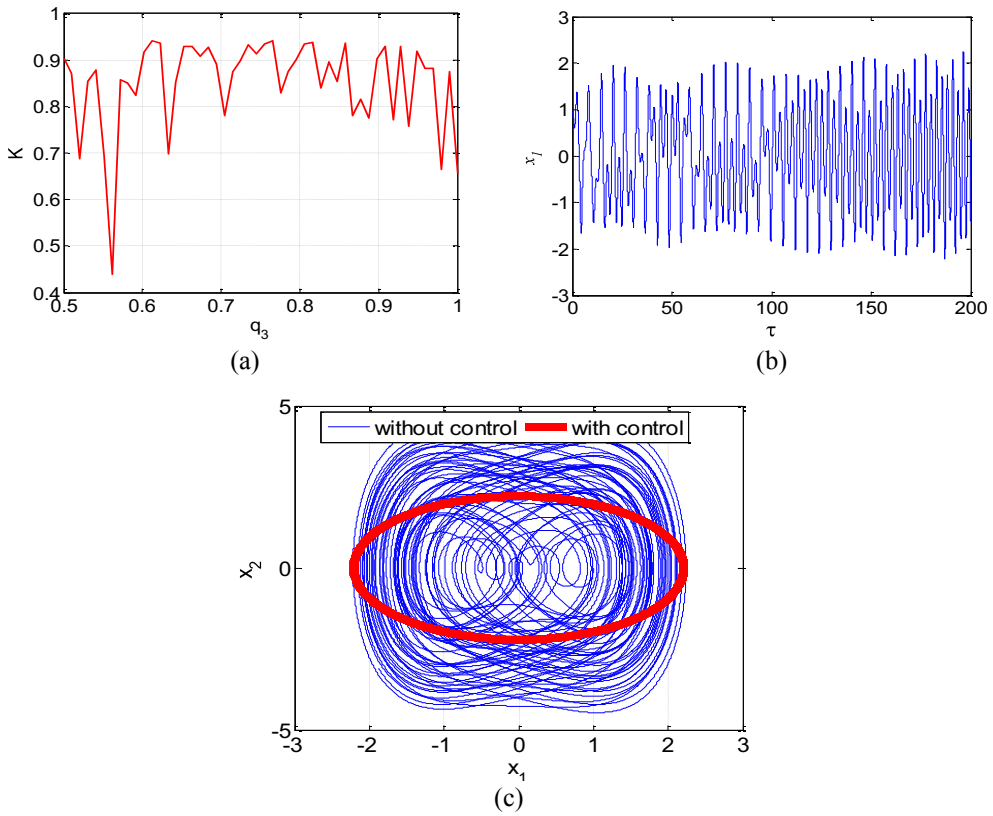

Figure. 2 (a) Variation of K vs q_3; (b) time history of the displacement of the tip; (c) the chaotic orbit in blue and the controlled orbit in red

Acknowledgments

The authors acknowledgment support from CNPq, a Brazilian Funding Agency.

References

[1] G. Binnig, C. Gerber, C. Quate, Atomic force microscope, *Physical Review Letter,* **56**, 930-933, 1986.

[2] N. Jalili, K. Laxminarayana, A review of atomic force microscopy imaging systems: application to molecular metrology and biological sciences, *Mechatronics*, **14**, 907-945, 2004.

[3] J. M. Balthazar, A. M. Tusset, A. M. Bueno, B. P. Rodrigues, On an overview of nonlinear and chaotic behavior and their controls of an atomic force microscopy (AFM) Vibrating Problems. *Nonlinearity, Bifurcation and Chaos - Theory and Applications,* J. Awrejcewicz, P. Hagedorn, Eds, Proceedings InTech, pp. 45-68, 2017

[4] L. Ruzziconi, S. Lenci, M. I. Younis, Nonlinear phenomena in the single-mode dynamics in an AFM cantilever beam. *12th International Conference on Multibody Systems, Proceedings of Nonlinear Dynamics, and Control Charlotte*, North Carolina, USA, August 21–24, 1-7, 2016.

[5] V. Settimi, G. Rega, Response robustness and safety against jump to contact in AFMs controlled via different techniques. *Procedia IUTAM*, **22**,184-191, 2017

[6] V. Settimi, O. Gottlieb, G. Rega, Asymptotic analysis of a noncontact AFM microcantilever sensor with external feedback control. *Nonlinear Dynamics*, **79**, 2675–2698, 2015.

[7] J. M. Balthazar, A. M. Tusset, S. L. T. Souza, A.M. Bueno, Microcantilever chaotic motion suppression in tapping mode atomic force microscope, *Proceedings of the Institution of Mechanical Engineers, Part C: Journal of Mechanical Engineering Science*, **227**, 1730-1741, 2013.

[8] R. Nozaki, J. M. Balthazar, A. M. Tusset, A. M. Bueno, B. R. Pontes, Nonlinear control system applied to atomic force microscope including Parametric Errors, *Journal of Control, Automation and Electrical Systems*, **24(3)**, 223–231, 2013.

[9] K. S. Rodrigues, J. M. Balthazar, A. M. Tusset, A. M. Bueno, B.R. Pontes, Preventing chaotic motion in tapping-mode atomic force microscope, *Journal of Control, Automation and Electrical Systems,* **25**, 732-740, 2014.

[10] J. M. Balthazar, A. M. Tusset, S. L. T. de Souza, A. M. Bueno, Microcantileve chaotic motion suppression in tapping mode atomic force microscope, *Proceedings of the Institution of Mechanical Engineers, Part C: Journal of Mechanical Engineering Science,* **227(8),** 1730-1741, 2013.

[11] A. M. Bueno, J. M. Balthazar, J. R. C. Piqueira, simulations of the frequency modulated - Atomic Force Microscope (FM-AFM) *Nonlinear Control System*, *Chaotic Modeling and Simulation*, **1**, 173–186, 2011.

[12] A. M. Tusset, J. M. Balthazar, J. J. De Lima, R.T. Rocha, F. C. Janzen, P. S. Yamaguchi, On an optimal control applied in atomic force microscopy (AFM) including fractional-order, *Proceedings of the ASME 22nd Design for Manufacturing and the Life Cycle Conference*; *11th International Conference on Micro- and Nanosystems*, Cleveland**,** Ohio, USA, 2017.

[13] D. Bernardini, G. Litak, An overview of 0–1 test for chaos. *Journal of the Brazilian Society of Mechanical Sciences and Engineering.* **1-8**, 1433–1450, 2015

[14] R. Nozaki, H. A. Navarro, A. M. Tusset, R. T. Rocha, M. A. P. Da Silva, J. M. Balthazar. On a time series analysis generated by a sensor of an atomic force microscope (AFM), *preprint, submitted*, 1-10, 2018.

[15] R. Hegger, H. Kantz, T. Schreiber, Practical implementation of nonlinear time series methods: The TISEAN package*, Chaos*, **9**, 413-435, 1999.

[16] T. Çimen, State-Dependent Riccati Equation (SDRE) Control: A Survey. *Proceedings of the 17th World Congress The International Federation of Automatic Control Seoul*, Korea, July 6-11, pp. 3761- 3775, 2008.

EUROMECH Colloquium 603
Dynamics of micro and nano systems
5 – 7 September 2018, Porto, Portugal

A note on dynamics and control of a mems oscillator with chaotic behavior

Angelo M. Tusset[1], Giane G. Lenzi[1], Stefania Specchia[2], Rodrigo T. Rocha[1] and Josê M. Balthazar[1]

[1] Federal University of Technology – Paraná, Ponta Grossa, Brazil
tusset@utfpr.edu.br
gianeg@utfpr.edu.br
digao.rocha@gmail.com
jmbaltha@gmail.com

[2] Politecnico di Torino, Torino, Italy
stefania.specchia@polito.it

Summary. In this work, it is considered the dynamics and control of a micro-electromechanical system "MEMS" represented by an oscillator. Numerical simulations have shown that for certain parameters, the system has a chaotic behavior. Two control techniques are presented with the objective of controlling the system trajectory in a periodic orbit, which are the Optimal Linear Feedback Control (OLFC control) and Time-Delayed Feedback control. The results obtained by using the controllers showed that they were effective in controlling the trajectory of the studied system.

Keywords: MEMS resonators, OLFC control, Time Delayed Feedback Control, Chaos Control.

1 Introduction

Currently, a large number of researches have been performed to report nonlinear dynamical phenomena on MEMS resonators [1], as well as application of control techniques in such resonators to obtain a desired behavior [2]. The nonlinearities in MEMS include nonlinear springs and damping mechanisms [3], nonlinear resistive, inductive and capacitive circuit elements [4] and nonlinear surface, fluid, electric and magnetic forces [5]. In Pandey [6], the Mathieu–van der Pol–Duffing equation was considered to present a MEMS model, and the authors investigated the dynamics of the system considering forced both parametrically and nonparametrically. In [7], a thermomechanical model of a MEMS was developed, and its predictions were explored to explain and predict the entrainment phenomenon. In Fig. 1, a MEMS oscillator is observed composed of a DC source and an alternating current (AC) with a movable micro beam.

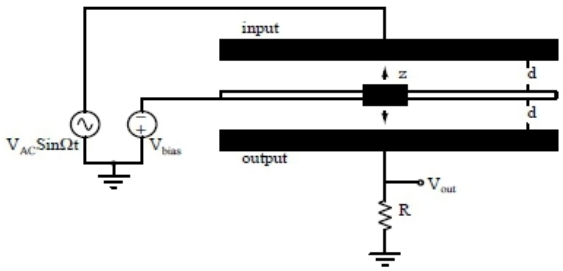

Figure 1. Microelectromechanical oscillator (MEMS) [8]

According to [8], the mathematical model of a MEMS oscillator with a cubic nonlinear term is represented by Fig. 1, and can be written as follows:

$$\ddot{x} = -\mu\dot{x} - k_l x - k_{nl} x^3 + \alpha\left(1 + 2x + 3x^2 + 4x^3\right)\sin(wt) \tag{1}$$

where k_l, k_{nl} represent the linear and nonlinear restoration coefficients, respectively, μ is a damping coefficient obtained from the combination of DC and AC current bias, and α and w are the amplitude and frequency of actuation, respectively.

2 Numerical Simulation

Considering Eq. (1) in the state-space notation, given as:

$$\begin{aligned} \dot{x}_1 &= x_2 \\ \dot{x}_2 &= -\mu x_2 - k_l x_1 - k_{nl} x_1^3 + \alpha\left(1 + 2x_1 + 3x_1^2 + 4x_1^3\right)\sin(wt) \end{aligned} \tag{2}$$

Figures 2 show the dynamic behavior of the MEMS (2). The parameters which were considered to carry out the numerical simulations are the following ones: $x_1(0)$=0.0001, $x_2(0)$=0.0006, α = 0.64, μ = 0.03, k_l = -0352, $3 \le k_{nl} \le 15$, α=0.64 and w=1 [8].

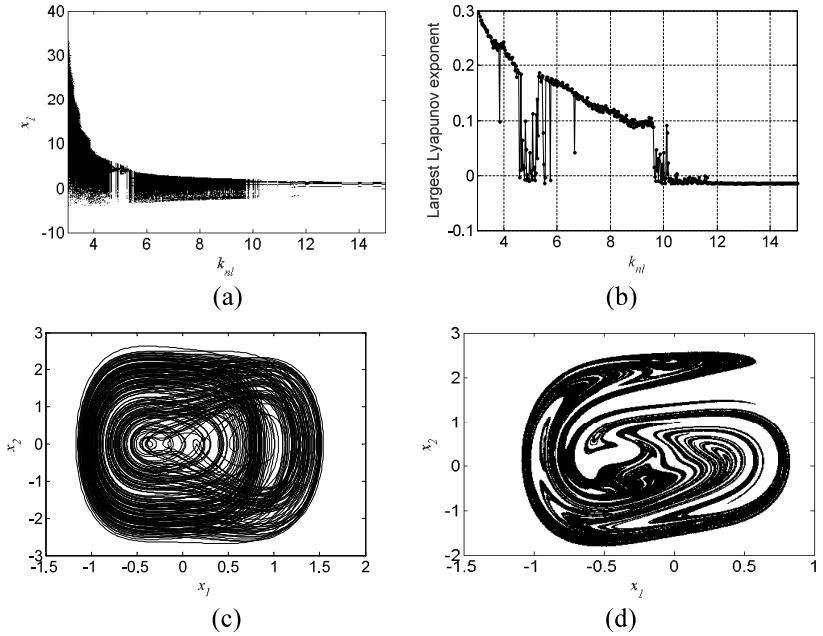

Figure 2. (a) Bifurcation diagram for $3 \le k_{nl} \le 15$; (b) Largest Lyapunov exponent for $3 \le k_{nl} \le 15$; (c) Phase portrait for $k_{nl} = 7.5$; (d) Poincare map for $k_{nl} = 7.5$

As can be observed in Fig. 2, the system (2) has a chaotic behavior. As chaos is commonly undesired by its irregular and disorderly trajectory in most of dynamical systems, some control techniques are presented and discussed in the next section.

3 Chaos control

The objective here is to define a control law U that leads the MEMS of Eq. (1) from any initial condition $x(0) = x_0$ to a desired orbit $x(t) = x^*$, where x^* is previously due or obtained by the control law. Considering the introduction of the control signal U in Eqs. (2), the control system is obtained as:

$$\begin{aligned} \dot{x}_1 &= x_2 \\ \dot{x}_2 &= -\mu x_2 - k_l x_1 - k_{nl} x_1^3 + \alpha\left(1 + 2x_1 + 3x_1^2 + 4x_1^3\right)\sin(wt) + U \end{aligned} \tag{3}$$

Furthermore, the following orbits are considered as the desired ones:

$$[\sin(2t) \quad 2\cos(2t)]^T \tag{4}$$

3.1 Chaos Control by Time Delayed Feedback Control

The time-delayed feedback control was proposed by Pyragas considering the difference of the current velocity and the last velocity with a time lag (τ) [9].

In this way, the control signal U can be obtained from the following equation:

$$U = k_{td}\left(x_2(t-\tau) - x_2(t)\right) \tag{5}$$

The value of τ is set at $\tau = \frac{2\pi}{w}$. In Fig. 3, it can be observed the control system (3) with the application of the control signal (5), being that $\tau = \frac{2\pi}{1}$, and defining $k_{td} = 0.46$.

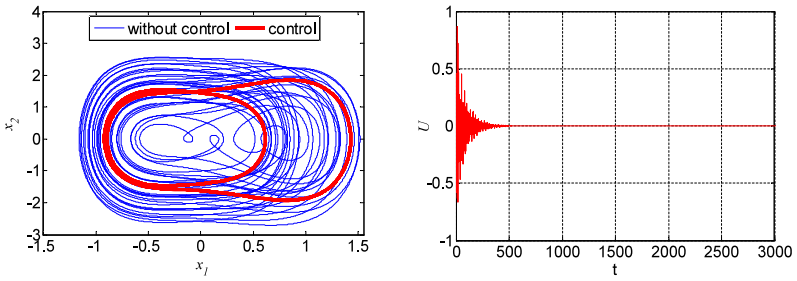

Figure 3. (a) Phase portrait at steady state. (b) Variation of the control signal U.

3.2 Chaos Control by OLFC

The technique of Optimum Linear Feedback Control (OLFC) was developed by Rafikov and Balthazar [10]. Such control is obtained considering two control strategies: $U = \tilde{u} + u$ being that $\tilde{u}$ is the feedforward control and u is the feedback control. The feedforward control can be obtained by considering that the system is already in the desired point $[\tilde{x}_1 \quad \tilde{x}_2]^T$, in this case the feedback control is $u = 0$. Thus, the control signal u is given by:

$$\tilde{u} = \dot{\tilde{x}}_2 + \mu\tilde{x}_2 + k_l\tilde{x} + k_{nl}\tilde{x}_1^3 - \alpha\left(1 + 2\tilde{x}_1 + 3\tilde{x}_1^2 + 4\tilde{x}_1^3\right)\sin(t) \tag{6}$$

Substituting Eq. (6) into Eq. (3) and considering $[x_1 - \tilde{x}_1 \quad x_2 - \tilde{x}_2]^T$ as an error, the control system is given as:

$$\begin{aligned}
&\dot{e}_1 = e_2 \\
&\dot{e}_2 = -\mu e_2 - k_l e_1 - k_{nl}\left(e_1 + \tilde{x}_1\right)^3 + \alpha\left(1 + 2\left(e_1 + \tilde{x}_1\right) + 3\left(e_1 + \tilde{x}_1\right)^2 + 4\left(e_1 + \tilde{x}_1\right)^3\right)\sin(wt) + \\
&+ \dot{\tilde{x}}_2 + \mu\tilde{x}_2 + k_l\tilde{x} + k_{nl}\tilde{x}_1^3 - \alpha\left(1 + 2\tilde{x}_1 + 3\tilde{x}_1^2 + 4\tilde{x}_1^3\right)\sin(t) + u
\end{aligned} \tag{7}$$

The system of equations (7) can be represented in the following matrix form:

$$\dot{\mathbf{e}} = \mathbf{A}\mathbf{e} + \mathbf{B}\mathbf{u} + \mathbf{G}(\mathbf{e}, \tilde{\mathbf{x}}) \tag{8}$$

where $\mathbf{G}(\mathbf{e}, \tilde{\mathbf{x}})$ represents the matrix of nonlinear terms, $\mathbf{A} = \begin{bmatrix} 0 & 1 \\ -k_l & -\mu \end{bmatrix}$ and $\mathbf{B} = \begin{bmatrix} 0 \\ 1 \end{bmatrix}$. The control $\mathbf{u}$ is obtained from the following equation:

$$\mathbf{u} = -\mathbf{R}^{-1}\mathbf{B}^{\mathrm{T}}\mathbf{P}\mathbf{e} \tag{9}$$

where $\mathbf{P}$ is a symmetric matrix and can be obtained from the Riccati algebraic equation:

$$\mathbf{PA} + \mathbf{A}^{\mathrm{T}}\mathbf{P} - \mathbf{PBR}^{-1}\mathbf{B}^{\mathrm{T}}\mathbf{P} + \mathbf{Q} = 0 \tag{10}$$

where **Q** is a definite symmetric or semi-definite positive matrix, and **R** is a symmetric positive definite matrix. The matrices **Q** and **R** are defined as:

$$\mathbf{Q} = \begin{bmatrix} 100 & 0 \\ 0 & 100 \end{bmatrix} \qquad \mathbf{R}=1 \tag{11}$$

In Fig. 4, it can be seen the MEM systems with the introduction of the OLFC control.

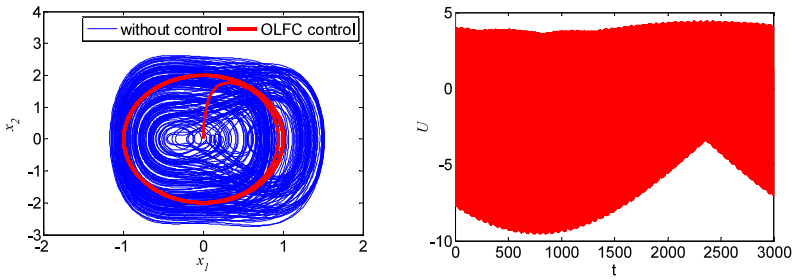

(a) (b)

Figure 4. (a) Phase portrait. (b) Variation of the control signal **U**.

4 Conclusions

In this work two control techniques were presented in a MEM system. The aim of the techniques is to eliminate the chaotic behavior of the system. As can be observed, both strategies were efficient in maintaining the amplitude and frequency of the oscillator in a periodic orbit. For the case where the orbit is imposed, the OLFC control has proven to be efficient in keeping the system within the imposed limits. As expected, the time delayed feedback control led the system to a periodic orbit using the lowest energy, the only problem of its usage is in the event that a different orbit is obtained from the control.

References

[1] R. M. C. Mestrom, R. H. B. Fey, J. T. M. van Beek, K.L. Phan, H. Nijmeijer, Modeling the dynamics of a MEMS resonator. *Simulations and experiments. Sens Actuators A*, **142**, 06 -15, 2007.

[2] A. M. Tusset, J. M. Balthazar, D. Bassinello, B. R. Pontes Jr, J. L. P Felix, Statements on chaos control designs, including a fractional order dynamical system, applied to a "MEMS" comb-drive actuator. *Nonlinear Dynamics*, **69**, 1837-1857, 2012.

[3] M. Roukes, Nanoelectromechanical systems face the future. *Phys. World,* **14**, 2001.

[4] H. Xie, G. Fedder, Vertical comb-finger capacitive actuation and sensing for coms-MEMS, *Sensors Actuators A*, **95**, 212-221, 2002.

[5] M. I. Younis, A. H. Nayfeh, A study of the nonlinear response of a resonant microbeam to an electric actuation, *Nonlinear Dyn,* **31**, 91-117, 2003.

[6] M. Pandey, R. H. Rand, A. T. Zehnder, Frequency locking in a forced Mathieu–van der Pol–Duffing system, *Nonlinear Dyn*, **54**, 3–12. 2008.

[7] M. Pandey, K. Aubin, M. Zalalutdinov, R. B. Reichenbach, A. T. Zehnder, R. H. Rand, J. Parpia, H. G. Craighead, Limit Cycle Oscillations in CW Laser-Driven NEMS, *Journal of Microelectromechanical Systems*, **13**, 1018:1026, 2004,

[8] S. Sabarathinam, K. Thamilmaran, Implementation of analog circuit and study of chaotic dynamics in a generalized Duffing-type MEMS resonator. *Nonlinear Dyn*, **87**, 2345–2356. 2017.

[9] K. Pyragas, Continuous control of chaos by self-controlling feedback. *Phys. Lett. A*, **170,** 421-428, 1992.

[10] M. Rafikov, J. M. Balthazar, On control and synchronization in chaotic and hyperchaotic systems via linear feedback control. *Communications in Nonlinear Science and Numerical Simulation*, **13,** 1246-1255, 2008.

EUROMECH Colloquium 603
Dynamics of micro and nano systems
5 – 7 September 2018, Porto, Portugal

Free, geometrically non-linear, periodic vibrations of non-local plates by a mixed model

Pedro Ribeiro[1] and Tomás Chuaqui[2]

[1] DEMec/INEGI, Faculty of Engineering, University of Porto, Porto, Portugal
pmleal@fe.up.pt

[2] University of Bath, Bath, UK
trcc20@bath.ac.uk

Summary. A multi-degree-of-freedom mixed formulation is applied to investigate free, non-linear, periodic vibrations of nanoplates. In order to take small scale effects into account, a non-local theory is employed. The formulation is mixed in the sense that it resorts to Airy's stress function and to the transverse displacement. With this formulation, it is feasible to arrive at solvable equations of motion that are, simultaneously, non-local and non-linear. With the multi-degree-freedom approach followed, it is possible to investigate modal interactions promoted by the non-linearity, an originality in non-linear free vibrations of non-local plates. In order to illustrate the importance of non-local effects, an example on an orthotropic plate is provided.

Keywords: Nanoplates, mixed formulation, multi-degree-of-freedom, non-local, non-linear, vibrations.

1 Introduction

It is envisaged that plates with dimensions of a few nanometres will be increasingly employed, with expected applications including devices for holographic data storage, devices for electroanalysis, field effect transistors and solar cells [1, 2]. These nanoplates have very small thickness; if they undergo amplitudes larger than about a tenth of that thickness, then non-linear effects become noticeable [3-6]. Furthermore, at the nanoscale, the classical theory of elasticity may fail to provide accurate enough results, because it does not account for effects that become important when the dimensions are very small [7].

The non-local elasticity theory of Eringen [8] takes into account the effect of long range forces and has been often used to derive mathematical models for nanoplates. In the non-linear regime, it is difficult to arrive at a solvable displacement based non-local model [9], and models that employ a stress function and the transverse displacements – which we will call "mixed models" - have been proposed [3-6]. To the best of the authors' knowledge, single degree of freedom mixed models have essentially been applied in the literature to investigate non-linear vibrations of nanoplates. Non-linear effects are known to be behind modal coupling in plates, which can cause significant changes in the dynamic behaviour, but can only be studied using multi-degree-of-freedom mathematical models [10, 11].

In the work briefly described in this short paper, a multi-degree-of-freedom mixed and non-local model is derived and applied to investigate free, periodic, vibrations of nanoplates. The influence of the small scale in the free non-linear vibrations of nanoplates is discussed.

2 Mathematical model

The displacement field applied is based on Kirchhoff's hypotheses, with the displacement components of any point of the nanoplate determined by the displacement components of points on its middle surface (u^0, v^0 and w^0, along the directions of Cartesian axes x, y and z, respectively). Rectangular nanoplates are of interest here, with the length, width and thickness respectively represented by a, b and h.

Eringen originally presented the non-local constitutive relation as an integro-partial differential equation; however, in the case of plates that equation can be reduced to a second-order differential equation [8]. More, specifically, for thin orthotropic plates with a Von Kármán type non-linearity, the following vector differential equation holds [6, 12]

$$\begin{Bmatrix}\sigma_{xx}\\ \sigma_{yy}\\ \sigma_{xy}\end{Bmatrix}-\mu\nabla^2\begin{Bmatrix}\sigma_{xx}\\ \sigma_{yy}\\ \sigma_{xy}\end{Bmatrix}=\begin{bmatrix}\tilde{c}_{11} & \tilde{c}_{12} & 0\\ \tilde{c}_{12} & \tilde{c}_{22} & 0\\ 0 & 0 & \tilde{c}_{33}\end{bmatrix}\begin{Bmatrix}\dfrac{\partial u^0}{\partial x}+\dfrac{1}{2}\left(\dfrac{\partial w^0}{\partial x}\right)^2\\ \dfrac{\partial v^0}{\partial y}+\dfrac{1}{2}\left(\dfrac{\partial w^0}{\partial y}\right)^2\\ \dfrac{\partial u^0}{\partial y}+\dfrac{\partial v^0}{\partial x}+\dfrac{\partial w^0}{\partial x}\dfrac{\partial w^0}{\partial y}\end{Bmatrix} \tag{1}$$

where σ_{ij} represent stresses, $\tilde{c}_{ij}$ are reduced stiffnesses, obtained assuming plane stress conditions [13], and ∇^2 represents the Laplacian operator. Non-local parameter μ is equal to $(e_0 a)^2$, where a is an internal characteristic length (as a lattice parameter) and e_0 is a constant that depends on the material.

Applying the non-local operator $L_{nlocal}=1-\mu\nabla^2$ to the equations of motion (which can be derived by a variational principle) and neglecting rotary inertia, the following equation is obtained

$$\begin{aligned}&\left(1-\mu\nabla^2\right)\frac{\partial^2 M_{xx}}{\partial x^2}+2\left(1-\mu\nabla^2\right)\frac{\partial^2 M_{xy}}{\partial y\partial x}+\left(1-\mu\nabla^2\right)\frac{\partial^2 M_{yy}}{\partial y^2}+\\ &+\left(1-\mu\nabla^2\right)\left(N_{xx}\frac{\partial^2 w^0}{\partial x^2}+2N_{xy}\frac{\partial^2 w^0}{\partial y\partial x}+N_{yy}\frac{\partial^2 w^0}{\partial y^2}\right)=\left(1-\mu\nabla^2\right)\left(\rho h\frac{\partial^2 w^0(x,y,t)}{\partial t^2}\right),\end{aligned} \tag{2}$$

where the stress resultants are represented by N_{xx}, N_{xy} and N_{yy} (in-plane forces per unit length), and by M_{xx}, M_{xy} and M_{yy} (bending and twisting moments per unit length). Introducing Airy's stress function Φ [13], equation (2) can be transformed into

$$\begin{aligned}&D_{11}\frac{\partial^4 w^0}{\partial x^4}+2\left(D_{12}+2D_{66}\right)\frac{\partial^4 w^0}{\partial x^2\partial y^2}+D_{22}\frac{\partial^4 w^0}{\partial y^4}\\ &-\left(1-\mu\nabla^2\right)h\left(\frac{\partial^2\Phi}{\partial y^2}\frac{\partial^2 w^0}{\partial x^2}-2\frac{\partial^2\Phi}{\partial x\partial y}\frac{\partial^2 w^0}{\partial y\partial x}+\frac{\partial^2\Phi}{\partial x^2}\frac{\partial^2 w^0}{\partial y^2}\right)=-\left(1-\mu\nabla^2\right)\left(\rho h\frac{\partial^2 w^0}{\partial t^2}\right),\end{aligned} \tag{3}$$

where D_{ij}, i,j=1,2,6 are the bending stiffnesses [13]. Airy's stress function allows us to circumvent difficulties associated with non-local, non-linear displacement based formulations, difficulties which are discussed in [9, 14]. There are two unknown functions in equation (3) and the compatibility equation, including the non-local effects as in reference [6], is employed to complement it.

The transverse displacement and Airy's stress function are expanded in series

$$\begin{cases}w^0(\xi,\eta,t)\cong\displaystyle\sum_{i=1}^{p_o}\sum_{j=1}^{p_o}f_i(\xi)f_j(\eta)q_{ij}^w(t)\\ \Phi(\xi,\eta,t)\cong\displaystyle\sum_{r=1}^{p_\Phi}\sum_{s=1}^{p_\Phi}t_r(\xi)t_s(\eta)q_{rs}^\Phi(t)\end{cases}, \tag{4}$$

where $f_i(\xi)$ and $t_r(\xi)$ are one-dimensional shape functions, and $q_{ij}^w(t)$ and $q_{rs}^\Phi(t)$ represent generalized coordinates. The $f_i(\xi)$ approximation functions used are the ones successfully employed in [15, 16]. The $t_r(\xi)$ approximation functions should be chosen in accordance with the normal stress at the boundaries.

Inserting expansions (4) in equation (3) and in the compatibility equation, one arrives at a set of non-linear ordinary differential equations which, after condensation, only contain non-linear terms of cubic type. It is re-emphasised that, unlike generally done in the literature, a multi-degree-of-freedom model is here applied. This is important not only due to increased accuracy, but also because it allows one to investigate modal couplings.

Applying the harmonic balance method, the ordinary differential equations of motion are transformed to algebraic equations in the frequency domain; the latter are solved by a continuation method [17].

3 Sample results

To illustrate the analysis carried out, backbone curves of a square orthotropic nanoplate constituted by a two-phase ferroelectromagnetic nanocomposite ($BiTiO_3$-$CoFe_2O_4$) [6, 18] are presented in this short paper. The material properties, taken from [6], are: c_{11}=c_{22}=226 GPa, c_{12}=125 GPa, c_{13}=124 GPa, c_{33}=216 GPa and c_{66}=50.5 GPa; χ=0 and χ=0.3 (where χ=e_0a_i/a). The reduced stiffnesses, which relate stresses and strains when a plane stress state is assumed, are obtained from elastic stifnesses c_{ij} using equations given in [6, 13]. The boundaries are simply-supported and movable in-plane; the latter condition was here approached by making in-plane normal stresses at the edges equal to zero. Employing just a one degree of freedom model, as in [6], the present approach provided backbone curves fairly similar to the ones of that reference.

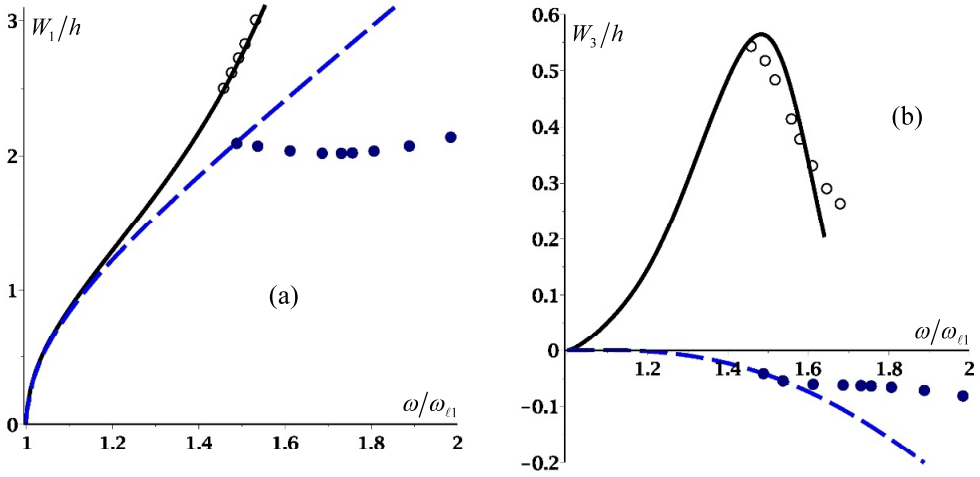

Figure 1. (a) First harmonic, (b) Third harmonic; χ=0.0 (local): main branch – –, secondary branch ●;χ=0.3 (non-local): main branch ——, secondary branch o.

Figure 1 shows the amplitudes (with sign) of the first (W_1) and third (W_3) harmonics at the centre of the plate, calculated considering non-local effects (χ=0.3) and neglecting them (χ=0.0); the number of one dimensional approximation functions employed to compute these values is p_o=6 and p_Φ=12 (equation (4)). Initially, as the vibration amplitude increases, the evolution of the first harmonic, considering and neglecting non-local effects, is approximately the same. However, for larger vibration amplitudes, the amplitude of the first harmonic is very different in the local and non-local cases. The deviation in the first harmonic is accompanied by a, relatively larger, change in the third harmonic. Bifurcations occur at different amplitudes of the harmonics in local and non-local plates. Furthermore, the secondary branches that appear at bifurcations have rather distinct evolutions. It was verified that these very significant differences in the backbone curves are accompanied by dissimilarities in the shapes assumed by the nanoplate along a cycle of vibration.

4 Concluding remarks

A mixed, multi-degree-of-freedom, non-linear and non-local mathematical model is proposed to investigate free, periodic vibrations of nanoplates. It is found that non-local effects can lead to considerable differences in the dynamic behaviour of these very small plates in the non-linear regime, chiefly due to differences in the modal interactions that occur with and without them. It is well known that the importance of non-local effects increases as the reference dimensions decrease. Hence, one immediately realises that higher order modes of vibration, which are related with shorter wavelengths, should be more influenced than the first mode by non-local effects. Since the non-linearity can promote interaction between the first and higher order modes, the non-local effects can alter very significantly the dynamics of nanoplates experiencing large amplitude oscillations.

Acknowledgments

The first author gratefully acknowledges the funding of Project NORTE-01-0145-FEDER-000022 - SciTech - Science and Technology for Competitive and Sustainable Industries, cofinanced by Programa Operacional Regional do Norte (NORTE2020), through Fundo Europeu de Desenvolvimento Regional (FEDER).

References

[1] K.S. Novoselov, A.K. Geim, S.V. Morozov, D. Jiang, Y. Zhang, S.V. Dubonos, I.V. Grigorieva, A.A. Firsov, Electric Field Effect in Atomically Thin Carbon Films. *Science*, **306**, 666-669, 2004.
[2] F. Bonaccorso, Z. Sun, T. Hasan, A.C. Ferrari, Graphene photonics and optoelectronics. *Nature Photonics*, **4**, 611-622, 2010.
[3] L. Shen, H.-S. Shen, C.-L. Zhang, Nonlocal plate model for nonlinear vibration of single layer graphene sheets in thermal environments. *Computational Materials Science*, **48**, 680-685, 2010.
[4] E. Jomehzadeh, A.R. Saidi, A study on large amplitude vibration of multilayered graphene sheets. *Computational Materials Science*, **50**, 1043-1051, 2011.
[5] H.B. Li, Y.D. Li, X. Wang, X. Huang, Nonlinear vibration characteristics of graphene/piezoelectric sandwich films under electric loading based on nonlocal elastic theory. *Journal of Sound and Vibration*, **358**, 285-300, 2015.
[6] A. Farajpour, M.R. Hairi Yazdi, A. Rastgoo, M. Loghmani, M. Mohammadi, Nonlocal nonlinear plate model for large amplitude vibration of magneto-electro-elastic nanoplates. *Composite Structures*, **140**, 323-336, 2016.
[7] L.F. Wang, H.Y. Hu, Flexural wave propagation in single-walled carbon nanotubes, *Physical Review B*, **71**, 195412, 2005.
[8] A. Eringen, On differential equations of nonlocal elasticity and solutions of screw dislocation and surface waves. *Journal of Applied Physics*, **54**, 8, 1983.
[9] T.R.C. Chuaqui, P. Ribeiro, On displacement based non-local models for non-linear vibrations of thin nano plates. *MATEC Web of Conferences*, **148**, 07004, 2018.
[10] M.H. Matheny, L.G. Villanueva, R.B. Karabalin, J.E. Sader, M.L. Roukes, Nonlinear Mode-Coupling in Nanomechanical Systems. *Nano Letters*, **13**, 1622-1626, 2013.
[11] P. Ribeiro, M. Petyt, Non-linear free vibration of isotropic plates with internal resonance. *International Journal of Non-Linear Mechanics*, **35**, 263-278, 2000.
[12] C. Liu, L.-L. Ke, Y.-S. Wang, J. Yang, S. Kitipornchai, Thermo-electro-mechanical vibration of piezoelectric nanoplates based on the nonlocal theory. *Composite Structures*, **106**, 167-174, 2013.
[13] C.Y. Chia, *Nonlinear Analysis of Plates*. McGraw-Hill International Book Company, New York, 1980.
[14] T.R.C. Chuaqui, *Linear and non-linear vibrations of single-layer graphene sheets*, Master dissertation, DEMec, Faculty of Engineering, University of Porto, Porto, pp. 93, 2016.
[15] N.S. Bardell, Free-vibration analysis of a flat-plate using the hierarchical finite-element method. *Journal of Sound and Vibration*, **151**, 263-289, 1991.
[16] W. Han, M. Petyt, K.M. Hsiao, An investigation into geometrically non-linear-analysis of rectangular laminated plates using the hierarchical finite element method. *Finite Elements in Analysis and Design*, **18**, 273-288, 1994.
[17] R. Lewandowski, Nonlinear free-vibrations of beams by the finite-element and continuation methods. *Journal of Sound and Vibration*, **170**, 577-593, 1994.
[18] L.-L. Ke, Y.-S. Wang, J. Yang, S. Kitipornchai, Free vibration of size-dependent magneto-electro-elastic nanoplates based on the nonlocal theory. *Acta Mechanica Sinica*, **30**, 516-525, 2014L.-L. Ke, Y.-S. Wang, J. Yang, S. Kitipornchai, Free vibration of size-dependent magneto-electro-elastic nanoplates based on the nonlocal theory, Acta Mechanica Sinica, 30 (2014) 516-525.

Multiple scales analysis of MEMS resonators under the simultaneous excitation of subharmonic and primary resonances

Saad Ilyas, Feras K. Alfosail and Mohammad I. Younis

Physical Sciences and Engineering Division,
King Abdullah University of Science and Technology, Thuwal, KSA
saad.ilyas@kaust.edu.sa, feras.alfosail@kaust.edu.sa, mohammad.younis@kaust.edu.sa

Summary. We present a comprehensive analytical solution for an electrostatically actuated MEMS resonator via the method of Multiple Time Scales (MTS) and verify it against experiments. Furthermore, we compare the results from different techniques used to solve for such systems and draw conclusions. Finally, we propose application of MEMS resonator for small charge sensing by using strong subharmonic and weak primary-resonance excitation.

Keywords: Multiple Time Scales, subharmonic excitation, MEMS electrometer

1 Introduction

Perturbation techniques such as the Method of Multiple Time Scales (MTS) have been extensively used to analytically predict the behaviour of nonlinear oscillators [1,2]. Electrostatically actuated MEMS resonators have been also studied using such techniques under primary as well as secondary excitations [2, 3].

When actuating a MEMS resonator using a parallel-plate electrostatic force with a DC component superimposed to an AC harmonic load around its primary resonance; the quadratic form of the electrostatic voltage transforms the actuation into two source excitation with one frequency around the primary resonance and the other of twice that. However, the contribution from the double frequency component is usually considered negligible compared to the dominant effect of the primary resonance excitation. In this work however, we consider the case of large AC voltages, where the resonator gets excited considerably from both frequency components, leading to competing effects from subharmonic and primary resonance excitations. We present a comprehensive analytical solution based on MTS for general loading cases, which account for most practical excitation conditions.

2 Problem formulation

The equation of motion for an electrostatically actuated MEMS microbeam using lumped parameter modelling is given by

$$\ddot{x}(t)+2\mu\dot{x}(t)+x(t)=\frac{\beta}{(1-x(t))^2}\left[\overbrace{\left(V_{DC}^2+\frac{V_{AC}^2}{2}\right)}^{V_{eff}\ \text{(static)}}+\overbrace{2V_{DC}V_{AC}\cos(\Omega t)}^{\text{Primary}}+\overbrace{\frac{V_{AC}^2}{2}\left(\cos(2\Omega t)\right)}^{\text{subharmonic}}\right] \tag{1}$$

Where μ and β are nondimensional damping and voltage terms, respectively.

In this work, we perform the multiple scale analysis on the following three cases derived by expanding the RHS of (1) in Taylor expansion and considering different higher order terms, and compare against the long time integration (LTI) solution of (1)

1) The case of primary excitation only (assuming $V_{DC}>>V_{AC} \Rightarrow V_{eff}=V_{DC}^2$)

$$\ddot{u}+2\mu\dot{u}+\alpha_q u^2+\alpha_c u^3+\omega^2 u=F_p\cos(\Omega t) \tag{2}$$

2) The case of combination of primary and subharmonic excitation

$$\ddot{u}+2\mu\dot{u}+\alpha_q u^2+\alpha_c u^3+\omega^2 u=F_p\cos(\Omega t)+F_s\cos(2\Omega t) \tag{3}$$

3) The case of combination of primary and subharmonic excitation including the parametric terms

$$\ddot{u}+2\mu\dot{u}+\alpha_q u^2+\alpha_c u^3+\omega^2 u=F_p\cos(\Omega t)+F_s\cos(2\Omega t)+F_{spar1}\cos(2\Omega t)u+F_{spar2}\cos(2\Omega t)u^2 \tag{4}$$

where $\alpha_q = \frac{-3\beta V_{eff}}{(1-\delta)^4}$; $\alpha_c = \frac{-4\beta V_{eff}}{(1-\delta)^5}$; $\omega^2 = 1 - \frac{2\beta V_{eff}}{(1-\delta)^3}$; $F_p = \frac{2\beta V_{DC} V_{AC}}{(1-\delta)^2}$; $F_s = \frac{\beta V_{AC}^2}{2(1-\delta)^2}$; $F_{spar1} = \frac{\beta V_{AC}^2}{(1-\delta)^3}$; $F_{spar2} = \frac{3\beta V_{AC}^2}{2(1-\delta)^4}$

3 Results

We observe from figure 1, that for cases where the V_{DC}>>V_{AC}, case 1 accurately predicts the response of the microresonator. However, as V_{AC} becomes large, the contribution from the subharmonic excitation term becomes not negligible and case 1 fails. It is interesting to note that even case 2 fails here to predict the accurate response. This is attributed to the missing parametric terms that have significant contribution to the resonator's response. A more comprehensive form is given by case 3, which includes the higher order parametric terms and is able to predict the response more accurately. A slight deviation from the response of LTI of (1) is noticed due to the truncation of higher order forcing terms. This is confirmed by performing LTI on (4), Figure 1(c).

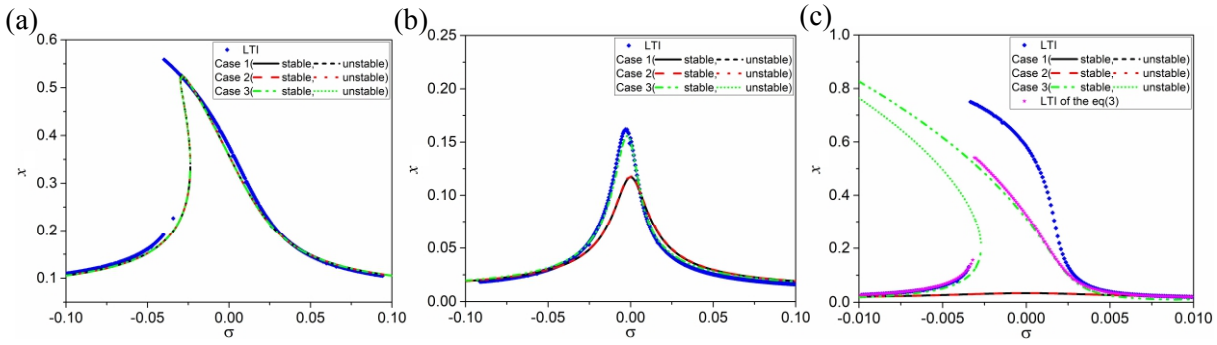

Figure 1. A c-c beam of length 500µm, width 50µm, thickness 3µm, and an operating gap of 3µm is used. Analytical response of the resonator against the frequency detuning parameter σ for (a) V_{DC}=27V, V_{AC}=2V and μ=0.01. (b) V_{DC}=1V, V_{AC}=15V and μ=0.01. (c) V_{DC}=0.1V, V_{AC}=16.5V and μ=0.005.

We observe that there is a competition between the primary and subharmonic excitation, and the response of the resonator is associated to the dominant component. Figure 2 shows that as the V_{DC} is increased; (1) the abrupt onset of the resonance (subharmonic like) diminishes and starts to become more gradual increase in amplitude (primary like), (2) the monostable regime starts to increase. This shows that the influence of primary is very strong as a very small amount of V_{DC} can yield primary dominated response. This behavior is also confirmed experimentally, Figure 2(b), and proposed for applications in MEMS electrometers, where a small amount of added charge (V_{DC}) can be detected by following the frequency jump up point "Ω_j".

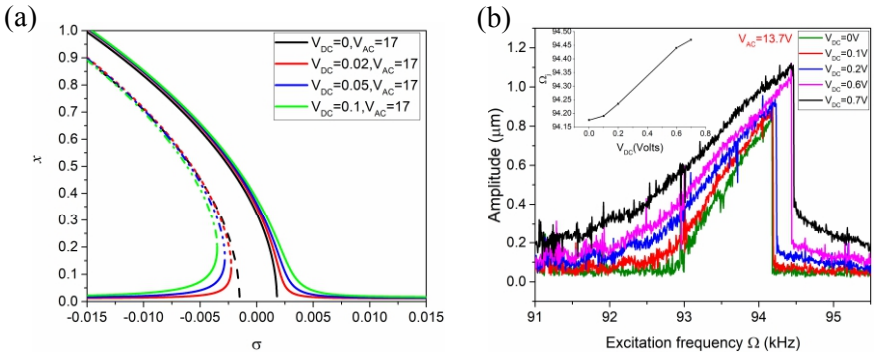

Figure 2. Analytical response of the resonator (case-3) against the frequency detuning parameter σ for variable V_{DC} and V_{AC} values with μ=0.01. (b) Experimental response of a SiN_3 c-c beam of length 500µm, width 50µm, thickness 1.25µm, and an operating gap of 2.5µm.

References

[1] A. H. Nayfeh, M.I. Younis, Dynamics of MEMS resonators under superharmonic and subharmonic excitations. *Journal of Micromechanics and Microengineering*, **15-10**, 1840, 2005.

[2] E.M. Abdel-Rahman, A.H. Nayfeh, Secondary resonances of electrically actuated resonant microsensors. *Journal of Micromechanics and Microengineering*, **13-3**, 491, 2003.

[3] A. H. Nayfeh, *Introduction to perturbation techniques*. John Wiley & Sons, 2011.

Investigating the phenomenon of mode localization in electrostatically and mechanically coupled MEMS resonators

Saad Ilyas and Mohammad I. Younis

Physical Sciences and Engineering Division,
King Abdullah University of Science and Technology, Thuwal, KSA
saad.ilyas@kaust.edu.sa, mohammad.younis@kaust.edu.sa

Summary. We present an experimental investigation of the mode localization phenomenon in mechanically and electrostatically coupled laterally actuated MEMS microbeams. In the first case study, two clamped-clamped beams with a weak mechanical coupling are fabricated and experimentally characterized in air via optical measurement techniques. In the second case study, two cantilever beams with electrostatic coupling are characterized in vacuum (~3-6mTorr) via electrical measurement techniques.

Keywords: Mode localization, Mechanical coupling, Electrostatic coupling

1 Introduction

Static and dynamic behaviours of MEMS resonators when coupled together and interacting with each other become increasingly complex and warrant thorough investigation in order to exploit them or avoid them, when necessary. Recently, significant attention is given to understanding the phenomenon of mode localization and it has been exploited for developing various MEMS sensors [1-3].

In this work, we experimentally investigate two cases, 1) weakly mechanically coupled c-c beams vibrating in air, 2) electrostatically coupled cantilever beams operating in vacuum.

2 Design and fabrication

The devices are fabricated on an SOI wafer via conventional surface micromachining techniques. Figure 1 shows the 3D schematic and important specifications of the coupled systems.

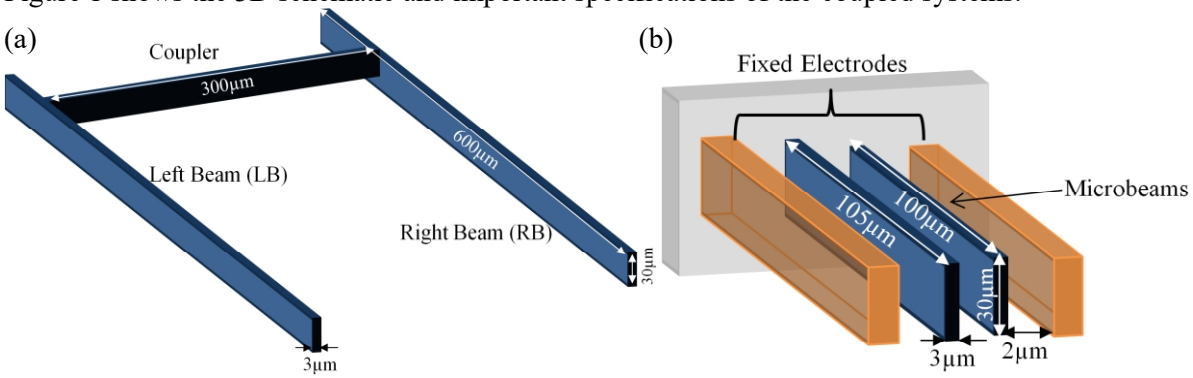

Figure 1. (a) Schematic of the mechanically coupled structure. Each of the beam and the coupler can be separately actuated (operating gap 8µm). (b) Schematic of the electrostatically coupled structure.

3 Results

In order to investigate the dynamics of the mechanically coupled structure, an electrostatic actuation is applied through the LB while the stiffness of each of the beam is separately modulated by passing current through it via application of an electrothermal voltage V_T across the respective beam. Figure 2 shows the response of the mechanically coupled structure. First, by modulating the stiffness of the LB only, we notice that the response of the LB gets localized into first mode, Figure 2(a). However, the RB does not exhibit mode localization but exhibits a split in the frequency of the two modes with decreasing amplitude, Figure 2(a). Next, by modulating the stiffness of RB only, we observe that the

LB now exhibits mode localization into the second mode but the frequency shift observed in Figure 1(a) is absent here. Figure 1(d) shows that the RB shows an almost similar behavior as given by Figure 1(b) in this case as well. The behavior of LB under the two different electrothermal excitations is interesting and can be potentially used for mechancial resonator based logic applications where jump from on-resonance to off-resonance is a key element, Figure 1(e).

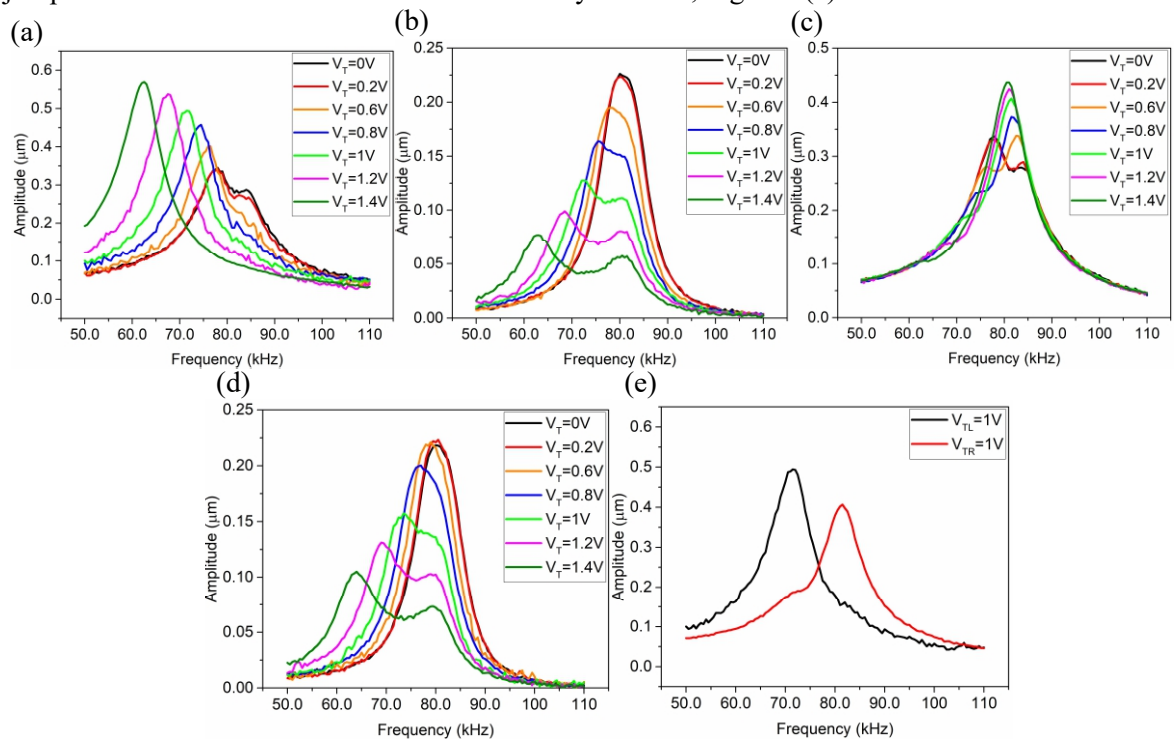

Figure 1. An excitation of V_{DC}=20V, V_{AC}=20V is applied to the LB at atmospheric pressure. Experimental response of the (a) LB and (b) RB with electrothermal voltage V_T applied to the LB, and (c) LB and (d) RB with electrothermal voltage V_T applied to the RB is shown.

Next, we investigate mode localization in the electrostatically coupled structure via modulating the coupling strength by varying the DC bias in between the two cantilevers, Figure 2. We notice here that only the first mode of the coupled structure is affected while the second mode saturates and does not show any shift in resonance frequency or amplitude. Further, experiments on modulating the stiffness of each of the microbeam are to be performed in the future.

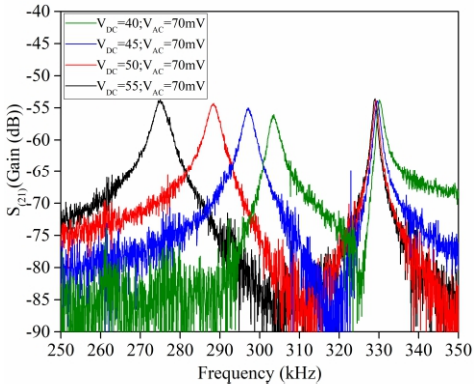

Figure 2. Frequency response of the 105μm beam recorded as the S_{21} transmission signal.

References

[1] C. Zhao, M.H. Montaseri, G.S. Wood, S.H Pu, A.A Seshia, M. Kraft, A review on coupled MEMS resonators for sensing applications utilizing mode localization. *Sensors and Actuators A: Physical*, **249**, 93-111, 2016.

[2] M. Spletzer, A. Raman, A.Q. Wu, X. Xu, R. Reifenberger, Ultrasensitive mass sensing using mode localization in coupled microcantilevers. *Applied Physics Letters*, **88-25**, p.254102, 2006.

[3] C. Zhao, G.S. Wood, J. Xie, H. Chang, H., S.H Pu, M. Kraft, A three degree-of-freedom weakly coupled resonator sensor with enhanced stiffness sensitivity. *Journal of Microelectromechanical Systems*, **25-1**, 38-51, 2016.

EUROMECH Colloquium 603
Dynamics of micro and nano systems
5 – 7 September 2018, Porto, Portugal

Structure and properties of helical carbon nanotubes using MM simulations

Akshay Dahiya[1], **Shakti S. Gupta**[2] **and Romesh C. Batra**[1]

[1]Department of Biomedical Engineering and Mechanics, Virginia Tech, Blacksburg 24061, USA
dakshay7@vt.edu
rbatra@vt.edu

[2] Department of Mechanical Engineering, IIT Kanpur, Kanpur 208016, India
ssgupta@iitk.ac.in

Summary. Helical Carbon Nanotubes (HCNTs) are coiled 3-valent carbon networks which represent pure carbon helix. Here we study the geometry of a helix with 5- and 7-membered rings besides hexagons. For generating this class of helix, molecular graph theory is applied which utilizes 3-coordinated tiling of the plane containing 5-, 6-, and 7-membered rings. The role of eigenvectors of this 2D graph's adjacency matrix is crucial for helix generation as it is based on an appropriate choice of bi-lobial eigenvectors quartet which can be selected on the basis of their nodal properties. To obtain the final structure of an HCNT, we employ MM3 forcefield in Tinker molecular simulation code. The spring constants of various HCNTs are computed through molecular mechanics (MM) simulations.

Keywords: helical carbon nanotubes, molecular modeling, molecular graph theory, molecular mechanics simulations.

1 Introduction

Coiled CNTs, first observed experimentally in 1994 [1], are attractive because of their peculiar morphology and excellent mechanical and electro-magnetic properties. Their structure, formation mechanism and theoretical aspects are still subjects of scientific investigations. In this work, we have implemented Laszlo's [2] method which utilizes three-coordinated tiling in a plane, also known as topological graphs, made of hexagons, pentagons, and heptagons. These topological graphs are used for constructing toroidal and helical carbon structures formed from the corresponding adjacency matrices. The final structure is obtained by using the MM3 [3] based molecular simulations.

Furthermore, we have investigated HCNTs with varying size, shape and structure. To specify the geometry of a coiled CNT, this construction procedure offers complete control over the morphology of the structure. We have analysed the mechanical response of these HCNTs by means of molecular mechanics simulations using Tinker [4] code, employing the MM3 force field, and determined the spring constants of these HCNTs.

2 Modelling HCNTs

Coiled CNTs are created when paired pentagon-heptagon atomic rings arrange themselves periodically in the hexagonal carbon network. The elastic energy of graphene based tubular structures [5] shows that straight helical conformation are stable, without introducing pentagon/heptagon defects. However, we work with HCNTs incorporating 5-7 defects.

Using Laszlo's approach, we take a topological graph containing a particular arrangement of pentagons, hexagons and heptagons as shown in Figure 1. Then, this triply connected tiling is converted into a toroidal structure using an appropriate transformation. For this 3-D transformation, we need to select the four bi-lobial eigenvectors, of the adjacency matrix obtained for the 2-D tiling, which basically represent the four symmetries present in a torus, namely, x, y, z - symmetries and $radial$ symmetry [6]. The final structure is obtained by relaxation using the MM3 force field potential on Tinker platform.

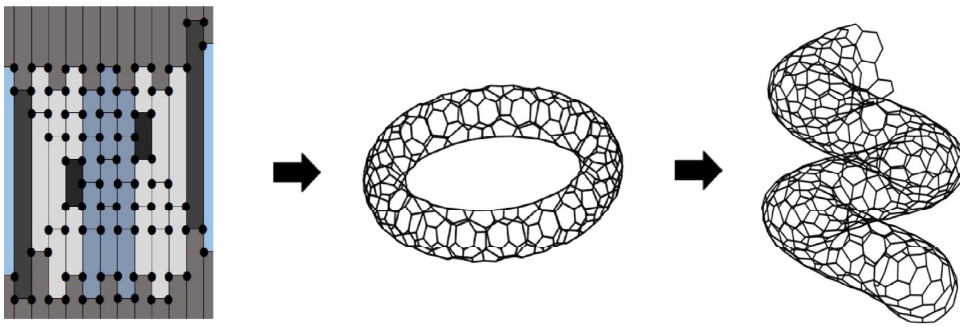

Figure 1. Step-by-step process for making a helical carbon nanotube

3 Molecular mechanics (MM) simulations

The MM3 potential is described as

$$U_{\text{MM3}} = \sum_i \sum_j (U_s + U_\theta + U_\phi + U_{s\theta} + U_{\phi s} + U_{\theta\theta'}) + \sum_i \sum_k (U_{\text{vdW}}), \tag{1}$$

where U_s, U_θ and U_ϕ account for energies associated with changes in bond, angle and dihedral respectively. $U_{s\theta}$, $U_{\theta\theta'}$ and $U_{\phi s}$ account for cross-term interactions among stretching (s), bending (θ), torsional (ϕ), and out-of-plane bending (θ'), respectively. U_{vdW} defines the van der Waals (vdW) potential, is different than the standard 12-6 form, and has terms $(r_c/r)^6$ and $exp(-12r/r_c)$ with r_c as the cut-off distance.

For simulations the nanotubes are first relaxed to the minimum energy configuration using the MINIMIZE subroutine within root mean square gradient of 0.001 Kcal/mol-Å, without employing any constraints. The axial extension and compression tests were performed by fixing the end layer atoms at one end of the tube and incrementing the displacement in the axial direction of the atoms of the other end step-by-step and relaxing the structure at each step.

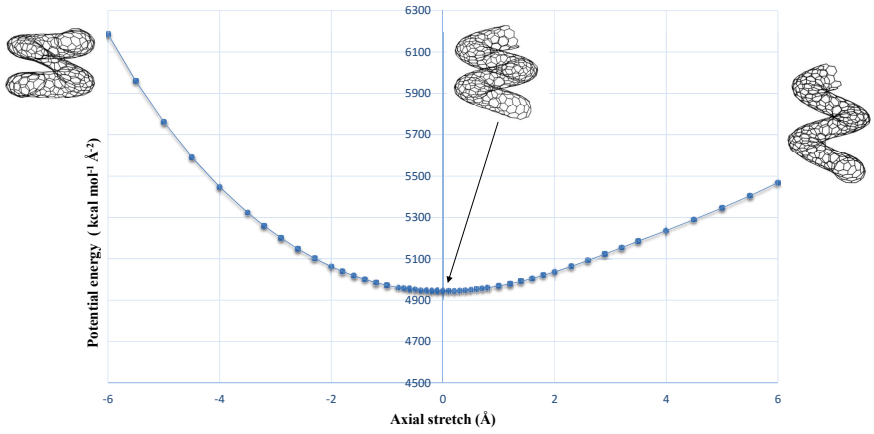

Figure 2. Potential energy vs axial stretch curve for the HCNT generated from the graph parameters depicted by (4, 1, 0, 0, (1, -1), (5, 5)).

4 Results and discussion

In Figure 2, we can see the variation in the potential energy of the HCNT deformed in tension and compression with respect to the relaxed configuration. The rapid rise of the potential energy curve on the compression side as compared to that on the tension side is due to the increase in van der Waal's

interaction energy when two coils come closer during compression. The spring constant in the vicinity of the origin for the tested HCNT is found to be nearly 50 kcal mol^{-1}Å^{-2} or 34.74 N/m.

In Figure 3, we have plotted the k (stiffness) vs n (number of coils) for a variety of HCNTs. The outer coil diamter D (nm), the tubular diameter d (nm), and the helix angle χ (degrees) are listed against their respective curves. In a linear spring, the increase in the number coils, in general, will decrease the spring stiffness. However that trend is not being followed by all the HCNTs thus providing evidence of their non-linear behavior.

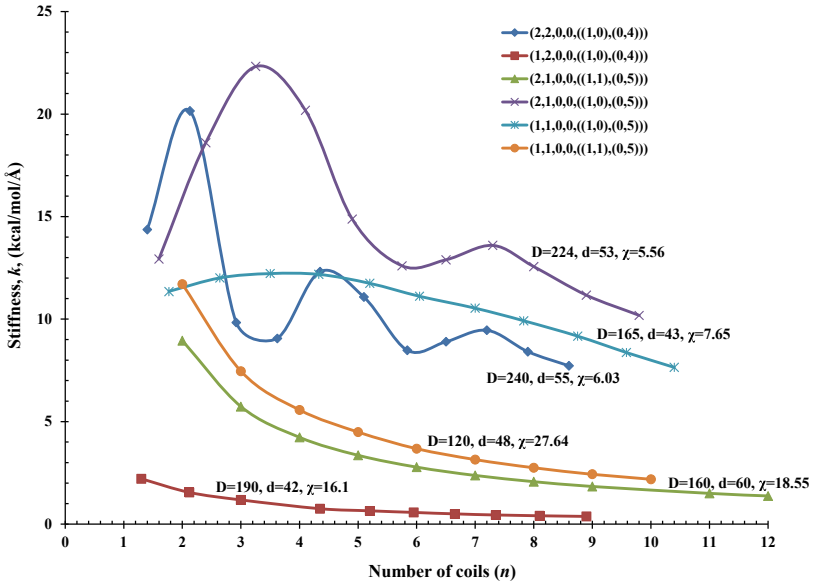

Figure 3. k (stiffness) vs n (number of coils) for different helical carbon nanotubes. The outer coil diamter D (nm), the tubular diameter d (nm), and the helix angle χ (degrees) are listed for all the tubes.

5 Conclusions

We have successfully modelled and obtained stable configurations of helical carbon nanotubes. Using a given periodic tiling by hexagons, pentagons and heptagons, the final relaxed structure depends on the tiling and on the particular position of the super cell. We have computed the spring constant for a number of HCNTs having different morhological parameters. Assuming that an 18% increase in bond length signifies a bond breakage then, in our simulations, no bond failure was observed indicating the superelastic behavior of the HCNTs.

Acknowledgments

We acknowledge the support from the IT and the Computing centres of Virginia Tech USA, IIT Kanpur and IIT Ropar.

References

[1] X. B. Zhang, X. F. Zhang, D. Bernaerts, G. Van Tendeloo, S. Amelinckx, J. Van Landuyt, V. Ivanov, J. B. Nagy, Ph. Lambin, and A. A. Lucas. The Texture of Catalytically Grown Coil-Shaped Carbon Nanotubules, *Europhys. Lett.* (27):**141**, 1994.

[2] Istvan Laszlo and Andre Rassat. The geometric structure of deformed nanotubes and the topological coordinates. *J. Chem. Inf. Comput. Sci.*, (43):**519-524**, 2003.

[3] Norman L. Allinger, Young H. Yuh, and Jenn Huei Lii. Molecular Mechanics. The MM3 Force Field for Hydrocarbons. 1. *Journal of the American Chemical Society*, **111**, (23):85518566, 1989.

[4] J.W. Ponder. Users guide computer code tinker molecular modelling package 4.2, 2004.

[5] O. Y. Zhong can, S. Z. B. Zhao-Bin, C. L. Wang. Coil Formation in Multishell Carbon Nanotubes: Competition between Curvature Elasticity and Interlayer Adhesion, *Phys. Rev. Lett.*, (21) **78**:4055, 1997.

[6] Istvan Laszlo, Andre Rassat, P.W. Fowler, Ante Graovac. Topological coordinates for toroidal structures, *Chemical Physics Letter*, 342: **369-374**, 2001.

EUROMECH Colloquium 603
Dynamics of micro and nano systems
5 – 7 September 2018, Porto, Portugal

Toward Electrostatic Atomic Force Microscopy

Hamidreza Nafissi[1], Ayman Alneamy[2], Eihab Abdel-Rahman[2] and Raafat Mansour[1]

[1]Dept. of Electrical & Computer Engineering, University of Waterloo, Waterloo, Canada
[2]Dept. of Systems Design Engineering, University of Waterloo, Waterloo, Canada

Summary. A scanning force microscope combining electrostatic actuation and capacitive detection is presented. The microscope is composed of off-shelf AFM probes and printed circuit boards (PCBs). A fixed trace on a PCB actuates the AFM probe. The excitation signal is a biased harmonic voltage with a frequency in the vicinity of the probe's resonant frequency. The separation distance between the probe tip and specimen surface is controlled to execute tapping mode scans. Capacitive detection is implemented by measuring the second harmonic of the excitation frequency in the current output of the actuator using a lock-in amplifier. Preliminary results of the magnitude and phase of output current resemble the specimen topography.

Keywords: Atomic Force Microscopy, Electrostatic Actuation, Capacitive Detection, Tapping Mode.

1 Introduction

Scanning probe microscopy (SPM) plays a crucial role in atomic scale investigation of material physical and structural properties in many aspects of science [1]. Since its inception in the eighties, it has experienced immense advancement in design and applications leading to complex and expensive modern SPMs. Cost and complexity have limited access to SPMs and fueled research to simplify them by eliminating, integrating, or miniaturizing various components. Most of these efforts relay on proprietary micromachined device to achieve system integration [2, 3] or to eliminate the need for optical detection [4, 5] by exploiting electromechanical actuation or detection.

Despite the intrinsic nonlinearity of electrostatic actuation, integrating electrostatic actuation and detection in a single device is quite simple. The goal of this research is to develop a simple and cheap atomic force microscope (AFM) made of readily available printed circuit boards (PCBs) and off-shelf AFM probes. Following this approach, a demonstration of a tapping mode electrostatic AFM (EAFM) is carried out. First, we present simulation results for the response of the AFM in tapping mode followed by experimental results of an open-loop raster scan of a calibration grating.

2 Device and operation principle

A schematic of the prototype is depicted in Figure 1. The probe chip, shown in gray, resta on a copper layer that serves as the ground electrode. The probe extends over a thickened copper trace patterned at the edge of the PCB. A harmonic voltage is applied to the trace to electrostatically actuate the grounded probe. Figure 1(b) shows a side view picture of the mounted probe and the actuation trace. The probe is $450\,\mu$m long and the average gap between its upper surface and the trace was measured as $43\,\mu$m. The stylus at the probe tip is $15\,\mu$m in height.

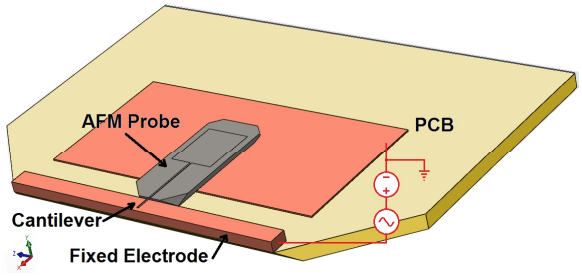

(a) Schematic of the bottom side

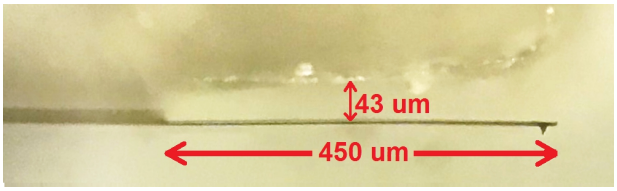

(b) Side-view image

Figure 1: Electrostatic atomic force microscope.

A lumped-mass model is deployed to analyze the motion of the probe. The resulting equation of motion describing the beam tip displacement $x(t)$ can be written as [6]:

$$m\ddot{x} + c\dot{x} + kx = \frac{\epsilon A_{eff}(V_{DC} + V_{AC}\sin(\Omega t))^2}{2(g_\circ - x)^2}, \tag{1}$$

where m is the effective probe mass, c is the damping coefficient, k is the mechanical stiffness of the probe, ϵ is the medium permittivity, $A_{eff} = 3A/8$ is the actuator's effective overlap area, V_{DC} is the bias voltage, V_{AC} and Ω are the amplitude and frequency of the actuation voltage, and $g_\circ$ is the average distance between the probe and actuation trace at rest.

Based on the harmonic balance method, the general solution for this equation can be written as:

$$x(t) = X_\circ + \sum_{n=1}^{p} \epsilon^n X_n \sin(n\Omega t + \phi_n) \tag{2}$$

For small probe oscillations, terms of order $O(\epsilon^2)$ and higher are negligible compared to X_1. Therefore, the tip displacement and velocity can be expressed as:

$$x(t) = X_\circ + X_1 \sin(\Omega t + \phi_1) + O(\epsilon^2) \tag{3}$$

$$\dot{x}(t) = \Omega X_1 \cos(\Omega t + \phi_1) + O(\epsilon^2) \tag{4}$$

where $X_\circ$, X_1 and ϕ_1 are [7, 8, 9]:

$$X_\circ = \frac{\epsilon k A_{eff}}{2g_\circ^2} V_{DC}^2 \ , \quad X_1 = \frac{\epsilon A_{eff}}{k g_\circ^2} V_{DC} V_{AC} \beta \ , \quad \phi_1 = \tan^{-1}\Big(\frac{\Omega/Q\omega}{1 - \frac{\Omega^2}{\Omega_\circ^2}}\Big) \tag{5}$$

β is a magnification factor related to the quality factor Q by

$$\beta = \frac{1}{\sqrt{\Big(1 - \frac{\Omega^2}{\Omega_\circ^2}\Big)^2 + \Big(\frac{\Omega}{Q\omega}\Big)^2}} \quad , \quad Q = \frac{m\omega}{c} \tag{6}$$

and $\omega = \sqrt{\frac{k}{m}}$ is the probe's fundamental natural frequency

The actuator current induced by the probe motion serves as the sensing signal. It can be expressed as:

$$I(t) = \frac{dq}{dt} = \frac{d(CV)}{dt} = V\frac{dC}{dt} + C\frac{dV}{dt}. \tag{7}$$

where $C(t) = C_p + C_a(t)$ is the total capacitance of the electrostatic actuator, C_p is the time-invariant parasitic capacitance, and $C_a(t) = \frac{\epsilon A}{g_\circ}\frac{1}{1-x(t)} = C_\circ \frac{1}{1-x(t)}$ is the actuator capacitance which varies over time because of the probe vibrations. The typical values of $C_a(t)$ are two orders-of-magnitude smaller than C_p.

The actuator current $I(t) = i_p(t) + i_a(t)$ is composed of feed-through current $i_p(t) = V_{AC}C_p\Omega\cos(\Omega t)$, unaffected by the actuator motions, and motion-induced current:

$$i_a(t) = V_{DC}C_\circ \frac{\dot{x}(t)}{(1-x(t))^2} + V_{AC}C_\circ \frac{\dot{x}(t)}{(1-x(t))^2}\sin(\Omega t) + V_{AC}C_\circ\Omega\frac{1}{1-x(t)}\cos(\Omega t) \tag{8}$$

Using Equation (2) in equation (8), expanding around $X_\circ$, ignoring terms of order $O(\epsilon^3)$ and higher, and collecting similar harmonics, we obtain:

$$\begin{aligned} I(t) = {} & V_{AC}\big(C_p + C_\circ - \frac{1}{4}C_\circ X_1^2\big)\Omega\cos(\Omega t) - V_{DC}C_\circ\Omega X_1\sin(\Omega t) \\ & + V_{AC}C_\circ\Omega X_1\cos(2\Omega t) - V_{DC}C_\circ\Omega X_1^2\sin(2\Omega t) + Q(\epsilon^3) \end{aligned} \tag{9}$$

The first harmonic of the current is not useful in displacement detection because it is dominated by C_p. In fact, its average value is two to three orders-of-magnitude larger than the second harmonic. Using a current-to-voltage converter and a lock-in amplifier, the magnitude and phase of the motion induced current at the second harmonic are related to the beam tip displacement by:

$$\begin{aligned} |i_a(t)| &= C_\circ\Omega X_1\sqrt{V_{AC}^2 + (V_{DC}X_1)^2} \\ \angle i_a(t) &= \arctan\Big(\frac{V_{DC}X_1}{V_{AC}}\Big) \end{aligned} \tag{10}$$

3 Analysis of tapping mode

The probe dynamics in tapping mode were simulated [10] for a probe with the properties listed in Table 1 under the voltage waveform $V_a(t) = 47.5 + 47.5\sin(2\pi f_\circ t)$ and excitation frequency $f_\circ = 11.9kHz$. The average gap between the probe and the electrode was set to $g_\circ$ =20 µm.

Table 1: Specifications of CONTV-PT AFM Probe

Parameter	**Nom. Value**
Length L	450 µm
Width b	50 µm
Thickness h	2.0 µm
Spring Constant k	0. N/m
Natural Frequency f_1	13 kHz
Density ρ	2300 kg/m^3
Material	(n) doped silicon

Figure 2 depicts the frequency-response curves and phase portraits of the beam tip for four tip-sample distances. The flat-top of the displacement curves show the effect of restricting the displacement to the tip-sample distance. The results are similar to those of Bahrami and Nayfeh [11].

The fluctuations at the lower end of the flat top for smaller tip-sample distances are due to the existence of a chaotic attractor in that frequency range. This is a characteristic of an impact oscillators. The actuator settled down to periodic tapping oscillations as the frequency increased.

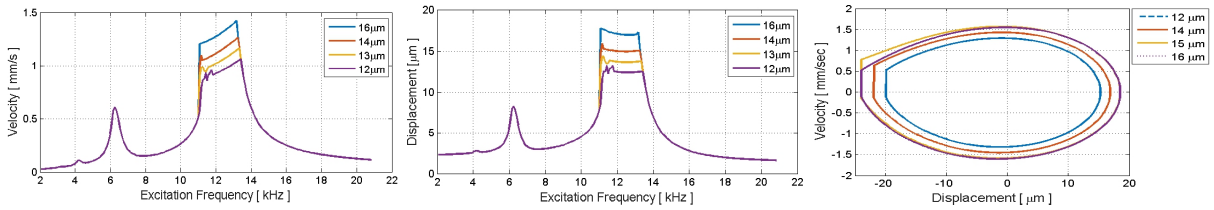

(a) Freq. response of velocity (b) Freq. response of displacement (c) Phase portraits

Figure 2: Response of the electrostatically actuated probe in tapping mode for four tip-sample distances.

Figure 2c shows that all phase portraits are asymmetric. While the electrostatic force pulls the probe above its equilibrium position, the sample surface limits its oscillations from below. The flat regions in the phase portrait represent the tip tapping on the sample surface.

4 Experimental results

The experimental test setup is illustrated in Figure 3. The open-loop configuration includes a lock-in amplifier, a voltage amplifier, a current-to-voltage amplifier and the EAFM. The lock-in amplifier measures the probe current's magnitude and phase at the second harmonic of the excitation signal (2Ω).

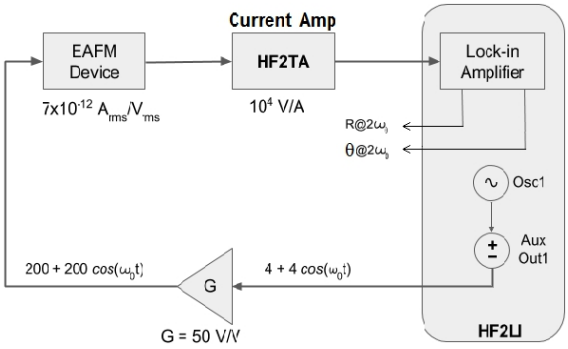

Figure 3: Open-loop test setup.

Figure 4 shows the frequency-response of the current magnitude and phase. Non-contact, tapping, and contact mode frequency-response curves are shown. The curves demonstrate clear differentiation among the current's magnitudes and phases for different tip-sample distances during tapping in contrast to non-contact and contact modes, which shows that both magnitude and phase of the measured current in tapping mode can represent the tip-sample distance and, therefore, the topography of the specimen surface.

Comparing Figure 2a to Figure 4a show that the magnitude of the current's second harmonic is indeed proportional the beam tip velocity (ΩX_1) as indicated by Equation (10). Decreasing the tip-sample distance, decrease the magnitude of current because the smaller oscillatory orbits of the probe produce a lower RMS velocity. This is similar to the contrast between the Non-contact and contact modes current magnitude. Further, tapping oscillations occur over a larger frequency range, which is typical of impact oscillators [11].

As noted above, a chaotic attractor exists at the onset of tapping mode oscillations. To examine

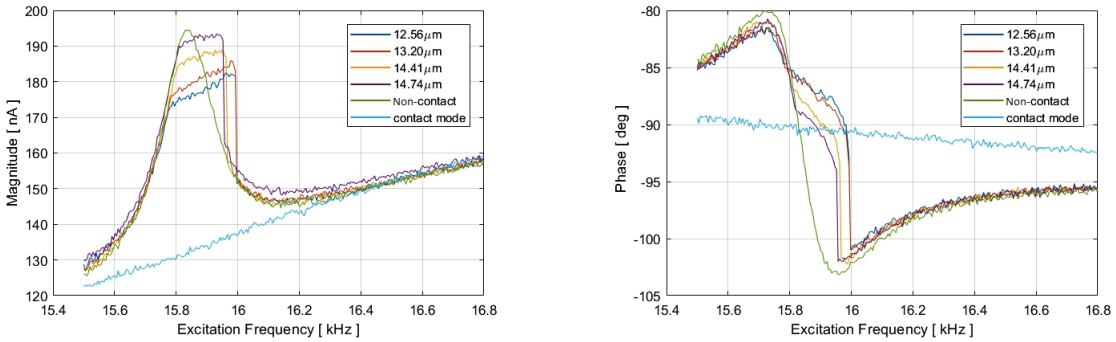

(a) Magnitude (b) Phase

Figure 4: The frequency response of the second harmonic's magnitude and phase in the EAFM current at various tip-sample distances.

the impact of chaos on current measurements, we designed a metric of current regularity by subtracting a smoothed frequency-response curve, obtained by local regression, from the measured frequency-response curve evaluated at the non-contact mode resonance frequency $f_\circ$. The smoothed curves were obtained using the robust version of the LOESS algorithm implemented in Matlab's 'smooth' function. In Figure 5, we plot the regularity metric for the magnitude and phase of the current second harmonic as functions of the tip-sample distance.

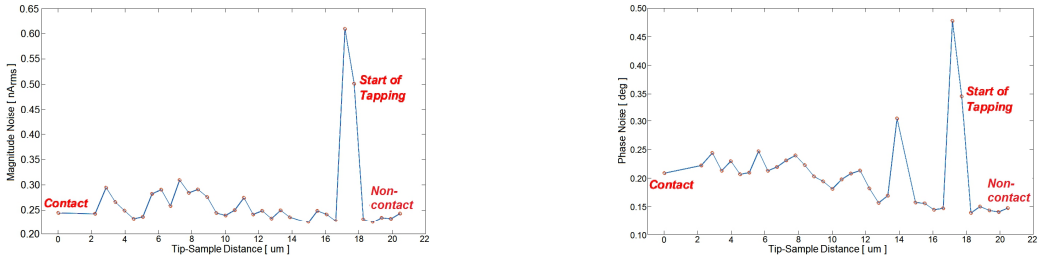

(a) Magnitude regularity (b) Phase regularity

Figure 5: Regularity of the current magnitude and phase as functions of the tip-sample distance for the voltage waveform $V(t) = 75 + 75\sin(2\pi f_\circ t)$ and $f_\circ = 10.54\,\text{kHz}$

Current regularity was evaluated for a probe with a non-contact resonance frequency of $f_\circ = 10.54\,\text{kHz}$. The magnitude and phase curves show that irregularity spikes at the onset of impact, where grazing bifurcation and chaos exist. As the tip-sample distance decreases, the probe oscillations became periodic once again as indicated by the drop in the value of the regularity metric in both magnitude and phase. Therefore, we can use the magnitude or phase of the current second harmonic provided to measure the tip-sample distance provided that we avoid the chaotic attractor at the onset of tapping.

5 Raster scanning

An experiment was carried out to demonstrate the EAFM capability to detect surface topography via tapping mode raster scanning. A high precision piezoscanner carried out 40-dwell line-scans at a speed of 0.25 μm/s along the x-direction. A manual stage advanced the line-scans along the y-direction in steps of 5 μm. A schematic and microscopic picture of the specimen, a TGZ2 calibration grating, are shown in Figure 6b. The grating is made of a set of parallel ridges 110 nm high at a pitch distance of 3 μm.

The scan was performed at an angle to the grating similar to that shown in the microscopic picture over a 10 μm × 70 μm grid with the open-loop EAFM depicted in Figure 3. The actuation voltage was set to $V_a(t) = 75 + 75\sin(2\pi f_\circ t)$ with $f_\circ = 10.54$ kHz. Images of the magnitude $\mathbf{R}$, phase $\boldsymbol{\theta}$, $\mathbf{X} = \mathbf{R}\cos(\boldsymbol{\theta})$ and $\mathbf{Y} = \mathbf{R}\sin(\boldsymbol{\theta})$ channel measurements of the current are shown in Figure 6a.

Further post-processing of the raw measurements is required to enhance the image quality. Reducing the scanning steps in the y-direction to match those in the x-direction will also improve the image quality. Further, improving the repeatability of the y-direction scanning is required to reduce misalignment

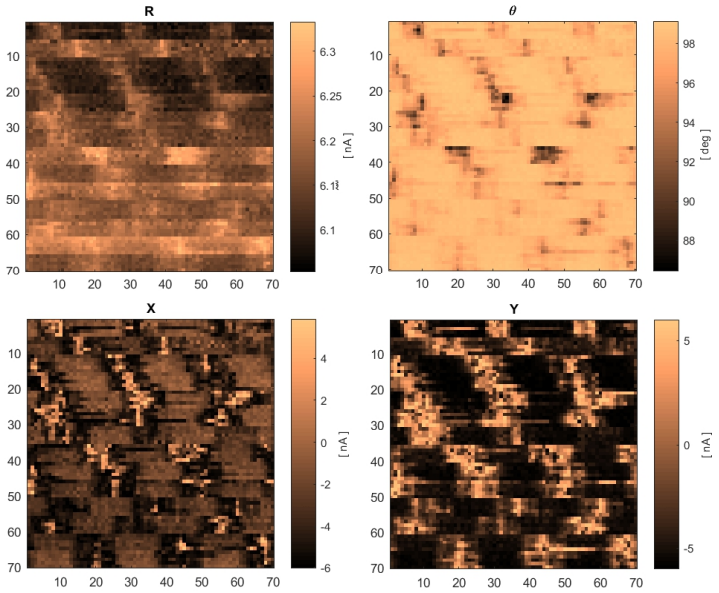

(a) Images of the magnitude, phase, **X** and **Y** channel measurements of the current over a $10 \times 70\,\mu$m grid

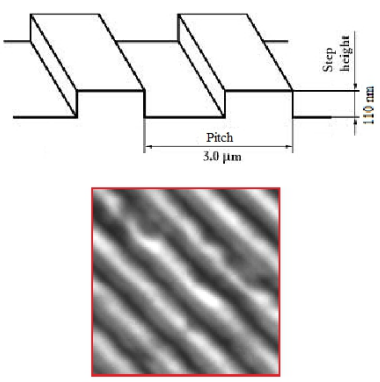

(b) A schematic and microscopic picture of the TGZ2 calibration grating

Figure 6: Open-loop AFM raster scan of TGZ2 calibration grating at a speed of 0.25 µm/s.

between the x-direction line-scans. However, comparing the raster scan results with the grating picture shows qualitative agreement. Contrast is highest for the **Y** channel measurements.

6 Conclusions

A simple, low-cost, integrated electrostatic atomic force microscope was demonstrated. It uses the AFM probe current as a measure of the tip-sample distance. The underlying theory exploits the relationship between the magnitude and phase of the current second harmonic and the probe tip displacement. The use of the EAFM in tapping mode was investigated analytically and experimentally. A preliminary image obtained from a raster scan of a calibration grating resembles the actual surface topography.

Acknowledgments

The authors would like to extend their thanks to Dr. Sangtak Park, Dr. Neil Sarkar, and Mr. Tom Rocko of nPoint® Inc.

References

[1] G Binnig, C F Quate, and C Gerber. Atomic force microscope. *Physics Review Letters*, 56:930–933, 1986.

[2] N Sarkar, G Lee, and R Mansour. CMOS-MEMS dynamic fm atomic force microscope. *IEEE Sensors Journal*, 2013.

[3] M G Ruppert, M Fowler, A G Maroufi, and S O R Moheimani. On-chip dynamic mode atomic force microscopy: A silicon-on-insulator MEMS approach. *Journal of Microelectromechanical Systems*, 26(1):215–225, 2017.

[4] N Blanc, J Brugger, and N F de Rooij. Scanning force microscopy in the dynamic mode using microfabricated capacitive sensors. *Journal of Vacuum Science & Technology*, B(14(2)), Mar/Apr 1996.

[5] F Müller, A D Müller, M Hietschold, and T Gesxner. Atomic force microscopy in dynamic mode with displacement current detection in double cantilever devices. *Japanese Journal of Applied Physics*, 45(3B):1974–1977, 2006.

[6] M I Younis. *MEMS Linear and Nonlinear Statics and Dynamics*. Springer, 2011.

[7] J Brugger, N Blamf, Ph Renaudb, and N F de Rooija. Microlever with combined integrated sensor/actuator functions for scanning force microscopy. *Sensors and Actuators*, 43:339–345, 1994.

[8] D Dickel, M J Skove, and A M Rao. An analytic characterization of the harmonic detection of resonance method. *Journal of Applied Physics*, 106, 2009.

[9] S Park, M Khater, D Effa, E M Abdel-Rahman, and Yavuz M. Detection of cyclic-fold bifurcation in electrostatic MEMS transducers by motion-induced current. *Journal of Micromechanics and Microengineering*, 27:119–126, 2017.

[10] A M Alneamy, M S Al-Ghamdi, M Khater, B Li, R S Almikhlafi, S Park, E M Abdel-Rahman, and G R Heppler. On the dynamics of dimpled electrostatic MEMS actuators. In *ENOC 2017, June 25-30, 2017, Budapest, Hungary*, Jun 2017.

[11] A Bahrami and A H Nayfe. On the dynamics of tapping mode atomic force microscope probes. *Nonlinear Dynamics*, 70:1605–1617, 2012.

EUROMECH Colloquium 603
Dynamics of micro and nano systems
5 – 7 September 2018, Porto, Portugal

Squeeze Film Damping Control of a Piezoresistive Micro Accelerometer for Neurological Disease Diagnosis

S.Biswas[1] and AK. Gogoi[2]

[1,2] Indian Institute of Technology Guwahati, Guwahati, India
b.sonali@iitg.ernet.in
akg@iitg.ernet.in

Summary. Inertial MEMS (micro electro mechanical system) accelerometers require adequate damping control for high performance applications like neurological disease diagnosis. Damping analysis determines the dynamic behaviour and squeeze film technique is employed in most of the MEMS sensors. In this paper squeeze film damping analysis has been done for two quad beam accelerometers having proofmass with same height but different aspect ratio, such that both have same mass and area. It has been observed that the air gap remains the same for a desired damping ratio. The air gap can be controlled by varying the height of the proofmass in order to achieve the desired damping ratio. The air gap obtained for both the design is 18.6 μm for a desired damping ratio of 0.7.

Keywords: MEMS, neurological, aspect ratio, damping ratio.

1 Introduction

Damping of the proofmass is a fundamental consideration in the design of accelerometers, and it determines the dynamic behaviour[1]. High performance piezoresistive microaccelerometers used for neurological disease diagnosis capture feeble tremor, seizure etc. (2Hz-12Hz, 0g to $\pm 6g$) and require adequate damping control [2]. Air damping is very important in this case unlike conventional machines where energy dissipated by air damping is much smaller than the energy dissipated by other mechanisms. In any micro device there is large surface area to volume ratio of the moving parts which makes dynamic performance analysis important [1]. The energy consumed by air damping must be minimized so that with a limited energy supply, the motion of the mechanical parts can be maximized. Also in order to have an optimum dynamic performance, air damping has to be controlled. Thus, one of the most important design steps is estimating the damping effect in MEMS accelerometer as like any other micro mechanical devices. The dynamic characteristic of the device is mainly determined by the damping material (air here) and the spacing between the proofmass and the housing. There are different mechanisms of damping out of which, the most significant damping in MEMS devices is the Squeeze film damping. In this work, the effect of change in geometry upon the damping control of the MEMS accelerometer has been simulated. A damping factor between 0.6 to 1.2 is usually desirable as it gives high response time, fast settling time, good bandwidth and linearity[1],[2]. For our accelerometer we desire damping ratio of 0.7, which gives an almost flat and stable response characteristic [3]. Here two similar quad beam structure microaccelerometers have been chosen having different aspect ratio of proofmasses, but same height. In this way both the designs have same area and mass thus the mechanical sensitivity and natural frequency remains the same. The squeeze film damping effect of both the structures have been simulated, and the air gap has been obtained in order to achieve the desired damping ratio. Both the piezoresistive accelerometer structures are made of silicon.

The entire accelerometer structure can be modeled by a simple mass spring damper that is attached to an enclosing casing. Let x be the displacement of the mass m relative to the casing. The equation of motion is

$$m\ddot{x} + \beta\dot{x} + kx = -ma \tag{1}$$

whereβ and k are the damping coefficient and spring constant, respectively. Thus by measuring the displacement, acceleration can be determined. The dynamic behavior is determined by the natural frequency

and damping ratio, thus the equation of motion becomes

$$\ddot{x} + 2\zeta\omega_n\dot{x} + \omega_n^2 x = -a \tag{2}$$

The schematic of the structure having piezoresistors as sensing element has been shown in Fig.1. The design specifications has been given below in terms of length, width and height respectively. Design configuration 1[2]:
Proof mass $3200\mu m \times 3200\mu m \times 250\mu m$, beam $1000\mu m \times 250\mu m \times 20\mu m$, piezoresistors p-doped $100\mu m \times 25\mu m \times 2\mu m$.
Design configuration 2:
Proof mass $3800\mu m \times 2700\mu m \times 250\mu m$, beam $1000\mu m \times 250\mu m \times 20\mu m$, piezoresistors p-doped $100\mu m \times 25\mu m \times 2\mu m$.
It has been observed that both the configurations have the same air gap for obtaining the desired damping

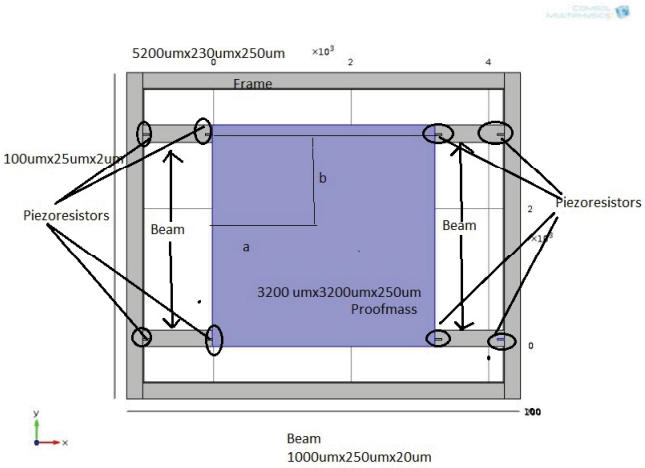

Figure 1. Quad beam accelerometer structure

ratio, as the area and mass is same for both. The damping can be controlled by varying the height of the proofmass. We observe different air gap is obtained when we consider different height of the proofmass. In this paper, section 2 discusses the squeeze film damping mechanism, which is followed by the FEM simulation and the results and discussion in section 3 and conclusion in section 4.

2 Squeeze Film Damping

When a parallel plate is moving vertical to the substrate, two things can happen. Either, the motion increases the pressure and squeezes the gas out of the gap or decreases the pressure and draws the gas into the gap. Due to the viscous behaviour of the gas, the movement of the mass is resisted which results in a pressure gradient inside the gas film. This pressure gradient opposes the movement of the seismic mass. Hence faster the mass moves, the larger the pressure gradient and therewith the reaction force. Here, the work done by the plate is consumed by the viscous flow of the air and transformed into heat. In other words, the air film acts as a damper and the damping is called squeeze-film air damping. The damping force of squeeze-film air damping is thus dependent on the gap distance; the smaller the gap, the larger the damping force [4]. When the plate is very far away from the wall, the pressure build-up is negligible and the damping force is mainly due to the drag force. The squeeze-film air damping has significant effects on the dynamic behaviour of microstructures. In many cases, it should be reduced and, in some other cases, it should be controlled to an expected level [2]. The damping ratio is mainly determined by the dimensions of the accelerometer structure, generalized mass of the proof mass, pressure, density, and viscosity of the gas in the enclosed volume of package accelerometer module[3].

The damping coefficient is given by

$$\beta = \frac{0.42\mu A^2}{d^3} \tag{3}$$

Here μ, A, d denote dynamic viscosity of air, area of the proofmass and the air gap thickness. Also the relation between the damping coefficient with the design parameters namely mass m and effective spring constant k is given by

$$\beta = 2\sqrt{mk} \tag{4}$$

The Squeeze film damping effect is the interaction of the silicon proofmass and the air film, trapped in the gap between mass and the encapsulation. The schematic of the Squeeze film damping is shown in Fig.2.

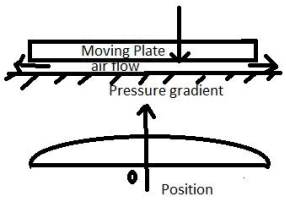

Figure 2. Schematic of the Squeeze film damping with the obtained pressure gradient.

3 Results and Discussion

The desired damping ratio of the designed MEMS accelerometer is 0.7 for flat response and stable characteristic. Here, we have chosen different width and length of proofmass of two different MEMS accelerometers structure (both quad beam type), such that they have same area and mass. Thus natural frequency and mechanical sensitivity remains the same for both the structures. The design dimensions of both accelerometer 1 and 2 shown in Table 1, results in air gap of 18.6 μm for obtaining damping ratio of 0.7. This shows that damping ratio remains the same for two different designs provided they have the same area and mass. The optimized proofmass height for which we obtain 0.7 damping ratio is 250 μm. It has been observed that in order to obtain the desired damping ratio we have to vary the height of the proofmass, so that the air gap can be controlled. The results have been obtained for a proofmass height

Table 1. Design parameters chosen for damping control

Design Parameters chosen	values
Dynamic Viscosity of air(N/m^2s)	1.85×10^{-5}
Atmospheric Pressure(Pa)	1.013×10^5
Height of the proofmass (μm)	250
Natural Frequency (rad/sec)	15061
(Design 1) Proofmass area (μm^2)	3200×3200
(Design 2) Proofmass area(μm^2)	3800×2700

of 250 μm and 500 μm as shown in Table2. Thus we observe that air gap varies with different height of proofmass.

Both the structures with proofmass height 250 μm, having different width and length but same area and mass, has a damping coefficient of 0.1239 and air gap of 18.6 μm. The simulated pressure distribution is shown in Fig.3.

Table 2. Simulated results for controlled squeeze film damping.

Optimized Proofmass height(μm)	Simulated Air gap(μm)	Damping coefficient,β	Damping ratio
250	18.6	0.1239	0.7
500	16.6	0.177	0.7

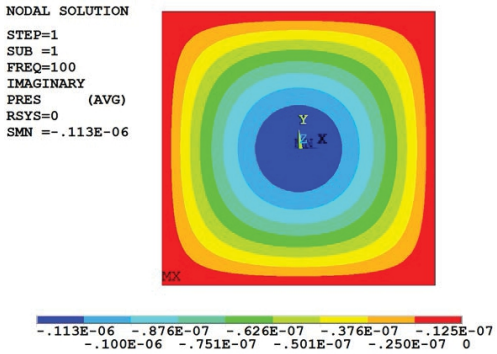

Figure 3. Simulated Pressure distribution for gap 18.6μm.

4 Conclusion

The damping analysis has been done and it is seen that by varying the height of the proofmass the air gap can be controlled to achieve the desired damping ratio. The air gap obtained as 18.6 μm which gives us a controlled squeeze film damping of 0.7. It has been observed that irrespective of the aspect ratio of the proofmass, if the mass and area of the proofmass is same for different structures, the air gap remains the same for the desired damping ratio. If the height of the proofmass increases, the air gap reduces in order to maintain the same damping ratio. Thus design geometry has to be optimized to control damping of MEMS accelerometer.

References

[1] M. Bao, *Analysis and Design principles of MEMS devices*. Elsevier - The Netherlands, 2005.

[2] S. Biswas, A. Gogoi, Design Issues of Piezoresistive MEMS Accelerometer for an Application Specific Medical Diagnostic System, *J. of IETE Tech. review*, **33**, No.1, 11-16, 2016.

[3] L. Chang, Piezoresistive Sensors: *Foundations of MEMS*," NG: Prentice Hall, ISBN 0131472860, 2006.

[4] R.P. Kampen, R.F. Wolffenbuttel, Modeling the mechanical behavior of bulk micromachining silicon accelerometer. *Sensors Actuators*, A **64**, 137-150, 1998.

EUROMECH Colloquium 603
Dynamics of micro and nano systems
5 – 7 September 2018, Porto, Portugal

Nonlinear interaction of a pair of nano/micromechanical resonators with different decay rates far away from internal resonance

Oriel Shoshani[1], **Steven W. Shaw**[2] **and Mark I. Dykman**[3]

[1]Ben-Gurion University of the Negev, Beer-Sheva, Israel
oriels@bgu.ac.il

[2] Florida Institute of Technology, Melbourne, FL, USA
sshaw@fit.edu

[3] Michigan State University, East Lansing, MI, USA
dykman@pa.msu.edu

Summary. We consider the dynamics of a nonlinear nano-resonator that is nonlinearly and nonresonantly coupled to a linear resonator that acts as a type of effective bath. In the case of interest the decay time of the bath mode is much shorter than that of the primary mode, so that it adiabatically tracks it. This model, which is motivated by ongoing experimental work in nano-resonators, is analyzed to show that the linear and nonlinear characteristics of the primary resonator can be altered in a significant manner from the coupling to the bath mode, even in the non-resonant case. Such an arrangement may provide a practical means of tuning resonator characteristics.

Keywords: Nonlinear interaction, Nanoresonator, Adiabatic tracking.

1 Introduction

Nonlinear interactions are ubiquitous. Their manifestations have many forms [1, 2, 3, 4, 5, 6], which span across multiple length scales [7, 8, 9, 10]. Perhaps, the most important nonlinear interaction is internal (autoparametric) resonance of vibrational systems, which occurs where two vibrational frequencies in the system are commensurate, i.e., their ratio is a rational number, typically of low order [11, 12, 13, 14]. These phenomena have recently received growing attention in nano- and micro-mechanical vibrational systems [7, 15, 16, 17, 18], which stems from the remarkable and unprecedented tunability and low damping of these systems. However, these properties also provide a means to alter the system dynamics, in particular those of an individual mode of interest, in a non-resonant manner. For example, it was shown in [16] that nonlinear coupling between two modes can result in an increase of the effective linear damping of the primary mode when its amplitude is sufficiently large, even when the system is far from resonance. In this work, we further explore such non-resonant nonlinear interactions and show that they can be used to tune the linear and nonlinear characteristics of the slow decaying primary resonator. The results developed here are in some sense close to the seminal work [19, 20] on a classical oscillator coupled to a bath of linear oscillators. Furthermore, the results of the current analysis can be viewed as a special case, with important potential applications, of the more general analyses of [21, 22].

2 Analysis and results

We consider a system with two resonators that are mutually coupled (see Fig. 1). We assume that the primary resonator (q_1) can experience a large amplitude oscillation around its stable equilibrium, $q_1 = 0$, and a potential, $U(q_1)$, provides a nonlinear restoring force. The bath resonator (q_2) is linear and oscillates with small amplitude around its stable equilibrium, $q_2 = 0$. To be consistent with the above assumptions, we model the interaction potential of the two resonators as $U_{\text{inter}} = -q_2 G(q_1)$. Thus, the Hamiltonian of the system is given by $\mathcal{H} = p_1^2/2 + U(q_1) + p_2^2/2 + \omega_2^2 q_2^2/2 - q_2 G(q_1)$. The equations of motion of the resonators with the inclusion of linear damping are formally given by $\ddot{q}_k = -2\Gamma_k \dot{q}_k - \partial\mathcal{H}/\partial q_k$, where the overdot denotes a time derivative, and $-2\Gamma_k \dot{q}_k$ models linear dissipation

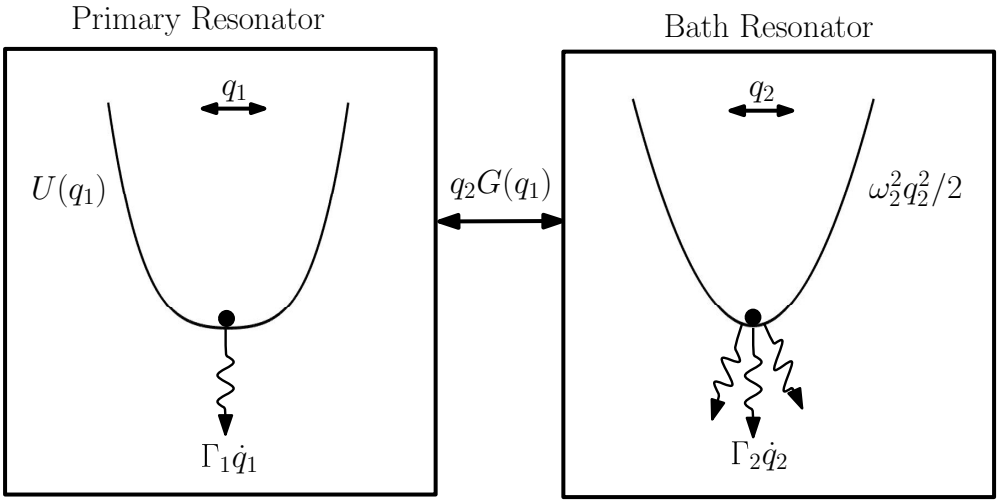

Figure 1. **Definition sketch.** Two resonators mutually and nonlinearly coupled via an interaction potential, $-q_2G(q_1)$. The primary resonator (q_1) has a nonlinear conservative restoring force, $-U'(q_1)$, and weak linear dissipation, $-\Gamma_1\dot{q}_1$. The bath resonator has a linear conservative restoring force, $-\omega_2^2q_2$, and a relatively strong linear dissipation, $-\Gamma_2\dot{q}_2$.

of the resonators. Furthermore, we assume that both resonators are lightly damped ($\Gamma_k/\omega_k \ll 1$) and that the decay times satisfy $\Gamma_2/\Gamma_1 \gg 1$ so that the bath resonator will adiabatically track the primary resonator. Formally solving the equation of motion of the bath resonator in terms of its Green's function and inserting the result to the equation of motion of the primary resonator we find that

$$\ddot{q}_1 = -2\Gamma_1\dot{q}_1 - U'(q_1) + G'(q_1)(L[q_1] + F), \tag{1}$$

where $L[q_1] = \frac{1}{\omega_{2d}}\int_0^t G(q_1(\tau))e^{-\Gamma_2(t-\tau)}\sin(\omega_2(t-\tau))d\tau$ describes the retarded reaction of the second resonator on the first resonator, and $F = e^{-\Gamma_2 t}\left[q_2(0)\cos(\omega_2 t) + \frac{p_2(0)+\Gamma_2 q_2(0)}{\omega_2}\sin(\omega_2 t)\right]$ describes the response of the second resonator to initial conditions. Note that Eq. (1) can be analyzed either in the Markovian limit, where $t \gg \Gamma_2^{-1}$, or for the general non-Markovian process, which is associated with memory friction.

Restricting our attention to the essential leading order nonlinear terms, we take $U(q_1) = \omega_1^2q_1^2/2 + \gamma q_1^4/4$, where the non-secular term $\beta q_1^3/3$ has been omitted. Furthermore, we assume that $G(q_1)$ can be similarly represented, $G(q_1) = G_1q_1 + G_2q_1^2/2 + O(q_1^3)$, where $G_1 \equiv G'(0)$ and $G_2 \equiv G''(0)$. Consequently, for times $t \gg \Gamma_2^{-1}$ we find that the system dynamics can be mapped onto a modified van der Pol-Duffing resonator

$$\ddot{q}_1 + 2(\Gamma_{1\text{eff}}\dot{q}_1 + \alpha_2^2\Gamma_2q_1^2)\dot{q}_1 + \hat{\omega}_1^2q_1 + \hat{\gamma}q_1^3 = 0. \tag{2}$$

From Eq. (2) we deduce that the linear and nonlinear dynamics of the primary resonator are strongly affected by the bath resonator. To be specific, we see that at leading order, the interaction between the two resonators leads to: (i) an increase in the linear decay rate $\Gamma_{1\text{eff}} = \Gamma_1 + \alpha_1^2\Gamma_2$, (ii) the addition of nonlinear cubic (van der Pol type) damping term $-\alpha_2^2\Gamma_2q_1^2\dot{q}_1$, (iii) a shift in the eigenfrequency $\hat{\omega}_1^2 = \omega_1^2 - \alpha_1^2(\omega_2^2 - \omega_1^2)$ and, (iv) a modification to the Duffing nonlinearity $\hat{\gamma} = \gamma - \frac{2}{3}\alpha_2^2\left[3\omega_2^2 - 20\omega_1^2 + 8\omega_1^2(\Gamma_2^2 + \omega_1^2)/\omega_2^2\right]$, where $\alpha_1^2 = G_1^2/[(\omega_2^2 - \omega_1^2)^2 + (2\Gamma_2\omega_1)^2]$, $\alpha_2^2 = G_2^2/[(\omega_2^2 - 4\omega_1^2)^2 + (4\Gamma_2\omega_1)^2]$. Application of the rotating wave approximation ($q_1(t) = A_1(t)e^{i\omega_1 t} + A_1^*(t)e^{-i\omega_1 t}$) to Eq. (2) yields the following closed form solution in terms of the complex amplitude ($A_1 = |A_1|e^{i\phi}$)

$$|A_1(t)| = |A_1(0)|e^{-\Gamma_{1\text{eff}}t}\left[1 + \frac{\alpha_2^2\Gamma_2}{\Gamma_{1\text{eff}}}|A_1(0)|^2(1 - e^{-2\Gamma_{1\text{eff}}t})\right]^{-1/2}, \tag{3}$$

$$\phi(t) = \phi(0) - \Delta\omega_1 t + \frac{3\hat{\gamma}}{4\omega_1\alpha_2^2\Gamma_2}\ln\left[1 + \frac{\alpha_2^2\Gamma_2}{\Gamma_{1\text{eff}}}|A_1(0)|^2(1 - e^{-2\Gamma_{1\text{eff}}t})\right]. \tag{4}$$

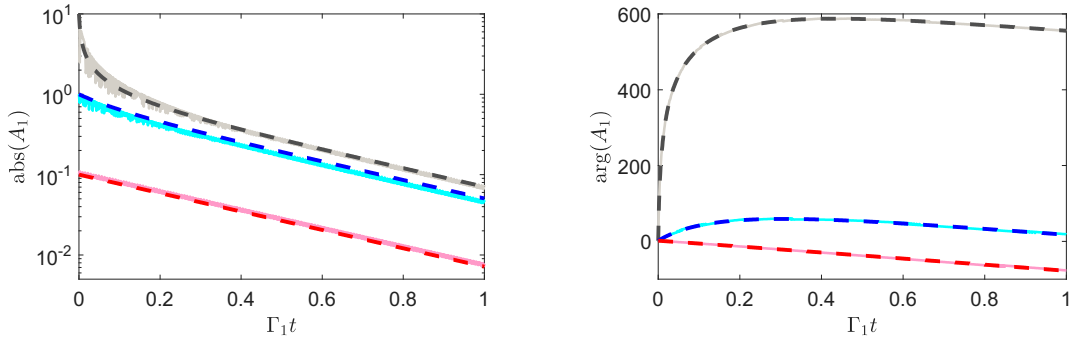

Figure 2. **Numerical and theoretical predictions of the amplitude and phase dynamics of the first resonator.** The amplitude (left panel, showing decay) and phase (right panel, showing effective frequency) dynamics are shown for $\omega_1 = 1,\ \omega_2 = 10,\ \Gamma_1 = 10^{-3},\ \Gamma_2 = 1,\ G_1 = 4, G_2 = 5,\ \gamma = 1$, and three different initial conditions: (i) $A_1(0) = 10i,\ A_2(0) = 0.01$ - grey curves, (ii) $A_1(0) = i,\ A_2(0) = 0.01$ - blue curves, and (iii) $A_1(0) = 0.1i,\ A_2(0) = 0.01$ - red curves. The light color solid curves indicates numerically calculated curves and the dark color dashed curves indicates theoretical predictions.

Fig. 2 shows a comparison between the numerical integrations of the full system and the theoretical approximation of Eqs. (3)-(4). The numerical integration and the theoretical approximation are in excellent agreement. Furthermore, due to the linear interaction of the resonators (G_1, α_1^2), there is almost a threefold increase in the linear decay rate $\Gamma_{1\text{eff}}/\Gamma_1 = 2.63$, and the eigenfrequency is shifted downward by 8%, $\Delta\omega_1/\omega_1 = 0.08$. The nonlinear interaction of the resonators (G_2, α_2^2) is responsible for the van der pol nonlinear damping term with a coefficient of $\alpha_2^2\Gamma_2 = 2.7 \times 10^{-3}$, which significantly changes the amplitude dynamics and leads to a non-exponential decay, and for a twofold decrease in the Duffing parameter $\hat{\gamma}/\gamma = 0.49$. The results also confirm that the nonlinear effects are most pronounced for large initial initial energies of the first resonator $(|A_1(0)|^2)$ and at the beginning of the transient response $(t \to 0)$.

3 Conclusions

We analyzed the non-resonant nonlinear interaction of two mutually coupled resonators with significantly different decay rates. We showed that such an interaction can change both the linear and nonlinear characteristics of the primary resonator. That is, by coupling a nonlinear resonator to relatively fast decaying linear resonator, one can tune its eigenfrequency, linear damping rate, Duffing parameter, and add nonlinear damping. Practically, the results of this paper show that in highly tunable systems, such as nano- and micro-mechanical systems, one can adjust the response of a nonlinear resonator according to desired specifications by controlling its interaction with a fast decaying linear resonator. This ability to tailor the response of a nonlinear resonator can be extremely useful in NEMS and MEMS applications.

Acknowledgments

The efforts of SWS on this topic are supported by the US NSF under awards CMMI-1561934 and CMMI-1662619.

References

[1] P. Müller, G. Holloway, F. Henyey, and N. Pomphrey, "Nonlinear interactions among internal gravity waves," *Reviews of Geophysics*, vol. 24, no. 3, pp. 493–536, 1986.

[2] A. Bajaj and S. Tousi, "Torus doublings and chaotic amplitude modulations in a two degree-of-freedom resonantly forced mechanical system," *International Journal of Non-Linear Mechanics*, vol. 25, no. 6, pp. 625–641, 1990.

[3] S. Nayfeh and A. Nayfeh, "Nonlinear interactions between two widely spaced modesexternal excitation," *International Journal of Bifurcation and Chaos*, vol. 3, no. 02, pp. 417–427, 1993.

[4] K. E. Strecker, G. B. Partridge, A. G. Truscott, and R. G. Hulet, "Formation and propagation of matter-wave soliton trains," *Nature*, vol. 417, no. 6885, p. 150, 2002.

[5] P. K. Shukla and B. Eliasson, "Nonlinear interactions between electromagnetic waves and electron plasma oscillations in quantum plasmas," *Physical review letters*, vol. 99, no. 9, p. 096401, 2007.
[6] J. Sun, C. J. Nappo, L. Mahrt, D. Belušić, B. Grisogono, D. R. Stauffer, M. Pulido, C. Staquet, Q. Jiang, A. Pouquet, *et al.*, "Review of wave-turbulence interactions in the stable atmospheric boundary layer," *Reviews of geophysics*, vol. 53, no. 3, pp. 956–993, 2015.
[7] J. Güttinger, A. Noury, P. Weber, A. M. Eriksson, C. Lagoin, J. Moser, C. Eichler, A. Wallraff, A. Isacsson, and A. Bachtold, "Energy-dependent path of dissipation in nanomechanical resonators," *Nature nanotechnology*, vol. 12, no. 7, p. 631, 2017.
[8] D. Antonio, D. H. Zanette, and D. López, "Frequency stabilization in nonlinear micromechanical oscillators," *Nature communications*, vol. 3, p. 806, 2012.
[9] G. Arioli and F. Gazzola, "A new mathematical explanation of what triggered the catastrophic torsional mode of the tacoma narrows bridge," *Applied Mathematical Modelling*, vol. 39, no. 2, pp. 901–912, 2015.
[10] M. Zilhão, H. Witek, and V. Cardoso, "Nonlinear interactions between black holes and proca fields," *Classical and Quantum Gravity*, vol. 32, no. 23, p. 234003, 2015.
[11] C. Van der Avoort, R. Van der Hout, J. Bontemps, P. Steeneken, K. Le Phan, R. Fey, J. Hulshof, and J. Van Beek, "Amplitude saturation of mems resonators explained by autoparametric resonance," *Journal of Micromechanics and Microengineering*, vol. 20, no. 10, p. 105012, 2010.
[12] C. R. Kirkendall and J. W. Kwon, "Multistable internal resonance in electroelastic crystals with nonlinearly coupled modes," *Scientific reports*, vol. 6, p. 22897, 2016.
[13] L. Mi and O. Gottlieb, "Nonlinear dynamics and internal resonances of a planar multi-tethered spherical aerostat in modulated flow," *Meccanica*, vol. 51, no. 11, pp. 2689–2712, 2016.
[14] E. Hacker and O. Gottlieb, "Application of reconstitution multiple scale asymptotics for a two-to-one internal resonance in magnetic resonance force microscopy," *International Journal of Non-Linear Mechanics*, vol. 94, pp. 174–199, 2017.
[15] C. Chen, D. H. Zanette, D. A. Czaplewski, S. Shaw, and D. López, "Direct observation of coherent energy transfer in nonlinear micromechanical oscillators," *Nature communications*, vol. 8, p. 15523, 2017.
[16] O. Shoshani, S. Shaw, and M. Dykman, "Anomalous decay of nanomechanical modes going through nonlinear resonance," *Scientific reports*, vol. 7, no. 1, p. 18091, 2017.
[17] A. H. Ramini, A. Z. Hajjaj, and M. I. Younis, "Tunable resonators for nonlinear modal interactions," *Scientific reports*, vol. 6, p. 34717, 2016.
[18] A. Z. Hajjaj, M. A. Hafiz, and M. I. Younis, "Mode coupling and nonlinear resonances of mems arch resonators for bandpass filters," *Scientific Reports*, vol. 7, p. 41820, 2017.
[19] A. Einstein and L. Hopf, "Statistical investigation of a resonators motion in a radiation field," *Ann. Phys*, vol. 33, pp. 1105–1115, 1910.
[20] N. Bogolyubov, "On some statistical methods in mathematical physics," *Izdat. Akad. Nauk Ukr. SSR, Kiev*, 1945.
[21] M. Dykman and M. Krivoglaz, "Spectral distribution of nonlinear oscillators with nonlinear friction due to a medium," *physica status solidi (b)*, vol. 68, no. 1, pp. 111–123, 1975.
[22] J. Atalaya, T. W. Kenny, M. Roukes, and M. Dykman, "Nonlinear damping and dephasing in nanomechanical systems," *Physical Review B*, vol. 94, no. 19, p. 195440, 2016.

EUROMECH Colloquium 603
Dynamics of micro and nano systems
5 – 7 September 2018, Porto, Portugal

Gas flow in a micro-channel with an elastic obstacle

Kiril Shterev[1], Emil Manoach[1], Stefan Stefanov[1]
[1]Institute of Mechanics – Bulgarian Academy of Sciences, Sofia, Bulgaria

kshterev@imbm.bas.bg
e.manoach@imbm.bas.bg
stefanov@imbm.bas.bg

Summary. A two-dimensional slip regime compressible gas flow around an elastic beam (cantilever) and fixed to one of the walls in microchannel is considered. The numerical analysis is separated into two parts: obtaining the distribution of normal stress exerted on the elastic body by using a continuum model based on the Navier-Stokes-Fourier (NSF) equations [1] with slip boundary conditions on all solid walls and applying the obtained pressure distribution on the beam to find the beam motion.

Keywords: micro channel, gas flow, elastic obstacle, cantilever beam vibration.

1. Introduction

The analyses of gas flow at microscale level are important tasks for many high technological devices and they are subjects of studies of many researchers. As a recent example can be shown the work of Jayne et al. [2] where MEMS actuator manufactured using 3D printing is considered. The essential and intriguing element is that there are fundamental differences in the microfluidic considerations with respect to those of conventional flows at macroscales scales.

In many cases in micro channels, where the gas flows, there are obstacles with different shapes. In most of the cases they are considered as rigid bodies. The proper model of such system requires considering the deformability of parts of MEMS. The consideration of the elastic properties of the obstacle means that it will deform due to the gas flow and due to its motion the gas flow will be disturbed.

For model description of MEMS, the number of Knudsen Kn (the ratio of mean free path of molecules to specific geometrical dimension) is a key dimensionless parameter. In such a devices, the Knudsen number at standard temperature and pressure (STP) is large due to the small characteristic size that is comparable to molecular mean free path, ([3], [4]). One can define provisionally the following regimes of gas flow:

- non-slip regime (continuum flow), for Kn <0.001. Standard non-slip boundary conditions between the fluid and the surface of the body are considered as valid;
- slip-flow regime within 0.001 <Kn <0.1. Navier-Stokes equations are applicable for fluid flow, but slippage on the border between the gas and the surface of the body should be taken into account ;
- transition regime, within 0.1<Kn<10.0. The Navier-Stokes equation are no longer valid;
- free-molecule regime, for Kn> 10.0. The mean free path is much larger than the typical size and frequency of collisions between molecules of the gas is very small and the impact of the binary collisions can be ignored.

These regimes determine the relationship between dilute gas and gas micro flows. In micro scale the properties of the gas at standard conditions correspond to the properties of a rarefied gas and differ significantly from the properties of the dense fluid. The air under standard conditions can be regarded as a slightly diluted ideal gas. It is obvious that all discussed above regimes can have a place in a micro device. Continuum approach is applicable only at small Knudsen numbers and under

special boundary conditions, taking into account small deviations from local equilibrium.

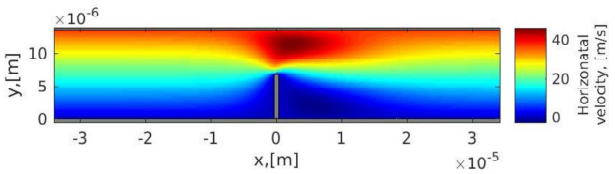

a) Horizontal velocity field

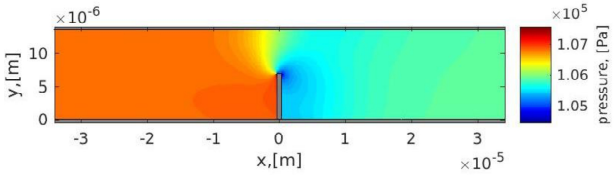

b) Pressure field

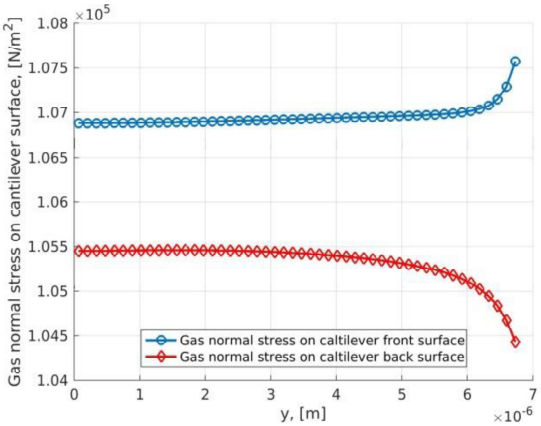

c) Gas pressure on cantilever front and back surfaces.

Figure 1: Horizontal velocity field (a), pressure field (b) and gas pressure on cantilever front and back surfaces (c).

2. Problem description

A microchannel with channel high 13.6. 10^{-6} m is considered. In the channel there is an obstacle, which deformable properties are taken into account (see Fig. 1 a) and b)). Here are considered four cases: the upper channel wall is moving with constant velocities 37m/s, 74m/s, 148m/s, and 296m/s (M=0.1, 0.2, 0.4, and 0.8, respectively) while the bottom is at rest. Temperature of the channel and cantilever walls is 288K. At the inlet, the pressure is fixed to 1Atm and gradients of velocities and temperature are equal to zero. The gradients of velocities, temperature, and pressure at the channel outlet are zeros. The Knudsen number is 0.01 and it is based on molecules mean free path in free-stream flow and cantilever's length. The obstacle – a cantilever beam is vertical and clamped to the bottom channel wall. Its dimensions are: length l=6.8∗10^{-6} m, thickness h=1.7∗10^{-7}m, width b=4.7∗10^{-7} m. The beam was considered to be made of copper. The physical properties are: Young's modulus E= 1128 ∗10^{9} N/m^2, density ρ=8960 kg/m^3, Poisson's ratio 0.34.

The gas is described by using a continuum model on the basis of the Navier-Stokes-Fourier (NSF) equations [1] for a compressible viscous gas with transport coefficients determined by the first approximation of the Chapman-Enskog theory for low Knudsen numbers. In accordance with the microfluidic assumptions velocity-slip and temperature-jump boundary conditions are imposed on the walls of the channel and cantilever, [5]. The NSF system of equations was calculated numerically using finite volume algorithm SIMPLE-TS [6]. The cantilever is modelled as an elastic Timoshenko beam and the shear stress and rotary inertia during the beam motion are taken into account. The geometrically nonlinearities due to large deflections are taken also considered.

3. Results

To determine influence of gas flow on the cantilever we take into account the normal pressure of gas on cantilever's front and back surfaces (see Fig. 1 c)) and neglect shear stresses on all cantilever's surfaces and normal stress on cantilever top surface. The first 10 natural frequencies of the cantilever were calculated. Due to the small dimensions of the beam the frequencies are very high – the first one is ω_1= 6.66. 10^7 Hz. The obtained pressure on the front and back side of the beam was applied as a step load and the motion of the cantilever was studied. Time history diagrams of the tip of the beam for different numbers of Mach number of the flow are shown in Figure 2. The considered gas flow leads to very small deflections of the beam (Fig. 3). Small oscillations can be observed at the beginning of the flow (transient vibration) and after that the beam deforms in a shape similar to the ones shown in Fig. 4.

The work is a first attempt to study the interaction of the gas flow with a deformable body during its flow in a microchannel. When the elasticity of the obstacle is considered and the obstacle oscillates disturbing the flow the problem becomes very complicated and it could influence essential changes in the flow. A more precise analysis of this work in progress, considering the influence of the beam (obstacle) vibration of the gas flow, will be studied by the direct simulation Monte Carlo (DSMC) method.

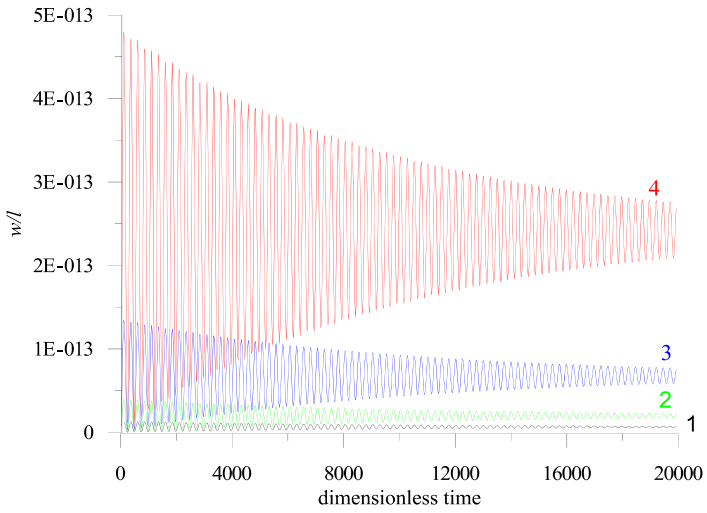

Fig. 2 Time history diagram of the cantilever's tip for different values of the Mach number of the flow. 1 (black) – Mach=0.1; 2 (green) - Mach=0.2; 3 (blue) - Mach=0.4; 4 (red) - Mach=0.8

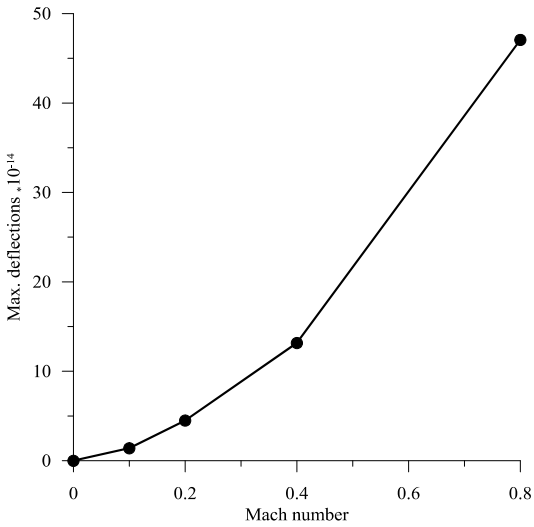

Fig. 3. The influence of the Mach number on maximal deflection of the cantilever.

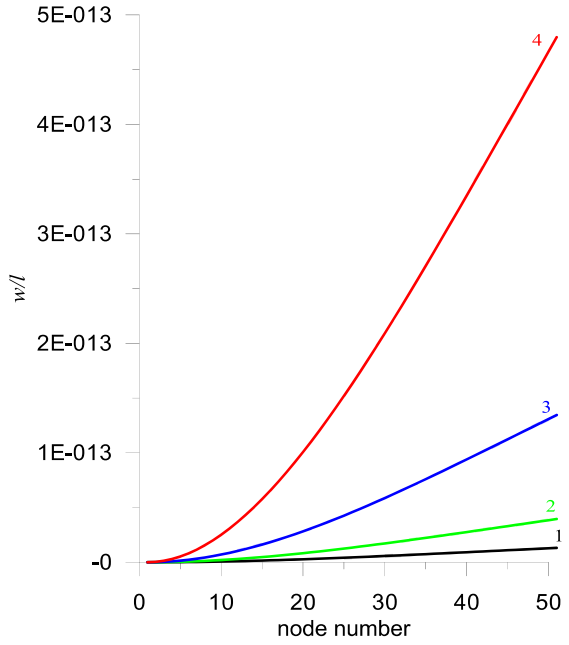

Figure 4. The deflection of the obstacle (cantilever beam) along its length at moment t=2.36. 10^{-8} s. 1 (black) – Mach=0.1; 2 (green) - Mach=0.2; 3 (blue) - Mach=0.4; 4 (red) - Mach=0.8

4. Conclusions

The main conclusion of the present research is that the velocity of the flow could influence essentially the cantilever behavior and this effect could be used to study important phenomena in many high technological devices. If the obstacle has a piezo-electric properties (see for example the model

developed in [7] the developed model of fluid structure interaction can be used to detect or measure gas flows in micro channels. The natural frequencies of vibrations of the cantilever are of the same order of magnitude as the frequencies of the molecules collisions. This fact allows using the DSMC method to study the problem in details including the full coupling between the fields of the gas flow and beam's oscillation.

Acknowledgements

The authors would like to acknowledge the financial support provided by the Bulgarian NSF under Grant DN-02/7-2016.

References

[1] S. Stefanov, V, Roussinov, C. Cercignani,. Rayleigh-Benard flow of a rarefied gas and its attractors. I. Convection regime, *Physics of Fluids*, **14** (7), 2255–2269, 2002.

[2] R. K. Jayne, T. J. Stark, J. B. Reeves, D. J. Bishop, A. E. White, Dynamic Actuation of Soft 3D Micromechanical Structures Using Micro- Electromechanical Systems (MEMS). *Adv. Mater. Technol*. , https://doi.org/10.1002/admt.201700293, 2018

[3] G. Karniadakis, A. Beskok and N. Aluru*, Microflows and nanoflows. Fundamentals and simulation*, Springer Science+Busness Media, Inc., 2005.

[4] M. Gad-el-Hak, MEMS: Introduction and Fundamentals, CRC Press Taylor & Francis Group, 2006

[5] C. Cercignani, *The Boltzmann Equation and its Applications*, Springer, New York, 1988.

[6] K. Shterev, S Stefanov, Pressure based finite volume method for calculation of compressible, viscous gas flows, *J. Comp. Phys*, **229**, 461-480, 2010.

[7] S. Stoykov, G. Litak, E. Manoach. Vibration energy harvesting by a Timoshenko beam model and piezoelectric transducer, *Eur. Phys. J. Spec. Top*. **224**:, pp 2755–2770, 2015.

EUROMECH Colloquium 603
Dynamics of micro and nano systems
5 – 7 September 2018, Porto, Portugal

Free, periodic, large amplitude vibrations of small-scale piezoelectric beams by a modified couple stress theory

Batool Soleimani Roody[1], Hamed Akhavan[2], Pedro Ribeiro[2] and Ali Reza Fotuhi[1]

[1] Department of Mechanical Engineering, Yazd University, Yazd, Iran
solaimani_b2003@yahoo.com
afotuhi@yazd.ac.ir

[2] DEMec/INEGI, Faculty of Engineering, University of Porto, Porto, Portugal
hamed@fe.up.pt
pmleal@fe.up.pt

Summary. With the goal of studying the evolution of their natural frequencies with the vibration amplitude, free, periodic vibrations of small-scale beams in piezoelectric materials are investigated. A modified couple stress theory is applied, in order to take the small-scale effects into consideration. The partial differential governing equations are transformed to ordinary differential equations by Bubnov-Galerkin's method. The latter equations are solved by the method of Multiple Scales. The results of this perturbation method are compared with solutions computed using a numerical method for boundary value problems, known as shooting method. The small-scale effects on the non-linear natural frequencies of piezoelectric beams are discussed.

Keywords: Small beams, piezoelectric materials, non-linear, natural frequencies of vibration.

1 Introduction

Beams in piezoelectric materials can be used as sensors, actuators or for energy harvesting [1, 2]. Increasingly, beams in piezoelectric materials with dimensions on the order of the micrometre or less are appearing [2-4]. Classical solid mechanics does not seem to accommodate small-scale effects as the ones independently found by Macfarland and Colton [5] and by Lam et al. [6], who experimentally detected that the bending stiffness of small beams augments when the thickness diminishes. A theory that has been suggested to capture small-scale effects is the modified couple stress theory [4, 7-9]. In couple stress theories, the material particle should possess the conventional characteristics of translation (as in conventional mechanics), but can also experience rotations and deformations. Rotations of material particles can be realized by encasing the material particle with a representative volume element [7]. In the modified couple stress theory proposed by Yang et al [7], the strain energy density function depends only on the strain and on the symmetric part of the curvature tensor; furthermore, there is only one length scale parameter in this theory.

In the communication supported by this short paper, non-linear free vibrations of piezoelectric small-scale beams are investigated, using a modified couple stress theory. The partial differential equations of motion are obtained via Hamilton's principle and Bubnov-Galerkin's method is employed to arrive at ordinary differential equations. The method of multiple scales is employed to solve the latter equations, the solutions obtained using this perturbation method are compared with solutions computed by the shooting method, which is applied to this very same problem in [10]. The variation of the fundamental non-linear natural frequency of vibration with the length scale parameter is discussed.

2 Mathematical model

Beams of rectangular cross section with length L, width b, and thickness h are considered. Bernoulli-Euler's displacement field is adopted, with the displacement components of any point of the beam determined by the displacement components of points on its middle line (the neutral line in linear bending); the latter displacement components are represented by u and w, along the directions of longitudinal axis x and the transverse axis z, respectively.

The electric potential function $\phi(x,z,t)$ is based on references [11-13]; if no external voltage is applied to the electrodes, it is given by

$$\phi(x,z,t) = -\cos(\beta z)\,\varphi(x,t), \tag{1}$$

where $\beta = \pi/h$ and $\varphi(x,t)$ is the spatial function of the electric potential, which is one of the unknowns of the problem under analysis.

The following constitutive equations are assumed [12]

$$\sigma_x = C_{11}\varepsilon_x - e_{31}E_z, \tag{2}$$

$$D_x = \in_{11} E_x, \tag{3}$$

$$D_z = e_{31}\varepsilon_x + \in_{33} E_z, \tag{4}$$

$$m_{xy} = 2\mu l^2 \chi_{xy}. \tag{5}$$

In these equations, ε_x represents the axial strain, χ_{xy} the curvature, σ_x the axial stress, m_{xy} the deviatoric part of the couple stress, D_i the so-called electric displacements, E_i the electric field components, e_{31} is a piezoelectric coefficient and $\in_{ij}$ are dielectric coefficients. *l* is a length scale parameter, which is equal to the square root of the ratio of the modulus of curvature to the modulus of shear as explained, for example, in [7, 9, 14]. The length scale parameter gives a measure of the importance of the couple stress and, therefore, its relevance grows as the dimensions of the beam diminish. C_{11} is an equivalent elastic modulus as defined in [9], it reduces to the modulus of elasticity, E, when Poisson's effect, ν, is neglected. Letter μ represents the shear modulus.

Applying Hamilton's principle and neglecting the longitudinal inertia, the ensuing differential equations of motion are obtained

$$\frac{\partial^2 \bar{w}}{\partial \bar{t}^2} + \alpha_1 \frac{\partial^4 \bar{w}}{\partial \bar{x}^4} + \alpha_2 \left[\int_0^1 \left(\frac{\partial \bar{w}}{\partial \bar{x}}\right)^2 \mathrm{d}\bar{x}\right] \frac{\partial^2 \bar{w}}{\partial \bar{x}^2} + \alpha_3 \frac{\partial^2 \bar{\varphi}}{\partial \bar{x}^2} + \alpha_4 \frac{\partial^2 \bar{w}}{\partial \bar{x}^2 \partial \bar{t}^2} = 0, \tag{6}$$

$$\beta_1 \frac{\partial^2 \bar{\varphi}}{\partial \bar{x}^2} + \beta_2 \frac{\partial^2 \bar{w}}{\partial \bar{x}^2} + \beta_3 \bar{\varphi} = 0, \tag{7}$$

where the following parameters were introduced, in order to arrive at non-dimensional equations

$$\alpha_1 = \frac{C_{11}}{E} + \frac{12\mu l^2}{Eh^2}, \quad \alpha_2 = -6\frac{L^2}{h^2}\frac{C_{11}}{E}, \quad \alpha_3 = -\frac{24}{\pi}\frac{L^3}{h^3}\frac{C_{11}}{E}, \quad \alpha_4 = -\frac{1}{12}\frac{h^2}{L^2},$$
$$\beta_1 = \frac{\in_{11} C_{11}}{2{e_{31}}^2}, \quad \beta_2 = -\frac{2}{\pi}\frac{h}{L}, \quad \beta_3 = -\frac{\pi^2}{2}\frac{L^2}{h^2}\frac{\in_{33}}{{e_{31}}^2}C_{11}, \quad \bar{w} = \frac{w}{L}, \quad \bar{\varphi} = \frac{\varphi}{\varphi_0}, \quad \bar{t} = \frac{t}{t_0}, \tag{8}$$
$$\varphi_0 = \frac{L^2 C_{11}}{h e_{31}}, \quad t_0 = \frac{L^2}{h}\sqrt{\frac{12\rho}{E}}.$$

As explained in [10], $\bar{w}$ and $\bar{\varphi}$ are written as a sum of products of known functions of space (of *x*), which respect, at least, the geometric boundary conditions, and functions of time, which become the unknowns of the problem. Then Bubnov-Galerkin's method is applied. To solve the ordinary differential equations of motion, three independent variables $T_n = \epsilon^n \bar{t}$, *n*=1-3, are introduced and the method of multiple scales [15] is employed. If a one mode approach is implemented, the non-linear, non-dimensional, first natural frequency of vibration is

$$\bar{\omega}_1^{n\ell} = \bar{\omega}_1^{\ell} - \frac{3\alpha_2 \pi^4}{16(1-\pi^2\alpha_4)\bar{\omega}_1^{\ell}} {\bar{W}_1}^2 \tag{9}$$

where $\bar{W}_1$ is the non-dimensional vibration amplitude at the middle of the piezoelectric beam.

3 Numerical tests

The theoretical model was tested by carrying out comparisons, described in [10], with natural frequencies of various beams computed by other researchers. We now call the reader's attention to Figure 1, which portrays backbone curves – here, these curves relate non-dimensional fundamental frequency $\bar{\omega}_n = \omega_n L^2 \sqrt{\frac{12\rho}{Eh^2}}$ with the amplitude of the transverse vibration at the middle point of the beam - of micro-beams, for diverse values of dimensionless height *h/l*. This example is taken from reference [16] and Figure 1 (a) is very similar to Figure 1 of that reference. For moderate vibration amplitudes, the values obtained using equation (9), Figure 1 (b), are also close to the ones computed using the shooting method [10], Figure 1 (a). As the vibration amplitude increases, the values of the multiple

scales and shooting methods deviate, due to the typical loss of accuracy of perturbation methods with the growth of the vibration amplitude.

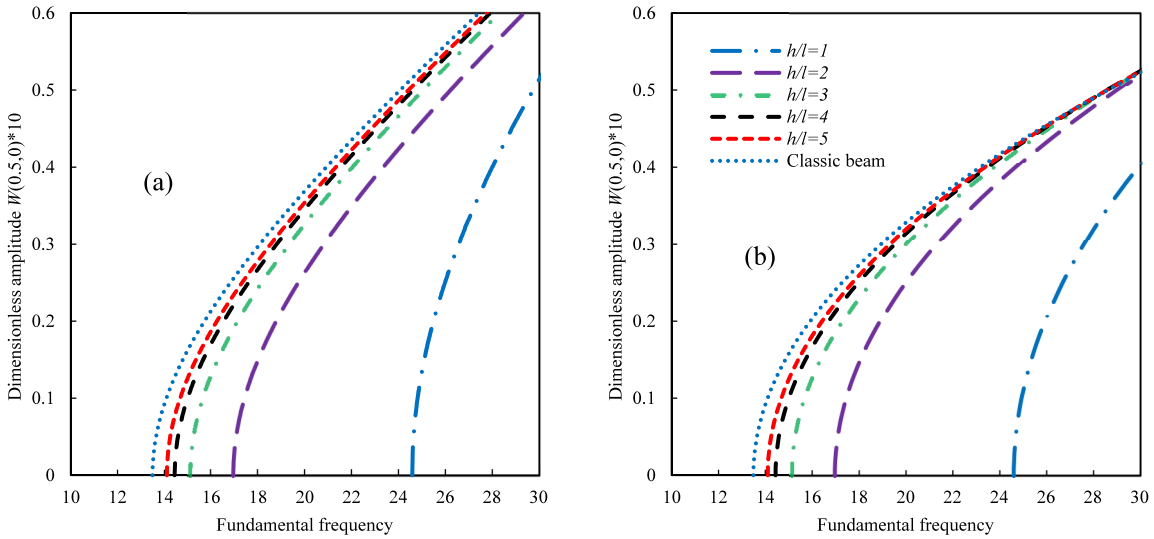

Figure 1. Backbone curves: (a) shooting method, (b) multiple scales method.

To illustrate the effects of the length scale on the non-linear fundamental frequency of vibration of piezoelectric beams, a beam in a piezoelectric material and with length to thickness ratio equal to 20 is now addressed. Figure 2 shows the backbone curves of the beam for different values of h/l, calculated using equation (9). As occurs in non-piezoelectric and classic beams [15], it is found that, regardless of the value of h/l, piezoelectric beams always show hardening spring behaviour. Moreover, as in beams that are not in piezoelectric materials [16], the natural frequencies of vibration of the size-dependent beam model are larger than those of the classical beam model.

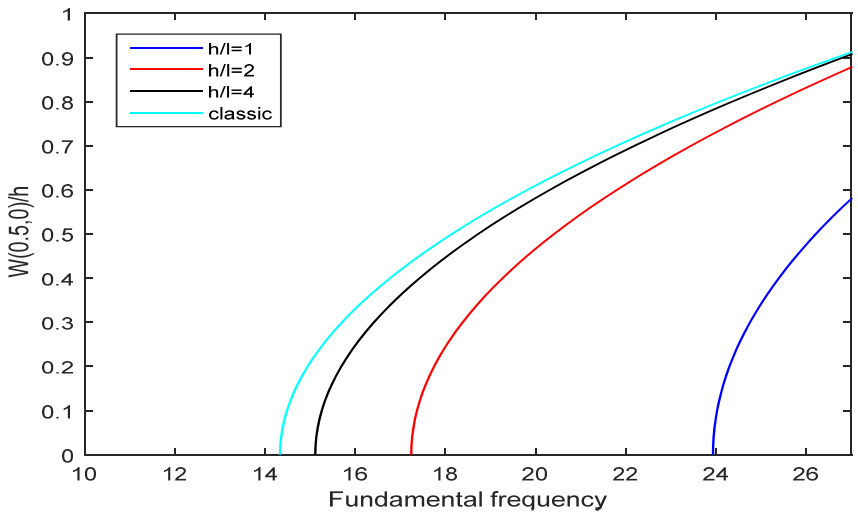

Figure 2. Fundamental frequency of vibration $\bar{\omega}_n = \omega_n L^2 \sqrt{\frac{12\rho}{Eh^2}}$ vs. central vibration amplitude, for various height to length scale ratios, hinged-hinged piezoelectric micro-beam ($v = 0.39$) - multiple scales method.

The brief study presented in this short paper is complemented in reference [10], where bifurcation and stability analyses are performed in micro beams in piezo-electric materials.

4 Concluding remarks

The evolution of the fundamental frequency of vibration with the vibration amplitude, on very small beams in piezoelectric materials, is examined. It is investigated how a modified couple stress theory, which has been suggested to capture the effect of the small size, affects the fundamental frequency. It is found that the piezoelectric effect does not change significantly the fundamental natural frequency: it leads to slightly different values, but hardening spring is still verified, as in non-piezoelectric beams. The couple stress theory employed increases the stiffness of the beam, but its contribution does not change with the vibration amplitude, therefore, it only appears in the linear part of the model. According to the modified couple stress theory, the importance of the size effect increases as the ratio of the beam height (h) to material length scale parameter (l) decreases. When the ratio h/l is equal to 5, the fundamental natural frequency already differs visibly from the classic one.

With the multiple scales method, an analytical solution for hinged-hinged piezoelectric, small-scale beams in piezoelectric materials is obtained, following steps similar to the ones applied in classic beams. An analytical solution brings the benefits of turning evident the influence of diverse parameters on the non-linear fundamental frequency of vibration and of allowing one to quickly perform parametric studies. On the other hand, the closed form solution derived deviates from more accurate, numerical, solutions as the vibration amplitude grows.

Acknowledgments

Hamed Akhavan and Pedro Ribeiro gratefully acknowledge the funding of Project NORTE-01-0145-FEDER-000022 - SciTech - Science and Technology for Competitive and Sustainable Industries, cofinanced by Programa Operacional Regional do Norte (NORTE2020), through Fundo Europeu de Desenvolvimento Regional (FEDER).

References

[1] S. Leadenham, A. Erturk, Unified nonlinear electroelastic dynamics of a bimorph piezoelectric cantilever for energy harvesting, sensing, and actuation. *Nonlinear Dynamics*, **79**, 1727-1743, 2015.
[2] M. I. Younis, *MEMS Linear and Nonlinear Statics and Dynamics*. Springer US, 2011.
[3] K. L. Ekinci, Electromechanical Transducers at the Nanoscale: Actuation and Sensing of Motion in Nanoelectromechanical Systems (NEMS). *Small*, **1**, 786–797, 2005.
[4] M. Asghari, M. Kahrobaiyan, M. Ahmadian, A nonlinear Timoshenko beam formulation based on the modified couple stress theory. *International Journal of Engineering Science*, **48**, 1749-1761, 2010.
[5] A. W. McFarland, J. S. Colton, Role of material microstructure in plate stiffness with relevance to microcantilever sensors. *Journal of Micromechanics and Microengineering*, **15**, 1060-1067, 2005.
[6] D. C. C. Lam, F. Yang, A. C. M. Chong, J. Wang, P. Tong, Experiments and theory in strain gradient elasticity. *Journal of the Mechanics and Physics of Solids*, **51**, 1477-1508, 2003.
[7] F. Yang, A. C. M. Chong, D. C. C. Lam, P. Tong, Couple stress based strain gradient theory for elasticity. *International Journal of Solids and Structures*, **39**, 2731–2743, 2002.
[8] M. H. Ghayesh, H. Farokhi, M. Amabili, Nonlinear behaviour of electrically actuated MEMS resonators. *International Journal of Engineering Science*, **71**, 137-155, 2013.
[9] J. Reddy, Microstructure-dependent couple stress theories of functionally graded beams. *Journal of the Mechanics and Physics of Solids*, **59**, 2382-2399, 2011.
[10] H. Akhavan, B. Soleimani Roody, P. Ribeiro, A. R. Fotuhi, Modes of vibration, stability and internal resonances on non-linear piezoelectric small-scale beams. Submitted on 2017.
[11] J. Yang, H. Xiang, Thermo-electro-mechanical characteristics of functionally graded piezoelectric actuators. *Smart Materials and Structures*, **16**, 784-797, 2007.
[12] M. Komijani, Y. Kiani, S. Esfahani, M. Eslami, Vibration of thermo-electrically post-buckled rectangular functionally graded piezoelectric beams. *Composite Structures*, **98,** 143-152, 2013.
[13] Q. Wang, S. Quek, A model for the analysis of beams with embedded piezoelectric layers. *Journal of Intelligent Material Systems and Structures*, **13**, 61-70, 2002.
[14] S. K. Park, X.-L. Gao, Bernoulli–Euler beam model based on a modified couple stress theory. *Journal of Micromechanics and Microengineering*, **16**, 2355-2359, 2006.
[15] A. H. Nayfeh, D. T. Mook, *Nonlinear oscillations*. Wiley, New York, 1979.
[16] Y.-G. Wang, W.-H. Lin, N. Liu, Nonlinear free vibration of a microscale beam based on modified couple stress theory. *Physica E-Low-Dimensional Systems & Nanostructures*, **47**, 80-85, 2013.

EUROMECH Colloquium 603
Dynamics of micro and nano systems
5 – 7 September 2018, Porto, Portugal

Ballistic thermal transport in two-dimensional $MoSe_2$ lattices

Nicolas Morell[1], Slaven Tepsic[1], Antoine Reserbat-Plantey[1], Andrea Cepellotti[2], Marco Manca[3], Andreas Isacsson[4], Xavier Marie[3], Francesco Mauri[5] and Adrian Bachtold[1]

[1]ICFO-The institute of photonic sciences, Av. Carl Friedrich Gauss, 3, Castelldefels (Barcelona), Spain.
slaven.tepsic@icfo.eu

[2] University of California at Berkeley, LeConte Hall 366, Berkeley (California),USA.

[3] INSA, 135 Avenue de Rngueil, Toulous, France.

[4] Chalmers University of Technology, Gothenburg, Sweden.

[5] Università di Roma La Sapienza, Pizzale Aldo Moro 5, Roma, Italy.

Summary. Nanomechanical resonators have emerged as sensors with exceptional sensitivities. These sensing capabilities are of interest for studying thermodynamic properties in condensed matter regimes that are difficult to access. We use optomechanical systems based on a $MoSe_2$ monolayer to probe the thermal properties of phonons in two-dimensional lattices. We measure the thermal conductivity and the specific heat capacity down to cryogenic temperature. The phonon transport crossovers from the diffusive to the ballistic regime when lowering the temperature below 100 K. The temperature dependence of the specific heat capacity approaches a quadratic dependence, the signature of two-dimensional lattices. Both the thermal conductivity and the specific heat capacity measurements are consistent with predictions based on first-principles. Our result establishes a new strategy to investigate thermal transport in two-dimensional materials, and allows for exploring the phonon hydrodynamic regime, the anomalous heat conduction, and the phase transitions of electronic many-body collective phenomena in monolayers.

Keywords: thermal transport, 2D materials, ballistic transport, low temperature

1 Introduction

Here we show how optomechanical systems can be used to study heat transport in low-dimensional materials(Fig. 1). Heat transport at the nanoscale is of major fundamental interest for a broad range of research fields, such as nanophononics, spintronics, and quantum thermodynamics. Phonons are the main carriers of heat in a large variety of low-dimensional materials, including carbon nanotubes [2, 3], graphene [4], and semiconductor monolayers [5]. Heat transport enters into interesting regimes at low temperature, such as the dissipationless transport through the low-dimensional material in the ballistic regime. However, measuring the thermal conductance at cryogenic temperature remains a challenging task. It requires the fabrication of sophisticated devices, which incorporate local heaters and thermometers, and a careful calibration of the latter. A complication for interpreting these measurements comes from the fact that the thermal conductance depends on various quantities that have not been measured independently thus far. These include the heat capacity and the phononic mean-free path.

2 Results

We measure the thermal conductance in a way similar to the well-established method based on Raman measurements [6, 7]. The laser beam is focused onto the centre of the $MoSe_2$ membrane. The static backaction is a simple absorption heating effect, which results in a temperature gradient ΔT between the centre of the membrane and its circular clamp. The temperature dependence of the thermal conductance suggests the crossover between ballistic and diffusive regimes (Fig. 2B). Below $\sim$100 K, the conductance gets larger when increasing temperature, which indicates ballistic transport. In this regime, the mean-free path is expected to be given by the characteristic size of the drum. Upon increasing temperature above

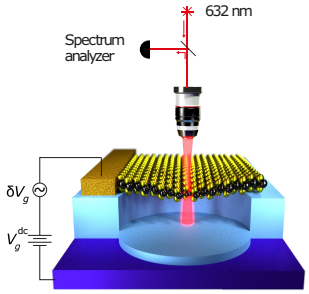

Figure 1. Schematic of the optomechanical device. The transition metal dichalcogenide monolayer drum is fabricated with the dry transfer of thin $MoSe_2$ crystals over prestructured holes. The mechanical vibrations are driven capacitively and detected by optical interferometry. The $MoSe_2$ monolayer is a mobile absorber in an optical standing wave produced by a 632 nm probe laser. The modulated laser refection intensity is measured with an avalanche photo-detector feeding a spectrum analyzer.

$\sim$100 K, the conductance starts to decrease, which is attributed to the reduction of due to phonon-phonon scattering.

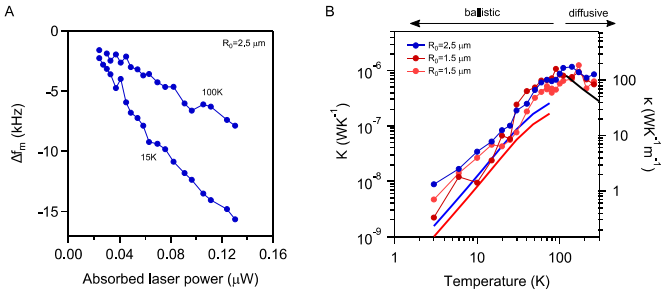

Figure 2. Thermal conductance of $MoSe_2$ monolayers. (A) Shift of the resonant frequency as a function of absorbed laser power. (B) Thermal conductance as a function of temperature.

3 Conclusion

Our optomechanical measurements provide a clear and detailed picture of thermal transport in monolayer $MoSe_2$ lattices down to cryogenic temperature. Our work opens the possibility to measure thermal properties in a large variety of different two-dimensional materials, because the devices required for these measurements are simple to fabricate. This new measurement method may allow the exploration of the phonon hydrodynamics regime, which is expected to be robust in monolayer systems.

References

[1] N. Morell, A. Reserbat-Plantey, I. Tsioutsios, K. G. Schadler, F. Dubin, F. H. L. Koppens, and A. Bachtold, High Quality Factor Mechanical Resonators Based on WSe_2 Monolayers. *NanoLetters* 16, 5102-5108, 2016.

[2] P. Kim, L. Shi, A. Majumdar, and P. McEuen, Thermal Transport Measurements of Individual Multiwalled Nanotubes. *Phys. Rev. Lett*, 87, 215502, 2001.

[3] C. Yu, L. Shi, Z. Yao, D. Li, and A. Majumdar, Thermal Conductance and Thermopower of an Individual Single-Wall Carbon Nanotube. *Nano Lett.* 5, 1842, 2005.

[4] A. A. Balandin, Thermal properties of graphene and nanostructured carbon materials. *Nat Mater* 10, 569, 2011.

[5] R. Yan, J. R. Simpson, S. Bertolazzi, J. Brivio, M. Watson, X. Wu, A. Kis, T. Luo, A. R. Hight Walker, and H. G. Xing, Thermal conductivity of monolayer molybdenum disulfide obtained from temperature-dependent Raman spectroscopy.*ACS Nano* 8, 986, 2014.

[6] A. A. Balandin, S. Ghosh, W. Bao, I. Calizo, D. Teweldebrhan, F. Miao, and C. N. Lau, Superior Thermal Conductivity of Single-Layer Graphene. *Nano Lett.* 8, 902, 2008.

[7] W. Cai, A. L. Moore, Y. Zhu, X. Li, S. Chen, L. Shi, and R. S. Ruo, Thermal conductance modulator based on folded graphene nanoribbons, *Nano Lett.* 10, 1645, 2010.

Vibrational Analysis of Functionally Graded Nano-Mass Sensor based on a Nonlocal Continuum Theory

Omid Rahmani [1], Ali R. Mohammadi Niaei [1], Amir H. Hosseini [1] and Mahdi Faisal[2]

[1] Smart Structures and New Advanced Materials Laboratory, Department of Mechanical Engineering, University of Zanjan, Zanjan, Iran
omid.rahmani@znu.ac.ir
armn.mech@gmail.com
hosseini@znu.ac.ir
[2] Sharif University of Technology, Tehran, Iran
Mahdi.faisal51@yahoo.com

Summary. Free vibration model of a cantilever functionally graded (FG) nanobeam with an attached mass at tip is introduced. The vibration performance is considered using nonlocal Euler-Bernoulli beam theory. The governing equations of the system with both axial and transverse displacements are derived based on Hamilton's principle and solved utilizing the differential transformation method (DTM) to find the nondimensional natural frequencies. The effect of various parameters such as mass and position of the attached nano particle, FG power-law exponent and nonlocal parameter on the frequency of nano sensor are studied. The results of the present study can be used as a benchmark in future studies of the free vibration of FG Nano-Mass Sensors.

Keywords: Nano sensor, Attaches mass, Vibration, Nonlocal theory, Functionally gradient materials.

1 Introduction

Nano-scale is usually investigated by three common following ways: theoretical methods including molecular dynamics modelling which need more time to solve, experimental techniques which are very expensive and continuum mechanics approaches which are useful for modelling the micro/nanostructures. The formulations of Continuum mechanics methodologies are simple and, as compared with other methods, have less computational cost. Continuum mechanics comprises classical (local) theories that are used for large-scale problems and broadly used size-dependent nonlocal elasticity theories introduced by Eringen [1]. In fact, small-scale effects cause that the classical continuum mechanics to be unable to predict the precise mechanical behaviour of nanostructures. Thus, the widely used nonlocal elasticity theory, which is size-dependent continuum theory and contains material length scale parameter is utilized to predict the accurate behavior of nanostructures.

In recent years, there has been an increasing amount of literature on the use of single-walled carbon nanotubes (SWCNTs) as mass nanosensors in which a nanoparticle (spherical fullerenes [2] or viruses [3]) is located on the SWCNT. The mass nanosensors are based on the fact that the resonant frequency is sensitive to the resonator mass, which includes the self-mass of the resonator and the attached mass. The deviation of the resonant frequency from its original value is owing to the change of the attached mass on the resonator. The main problem of mass detection is in measuring the change in the resonant frequency due to the added mass. The axial vibration of CNTs with clamped-free boundary condition and attached buckyball at free tip were investigated by Murmu and Adhikari [4]. Shen et al. [5] investigated the transverse vibration of nanotube-based cantilever micro-mass sensor via nonlocal Timoshenko beam theory.

In this work, the free vibration of a cantilever nanobeam made of functionally graded material with an attached buckyball at tip is considered. The nonlocal Euler-Bernoulli beam theory is used to derive the equations of motion of the nanobeam utilizing the Hamilton's principle. Consequently, accurate results of system characteristics can simply be acquired applying straightforward numerical process.

2 Mathematical formulation

2.1 Material properties

Fig. 1 shows the model of a clamped-free nanobeam of length L, width b and thickness h with an attached mass at tip. It is assumed that the nanobeam is made of a functionally graded material. The FG nanobeam is composed of a mixture of a ceramic at the top and a metal at the bottom surfaces, respectively.

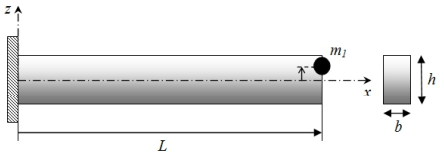

Figure 1. Schematic of the cantilever FG Nanobeam with an attached mass

According to the rule of mixture, the distribution of the effective material property P across the thickness is given as follow:

$$P(z) = (P_c - P_m)\left(\frac{z}{h} + \frac{1}{2}\right)^k + P_m \tag{1}$$

where k is the power-law exponent which determines the material variation contour through the thickness. The subscripts "c" and "m" relate the property to the ceramic and metal materials, respectively. By using the Hamilton's principle the governing equations based on Euler-Bernoulli beam theory (EBT) can be derived as follows:

$$\frac{\partial N}{\partial x} = I_0 \frac{\partial^2 u_0}{\partial t^2} - I_1 \frac{\partial^3 w_0}{\partial t^2 \partial x} - f(x) \tag{2}$$

$$\frac{\partial^2 M}{\partial x^2} = I_0 \frac{\partial^2 w_0}{\partial t^2} + I_1 \frac{\partial^3 u_0}{\partial t^2 \partial x} - I_2 \frac{\partial^4 w_0}{\partial t^2 \partial x^2} - q(x) \tag{3}$$

where N and M are stress resultants, I_i are mass inertia and u_0 and w_0 are midplane displacements.

2.2 Nonlocal theory

According to Eringen's theory for nonlocal elasticity which states that "the stress at a reference point x in the body depends not only on the strains at x but also on strains at all other points of the body", the nonlocal characteristic equation comes from [1]:

$$[1 - (e_0 a)^2 \nabla^2]\sigma_{ij} = \lambda \varepsilon_{kk} \delta_{ij} + 2\mu \varepsilon_{ij} \tag{4}$$

where $e_0 a$ is nonlocal parameter. For FG nanobeam, the constitutive relation can be simplified as:

$$\sigma_{xx} - (e_0 a)^2 \frac{\partial^2 \sigma_{xx}}{\partial x^2} = E(z)\varepsilon_{xx} \tag{5}$$

Integrating Eq. (5) over the beam's cross-section area, the axial normal force-displacement relation is obtained as follow [4]:

$$N - \eta^2 \frac{\partial^2 N}{\partial x^2} = S_0 \frac{\partial u_0}{\partial x} - S_1 \frac{\partial^2 w_0}{\partial x^2} \tag{6}$$

Multiplying Eq. (5) by z, integrating over the cross-section area, the bending moment-displacement relation can be obtained as:

$$M - \eta^2 \frac{\partial^2 M}{\partial x^2} = S_1 \frac{\partial u_0}{\partial x} - S_2 \frac{\partial^2 w_0}{\partial x^2} \tag{7}$$

In above equations, $\eta = e_0 a$ and S_0, S_1 and S_2 are cross-sectional rigidities which are defined as follow:

$$(S_0, S_1, S_2) = \int_A E(z)(1, z, z^2) dA \tag{8}$$

The explicit relation of the nonlocal axial normal force can be derived by substituting the second derivative of N from Eq. (2) into Eq. (6) and setting the axial distribution load f equal to zero under free vibration conditions:

$$N = \eta^2 \left[I_0 \frac{\partial^3 u_0}{\partial t^2 \partial x} - I_1 \frac{\partial^4 w_0}{\partial t^2 \partial x^2} \right] + S_0 \frac{\partial u_0}{\partial x} - S_1 \frac{\partial^2 w_0}{\partial x^2} \tag{9}$$

Also the explicit relation of the nonlocal bending moment can be derived by substituting the second derivative of M from Eq. (3) into Eq. (7) and setting the transverse distribution load q equal to zero under free vibration conditions:

$$M = \eta^2 \left[I_0 \frac{\partial^2 w_0}{\partial t^2} + I_1 \frac{\partial^3 u_0}{\partial t^2 \partial x} - I_2 \frac{\partial^4 w_0}{\partial t^2 \partial x^2} \right] + S_1 \frac{\partial u_0}{\partial x} - S_2 \frac{\partial^2 w_0}{\partial x^2} \tag{10}$$

Furthermore, substituting Eqs. (9) and (10) into Eqs. (6) and (7), leads to the following governing equations of FGM nanobeam with an attached mass which are presented in terms of the displacements.

$$\eta^2 \left[I_0 \frac{\partial^4 u_0}{\partial t^2 \partial x^2} - I_1 \frac{\partial^5 w_0}{\partial t^2 \partial x^3} \right] + S_0 \frac{\partial^2 u_0}{\partial x^2} - S_1 \frac{\partial^3 w_0}{\partial x^3} = I_0 \frac{\partial^2 u_0}{\partial t^2} - I_1 \frac{\partial^3 w_0}{\partial t^2 \partial x} \tag{11}$$

$$\eta^2 \left[I_0 \frac{\partial^4 w_0}{\partial t^2 \partial x^2} + I_1 \frac{\partial^5 u_0}{\partial t^2 \partial x^3} - I_2 \frac{\partial^6 w_0}{\partial t^2 \partial x^4} \right] + S_1 \frac{\partial^3 u_0}{\partial x^3} - S_2 \frac{\partial^4 w_0}{\partial x^4} = I_0 \frac{\partial^2 w_0}{\partial t^2} + I_1 \frac{\partial^3 u_0}{\partial t^2 \partial x} - I_2 \frac{\partial^4 w_0}{\partial t^2 \partial x^2} \tag{12}$$

The following boundary conditions of the clamped-free FG nanobeam with an attached mass at free tip are obtained by setting the individual terms from the variation integral equal to zero:

$$w_0(0,t) = u_0(0,t) = \frac{\partial w_0}{\partial x}(0,t) = 0 \tag{13}$$

and at $x=L$:

$$\eta^2 \left[I_0 \frac{\partial^3 u_0}{\partial t^2 \partial x} - I_1 \frac{\partial^4 w_0}{\partial t^2 \partial x^2} \right] + S_0 \frac{\partial u_0}{\partial x} - S_1 \frac{\partial^2 w_0}{\partial x^2} + m_1 \frac{\partial^2 u_0}{\partial t^2} - m_1 z \frac{\partial^3 w_0}{\partial t^2 \partial x} = 0 \tag{14}$$

$$\eta^2 \left[I_0 \frac{\partial^3 w_0}{\partial t^2 \partial x} + I_1 \frac{\partial^4 u_0}{\partial t^2 \partial x^2} - I_2 \frac{\partial^5 w_0}{\partial t^2 \partial x^3} \right] + S_1 \frac{\partial^2 u_0}{\partial x^2} - S_2 \frac{\partial^3 w_0}{\partial x^3} - I_1 \frac{\partial^2 u_0}{\partial t^2} + I_2 \frac{\partial^3 w_0}{\partial t^2 \partial x} + m_1 \frac{\partial^2 w_0}{\partial t^2} = 0 \tag{15}$$

$$\eta^2 \left[I_0 \frac{\partial^2 w_0}{\partial t^2} + I_1 \frac{\partial^3 u_0}{\partial t^2 \partial x} - I_2 \frac{\partial^4 w_0}{\partial t^2 \partial x^2} \right] + S_1 \frac{\partial u_0}{\partial x} - S_2 \frac{\partial^2 w_0}{\partial x^2} + m_1 z \frac{\partial^2 u_0}{\partial t^2} - m_1 z^2 \frac{\partial^3 w_0}{\partial t^2 \partial x} = 0 \tag{16}$$

Generally, it is very difficult to derive an analytical solution for Eqs (11) and (12) due to complication of governing equations and boundary conditions. In this case, the DTM (Differential Transformation Method) is employed to translate these equations into a set of ordinary equations and solve the problem.

3 Results

First, the results of the present investigation are verified with those previously published study in Table 1. In this table, to compare the results with Ref. [6], the attached mass is considered as zero (m_1=0) and the four first natural frequencies while varying the material distribution for a range of nonlocal parameter, is presented. The beam length is equal to L=10,000 *nm* and its width is b=1000 *nm*. The nondimensional form of the fundamental frequency of the beam is $\overline{\omega} = \omega L^2 \sqrt{\rho A / EI}$.

Table 4: Validation of nondimensional frequencies of clamped-free FG nanobeams

$\eta\times10^{-12}$	$\bar{\omega}_i$	*k=0*		*k=0.2*		*k=0.5*	
		Present	Ref. [6]	Present	Ref. [6]	Present	Ref. [6]
0	*i=1*	3.5160	3.5167	3.0976	3.0974	2.7596	2.76
	i=2	22.0333	22.0378	19.4115	19.415	17.2933	17.2967
1	*i=1*	3.5312	3.5292	3.1111	3.1123	2.7716	2.7693
	i=2	20.6782	20.6817	18.2176	18.2211	16.2297	16.2332
2	*i=1*	3.5469	3.5461	3.1248	3.1261	2.7838	2.7841
	i=2	19.5081	19.5105	17.1868	17.1897	15.3113	15.3141

In the following, the effects of the physical and geometrical parameters such as material distribution, nonlocal parameter and the nanoparticle mass on the vibrational behaviour of nanosensors are studied.

Fig. 2 demonstrates the variation of nondimensional fundamental frequency with varying of the nonlocality parameter and material distribution and attached buckyball mass at mid-plane (z=0) with the slenderness ratio and power index of L/h=20 and k=2. It can be seen that, the nondimensional frequency increases with the increase of nonlocality parameter. In addition, as the power index increases, the nondimensional frequency decreases and the curves of frequencies of higher power indices tend to close together.

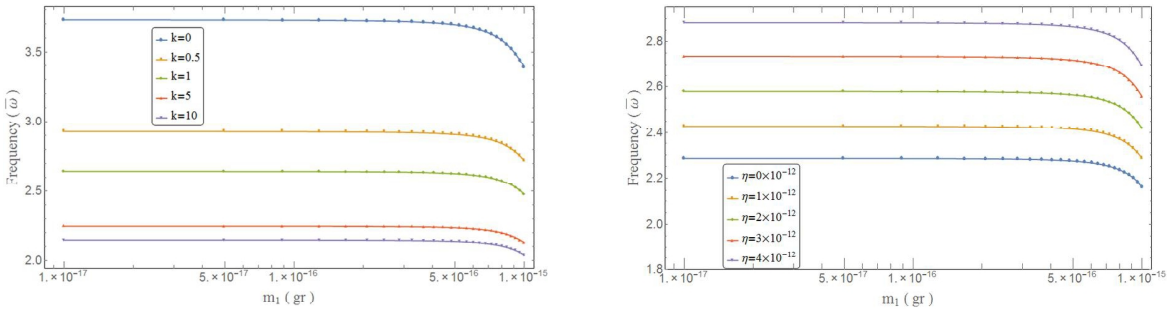

Figure 2. Variation of nondimensional fundamental frequency with variation of the nonlocality parameter (right) and material distribution (left) and attached buckyball

4 Conclusions

The free vibration analysis of a functionally graded nanobeam with an attached mass at tip was investigated. The results were validated by previous studies and showed that the proposed model without mass has good agreement with them. It was also shown that, the increasing the power index (k), causes the decrease of natural frequencies. On the other hand, the increase of first natural frequency occurs with high rate as the nonlocal parameter increases for the smaller attached masses.

References

[1] A.C. Eringen, *Nonlocal continuum field theories*. Springer; 2002.

[2] C.N.R. Rao, R. Seshadri, A. Govindaraj, R. Sen, Fullerenes, nanotubes, onions and related carbon structures. *Materials Science and Engineering: R: Reports,* **15**, 209–62, 1995.

[3] M Talati, P.K. Jha, Acoustic phonon quantization and low-frequency Raman spectra of spherical viruses. *Physical Review E*, **73(1)**, 011901, 2006.

[4] T. Murmu, S. Adhikari, Nonlocal vibration of carbon nanotubes with attached buckyballs at tip. *Mechanics Research Communications*, **38**, 62–7, 2011.

[5] B.Z. Bin Shen, P.L.P. Sheng, F.X.F. Li, J.G.J. Tang, Nonlocal Timoshenko beam theory for vibration of carbon nanotube-based biosensor. *Physica E: Low-dimensional Systems and Nanostructures*, **44**, 1169–75, 2012.

[6] M.A. Eltaher, S.A. Emam, F.F. Mahmoud, Free vibration analysis of functionally graded size-dependent nanobeams. *Applied Mathematics and Computation,* **218**:7406–20, 2012.

EUROMECH Colloquium 603
Dynamics of micro and nano systems
5 – 7 September 2018, Porto, Portugal

Parametric Study on Buckling Behavior of Piezoelectric Nanobeams based on Nonlocal Elasticity Theory

Mehdi Yarmohammad Tooski [1], Ali Akbar Jandaghian[2] and Omid Rahmani [3]

[1] Department of Mechanical Engineering, South Tehran Branch, Islamic Azad University, Tehran, Iran
M_yarmohammad@azad.ac.ir
[2,3] Smart Material and New Advanced Materials Laboratory, Department of Mechanical Engineering, University of Zanjan, Zanjan, Iran
a.a.jandaghian@znu.ac.ir
Omid.rahmani@znu.ac.ir

Summary. In this study, buckling behavior of the piezoelectric nanobeams is examined based on the nonlocal theory and Euler-Bernoulli beam theory. The electric potential is assumed linear through the thickness of the nanobeam and the governing equations are derived by Hamilton's principle. The governing equations are solved analytically for different boundary conditions. The effects of the nonlocal parameter and external electric voltage on the critical buckling load of the piezoelectric nanobeams are discussed in detail. This study should be useful for the design of piezoelectric nanodevices.

Keywords: Analytical Solution; Critical Buckling Load; Nonlocal Elasticity Theory; Piezoelectric Nanobeam.

1 Introduction

Because of the excellent properties of piezoelectric materials, they have many applications in smart structures or systems. They undergo mechanical deformations when placed in an electric field, and become electrically polarized under mechanical loads and therefore, they are appropriate for a variety of micro/nano electromechanical systems [1], nanoresonators [2], and biosensors [3]. Because of the demands in applications and high sensibility of MEMS/NEMS to external excitations, obtaining the mechanical properties of these nanoscale devices has attracted a lot of attention. Due to wide applications of nanobeams in engineering, such as nanowires, nanoprobes, atomic force microscope (AFM), and nanosensors, they have attracted a lot of consideration [4]. Hence, many investigations have been carried out about buckling, vibration, noise control and bending of nanobeams [5]. However, the direct use of classical continuum theory in nanostructures leads to wrong results in predicting their mechanical behavior because the classical theory cannot capture the size effects. Since the experimental methods at the nanoscale are too time-consuming, many researchers in nanotechnology use modified continuum models based on the concept of nonlocal elasticity for modeling the nanostructures. Such theories contain information about the forces between atoms, and the internal length scale is introduced into the constitutive equations as a material parameter. Between these theories, Eringen's theory, due to its simplicity and high accuracy, has found wide application in studying the behavior of nanostructures. Studies show that the results obtained from this theory are in good agreement with the results obtained by the method of molecular dynamics [6]. Ke et al. [7] investigated the nonlinear vibration of the piezoelectric nanobeams based on the nonlocal theory and Timoshenko beam theory by using the differential quadrature (DQ) method. Because nanobeams are important structures widely used in the piezoelectric nanodevices, the buckling analyses of piezoelectric nanobeams are of primary importance in the design of piezoelectric nanodevices such as nanoresonators, field effect transistors and sensors. According to the best of the authors' knowledge, there is no exact solution for the buckling analyses of the piezoelectric nanobeams based on the nonlocal theory. Therefore, in this article we have tried to provide an exact solution for the buckling analyses of piezoelectric nanobeams for various boundary conditions.

2 Nonlocal theory for piezoelectric materials

The layout of a problem is shown in Fig. 1. Consider a straight uniform nanobeam with the length L and

rectangular cross-section with width b, and thickness h. Based on the theory of nonlocal piezoelectricity, the stress tensor and the electric displacement at a reference point depend not only on the strain components and electric-field components at same position but also on all other points of the body [6]. The nonlocal constitutive behavior for the piezoelectric material can be given as follows:

$$\sigma_{ij} = \int_V \alpha\left(|x'-x|,\tau\right)\left[C_{ijkl}\varepsilon_{kl}(x') - e_{kij}E_k(x')\right]dx' \tag{1}$$

$$D_i = \int_V \alpha\left(|x'-x|,\tau\right)\left[e_{ikl}\varepsilon_{kl}(x') + \Xi_{ik}E_k(x')\right]dx' \tag{2}$$

$$\sigma_{ij,j} = \rho\ddot{u}_i,\ \ D_{i,i} = 0, \tag{3}$$

$$\varepsilon_{ij} = \frac{1}{2}\left(u_{i,j} + u_{j,i}\right),\ \ E_i = -\Phi_{,i} \tag{4}$$

where σ_{ij}, ε_{ij}, D_i, E_i and u_i are the stress, strain, electric displacement, electric field and displacement components, respectively; C_{ijkl}, e_{kij}, Ξ_{ik} and ρ are the fourth-order elasticity tensor, piezoelectric constants, dielectric constants and mass density, respectively; and Φ is the electric potential. $\tau = e_0a/l$ is defined as the scale coefficient. According to Eringen [6], the constitutive equations (1) and (2) can be converted to the equivalent differential constitutive equations form as

$$\sigma_{ij} - (e_0a)^2\nabla^2\sigma_{ij} = C_{ijkl}\varepsilon_{kl} - e_{kij}E_k, \tag{5}$$

$$D_i - (e_0a)^2\nabla^2 D_{ii} = e_{ikl}\varepsilon_{kl} + \Xi_{ik}E_k, \tag{6}$$

where ∇^2 is the Laplace operator.

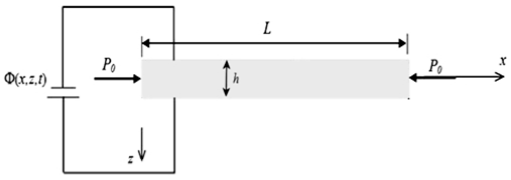

Fig. 1. Piezoelectric nanobeam under electro-mechanical loadings.

3 The governing equations

In this article, we use Wang [8] electric potential model to describe the electric potential distribution across the thickness of piezoelectric nanobeam. The electric potential at any point of the piezoelectric nanobeam is assumed as

$$\Phi(x,z,t) = -\cos(\beta z)\phi(x,t) + \frac{2zV_0}{h}e^{i\Omega t} \tag{7}$$

where $\beta = \pi/h$, z is measured from the mid-plane of the nanobeam in the transverse direction; $\phi(x,t)$ is the electric potential in the x direction; V_0 is the external electric voltage and Ω is the natural frequency of the piezoelectric nanobeam. According to Eqs. (4) and (7), the electric fields is given as

$$E_x = -\frac{\partial\phi}{\partial x} = \cos(\beta z)\frac{\partial\phi}{\partial x}, \tag{8}$$

$$E_z = -\frac{\partial\phi}{\partial z} = -\beta\sin(\beta z)\phi - \frac{2V_0}{h}e^{i\Omega t} \tag{9}$$

By applying, Hamilton's principal the governing equations of piezoelectric nanobeams based on Euler–Bernoulli beam theory can be rewritten as

$$\frac{\partial N_x}{\partial x} = m_0\left(1-(e_0a)^2\frac{\partial^2}{\partial x^2}\right)\frac{\partial^2 u_0}{\partial t^2} \tag{10}$$

$$F_{31}\frac{\partial^2 w_0}{\partial x^2} - X_{11}\frac{\partial^2\phi}{\partial x^2} - X_{33}\phi = 0 \tag{11}$$

$$D\frac{\partial^4 w_0}{\partial x^4} + F_{31}\frac{\partial^2\phi}{\partial x^2} + (N_p + N_E)\frac{\partial^2}{\partial x^2}\left(w_0 - (e_0a)^2\frac{\partial^2 w_0}{\partial x^2}\right) = m_0\left(1-(e_0a)^2\frac{\partial^2}{\partial x^2}\right)\frac{\partial^2 w_0}{\partial t^2} \tag{12}$$

where N_P is the normal force induced by the axial force and N_E is the normal force induced by the external electric voltage V_0, which may be written as

$$N_E = 2e_{31}V_0. \tag{13}$$

and

$$D=\int_{-h/2}^{h/2}-c_{11}z^2dz, F_{31}=\int_{-h/2}^{h/2}e_{31}\beta\sin(\beta z)zdz,\ X_{11}=\int_{-h/2}^{h/2}\Xi_{11}\cos^2(\beta z)dz, X_{33}=\int_{-h/2}^{h/2}\Xi_{33}\left[\beta\sin(\beta z)\right]^2dz \tag{14}$$

Note that for the homogeneous piezoelectric nanobeam Eq. (10) is decoupled with Eqs. (11) and (12). Therefore, in the following analysis, we only consider the governing equations (11) and (12) to describe the buckling behavior of the piezoelectric nanobeams [9, 10].

In the present study, the exact solutions for the buckling of piezoelectric nanobeams for different boundary conditions are obtained. It is assumed that the electric potential is zero at ends of the nanobeam. Setting $\partial/\partial t=0$ and solving equations (11) and (12) for ϕ gives

$$\phi=\frac{X_{11}D}{X_{33}F_{31}}\frac{\partial^4 w}{\partial x^4}+\frac{F_{31}}{X_{33}}\frac{\partial^2 w_0}{\partial x^2}+\frac{(N_p+N_E)X_{11}}{X_{33}F_{31}}\frac{\partial^2}{\partial x^2}(w_0-\mu\frac{\partial^2 w_0}{\partial x^2}) \tag{15}$$

Applying the operator $\partial^2/\partial x^2$ to ~~the~~ equation (15) and ~~substitute~~ substituting the obtained equation into equation (11) gives a decoupled fourth-order ordinary differential equation as follow:

$$\frac{d^4w}{dx^4}+\eta\frac{d^2w}{dx^2}+Nw=0 \tag{16}$$

where $\eta=\dfrac{D+F_{31}^2/X_{33}+NX_{11}/F_{31}X_{33}-\mu N}{X_{11}D/X_{33}-\mu NX_{11}/F_{31}X_{33}}$ and $N=N_p+N_E$

The general solution of Eq. (16) can be written as

$$w(x)=C_1\sinh(\lambda_1 x)+C_2\cosh(\lambda_1 x)+C_3\sinh(\lambda_2 x)+C_4\cosh(\lambda_2 x)\partial \tag{17}$$

where $\lambda_1=\left(\dfrac{-\eta+\sqrt{\eta^2-4N}}{2}\right)^{1/2}$, $\lambda_2=\left(\dfrac{-\eta-\sqrt{\eta^2-4N}}{2}\right)^{1/2}$ and C_k (k = 1,...4) are four unknown constants to be determined from four boundary conditions at each ends of nanobeam, x = 0, L.

By imposing the four boundary conditions at x = 0 and L a system of four homogeneous linear algebraic equations is obtained. Setting the determinant of the coefficient matrix equal to zero, we obtain an algebraic equation for the determination of critical buckling loads of the piezoelectric nanobeam.

4 Numerical Results

In this section, we will present the analytical study on the electro-mechanical buckling and vibration of piezoelectric nanobeam developed in the previous sections. Assume that the nanobeam is made of PZT-4 with the material properties presented in reference [8]. The following parameters are used in computing the numerical values: L =10000 (nm) and h = 500 (nm). The nondimensional buckling loads for clamped-clamped (C-C), simply supported-simply supported (S-S), clamped-simply supported (C-S), and clamped-free (C-F) boundary conditions are tabulated in Table1. Based on these results, it can be seen that the critical buckling loads related to all boundary conditions are reduced with growing the value of nonlocal parameter, which demonstrates this fact that with incorporating the nanoscale size-effects, the stiffness of nanobeam decreases. Also, it is observed that for lower L/h, nonlocality is more important and this effect is lost for higher L/h.

Table 1. Nondimensional critical buckling loads of the piezoelectric nanobeam for different boundary conditions.

L/h	$\mu=e_0a$	Boundary Conditions			
		C-C	S-S	C-S	C-F
100	0	38.3453	9.6957	19.8107	2.4639
	1	34.9006	8.8247	18.0311	2.2426
	2	32.0238	8.0974	16.5450	2.0578
	3	29.5852	7.4808	15.2851	1.9011
	4	27.4919	6.9514	14.2034	1.7665
20	0	38.7815	9.6954	19.8101	2.4638
	1	35.2977	8.8244	18.0305	2.2425
	2	32.3883	8.0971	16.5444	2.0577

	3	29.9219	7.4805	15.2845	1.9010
	4	27.8046	6.9512	14.2030	1.7665

To illustrate the effect of small scale on the buckling load of piezoelectric nanobeam, nondimensional buckling load versus the variation of nonlocal parameter at different length are plotted in Fig. 2. It can be observed that for all the slender ratios when the nonlocal parameter increases, the nondimensional buckling load decreases.

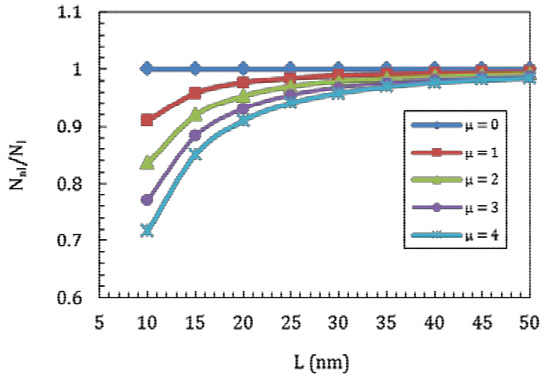

Fig. 2. Variation of the critical buckling load ratio with piezoelectric nanobeams length for different nonlocal parameters ($V = 0$).

5 Conclusion

In this study, buckling behavior of the piezoelectric nanobeams based on the nonlocal and Euler-Bernoulli beam theory is investigated. The Hamilton's principle is used to obtain the governing equations and is solved analytically to obtain the critical buckling loads of piezoelectric nanobeams. The various boundary conditions such as clamped-clamped, simply supported-simply supported, clamped-simply supported, and clamped-free have been considered. It can be observed that critical buckling loads decreased as the nonlocal parameter increased for all boundary conditions.

References

[1] A. Lazarus, O. Thomas, J.-F. Deü, Finite element reduced order models for nonlinear vibrations of piezoelectric layered beams with applications to NEMS. *Finite Elements in Analysis and Design,* **49 (1),** 35-51, 2012.

[2] S.M. Tanner, J. Gray, C. Rogers, K. Bertness, N. Sanford, High-Q GaN nanowire resonators and oscillators. *Applied Physics Letter,* **91 (20)**, 117-203, 2007.

[3] T. Murmu, S. Adhikari, Nonlocal frequency analysis of nanoscale biosensors. *Sensors and Actuators A: Physical,* **173 (1)**, 41-48, 2012.

[4] M. Moghimi Zand, M. Ahmadian, Vibrational analysis of electrostatically actuated microstructures considering nonlinear effects. *Communications in Nonlinear Science and Numerical Simulation,* **14 (4)**, 1664-1678, 2009.

[5] C. Li, C.W. Lim, J. Yu, Dynamics and stability of transverse vibrations of nonlocal nanobeams with a variable axial load. *Smart Materials and Structures*, **20 (1)**, 015-023, 2011.

[6] A.C. Eringen, Nonlocal continuum mechanics based on distributions. *International Journal of Engineering Science*, **44 (3)**, 141-147, 2006.

[7] L.-L. Ke, Y.-S. Wang, Z.-D. Wang, Nonlinear vibration of the piezoelectric nanobeams based on the nonlocal theory. *Composite Structures*, **94 (6)**, 2038-2047, 2012.

[8] Q. Wang, On buckling of column structures with a pair of piezoelectric layers. *Engineering Structures,* **24 (2)**, 199-205, 2002.

[9] C. Liu, L.-L. Ke, Y.-S. Wang, J. Yang, S. Kitipornchai, Thermo-electro-mechanical vibration of piezoelectric nanoplates based on the nonlocal theory. *Composite Structures,* **106 (0)**, 167-174, 2013.

[10] H.-T. Thai, T.P. Vo, A nonlocal sinusoidal shear deformation beam theory with application to bending, buckling, and vibration of nanobeams. *International Journal of Engineering Science*, **54 (0)**, 58-66, 2012.

EUROMECH Colloquium 603
Dynamics of micro and nano systems
5 – 7 September 2018, Porto, Portugal

On the quasiperiodic motion in nonlinear graphene resonators

Pierpaolo Belardinelli[1,2], Robin J. Dolleman[3], Peter G. Steeneken[1,3] and Farbod Alijani[1]

[1]Precision and Microsystems Engineering, TU Delft, Delft, The Netherlands
p.belardinelli@tudelft.nl, p.g.steeneken@tudelft.nl, f.alijani@tudelft.nl

[2] DICEA, Polytechnic University of Marche, Ancona, Italy

[3] Kavli Institute of Nanoscience, Delft University of Technology, Delft, The Netherlands
r.j.dolleman@tudelft.nl

Summary. In this work we demonstrate the presence of quasiperiodic oscillations in a graphene resonator. We present theory and experiments designed to assess the prevalence of attracting solutions for the flow on a torus. The equation of motion is obtained by fitting the nonlinear hardening behavior of the resonator and is expressed in two slow dynamical variables. The simulations can very well reconstruct the quasiperiodic behavior established in the resonating motion with a slow frequency modulation.

Keywords: Quasiperiodic motion, graphene membrane, slow modulation, structural motion stability.

1 Introduction

In the realm of studying the attractors of dynamical systems, a great deal of interest is in quasiperiodicity because this motion is present in a large number of nonconservative dynamical systems. In terms of complexity, it can be classified immediately after periodicity and preceding nonchaotic strange attractors [1]. There are numerous examples of the presence of quasiperiodic behaviors in both natural and technological fields such as neurodynamics, astrophysics and geology [2, 3].

The case in which it is possible to observe quasiperiodic oscillations is in systems characterized by the presence of two incommensurable frequencies and as a result of secondary Hopf bifurcations. In phase space, attractors corresponding to such oscillations have the form of invariant tori. However, since the study in terms of flow systems (differential equations) is quite involved, it is preferable to deal with discrete maps describing the delicate quasiperiodic scenario [4]

In this work, we study the dynamic phenomena of a nonlinear graphene resonator with the particular focus of obtaining quasiperiodic attractors. Graphene is a two-dimensional material that has recently gained attention for several potential applications, e.g. pressure, gas and mass sensors [5]. Graphene membranes exhibit signature of nonlinearity at pN forces, which makes them interesting candidates to improve their performance as sensors. However, the nanomechanical characterization of the material and its complete phenomenological understanding is far from being understood [6]. In view of these prospects and research challenges, the primary objective should be a fully comprehensive study of the dynamical response in all its facets. Here, we address one of the most interesting points in the nonlinear dynamics regarding graphene membranes, the borders and transitions between order and chaos.

2 Experimental setup

Figure 1(a) sketches the samples used in the experiment composed of a circular resonator with a venting channel on one side [7]. Figure 1(b) shows the laser interferometer setup used for the actuation and the readout of the motion of the membrane. The sample is placed inside a vacuum chamber with optical access to enable the measurement by using Fabry-Perot interferometry. The tension in the membrane is modulated with a blue laser that induces a variation in the membrane temperature. A vector network analyzer controls the modulation signal of the blue laser and measures the amplitude and phase of the signal at the same frequency detected at the photodetector.

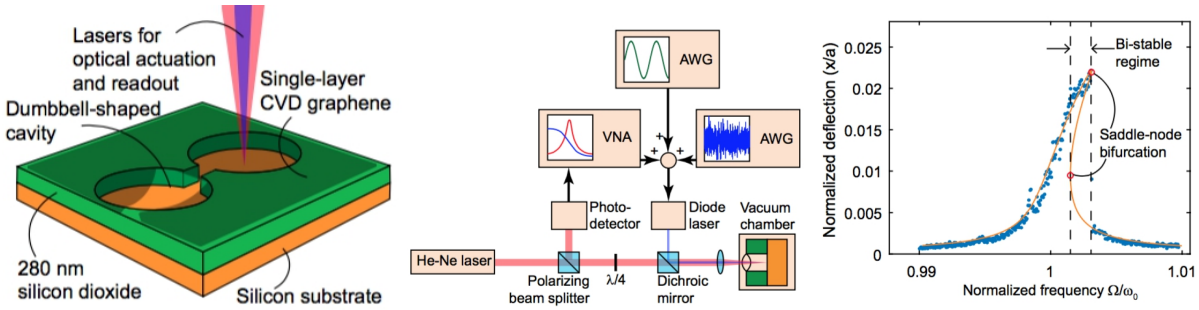

(a) (b) (c)

Figure 1: a) Schematic figure of the sample used in the experiment. Dumbbell shaped cavities are etched in a 280 nm thick layer of silicon dioxide. Single layer graphene covers the dumbbell and one side of the cavity is intentionally broken, leaving a resonator with a venting channel on the other side. (b) Laser interferometer setup used to actuate and readout the motion of the suspended graphene resonators. The red laser reads out the motion by Fabry-Perot interferometry and the blue laser provides thermal actuation. The electronic modulation channel is used to provide the high-frequency drive from the vector network analyzer (VNA), slow modulation from an arbitrary waveform generator (AWG) and white noise from a second AWG. (c) Nonlinear mechanical response of the resonator to a high frequency drive. The motion is fitted to find the equation of motion. The frequency is normalized with respect to the resonance frequency $\omega_0/2\pi = 15.3$ MHz and radius $a = 2.5\ \mu$m.

3 General formulation in fast and slow variables

We describe the motion with a single deflection parameter x, which is the deflection of the center of the membrane. The simple phenomenological equation of motion approximating the nonlinear response of the fundamental resonance mode is of the form

$$\ddot{x} + 2\Gamma\dot{x} + {\omega_0}^2 x + \gamma x^3 = F\sin\omega_F t. \tag{1}$$

in which Γ is the damping constant, γ the cubic spring constants, F and ω_F the amplitude and frequency of the direct driving, respectively. The equation is normalized with respect to the mass, x is normalized with respect to the radius a of the resonator and the frequency is made dimensionless by the resonance frequency ω_0. Figure 1(c) shows the frequency response of the resonator measured by the vector network analyzer at the driving level used in the experiment. At this driving power, the response is nonlinear and can be fit in order to extract the nonlinear parameters in the equation of motion [6]. From the fit, a forcing amplitude $F = 32.4$ pN and cubic stiffness $k_3 = 3.04\times10^{17}$ N/m^3 are obtained. In what follows the analysis is performed with the dimensionless parameters obtained from the nonlinear identification: $\Gamma = 0.00045$, $\gamma = 17$, $F = 2\times10^{-5}$, $\omega_0 = 1$, $\omega_F = 1.002$.

The solution of Eq. 1 is assumed as

$$x = p(t)\cos\omega_F t + q(t)\sin\omega_F t \tag{2}$$

in which $p(t)$ and $q(t)$ are slowly varying functions of time. Following the standard procedure of the method of averaging [8], by ironing out the fast oscillating terms we obtain

$$\begin{cases} \dot{p} = \dfrac{{\omega_0}^2 - {\omega_F}^2}{2\omega_F} q - \Gamma p + \dfrac{3}{8}\dfrac{\gamma}{\omega_F} q\left(p^2+q^2\right) \\ \dot{q} = -\dfrac{{\omega_0}^2 - {\omega_F}^2}{2\omega_F} p - \Gamma q - \dfrac{3}{8}\dfrac{\gamma}{\omega_F} p\left(p^2+q^2\right) + \dfrac{F}{2\omega_F} \end{cases}. \tag{3}$$

This set of equations governs the slow dynamics of the system and can be used as reference for the deconvolution of the experimental data. In addition, the fundamental frequency has to be considered modulated, due to the effect of the blue laser that heats the membrane and thus modulates its tension via thermal expansion, as $\omega_0(t) = 1 + \tilde{\omega}_0\cos\omega_G t$, where ω_G is a slow modulation frequency which in our experiments is set to $10kHz$.

4 Results

The system in Eq. 1, considering $\omega_F = 1.002$, lies in a bistable region (see Fig. 1(c)). We can distinguish oscillations with small or large amplitude motion that corresponds to two fixed points in the $p-q$ plane. The periodic orbits for the system in the variables of the fast dynamic (x, $\dot{x}$) are reported in Fig. 2(a) with soft colours. When the slow modulation of ω_0 is applied to the system ($\tilde{\omega}_0 \neq 0$), the two stable configurations do not hold any more. Observing the dynamics with a discrete time mapping represented by the Poincaré section, it is possible to recognize the birth of quasiperiodic motion in the system. In detail, both the original limit cycles evolve towards the new regime, the system response defined by these new attractors is very different from the un-modulated scenario where only periodic solutions can occur. The magnitude of the loop in the return map is found to be increasing with the magnitude of the modulation as reported in Fig. 2(a), while the frequency is kept constant during the simulations. A spiraling pattern is observed with a feature encircling the low amplitude attractor even for relative low modulation.

Figure 2(b) shows a bifurcation diagram presenting the evolution of the map with respect to the modulation amplitude. The loops for the high and low amplitude attractors progressively increase until they start to intermix for values of $\tilde{\omega}_0 \sim 0.001$. Proceeding in the transition, they then merge in a unique attractor. Furthermore, the system quickly passes towards a region of quasichaotic motion with the presence of strange nonchaotic attractor. For larger modulation, the complexity of the attractor reduces again and the methamorphosis ends in the quasiperiodicity highlighted in yellow in Fig. 2(b)

In Fig. 2(c), the experimental data in the slow variable phase-space reports the cycling induced by the presence of the low modulation. The spread around the attractor is primarily due to noise in the system that induces strong fluctuation in the amplitude. The quasiperiodicicy in the membrane motion is the consequence of two incommensurate frequencies in the system (resonating frequency ω_F and slow modulation ω_G). This rather subtle characteristic is not only mathematical but also physically relevant. It follows that it is natural to investigate its range of appearance/disappearance understanding the structural stability of the quasiperiodic motion [9]. Finally, in Fig. 2(c), the simulated quasiperiodic attractor is overlapped in order to allow for a direct comparison between experiment and theory.

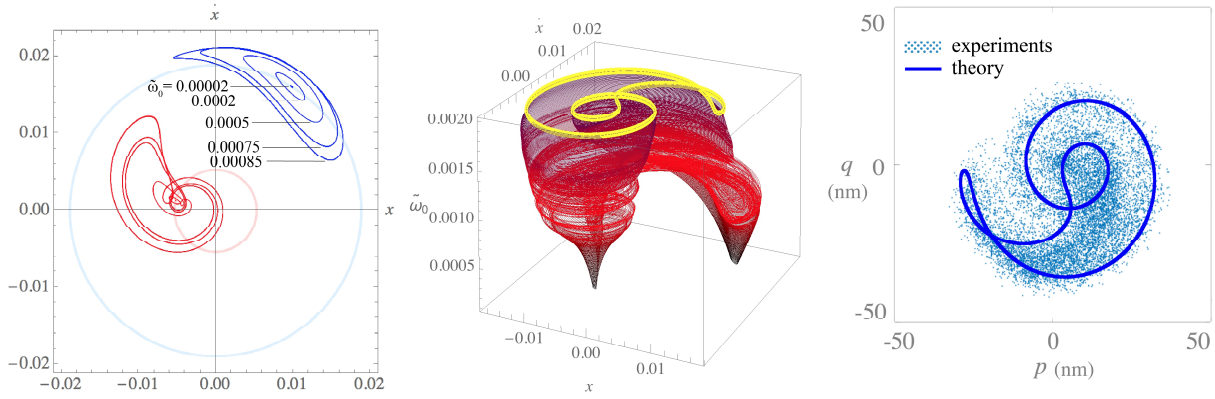

(a) (b) (c)

Figure 2: a) Phase-space showing the limit cycles in the absence of modulation: small/large amplitude motion shown in light red/blue colours. With red/blue colors the closed loops in the Poincaré maps for $\tilde{\omega}_0 \in \{0.00002, 0.0002, 0.0005, 0.00075, 0.00085\}$. b) Evolution of the quasiperiodic motion with respect to the amplitude of the laser power modulation $\tilde{\omega}_0$. The cycling encountered in the experiment is highlighted in yellow. c) Experimental time-trace represented in the in-phase (p) and out-of-phase component (q) . A phase-shift is added to the experimental data in order to correct for the additional phase shifts in the electronical and optical components. The quasiperiodic attractor is overlapped to the clouds of points.

5 Conclusions

This study reports the presence of quasiperiodic motion in graphene resonators with slow frequency modulation. This picture has been confirmed by numerical calculations able to describe the cycling pattern observed in experiments. The theoretical findings suggest that the low frequency thermomechanical tension modulation of graphene by a modulated laser in combination with a high frequency thermal expansion actuation force leads to a transition from a periodic, to a quasiperiodic orbit and eventually to a strange nonchaotic attractor.

References

[1] U. Feudel, S. Kuznetsov and A. Pikovsky. *Strange Nonchaotic Attractors: Dynamics Between Order And Chaos In Quasiperiodically Forced Systems*. World Scientific Series On Nonlinear Science Series A. World Scientific Publishing Company, 2006.

[2] J. A. Glazier and A. Libchaber. Quasi-Periodicity and Dynamical Systems: An Experimentalist's View. *IEEE Transactions on Circuits and Systems*, **35**(7), 790–809, 1988.

[3] F. K. Lamb, N. Shibazaki, M. A. Alpar and J. Shaham. Quasi-periodic oscillations in bright galactic-bulge x-ray sources. *Nature*, **317**, 681–691, 1985.

[4] A. P. Kuznetsov and Y. V. Sedova. The simplest map with three-frequency quasi-periodicity and quasi-periodic bifurcations. *International Journal of Bifurcation and Chaos*, **26**(8), 1630019, 2016.

[5] R. J. Dolleman, D. Davidovikj, S. J. Cartamil-Bueno, H. S. J. van der Zant and P. G. Steeneken. Graphene squeeze-film pressure sensors. *Nano Letters*, **16**(1), 568–571, 2016.

[6] D. Davidovikj, F. Alijani, S. J. Cartamil-Bueno, H. Zant, M. Amabili and P. G. Steeneken. Nonlinear dynamic characterization of two-dimensional materials. *Nature Communications*, **8**(1), 1253, 2017.

[7] R. J. Dolleman, S. Houri, D. Davidovikj, S. J. Cartamil-Bueno, Y. M. Blanter, H. S. van der Zant and P. G. Steeneken. Optomechanics for thermal characterization of suspended graphene. *Physical Review B*, **96**(16), 165421, 2017.

[8] M. I. Dykman, C. M. Maloney, V. N. Smelyanskiy and M. Silverstein. Fluctuational phase-flip transitions in parametrically driven oscillators. *Phys. Rev. E*, **57**, 5202–5212, 1998.

[9] C. Grebogi, E. Ott and J. Yorke. Attractors on an n-torus - quasiperiodicity versus chaos. *Physica. D, Nonlinear Phenomena*, **15**(3), 354–373, 1985.

EUROMECH Colloquium 603
Dynamics of micro and nano systems
5 – 7 September 2018, Porto, Portugal

Molecular dynamics for characterization of probe-sample interaction in atomic force microscopy

Pierpaolo Belardinelli, Abhilash Chandrashekar, Urs Staufer and Farbod Alijani

Precision and Microsystems Engineering, TU Delft, Delft, The Netherlands
p.belardinelli@tudelft.nl, a.chandrashekar@tudelft.nl, u.staufer@tudelft.nl, f.alijani@tudelft.nl

Summary. This work investigates the nature of tip-sample interaction in Atomic Force Microscopy (AFM). Unfolding the contact evolution between probe tip and specimen is especially needed when making the AFM a quantitative tool for identification purposes. Here, we illustrate the use of simulations for interpreting the physics of the interaction. Our analysis is based on extensive molecular dynamics simulations within the context of the AFM operational static instability. It is found that atomistic molecular dynamics can successfully reconstruct the experimental force-distance curve and catch the snap-to-contact event that represents a rich source of unexplored data for nanomechanical characterization.

Keywords: Atomic force microscopy, molecular dynamics, tip-sample interaction, static instability.

1 Introduction

In the characterization and manipulation of surface properties at atomic scale, Atomic Force Microscopy (AFM) plays certainly the role of the most prominent and ubiquitous tool [1]. By exploiting a variety of operational modes and thanks to its resolution, AFM has been successfully applied to study hard and soft materials in both air and liquid environments [2, 3]. However, the interactions between the AFM tip and sample are still not fully understood and this is still a topic under debate [4]. As a matter of fact, promising applications for the AFM as a deterministic tool for identification and metrology are unresolved. The whole understanding has been conceptually hindered by the nature of the interaction that is exerted at nanoscale. Thus, it is inappropriate to capture the atomic scale interplay between the tip and sample by means of continuum contact mechanics models [5]. The scale of the problem suggests the use of a molecular dynamics (MD) -based approach [6]. MD is a modeling technique that can capture atomic scale interactions and has played an important role in the study of other countless nanoscale contacts problems [7].

At present there have been few MD simulations focusing on AFM and looking to different aspects of the interaction [8]. A molecular approach can catch local contact stiffness and energy dissipation for the nanoscale tip [9]. This approach has the capability to unravel the interplay between the atomic interactions even for complex scenarios involving polymers [10]. It is worth to mention that the actual computational capabilities limit MD in presence of dynamic contacts. Simulations are restricted in both spatial (size of the objects) and time duration (period of the dynamical interaction), denying a direct comparisons with the experimental observables.

The main goal of this work is to introduce a molecular dynamic code able to properly reconstruct the dual interplay between the cantilever tip and the investigated specimen during spectroscopy. The new tool is meant for reverse identification path of mechanical properties at nanoscale and to get useful insight about dissipation phenomena arising from the tip/sample interaction.

2 Molecular dynamics approach

The MD simulations has been performed by using LAMMPS [11]. The software integrates the equations of motion by using the velocity-Verlet algorithm, with an integration time step of 0.25 fs. The geometry of the system is illustrated in Fig. 1(a) and it is composed of a conical probe with a rounded semispherical tip (red/blue atoms) and a parallelepipedal sample (yellow/white atoms). The lower thin layer of atoms (white coloured) is considered fixed and it represents the boundary condition for the sample. The tip movement is constrained to the direction along the normal to the sample. On the base of the probe (blue

atoms) and specifically on its center of mass, we have introduced a spring and a damping force to account for the spring constant and quality factor of the cantilever resonator. In our simulations $k = 0.25$ N/m and $Q = 50$. Finally, a shrink wrapped boundary condition is used for the MD environment in all three dimensions.

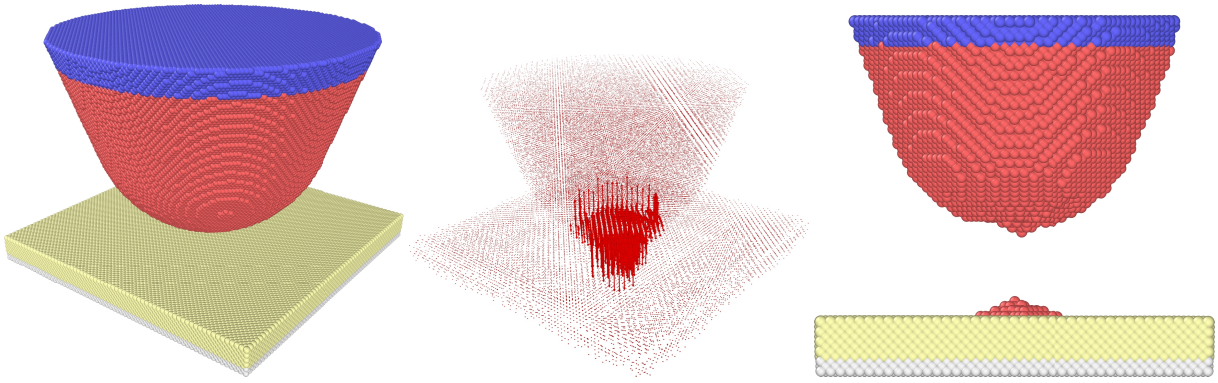

(a) (b) (c)

Figure 1: The schematics of the MD model. a) A snapshot of the molecular system. The red/blue colours are the moving/constrained atoms of the silicon tip. Moreover, the yellow/white colors represent the moving/constrained atoms of the silicon sample. The shown tip has a radius 8 nm and a semi-angle of the conical shape being 0.349 rad. b) The force field during the tip-sample interaction. Only the z-component (with normal perpendicular to the undeformed sample) is retained. c) A snapshot of the retracted tip in the presence of wear.

The forces between atoms are described by the Lennard-Jones potential, which is commonly used for modeling the atomic interactions [12]. The initial disposition of the atoms does not correspond to equilibrium or the minimum potential state. Therefore, we first minimize the total potential energy. The system is then equilibrated in the constant volume and constant temperature ensemble (NVT) by means of the Nosé-Hoover thermostat algorithm.

In order to simulate force-spectroscopy measurements, the movement of the dither piezo is mimicked by approaching and retracting the sample to the probe in a quasi static way and the response is studied in an energy conserving ensemble. During the macroscopic motion, the position of the atoms and the forces acting within the system are collected every 0.25 ps (1000 steps). Figure 1(b) reports the force field occurring during the contact, i.e. after the so-called 'pull-in' of the tip. The way the atoms interact is determined from the interatomic potential function, thus MD is able to catch specific interacting behaviours. For instance, by simulating a large setpoint (deflection of the cantilever at which the approach operation ends), it is likely to observe deterioration phenomena at the very end of the tip (Fig. 1(c)).

3 Results

To allow for quantitative comparison of the MD model with reality, a set of measurements has been performed. Figure 2(a) shows the topographic image of the silicon sample used for the experiments. An important role is played by the humidity present in the system and its possible effects in terms of capillarity and adhesion. Thus, the experiments has been conducted in a controlled environment with a low regime of humidity (less then 1%) and by choosing a point in the sample with high elevation (black arrow in Fig. 2(a)) able to minimize the effect of water film. At this location a force-distance curve was recorded with a small set-point of 5 nm in order to avoid deformation of the tip ($\sim$ 8 nm radius). Figure 2(b) reports the approach and the retract curves with gray and black lines, respectively. The perfect overlapping of the two phases underlines the absence of deformations or residual contamination. The cantilever, initially straight, starts to bend by the attractive tip-sample force. When the attractive forces overcome the elastic restoring force of the cantilever, the tip-sample gap collapses (snap-in). The

tip is in contact with the surface, and the deflection of the cantilever is linear with respect to the vertical displacement of the sample. The retraction from the sample follows the same path, however, due to adhesion forces the snap-out is retarded. This behaviour has already been reported in literature [13]. The inset of Fig. 2(b) magnifies the damped oscillations of the cantilever immediately after the snap-out.

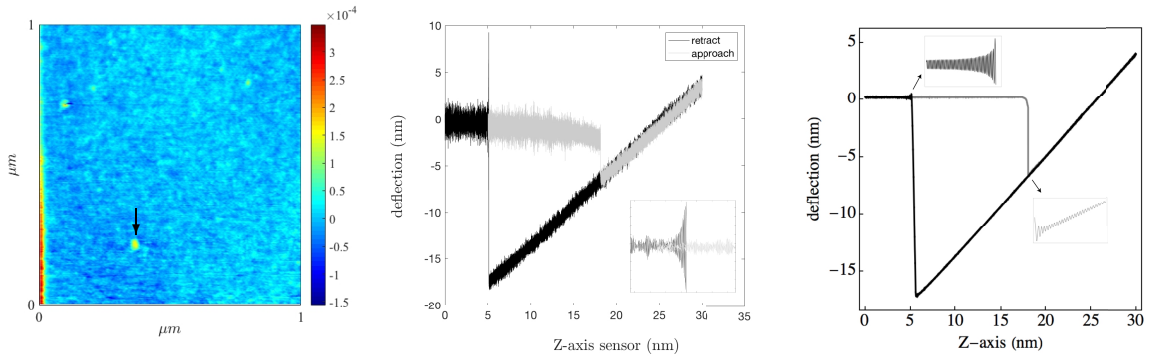

(a) (b) (c)

Figure 2: Experimental data and MD numerical simulations. a) AFM image of the silicon sample. The topology has in warm colors higher regions. The exact point for the spectroscopy of Fig. 2(b) is indicated with the arrow. b) Experimental force-distance curve. The gray/black curve shows the approach/retract operation. In the inset a magnified view of the ring-down of the cantilever after the snap-out. The latter is achievable only by using a high-resolution acquisition. c) Simulated force-distance curve with MD.

The experimental configuration in Fig. 2(a)-(b) is numerically simulated, Figure 2(c) illustrates the force-distance curve obtained within the MD environment. Beside the transient response at the snap-out (black curve in the inset), in Fig. 2(c) it is also possible to recognize a damped oscillating signal just after the point when the atomic force microscope tip contacts the sample surface (gray curve in the inset). The first ringdown is related only to the mechanical properties of the cantilever whereas the latter is related to the damping of the sample. Although the reconstructed static instability follows the behaviour of Fig. 2(b), there is still some discrepancy. We suppose the experimental data containing additional contributions, e.g. the presence of electrostatic forces or presence of water layer. This can be fixed for instance by an improved composition of different potentials and it requires further investigations.

4 Conclusions

In conclusion, we used molecular dynamics simulations to investigate the physics of tip-sample interaction in atomic force microscopy. The configuration analysed is the static instability occurring during a spectroscopic experiment. By employing an atomistic approach, the deterioration of the probe can be successfully reconstructed. This provides a new understanding of the involved tip-sample interaction and the tip wear. Our approach permits to reconstruct the force distance curve in its all peculiar features, namely the snap-in and snap-out and their relative transient responses. Further investigations are needed in order to have a quantitative match with the experimental data and develop a molecular dynamic based identification algorithm that can be used for real-time identification during AFM measurements.

Acknowledgement

The authors acknowledge financial support of NWO-TTW open technology program for grant number 15450 “a nice tip tap”.

References

[1] Y. Gan. Atomic and subnanometer resolution in ambient conditions by atomic force microscopy. *Surface Science Reports*, **64**, 99–121, 2009.

[2] S. N. Magonov and D. H. Reneker. Characterization of polymer surfaces with atomic force microscopy. *Annual Review of Materials Science*, **27**, 175–222, 1997.

[3] S. Basak and A. Raman. Dynamics of tapping mode atomic force microscopy in liquids: Theory and experiments. *Applied Physics Letters*, **91**, 064107, 2007.

[4] V. Vahdat, D. S. Grierson, K. T. Turner, and R. W. Carpick. Mechanics of interaction and atomic-scale wear of amplitude modulation atomic force microscopy probes. *ACS Nano*, **7**, 3221–3235, 2013.

[5] B. Luan and M. O. Robbins. The breakdown of continuum models for mechanical contacts. *Nature*, **435**, 929, 2005.

[6] Y. Dong, Q. Li, and A. Martini. Molecular dynamics simulation of atomic friction: A review and guide. *Journal of Vacuum Science & Technology A*, **31**, 030801, 2013.

[7] U. Landman, W. D. Luedtke, N. A. Burnham, and R. J. Colton. Atomistic mechanisms and dynamics of adhesion, nanoindentation, and fracture. *Science*, **248**, 454–461, 1990.

[8] X. Hu, P. Egberts, Y. Dong, and A. Martini. Molecular dynamics simulation of amplitude modulation atomic force microscopy. *Nanotechnology*, **26**, 235705, 2015.

[9] R.-G. Xu and Y. Leng. Contact stiffness and damping of liquid films in dynamic atomic force microscope. *The Journal of Chemical Physics*, **144**, 154702, 2016.

[10] N. Onofrio, G. N. Venturini, and A. Strachan. Molecular dynamic simulation of tip-polymer interaction in tapping-mode atomic force microscopy. *Journal of Applied Physics*, **114**, 094309, 2013.

[11] S. Plimpton, P. Crozier, and A. Thompson. Lammps-large-scale atomic/molecular massively parallel simulator. *Sandia National Laboratories*, **18**, 43, 2007.

[12] J. N. Israelachvili. *Intermolecular and Surface Forces (Third Edition)*. Academic Press, San Diego, 2011.

[13] S. J. Eppell, L. Li, and F. R. Zypman. Unexplored territory in the afm force curve contains nanomechanics information. *AIP Advances*, **7**, 105208, 2017.

EUROMECH Colloquium 603
Dynamics of micro and nano systems
5 – 7 September 2018, Porto, Portugal

Application of modified LuGre friction model to the analysis of friction-induced oscillations

Danylo Pikunov and Andrzej Stefanski

Lodz University of Technology, Lodz, Poland
dpikunov@gmail.com
steve@p.lodz.pl

Summary. This paper focuses on the analysis of the friction-induced mechanical oscillator with cubic nonlinearity and dynamic model of dry friction applied. The studied model is based on the classical LuGre approach to multi-scale modelling of friction phenomenon. Lyapunov exponents spectrum of the frictional oscillator is calculated by means of recently implemented method of their estimation for non-smooth systems. The results of the numerical research and observations of the nature of oscillator response and its interaction with the applied dynamic friction model are reported.

Keywords: multi-scale modelling of friction, modified LuGre model, hysteretic effects, friction-induced vibrations.

1 Introduction

Dry friction phenomenon implicates appearance of discontinuous differential equations, where the discontinuity character depends on the choice of the friction model. In general, there are many different types of dry friction models and it is crucial to appropriately choose one which suits best to the modelled problem. For example, if one considers the system's dynamics where the relative velocity remains constant, one can describe friction by the simplest case of Coulomb law [1] and there is no need to elaborate complex dry friction model. In such cases, friction force as a function of the relative velocity is single-valued and follows the same path during acceleration and deceleration phases. However, many of known experiments, in which the relative velocity oscillates, showed that the friction-velocity relation is multi-valued: friction force follows different curves during acceleration and deceleration, so the hysteretic loops are formed [2-5]. In simple words, hysteresis is a retardation of an effect when the forces (friction forces in our case) acting upon a body are changed. In such situations, the adopted model of friction force must provide a proper means of guiding the system through zero relative velocity, i.e., define a mechanism governing the switch between the stick phase (microscopic pre-sliding) and macroscopic sliding phase. Obliviously, these models should predict stick and slip phases of motion. During the stick phase the friction force is higher, than in slipping. All these facts are the reasons why the systems with dry friction may hold many different types of dynamic behaviours and it is important to appropriately provide an analysis of system's dynamics.

In general, the innovative character of the presented frictional oscillator analysis is based on the fact that the system response along with the friction force given by the dynamic model is studied. This research is focused on the mutual correlation (synchronization) of the oscillator and friction force dynamics

2 Analyzed system

The system under investigation consists of mass-spring structure with the mass undergoing to external harmonic forcing while situating on a belt, which moves with constant velocity V_b (Fig. 1). The assumed frictional oscillator is considered to be an oscillator of Duffing's type with the non-linear spring characteristic KX^2. The dynamics of this oscillator is governed by the following non-autonomous equation of motion.

$$M\ddot{X} + KX^3 = F(V_r) + U_0 \sin \Omega t \,. \tag{1}$$

If one considers the reference frequency as $\omega = \sqrt{g/x_0}$ [rad s^{-1}], where characteristic length is defined as $x_0 = \sqrt[3]{Mg/K}$ [m] one can derive the equation of motion in non-dimensional form as follows:

$$x'' = -x^3 + N_0 f(v_r) + u_0 \sin \eta t \,. \tag{2}$$

The primes in Eq.(2) and in the forthcoming equations denote differentiation with respect to the non-dimensional time $\tau = \omega t$.

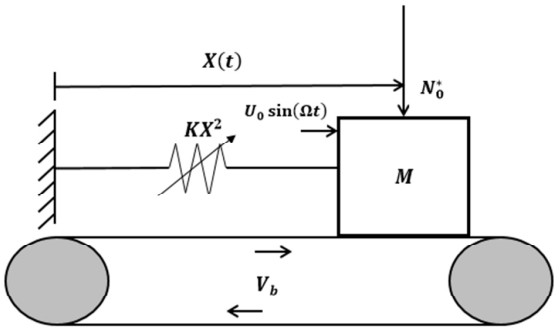

Figure 1. Analyzed stick-slip oscillator.

3 Modified LuGre model

One of the frequently used friction models is the LuGre one developed by de Wit et al. [6], which is a well-known example of dynamic friction approach. It follows that friction must depend not only on relative velocity v_r as it is in static friction models, but also on internal state variable. The LuGre friction model incorporates the microscopic degrees of freedom: the asperities of surface in contact are considered to behave as elastic spring-like bristles with damping. In such a case, the total friction force can be represented as a sum of all the forces generated from the bending of asperities and a viscous friction term, which is considered to be proportional to the relative velocity between contacting surfaces [6]. A mathematical interpretation of friction function is:

$$f(v_r, z) = \sigma_0 z + \sigma_1 \frac{dz}{d\tau} + \sigma_2 v_r \,, \tag{3}$$

where z is the average bristle deflection, which introduced as an internal state variable, σ_0 is the bristle stiffness, σ_1 is the bristle damping and σ_2 is the viscous friction coefficient between the surfaces, which move relative to each other. According to reference [6], the evolution of an average bristle deflection can be described as follows:

$$\frac{dz}{d\tau} = v_r - \frac{|v_r|}{g(v_r)} z \,, \tag{4}$$

where positive function $g(v_r)$ determines the Stribeck effect.

The desired purpose of this paper is to provide an analysis of an extended friction model, which may fit well with any of known experiments and demonstrates both clockwise and counter-clockwise hysteretic loops in pure sliding domain [2-5]. Due to that fact, there has been investigated a particular case of modified LuGre friction model, which was recently implemented by Saha et al. [7]. This model gives different description of the average asperity deflection in form of Eq. (6):

$$\frac{dz}{d\tau} = v_r w_1 \left(1 - \frac{\sigma_0 z}{g(v_r)} \operatorname{sign}(v_r)\right) + v_r w_2 \left(1 - \frac{\sigma_0 z}{g(v_r)} \operatorname{sign}(v_r)\right)^2 \operatorname{sign}\left(1 - \frac{\sigma_0 z}{g(v_r)} \operatorname{sign}(v_r)\right). \tag{5}$$

4 Numerical analysis

Finally, the equation of motion of the assumed friction-induced oscillator with application of the modified LuGre friction model in a state-space form is:

$$x' = y\,, \tag{6a}$$

$$y' = -x^3 + N_0 f(v_r) + u_0 \sin \eta t\,, \tag{6b}$$

$$z' = v_r\left(1-\frac{\sigma_0 z}{g(v_r)}\operatorname{sign}(v_r)\right)\left(w_1 + v_r w_2\left(1-\frac{\sigma_0 z}{g(v_r)}\operatorname{sign}(v_r)\right)\operatorname{sign}\left(1-\frac{\sigma_0 z}{g(v_r)}\operatorname{sign}(v_r)\right)\right), \tag{6c}$$

where v_r=v_b–y'.

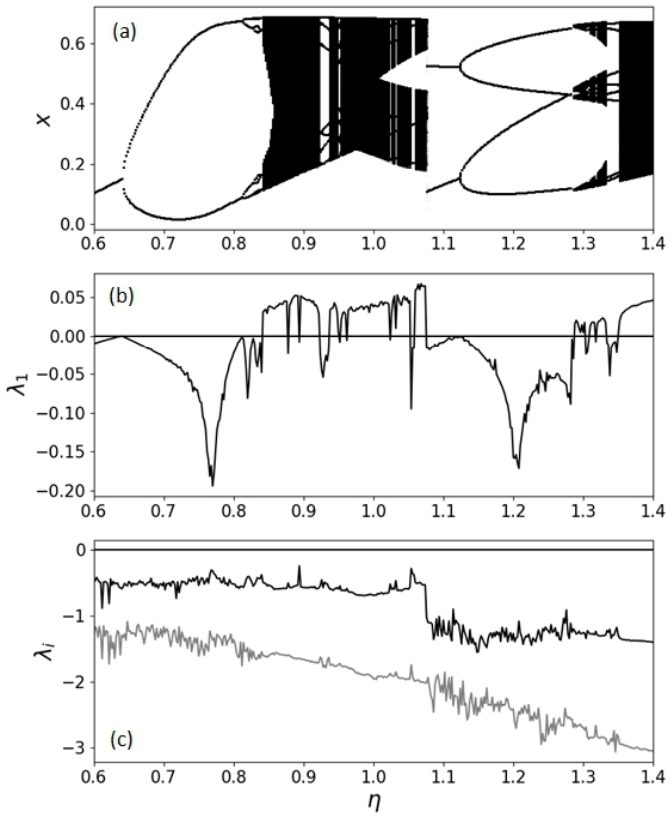

Figure 2. (a) Bifurcation diagram, (b) corresponding largest Lyapunov exponent graph of the system (Eqs.(6a-c)) and (c) the others Lyapunov exponents from the spectrum.

The analysis, provided in this Section, refers to the novel method of LEs estimation, described in [8]. Changing incrementally the forcing frequency η in the analyzed system, bifurcation diagram can be obtained along with the corresponding Lyapunov exponents graph. The dimensionless excitation frequency η was used as a control parameter in range from 0.6 to 1.4 with the step 0.002 to obtain the bifurcation diagram of the state variable x of the system (Eqs. (6a-c)). The results can be seen in Figs. 2a-c, where bifurcation diagram (Fig. 2a) of the system (Eqs. (6a-c)) and corresponding graphs of the largest one (Fig. 2b) and remaining negative LEs (Fig. 2c) are demonstrated. It can be noticed that the LEs graphs of the system under consideration are consistent with the bifurcation diagram: regular regions correspond to negative the largest LE, while positive dominant exponent (see Fig. 2b) indicate chaotic response of the frictional oscillator (see Fig. 3a). Comparing phase portrait from Fig. 3a with friction force characteristic depicted in Fig. 3b one can observe a tendency to correlation between them, i.e., chaotic dynamics of the system response is followed/reflected by the friction characteristic.

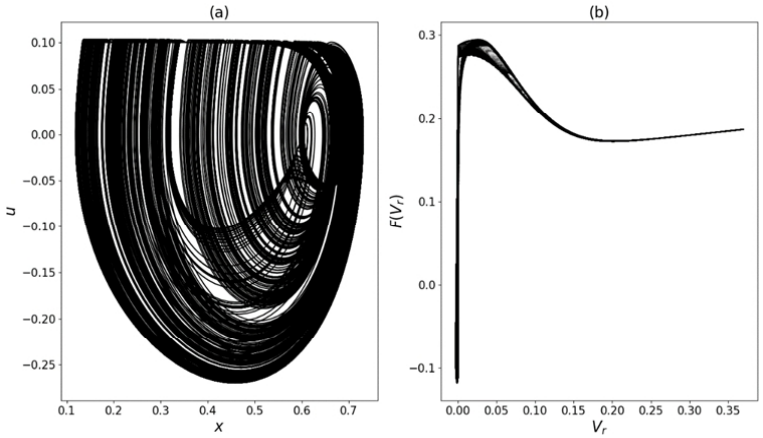

Figure 3. (a) Phase portrait and (b) friction force-relative velocity curve of the frictional oscillator (Eq.(6a-c)) for $\eta = 0.9$ – chaotic response ($\lambda_1 = 0.048$).

5 Conclusions

A detailed parametric study of a single degree-of-freedom frictional oscillator, presented in this paper, reveals the influence of different friction parameters on the friction force characteristics and on the dynamics of the system. The original character of the presented research lies in the fact that the analysis includes the internal variable, which characterizes the coefficient of friction in the applied model, as an integral part of the system under consideration. In this study, modified LuGre friction model was adopted. As a result, a dynamic system defined in a four-dimensional phase space (considering external harmonic excitation) consisting of two coupled subsystems, i.e., an oscillator and friction force coefficient, was obtained. The stability analysis of correlations between the response of the oscillator and the dynamics of the friction force shows the tendency to a mutual reflection between them. In the future, it's planned to introduce and study more different dynamic models of friction, which would correspond well to the experimental observations.

Acknowledgments

This work has been supported by Polish National Centre of Science (NCN) under Project no.DEC-2012/06/A/ST8/00356.

References

[1] C.A. Coulomb, *Théorie des machines simples*. Mémoires de Mathématique et de Physique de l'Academie des Sciences, 161-331, 1785.

[2] V. Lampaert, F. Al-Bender, J. Swevers, Experimental characterization of dry friction at low velocities on a developed tribometer setup for macroscopic measurements. *Tribology Letters*, **16**(1-2) 95-105, 2004.

[3] H. Yanada, Y. Sekikawa, Modeling of dynamic behaviors of friction, *Proc. Inst. Mech. Eng., Part C: J. Mech. Eng. Sci.* **220**, 273–284, 2006.

[4] J. Wojewoda, A. Stefanski, M. Wiercigroch, T. Kapitaniak, Hysteretic effects of dry friction: modelling and experimental studies. *Philosophical Transactions of the Royal Society of London A: Mathematical, Physical and Engineering Sciences*, **366**(1866), 747-765, 2008.

[5] K. Guo, X. Zhang, H. Li, G. Meng, Non-reversible friction modeling and identification. *Archive of Applied Mechanics*, **78**(10), 795-809, 2008.

[6] C.C. de Wit, P. Lischinsky, K.J. Astrom, H. Olsson, A New Model for Control of Systems with Friction. *IEEE Transactions on Automatic Control*, **40**(3), 419-425, 1995.

[7] A. Saha, P. Wahi, M. Wiercigroch, A. Stefanski, A modified LuGre friction model for an accurate prediction of friction force in the pure sliding regime. *Int. J. Nonlinear Mech*., **80,** 122-131, 2016.

[8] M. Balcerzak, A. Dabrowski, A. Stefanski, J. Wojewoda, Spectrum of Lyapunov exponents in non-smooth systems evaluated using orthogonal perturbation vectors. In MATEC Web of Conferences, EDP Sciences, **148** (2018) 10003.

Author Index

Abdel-Rahman, E. M. 88, 124
Akhavan, H. 141
Alfosail, F. K. 116
Alijani, F 6, 11, 155, 159
Allan, N. L. 28
Alneamy, A. M. 88, 124
Aziz, A. K. A. 88
Bachtold, A. 145
Baguet, S. 51
Bajaj, A. 71
Balthazar, J. M. 104, 108
Bastardo, P. 21
Batra, R. C. 120
Belardinelli, P. 11, 155, 159
Bellaredj, M. L. 41
Biswas, S. 129
Bueno, Á. M. 104
Campo-Deaño, L. 84
Castro, C. 21
Castro, P. T. de 21
Cepellotti, A. 145
Chandrashekar, A. 159
Chouvion, B. 59
Chuaqui, T. 112
Comi, C. 63
Corigliano, A. 63
Dahiya, A. 120
Davidovikj, D. 6
Degenfeld-Schonburg, P. 17
Deü, J.-F. 47
Dolleman, R.J. 6, 155
Dufour, R. 51
Dykman, M. I. 133
Faisal, M. 147
Falorni, L. 55, 63
Fey, R.H.B. 34
Fotuhi, A. R. 141
Frangi, A 55
Fuinel, C. 47
Galindo-Rosales, F.J. 100
Ghaffari, R. 43
Gilat, R. 76
Givois, A. 47
Gogoi, A. K. 129
Goldsche, M. 96
Gottlieb, O. 2
Grenat, C. 51
Grolet, A. 47
Guerrieri, A. 55
Gupta, S. S. 43, 120
Gutschmidt, S. 92
HaLevy, O. 80
Heppler, G. R. 88
Hollander, E. 2
Hosseini, A. H. 147
Ilyas, S. 116, 118
Isacsson, A. 145
Ivanov, D. 28
Jaber, N. 41
Jandaghian, A. A. 151
Janzen, F. C. 104
Kalafut, D. 71
Khater, M. E. 88
Khodkov, T. 96
Kirchhof, J. N. 96
Kosuru, L. 41
Krakover, N. 80
Krylov, S. 76, 80
Lamarque, C-H. 51
Langfelder, G. 63
Legrand, B. 47
Lenci, S. 11, 41
Lenzi, G. G. 108
Manca, M. 145
Manoach, E. 137
Mansour, R. 124
Marie, X. 145
Mathieu, F. 47
Matos, M. A. S. 25
Mauri, F. 145
McWilliam, S. 59, 67
Mehner, J. E. 17
Mihajlović, N. 34
Minotti, P. 63
Mokhalingam, A. 43
Morell, N. 145
Nabholz, U. 17
Nafissi, H. 124
Nakamura, T. 32
Napoli, V. Di 67
Niaei, A. R. M. 147
Nicu, L. 47
Nijmeijer, H. 34
Parras, L. 100
Pekař, M. 34
Pfusterschmied, G. 38
Pikunov, D. 163
Pinho, S. T. 25
Pinto, T. R. 84
Platz, D. 38
Popov, A.A. 59, 67
Rahmani, O. 147, 151
Raman, A. 71
Reserbat-Plantey, A. 145
Ribeiro, P. 112, 141
Rocha, R. T. 104, 108
Roody, B. S. 141
Roque, C. 14
Ruzziconi, L. 41
Sajadi, B. 11
Sattel, T. 92
Sauer, R. A. 43
Scarpa, F. 28
Schatz, F. 17
Schmid, U. 38
Shaw, S. W. 133
Shoshani, O. 133
Shterev, K. 137
Shulepov, S. 34
Sonntag, J. 96
Specchia, S. 108
Stampfer, C. 96
Staufer, U. 159
Steeneken, P.G. 6, 155
Stefanov, S. 137
Stefanski, A. 163
Tagarielli, V. L. 25
Tavares, S. 21
Tei, S. 74
Tepsic, S. 145
Thomas, O. 47
Tolladay, M 28
Tooski, M. Y. 151
Tusset, A. M. 104, 108
van der Zant, H.S.J. 6
van Nispen, S.H.M. 34
Verbiest, G. J. 96
Wagner, N. 92
Yabuno, H. 32, 74
Yano, M. 32
Younis, M. I. 4, 41, 116, 118
Zega, V. 55, 63